

AD-A219 595

NPS 68-89-010

NAVAL POSTGRADUATE SCHOOL

Monterey, California



THESIS

DTIC
ELECTE
MAR 23 1990

MODELING STUDIES OF THE LEEUWIN
CURRENT USING A HIGH-RESOLUTION
PRIMITIVE EQUATION MODEL

by

Martin J. Rutherford

September 1989

Thesis Advisor

Mary L. Batteen

Approved for public release; distribution is unlimited.

Prepared for:
National Science Foundation
1800 G Street, N.W.
Washington, DC 20550

NAVAL POSTGRADUATE SCHOOL
Monterey, CA. 93943


Rear Admiral Ralph W. West, Jr.
Superintendent

Harrison Shull
Provost

This project was funded by the National Science Foundation, 1800 G Street,
N.W., Washington, DC 20550.

Reproduction of this report is authorized.

Released By:


GORDON E. SCHACHER
Dean of Science and Engineering

Unclassified

security classification of this page

REPORT DOCUMENTATION PAGE

1a Report Security Classification Unclassified			1b Restrictive Markings		
2a Security Classification Authority			3 Distribution Availability of Report		
2b Declassification Downgrading Schedule			Approved for public release; distribution is unlimited.		
4 Performing Organization Report Number(s) NPS 68-89-010			5 Monitoring Organization Report Number(s)		
6a Name of Performing Organization Naval Postgraduate School		6b Office Symbol (if applicable) 68	7a Name of Monitoring Organization Naval Postgraduate School		
6c Address (city, state, and ZIP code) Monterey, CA 93943-5000		7b Address (city, state, and ZIP code) Monterey, CA 93943-5000			
8a Name of Funding Sponsoring Organization National Science Foundation		8b Office Symbol (if applicable)	9 Procurement Instrument Identification Number NSF Grant No. OCE-8809465		
3c Address (city, state, and ZIP code) 1800 G Street, N.W., Washington D.C. 20550		10 Source of Funding Numbers			
		Program Element No	Project No	Task No	Work Unit Accession No
11 Title (include security classification) MODELING STUDIES OF THE LEEUWIN CURRENT USING A HIGH-RESOLUTION PRIMITIVE EQUATION MODEL (Unclassified)					
12 Personal Author(s) Martin J. Rutherford in conjunction with M.L. Batteen					
13a Type of Report Master's Thesis		13b Time Covered From To		14 Date of Report (year, month, day) September 1989	15 Page Count 203
16 Supplementary Notation The views expressed in this thesis are those of the author and do not reflect the official policy or position of the Department of Defense or the U.S. Government.					
17 Cosati Codes		18 Subject Terms (continue on reverse if necessary and identify by block number)			
Field	Group	Subgroup	PE ocean model, eddy resolving, Leeuwin Current		
<input checked="" type="checkbox"/> Abstract (continue on reverse if necessary and identify by block number) A primitive equation model is run to investigate generation and instability mechanisms in the Leeuwin Current. The current is generated by the model using a combination of density forcing from the climatological Indian Ocean thermal structure, the influx of warm low salinity water from the North West (NW) Shelf, and the climatological wind stress. The current thus generated is compared with observations taken during the LeeUwin Current Interdisciplinary Experiment (LUCIE). In the absence of the NW Shelf water, which corresponds to the austral spring and summer flow, wind forcing is dominant at the equatorward end of the domain and geostrophic flow, driven by the Indian Ocean thermal gradient dominates at the poleward end. This leads to a weak coastal upwelling regime with equatorward and offshore flow at the equatorward end. Further poleward, the stronger Indian Ocean forcing establishes a poleward surface current and equatorward undercurrent which accelerates poleward, into the prevailing wind. The inclusion of NW Shelf waters, typical of the austral fall and winter seasons, completely dominates the wind forcing at the equatorward end of the model. The effects of the NW Shelf water weaken away from the source region but they continue to augment the Indian Ocean forcing, resulting in a stronger flow along the entire coastal boundary. The current generated by the model compares well with available observations. The current also has significant mesoscale variability. An analysis of the energy transfers in the period during which eddies are generated shows barotropic instability to be dominant over baroclinicity in the current forced by the Indian Ocean thermal structure. The addition of wind forcing adds to the barotropic instability and leads to an earlier development of eddies. The NW Shelf waters add strong baroclinicity, which weakens poleward, to the current. They also locally increase the barotropic instability near their source. Several scales of eddies are found to be dominant. The forcing by the Indian Ocean and wind stress leads to eddy growth on scales around 385 km. With the inclusion of the NW Shelf waters, the wavelengths associated with mesoscale variability are around 160 km and 330 km after 160 days, consistent with available observations.					
20 Distribution Availability of Abstract <input checked="" type="checkbox"/> unclassified unlimited <input type="checkbox"/> same as report <input type="checkbox"/> DTIC users			21 Abstract Security Classification Unclassified		
22a Name of Responsible Individual Mary L. Batteen			22b Telephone (include Area code) (408) 646-3265		22c Office Symbol 68Bv

Keywords: Thesis (kr)

Approved for public release; distribution is unlimited.

Modeling Studies of the Leeuwin Current using
a High-Resolution Primitive Equation Model

by

Martin J. Rutherford
Lieutenant Commander, Royal Australian Navy
B.Sc., University of New South Wales, 1977

Submitted in partial fulfillment of the
requirements for the degree of

MASTER OF SCIENCE IN METEOROLOGY AND PHYSICAL
OCEANOGRAPHY

from the

NAVAL POSTGRADUATE SCHOOL
September 1989

Author:



Martin J. Rutherford

Approved by:



Mary L. Batteen, Thesis Advisor



David C. Smith IV, Second Reader



Curtis A. Collins, Chairman,
Department of Oceanography



Gordon E. Schacher,
Dean of Science and Engineering

ABSTRACT

A primitive equation model is run to investigate generation and instability mechanisms in the Leeuwin Current. The current is generated by the model using a combination of density forcing from the climatological Indian Ocean thermal structure, the influx of warm low salinity water from the North West (NW) Shelf, and the climatological wind stress. The current thus generated is compared with observations taken during the LeeUwin Current Interdisciplinary Experiment (LUCIE). In the absence of the NW Shelf water, which corresponds to the austral spring and summer flow, wind forcing is dominant at the equatorward end of the domain and geostrophic flow, driven by the Indian Ocean thermal gradient dominates at the poleward end. This leads to a weak coastal upwelling regime with equatorward and offshore flow at the equatorward end. Further poleward, the stronger Indian Ocean forcing establishes a poleward surface current and equatorward undercurrent which accelerates poleward, into the prevailing wind. The inclusion of NW Shelf waters, typical of the austral fall and winter seasons, completely dominates the wind forcing at the equatorward end of the model. The effects of the NW Shelf water weaken away from the source region but they continue to augment the Indian Ocean forcing, resulting in a stronger flow along the entire coastal boundary. The current generated by the model compares well with available observations. The current also has significant mesoscale variability. An analysis of the energy transfers in the period during which eddies are generated shows barotropic instability to be dominant over baroclinicity in the current forced by the Indian Ocean thermal structure. The addition of wind forcing adds to the barotropic instability and leads to an earlier development of eddies. The NW Shelf waters add strong baroclinicity, which weakens poleward, to the current. They also locally increase the barotropic instability near their source. Several scales of eddies are found to be dominant. The forcing by the Indian Ocean and wind stress leads to eddy growth on scales around 385 km. With the inclusion of the NW Shelf waters, the wavelengths associated with mesoscale variability are around 160 km and 330 km after 160 days, consistent with available observations.



Accession For	
NTIS GRA&I	<input checked="" type="checkbox"/>
DTIC TAB	<input type="checkbox"/>
Unannounced	<input type="checkbox"/>
Justification	
By	
Distribution/	
Availability Codes	
Dist	Avail and/or Special

TABLE OF CONTENTS

I. BACKGROUND	1
A. INTRODUCTION	1
B. OBSERVATIONAL STUDIES	2
1. The Large Scale Circulation	2
2. A Poleward Flowing Coastal Current	3
3. Drifting Buoy Studies	3
4. Satellite Remote Sensing Studies	4
5. Mesoscale Features	4
C. LEEUWIN CURRENT MODELING STUDIES	7
D. THEORIES FOR THE LEEUWIN CURRENT	8
1. Generation	8
2. Seasonal Variation	9
3. Mesoscale Variability	9
E. OBJECTIVE OF THE THESIS	9
II. MODEL DESCRIPTION	10
A. MODEL EQUATIONS	10
B. FINITE DIFFERENCING	11
C. DOMAIN SIZE AND RESOLUTION	12
D. HEAT AND MOMENTUM DIFFUSION	12
E. WIND FORCING	12
F. SURFACE THERMAL FORCING	13
G. BOUNDARY CONDITIONS	13
III. INITIALIZATIONS, FORCING AND EXPERIMENTAL DESIGN	14
A. INITIALIZATIONS	14
1. Ocean Thermal Structure	14
a. Indian Ocean	14
b. North West Shelf	15
2. Wind Forcing	17
3. Atmospheric Thermal Forcing	18

B. EXPERIMENTAL DESIGN	20
1. Forcing by an Initialized Current (Case 1)	20
2. Forcing by the Indian Ocean Density Field (Case 2)	20
3. Inclusion of North West Shelf Waters (Case 3)	20
4. The Role of Wind Forcing (Case 4)	22
5. Combined Thermal and Wind Forcing (Case 5)	22
IV. ANALYSIS TECHNIQUES	23
A. ENERGY ANALYSIS	23
1. Kinetic Energy	23
2. Available Potential Energy	23
3. Energy Transfers	24
4. Energy Transfer Diagrams	24
B. SPECTRAL ANALYSIS	25
C. STABILITY ANALYSIS	25
V. RESULTS AND DISCUSSION	27
A. LEEUWIN CURRENT GENERATION	27
1. Equatorward End of Domain	29
a. Case 2. Forcing by Indian Ocean Density Field	30
b. Case 3. Forcing by Indian Ocean and NW Shelf	30
c. Case 4. Forcing by Indian Ocean and Winds	31
d. Case 5. Forcing by Indian Ocean, NW Shelf and Winds	31
e. Comparison with Observations	32
2. Center of Domain	36
a. Case 2. Forcing by Indian Ocean Density Field	37
b. Case 3. Forcing by Indian Ocean and NW Shelf	37
c. Case 4. Forcing by Indian Ocean and Winds	37
d. Case 5. Forcing by Indian Ocean, NW Shelf and Winds	38
e. Comparison with Observations	38
3. Poleward End of domain	42
a. Case 2. Forcing by Indian Ocean Density Field	43
b. Case 3. Forcing by Indian Ocean and NW Shelf	43
c. Case 4. Forcing by Indian Ocean and Winds	44
d. Case 5. Forcing by Indian Ocean, NW Shelf and Winds	44

e. Comparison with Observations	45
B. INSTABILITY IN THE LEEUWIN CURRENT	49
1. Case 1. Forcing by Initialized Current	49
a. Energy Analysis	49
b. Spectral Analysis	54
c. Instability Analysis	54
d. Conclusions	65
2. Case 2. Forcing by Indian Ocean Density Field	67
a. Energy Analysis	67
b. Spectral Analysis	67
c. Instability Analysis	79
d. Conclusions	89
3. Case 3. Forcing by Indian Ocean and NW Shelf	89
a. Energy Analysis	89
b. Spectral Analysis	101
c. Instability Analysis	107
d. Conclusion	107
4. Case 4. Forcing by Indian Ocean and Winds	115
a. Energy Analysis	115
b. Spectral Analysis	132
c. Instability Analysis	132
d. Conclusions	139
5. Case 5. Forcing by Indian Ocean, NW Shelf and Winds	139
a. Energy Analysis	142
b. Spectral Analysis	147
c. Instability Analysis	156
d. Conclusions	166
VI. SUMMARY AND RECOMMENDATIONS	179
A. SUMMARY	179
1. Leeuwin Current Generation	179
2. Instability and Eddies	180
B. RECOMMENDATIONS	182
APPENDIX A. VALUES OF CONSTANTS USED IN THE MODEL	183

INITIAL DISTRIBUTION LIST	188
---------------------------------	-----

LIST OF TABLES

Table 1.	INITIAL TEMPERATURE (°C) FOR INDIAN OCEAN	14
Table 2.	INITIAL TEMPERATURE (°C) FOR NORTH WEST SHELF	16
Table 3.	MONTHLY COMPONENTS OF WIND STRESS	17
Table 4.	MONTHLY COMPONENTS OF WIND VELOCITY	18
Table 5.	HEAT BUDGET PARAMETERS	19
Table 6.	MODEL RESULTS. POINT A	29
Table 7.	MODEL/OBSERVATIONS COMPARISON (B VERSUS CARNARVON)	36
Table 8.	MODEL RESULTS. POINT C	36
Table 9.	MODEL/OBSERVATIONS COMPARISON (D VERSUS DONGARA)	42
Table 10.	MODEL RESULTS. POINT E	42
Table 11.	MODEL/OBSERVATIONS COMPARISON (F VERSUS CAPE MENTELLE)	45
Table 12.	SUMMARY OF EDDY INSTABILITY AND GROWTH	181

LIST OF FIGURES

Figure 1. Leeuwin Current	2
Figure 2. AVHRR image of Leeuwin Current region	5
Figure 3. Tracks of buoys influenced by the Leeuwin Current	6
Figure 4. Indian Ocean temperature initialization	15
Figure 5. NW Shelf temperature initialization	16
Figure 6. Wind Forcing	19
Figure 7. Case 1. Forcing by Initialized Current	21
Figure 8. Location of points used for data analysis and comparison	28
Figure 9. Velocity & temperature time series	33
Figure 10. Velocity & temperature time series	34
Figure 11. Velocity & temperature time series	35
Figure 12. Velocity & temperature time series	39
Figure 13. Velocity & temperature time series	40
Figure 14. Velocity & temperature time series	41
Figure 15. Velocity & temperature time series	46
Figure 16. Velocity & temperature time series	47
Figure 17. Velocity & temperature time series	48
Figure 18. Case 1. Surface pressure field, days 0 - 40	50
Figure 19. Case 1. Surface velocity and temperature fields, days 0 - 10	51
Figure 20. Case 1. Surface velocity and temperature fields, days 20 - 30	52
Figure 21. Case 1. Surface velocity and temperature fields, day 40	53
Figure 22. Case 1. Energy time series	55
Figure 23. Case 1. Energy transfers	56
Figure 24. Case 1. Energy transfer diagram	57
Figure 25. Case 1. Energy transfer diagram	58
Figure 26. Case 1. Energy transfer diagram	59
Figure 27. Case 1. Spectral density at day 10	60
Figure 28. Case 1. Spectral density at day 20	61
Figure 29. Case 1. Spectral density at day 30	62
Figure 30. Case 1. Spectral density at day 40	63
Figure 31. Case 1. Spectral density time series	64

Figure 32. Case 1. Cross sections of dq/dx and alongshore velocity	66
Figure 33. Case 2. Surface pressure field, days 0 - 50	68
Figure 34. Case 2. Surface pressure field, days 60 - 110	69
Figure 35. Case 2. Surface pressure field, days 120 - 160	70
Figure 36. Case 2. Surface velocity and temperature fields, days 0 - 10	71
Figure 37. Case 2. Surface velocity and temperature fields, days 20 - 30	72
Figure 38. Case 2. Surface velocity and temperature fields, days 40 - 50	73
Figure 39. Case 2. Surface velocity and temperature fields, days 60 - 70	74
Figure 40. Case 2. Surface velocity and temperature fields, days 80 - 90	75
Figure 41. Case 2. Surface velocity and temperature fields, days 100 - 110	76
Figure 42. Case 2. Surface velocity and temperature fields, days 120 - 130	77
Figure 43. Case 2. Surface velocity and temperature fields, days 140 - 150	78
Figure 44. Case 2. Surface velocity and temperature fields, day 160	79
Figure 45. Case 2. Energy time series	80
Figure 46. Case 2. Energy transfers	81
Figure 47. Case 2. Energy transfer diagram	82
Figure 48. Case 2. Spectral density at day 70	83
Figure 49. Case 2. Spectral density at day 80	84
Figure 50. Case 2. Spectral density at day 90	85
Figure 51. Case 2. Spectral density at day 100	86
Figure 52. Case 2. Spectral density time series	87
Figure 53. Case 2. Cross sections of dq/dx and alongshore velocity	88
Figure 54. Case 3. Surface pressure field, days 0 - 50	90
Figure 55. Case 3. Surface pressure field, days 60 - 110	91
Figure 56. Case 3. Surface pressure field, days 120 - 160	92
Figure 57. Case 3. Surface velocity and temperature fields, days 0 - 10	93
Figure 58. Case 3. Surface velocity and temperature fields, days 20 - 30	94
Figure 59. Case 3. Surface velocity and temperature fields, days 40 - 50	95
Figure 60. Case 3. Surface velocity and temperature fields, days 60 - 70	96
Figure 61. Case 3. Surface velocity and temperature fields, days 80 - 90	97
Figure 62. Case 3. Surface velocity and temperature fields, days 100 - 110	98
Figure 63. Case 3. Surface velocity and temperature fields, days 120 - 130	99
Figure 64. Case 3. Surface velocity and temperature fields, days 140 - 150	100
Figure 65. Case 3. Surface velocity and temperature fields, day 160	101
Figure 66. Case 3. Energy time series	102

Figure 67. Case 3. Energy transfers	103
Figure 68. Case 3. Energy transfer diagram	104
Figure 69. Case 3. Energy transfer diagram	105
Figure 70. Case 3. Energy transfer diagram	106
Figure 71. Case 3. Spectral density at day 30	108
Figure 72. Case 3. Spectral density at day 40	109
Figure 73. Case 3. Spectral density at day 50	110
Figure 74. Case 3. Spectral density time series	111
Figure 75. Case 3. Spectral density time series	112
Figure 76. Case 3. Spectral density time series	113
Figure 77. Case 3. Cross sections of dq/dx and alongshore velocity	114
Figure 78. Case 4. Surface pressure field, days 0 - 50	116
Figure 79. Case 4. Surface pressure field, days 60 - 110	117
Figure 80. Case 4. Surface pressure field, days 120 - 160	118
Figure 81. Case 4. Surface velocity and temperature fields, days 0 - 10	119
Figure 82. Case 4. Surface velocity and temperature fields, days 20 - 30	120
Figure 83. Case 4. Surface velocity and temperature fields, days 40 - 50	121
Figure 84. Case 4. Surface velocity and temperature fields, days 60 - 70	122
Figure 85. Case 4. Surface velocity and temperature fields, days 80 - 90	123
Figure 86. Case 4. Surface velocity and temperature fields, days 100 - 110	124
Figure 87. Case 4. Surface velocity and temperature fields, days 120 - 130	125
Figure 88. Case 4. Surface velocity and temperature fields, days 140 - 150	126
Figure 89. Case 4. Surface velocity and temperature fields, day 160	127
Figure 90. Case 4. Energy time series	128
Figure 91. Case 4. Energy transfers	129
Figure 92. Case 4. Energy transfer diagram	130
Figure 93. Case 4. Energy transfer diagram	131
Figure 94. Case 4. Spectral density at day 40	133
Figure 95. Case 4. Spectral density at day 50	134
Figure 96. Case 4. Spectral density at day 60	135
Figure 97. Case 4. Spectral density time series.	136
Figure 98. Case 4. Spectral density time series	137
Figure 99. Case 4. Spectral density time series	138
Figure 100. Case 4. Cross sections of dq/dx and alongshore velocity	140
Figure 101. Case 4. Cross sections of dq/dx and alongshore velocity	141

Figure 102. Case 5. Surface pressure field, days 0 - 50	143
Figure 103. Case 5. Surface pressure field, days 60 - 110	144
Figure 104. Case 5. Surface pressure field, days 120 - 170	145
Figure 105. Case 5. Surface pressure field, days 180 - 230	146
Figure 106. Case 5. Surface pressure field, day 240	147
Figure 107. Case 5. Surface velocity and temperature fields, days 0 - 10	148
Figure 108. Case 5. Surface velocity and temperature fields, days 20 - 30	149
Figure 109. Case 5. Surface velocity and temperature fields, days 40 - 50	150
Figure 110. Case 5. Surface velocity and temperature fields, days 60 - 70	151
Figure 111. Case 5. Surface velocity and temperature fields, days 80 - 90	152
Figure 112. Case 5. Surface velocity and temperature fields, days 100 - 110	153
Figure 113. Case 5. Surface velocity and temperature fields, days 120 - 130	154
Figure 114. Case 5. Surface velocity and temperature fields, days 130 - 150	155
Figure 115. Case 5. Surface velocity and temperature fields, days 160 - 170	156
Figure 116. Case 5. Surface velocity and temperature fields, days 180 - 190	157
Figure 117. Case 5. Surface velocity and temperature fields, days 200 - 210	158
Figure 118. Case 5. Surface velocity and temperature fields, days 220 - 230	159
Figure 119. Case 5. Surface velocity and temperature fields, day 240	160
Figure 120. Case 5. Energy time series	161
Figure 121. Case 5. Energy transfers, days 30 to 40	162
Figure 122. Case 5. Energy transfer diagram, days 30 to 40	163
Figure 123. Case 5. Energy transfers, days 60 to 70	164
Figure 124. Case 5. Energy transfer diagram, days 60 to 70	165
Figure 125. Case 5. Spectral density at day 30	167
Figure 126. Case 5. Spectral density at day 40	168
Figure 127. Case 5. Spectral density at day 50	169
Figure 128. Case 5. Spectral density at day 60	170
Figure 129. Case 5. Spectral density at day 70	171
Figure 130. Case 5. Spectral density at day 160	172
Figure 131. Case 5. Spectral density time series	173
Figure 132. Case 5. Spectral density time series	174
Figure 133. Case 5. Spectral density time series	175
Figure 134. Case 5. Cross sections of dq/dx and alongshore velocity	176
Figure 135. Case 5. Cross sections of dq/dx and alongshore velocity	177

ACKNOWLEDGMENTS

I would like to thank my advisor, Dr. Mary L. Batteen for the use of her Primitive Equation model, and for the patience and understanding she showed throughout. The comments of my second reader, Dr. David C. Smith IV enhanced the thesis greatly and I am appreciative of his assistance and support. Discussions with Dr. Robert L. Haney and Dr. Albert J. Semtner, on ocean modeling, provided much needed background and insight, and without the assistance of Ms. Arlene A. Bird many of the analysis programs would not have come to fruition. Thanks also to the staff at CSIRO Division of Oceanography, particularly Stuart Godfrey and George Cresswell for providing unpublished manuscripts and other references.

I. BACKGROUND

A. INTRODUCTION

The Leeuwin Current is a surface flow of warm, low salinity, tropical water, poleward along the west coast of Australia, then eastward into the Great Australian Bight (Figures 1 and 2). It appears to have its source in the northeast Indian Ocean, and extends to Australia's southern coastal waters. Godfrey *et al.* (1986) reported detecting the current as far east as Portland (142°E) although based on water mass analysis, Rochford (1986) argues that its eastward limit is 130°E.

The current is narrow (< 100 km wide), shallow (generally < 300 m), has an underlying equatorward flow and is strongly seasonal in nature. Holloway and Nye (1985) showed that the maximum flow along the southern portion of the North West Shelf (NW Shelf) occurred from February to June and that it was not enhanced by the strengthening southeast trade regime during that period. Observations from the Leeuwin Current Interdisciplinary Experiment (LUCIE) reported by Boland *et al.* (1988) show that the maximum poleward flow at Dongara (29.5°S) occurs from April to June whilst further south at Cape Mentelle (34°S) it occurs in June and July. Rochford (1986) concludes that the Leeuwin Current reaches its eastward limit south of Australia in July.

The Leeuwin Current differs markedly in its characteristics, and hence presumably in its associated dynamics, from currents found in other eastern ocean regions. The other major eastern boundary currents, i.e., Peru, California, Benguela and Canary, are characterized by climatologically weak ($< 10 \text{ cm s}^{-1}$) surface flow toward the equator, cold upwelled water at the surface, shallow (< 30 m depth) thermoclines and high biological production (Parrish *et al.*, 1983). In contrast, the Leeuwin current has a poleward surface flow which exceeds 1.5 m s^{-1} at times (Cresswell and Golding, 1980; Godfrey *et al.*, 1986), anomalously warm water, downwelling, a deep (> 50 m) thermocline (Thompson, 1984) and low fish production. The other currents are part of the subtropical anticyclonic gyres which are driven primarily by the anticyclonic wind fields, and variations in current strength are highly coherent with variations in local wind stress. With such markedly different features, the Leeuwin Current may be expected to depart just as markedly in its generation mechanisms and dynamic features.

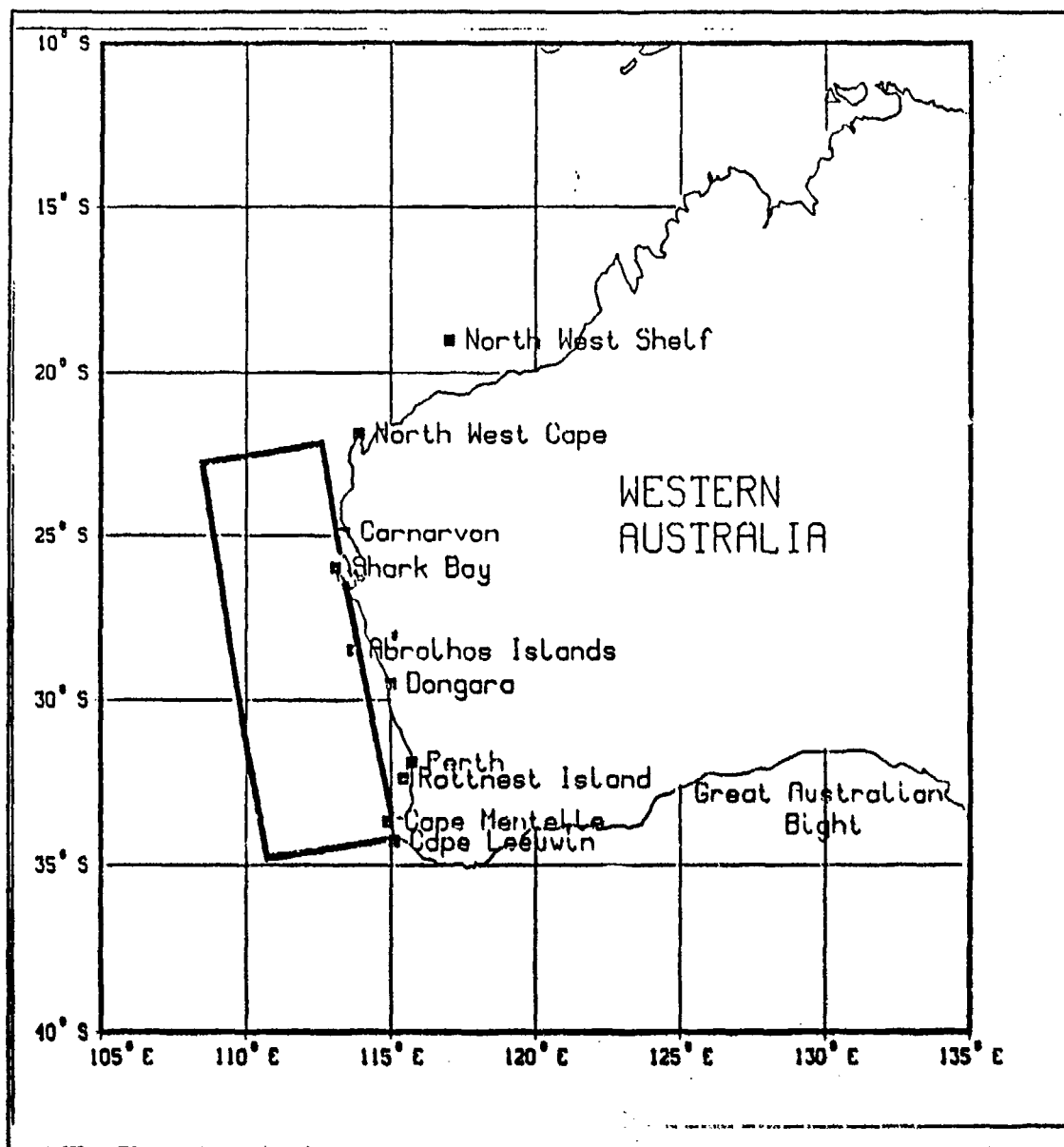


Figure 1. Leeuwin Current: Geographical locations referred to in text.

B. OBSERVATIONAL STUDIES

1. The Large Scale Circulation

Andrews (1977) provides an excellent synopsis of the large scale circulation in the area. A large semi-permanent trough centered near 39°S, 110°E extends northeast towards 30°S, 114.8°E. West of the trough the northeastward West Australian Current advects cool, saline water toward the coast. This current becomes more zonal

equatorward creating a confluence between 39°S and 31°S. The zonal onshore flow then extends north to 15°S.

Superimposed on this large scale circulation is the seasonal poleward flow of the Leeuwin Current. Thus, there is a zonal inflow into a meridional boundary current poleward of the North West Shelf area (Figure 1), becoming even more complex south of 31°S, where the West Australian Current is confluent, cyclonic and has an equatorward component, before turning sharply poleward, transporting its waters parallel to the coastal flow. It is not surprising therefore that temporal and spatial variability due to mesoscale features is at a maximum near 31°S to 32°S (Andrews, 1977).

2. A Poleward Flowing Coastal Current

The earliest documentation of the characteristics of a poleward flowing current was by Saville-Kent (1897) following studies of the marine fauna of the Abrolhos Islands (28.5°S). Anomalously warm water was found around the Islands but not on the mainland coast 50 miles to the east where temperatures were some 7°C cooler. This led to a suggestion that the water must be transported to the region. Dakin (1919) also noted that the temperature difference between the Abrolhos Islands to the mainland was greatest in the winter.

Rochford (1969) used drift bottles to ascertain that the poleward flow in winter extended to the south of Rottnest Island (32°S) and that a flow reversal occurred in summer. The reversal was also apparent in salinity records for the southwest coast of Australia. The salinity variation was over twice that attributable to evaporation and precipitation; hence the salinity became an effective tracer of the flow regime in the region. Kitani (1977) observed low salinity water at 32°S in November 1975 which showed that the occurrence of tropical water was not confined to the austral winter. The eastward continuation of the poleward flow into the Great Australian Bight was inferred by Colborn (1975) from temperature data, and by Markina (1976) from plankton data, which further emphasized its strong signal.

The poleward current was named the Leeuwin Current by Cresswell and Golding (1980). This was in honor of the first Batavia-bound Dutch vessel to explore the southwest of Australia.

3. Drifting Buoy Studies

The deployment of satellite tracked drifting buoys off Western Australia from 1975 to 1977 added a new dimension to the data collected on the circulation features. Cresswell and Golding (1979) illustrated the spatial and temporal complexity of the current in charts of buoy tracks and showed clear evidence for the existence of mesoscale

eddies on the western side of the current. The buoys were observed to accelerate as they entered the current and slow again when departing, providing evidence for a high speed core current which was measured at up to 1.7 m/sec from buoy positions.

4. Satellite Remote Sensing Studies

Infra-red imagery of the eastern Indian Ocean dates back to the mid 1970s but the analysis of its flow characteristics from these images is more recent, coinciding with the introduction of the Advanced Very High Resolution Radiometer (AVHRR) to NOAA platforms in 1978. Its high spatial resolution ($\sim 1\text{km}$) and temperature discrimination ($< 0.1^\circ\text{C}$) allows high definition images to reveal the temperature contrasts between the different currents and cyclonic and anticyclonic eddies. Figure 2, from Pearce and Cresswell (1985), shows a large wedge of warm water in the northeast Indian Ocean being funnelled into a narrow current near North West Cape, then moving south along the shelf and slope until reaching Cape Leeuwin, where it abruptly swings eastward and extends across the Great Australian Bight. Mesoscale features can be seen off Perth, and filament-like features can be seen off the south coast.

5. Mesoscale Features

The existence of eddies in the Eastern Indian Ocean was first postulated by Wyrski (1962). Using dynamic height calculations relative to 1750 decibars he showed a strong semi-permanent eddy present near 32°S 110°E with cyclonic circulation above the reference level and anticyclonic below. Analysis by Hamon (1965) suggested a double eddy structure in the region 30° to 32°S , east of 107°E during the austral winter period of late April to November. In a subsequent study Hamon (1972) found little seasonal variation in dynamic height anomalies in the same area, although a tendency toward greater variability during the months from August to November was noted.

Andrews (1977) investigated mesoscale features in the region and observed nearly zonal planetary Rossby waves in the West Australian Current and nearly meridional coastal waves in the coastal current south of 15°S where zonal inflow occurred. The interaction of the two wave types, particularly in the vicinity of the large trough resulted in meandering in both currents. No clear ring-like features (i.e. closed isopleths of velocity and temperature at several depths) were apparent to Andrews in his study although some mixed layer and surface temperature rings were analyzed.

Andrews (1983) attempted to reconcile the apparently contradictory findings of Hamon and Cresswell (1972) and Golding and Symonds (1978) who reported mesoscale structures with length scales of 200-300 km and 140 km, respectively. He concluded that both length scales can be present with the shorter at wavelength $\lambda = 157 \pm 25$ km as-

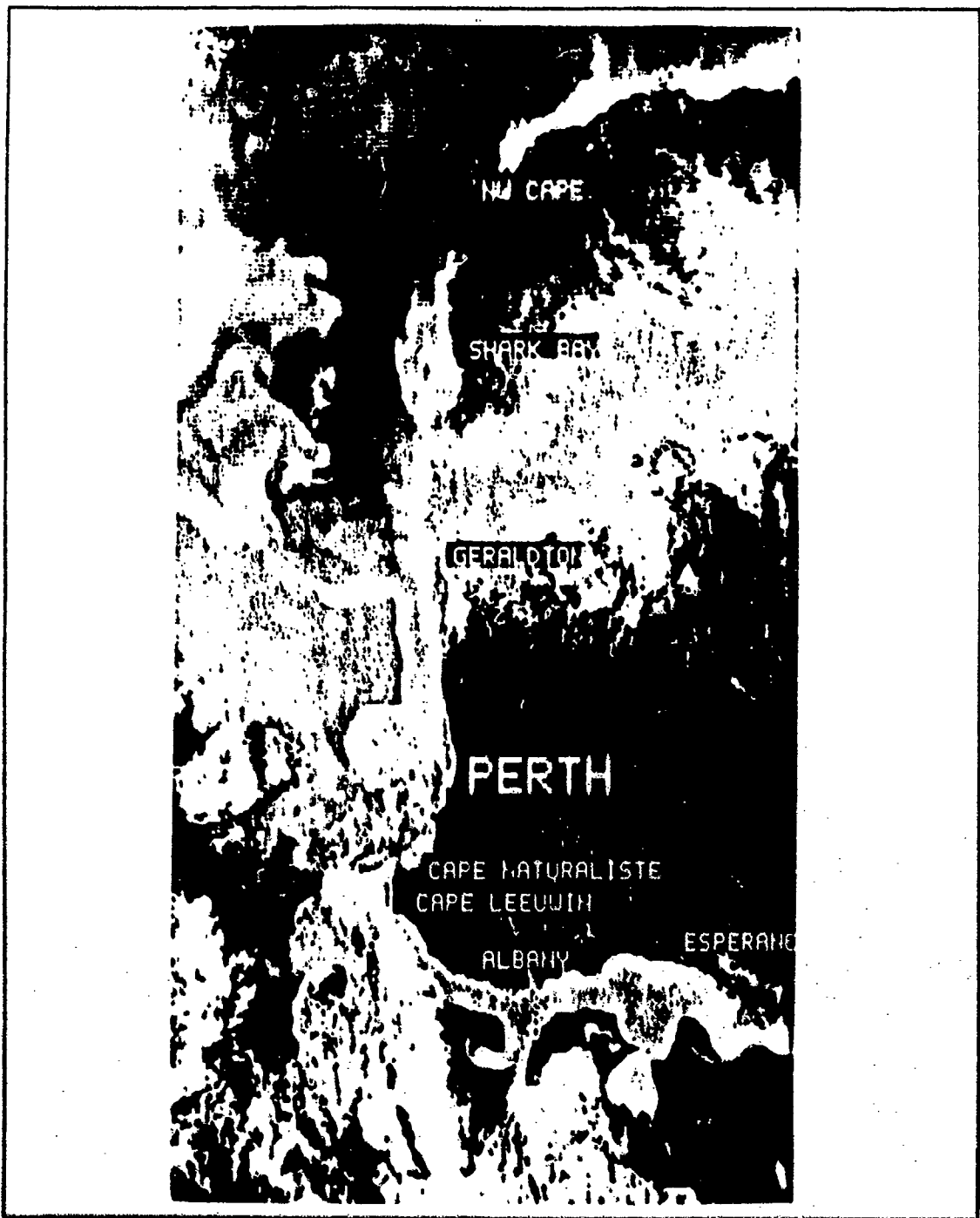


Figure 2. AVHRR image of Leeuwin Current region: (after Pearce and Cresswell, 1985).

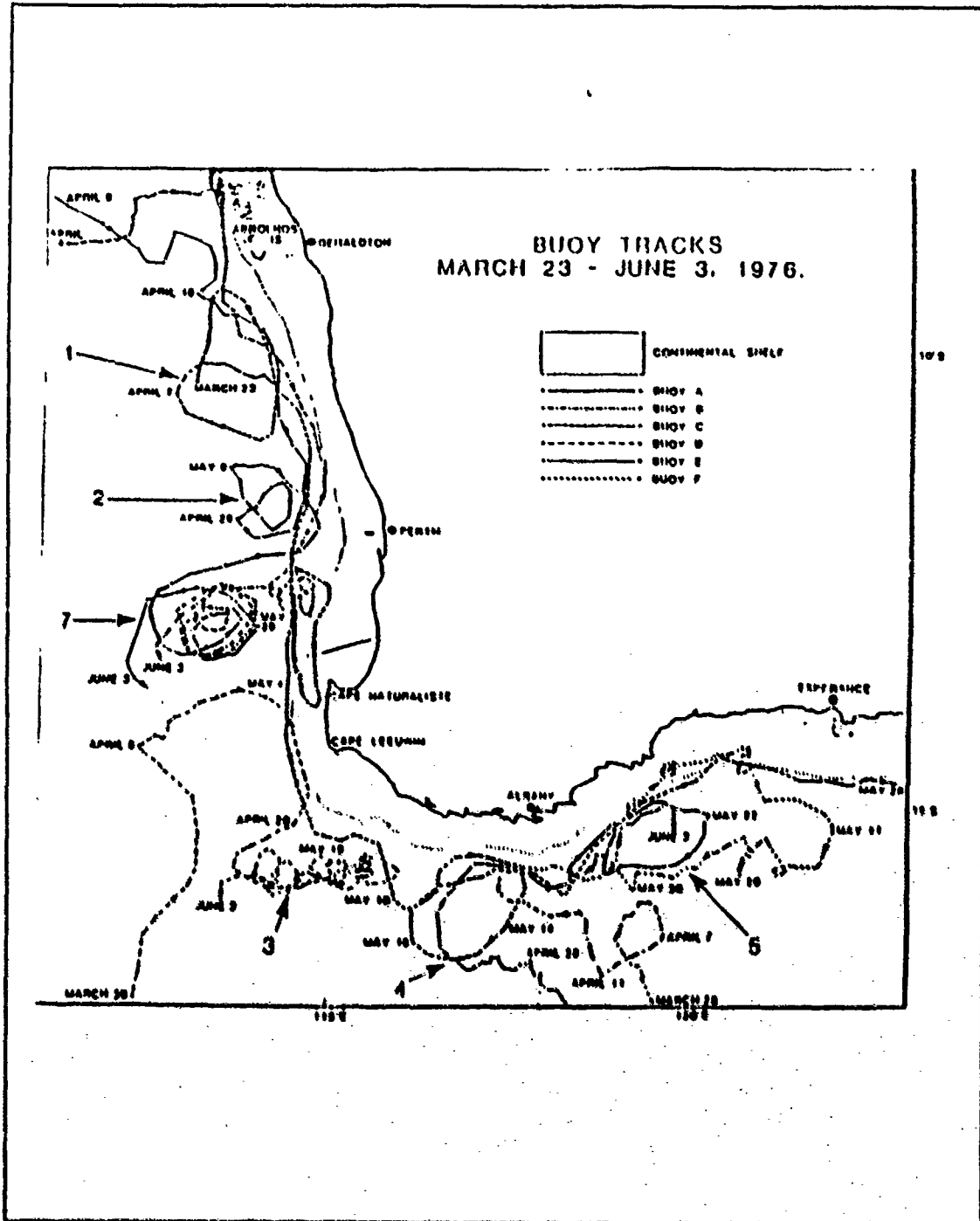


Figure 3. Tracks of buoys influenced by the Leeuwin Current: (after Cresswell, 1980).

sociated with Rossby deformation scale eddy structures in the strong poleward flow over the slope and the longer at $\lambda = 309 \pm 28$ km associated with the weaker, large scale, West Australian Current offshore. The inshore regime of cyclonic rings is clearly at a scale consistent with the trajectories of Lagrangian buoys (Figure 3). While Andrews suggests baroclinic instability in the poleward current as a likely generation mechanism, with both first and second mode rings identified, no explanation is offered for the larger offshore scale.

C. LEEUWIN CURRENT MODELING STUDIES

Thompson and Veronis (1983) were the first to model the Leeuwin Current and suggested that local winds on the North West Shelf could generate the current. This theory was refuted by the current meter observations of Holloway and Nye (1985). It was also rejected by Thompson (1984) who proposed instead an alongshore steric height gradient as the primary forcing mechanism with the winter deepening of the mixed layer offsetting the effects of the equatorward wind stress. Godfrey and Ridgeway (1985a) quantified the contributions of the alongshore pressure gradient and equatorward wind stress and strongly supported Thompson's (1984) finding. They further proposed that flow from the Pacific Ocean through the Indonesian Archipelago to the northeast Indian Ocean could be responsible for the large steric height gradient, a feature which makes the Leeuwin Current unique among eastern boundary currents.

McCreary *et al.* (1986) rejected the throughflow as being a primary forcing mechanism and proposed that thermohaline gradients were responsible for the alongshore pressure gradient. Their model results showed a poleward surface current and equatorward undercurrent comparable in strength to observations, but no mesoscale features were shown. Kundu and McCreary (1986) examined the throughflow theory separately and produced a weak poleward flow and concluded that the throughflow was a secondary forcing mechanism.

Thompson (1987) used an analytic model of the Leeuwin Current to investigate why the flow is poleward and why no upwelling occurred, despite the upwelling-favorable wind. Thompson (1987) concluded that the wind-mixed (or surface Ekman) layer is deep enough to reduce the effects of wind forcing below the level of the forcing due to the poleward pressure gradient.

Gentili (1972) suggested that a seasonal (austral autumn and winter) throughflow could be isolated in the northeast Indian Ocean during the austral summer and thus could provide a source for the subsequent Leeuwin Current generation. This theory is

supported by the satellite image of Pearce and Cresswell (1985) in Figure 2. The image is consistent with a large wedge-shaped mass of warm water off northwest Australia funnelling in to a poleward current. Weaver and Middleton (1989) used a Bryan-Cox ocean general circulation model to investigate the contributions to the Leeuwin Current from both the alongshore density gradient and the warmer, fresher North West Shelf waters. The model, which includes simple coastal geography and topography, produced a realistic Leeuwin Current, but the current lacks mesoscale variability. Weaver and Middleton (1989) concluded that the Leeuwin Current is a baroclinic current driven by the alongshore density gradient. They also believe the current is strengthened locally, by barotropic enhancement, in the vicinity of the source of the North West Shelf waters.

D. THEORIES FOR THE LEEUWIN CURRENT

Despite extensive modeling studies throughout the 1980's, a complete explanation for the Leeuwin Current and its different features in comparison with other eastern boundary currents remains outstanding. A synopsis of current theories is presented below.

1. Generation

There is general agreement (e.g., by Thompson, McCreary, Godfrey, Cresswell) that the Leeuwin Current is generated by a meridional pressure gradient which overwhelms the opposing equatorward wind stress. The wind forcing effects are diminished by deep mixed layers (Thompson, 1987), possibly formed in response to a strong heat flux out of the ocean, which is a feature unique to the Leeuwin Current among eastern boundary currents (Hsiung, 1985).

The source of the Leeuwin Current water is predominantly geostrophic inflow from the west (McCreary *et al.*, 1986; Thompson, 1987), and is augmented by a source from the North West Shelf (Kundu and McCreary, 1986; Weaver and Middleton, 1989), possibly having its origin in the Pacific Ocean (Godfrey and Ridgeway, 1985). The inflow of the North West Shelf water is consistent with the warm, low salinity signature of the Leeuwin Current surface waters.

The results of Weaver and Middleton (1989) suggest that both the poleward gradients of temperature and salinity are sufficient to establish a pressure gradient strong enough to support the observed flow. Godfrey (1988) proposes enhancement of this pressure gradient by the build up of warm fresh water near Indonesia due to the action of zonal winds in the equatorial Pacific. He further proposes a feedback loop in which: (1) the advection of warm water poleward by the Leeuwin Current causes high latitude

heat losses; (2) this enhances the alongshore pressure gradient, and; (3) drives the Leeuwin Current.

2. Seasonal Variation

The seasonal variation in the Leeuwin Current is addressed by Godfrey and Ridgeway (1985). They attribute its marked variability to changes in steric height, driven by monsoon winds to the north of Australia, coupled with the local variation in wind stress. In addition, they note the seasonal throughflow of warm tropical water proposed by Gentilli (1972). To these theories we must add the effect of seasonal variations in mixed layer depth which are central to Thompson's (1987) model of the current.

3. Mesoscale Variability

One of the major gaps in Leeuwin Current research is in the area of the complex eddy fields found in the current. Whilst observational studies (Hamon and Cresswell, 1972; Golding and Symonds, 1978; Andrews, 1977, 1983) reveal the nature and characteristics of the mesoscale features, no modeling studies have successfully produced eddy fields which would allow analysis of their generation mechanisms.

E. OBJECTIVE OF THE THESIS

The objective of the thesis is to use a full primitive equation (PE) numerical model to investigate the generation and stability of the Leeuwin Current. The roles of the Indian Ocean temperature field, North West Shelf water and local wind stress in generating the current will be investigated. The model generated current will be compared with LUCIE data and the resulting flow analyzed for energetics and stability. The use of a multi-level PE model with active thermodynamics and appropriate choices for diffusion parameters should result in the first eddy resolving modeling study of the Leeuwin Current and its eddy fields.

Initialization will be similar to that used by Weaver and Middleton (1989), but, with the inclusion of wind forcing, a more complete picture of the generation mechanisms should result. The use of a straight meridional vertical wall for the coastline and the absence of shelf and bottom topography should not severely limit this process oriented study as the coast is generally straight over the domain (22°S to 34°S) and, as Weaver and Middleton note, their modeled current is centered near the shelf break. This study should confirm and extend previous modeling studies and provide a firm basis for further research.

II. MODEL DESCRIPTION

A. MODEL EQUATIONS

The numerical model is that used by Batteen *et al.* (1989). It is a ten-level, PE model for a baroclinic ocean on a β - plane, based on the hydrostatic, Boussinesq, and rigid lid approximations. The governing equations, written in standard notation, are as follows:

$$\frac{du}{dt} = \frac{-1}{\rho_0} \frac{\partial p'}{\partial x} + fv - A_M \nabla^2 u + K_M \frac{\partial^2 u}{\partial z^2} + \delta_d(u) \quad [1]$$

$$\frac{dv}{dt} = \frac{-1}{\rho_0} \frac{\partial p'}{\partial y} - fu - A_M \nabla^2 v + K_M \frac{\partial^2 v}{\partial z^2} + \delta_d(v) \quad [2]$$

$$w = - \int_{-H}^z \left(\frac{\partial u}{\partial x} + \frac{\partial v}{\partial y} \right) d\zeta \quad [3]$$

$$p' = \int_z^0 \rho g d\zeta - \frac{1}{H} \int_{-H}^0 \left[\int_z^0 \rho g d\zeta \right] dz \quad [4]$$

$$\rho = \rho_0 (1 - \alpha(T - T_0)) \quad [5]$$

$$\frac{dT}{dt} = - A_H \nabla^2 T + K_H \frac{\partial^2 T}{\partial z^2} + Q_r + \delta_d(T). \quad [6]$$

In the equations, (x,y,z) is a right-handed coordinate system: with x toward shore, y alongshore and z upward. The corresponding velocity components are (u,v,w) , t denotes time, T is temperature, ρ density and p' the departure of the pressure from its vertical average. In equations [3] and [4], ζ is a dummy variable of integration. Equation [4] assumes a constant depth averaged pressure of zero which negates the barotropic mode in this study. The equation of state [5] assumes density that is a function of temperature only. Justification for this assumption is given in Chapter 3.

In [6], $Q_r = \frac{1}{C\rho_0} \frac{\partial S}{\partial z}$ is heating due to solar radiation with

$$S = S_0(R \exp(-\frac{z}{z_1}) + (1 - R) \exp(-\frac{z}{z_2})), \quad [7]$$

where S_0 is the downward flux of solar radiation at the surface, $R = 0.62$ is the fraction of solar radiation absorbed in depth $z_1 = 1.5$ m leaving $(1 - R) = 0.38$ to be absorbed by depth $z_2 = 20.0$ m (Paulson and Simpson, 1977). The terms $\delta_u(u)$, $\delta_u(v)$ and $\delta_u(T)$ represent the vertical turbulent mixing of zonal momentum, meridional momentum and heat, respectively, by a dynamic adjustment mechanism which maintains stability in the water column (Adamec *et al.*, 1981). Appendix A details other symbols used in the model equations and provides values for constants used in the study.

The boundary conditions at the surface ($z = 0$) are:

$$K_M \frac{\partial u}{\partial z} = 0 \quad [8]$$

$$K_M \frac{\partial v}{\partial z} = \frac{\tau}{\rho_0} \quad [9]$$

$$K_H \frac{\partial T}{\partial z} = -Q_H \quad [10]$$

$$w = 0 \quad [11]$$

and at the bottom ($z = -H$) are:

$$K_M \frac{\partial u}{\partial z} = C_D(u^2 + v^2)^{\frac{1}{2}}(u \cos \gamma - v \sin \gamma) \quad [12]$$

$$K_M \frac{\partial v}{\partial z} = C_D(u^2 + v^2)^{\frac{1}{2}}(u \sin \gamma + v \cos \gamma) \quad [13]$$

$$K_H \frac{\partial T}{\partial z} = 0 \quad [14]$$

$$w = 0. \quad [15]$$

B. FINITE DIFFERENCING

For the finite differencing, a space-staggered B-scheme patterned after Arakawa and Lamb (1977) is used in the horizontal. In the vertical, the 10 layers are separated by constant z levels at depths of 13, 46, 98, 182, 316, 529, 870, 1416, 2283 and 3656 m.

C. DOMAIN SIZE AND RESOLUTION

The eastern boundary of the model domain represents a straight idealization of the continental shelf of Western Australia. The model domain is a rectangular area 1280 km alongshore covering latitudes 22° to 34° and extends 576 km offshore. Horizontal resolution of the model is 20 km alongshore and 9 km cross-shore. Comparisons with numerical simulations made by a higher resolution model (10 km by 9 km) with half the latitudinal extent showed no significant degradation in the resolution of mesoscale features in the coarse grid model; hence the present grid resolution was adopted to enable coverage of the larger geographical region off Western Australia. To facilitate comparison with other eastern boundary currents (which could be in either hemisphere), model results will be discussed in terms of alongshore (poleward or equatorward) and cross-shore (onshore or offshore) flows.

Although Weaver and Middleton (1989) found the presence of a sloping shelf was necessary to trap the eastern boundary current generated by their model, both coastline features and topography are omitted from this process oriented study. The inclusion of coastline features and bottom topography, and an examination of their effects on the current and eddies, are considered a separate study. The constant depth used in the model is 4500 m.

D. HEAT AND MOMENTUM DIFFUSION

A biharmonic closure system is used for lateral diffusion of heat and momentum in preference to a Laplacian closure. Holland (1978) showed that the highly scale selective biharmonic diffusion acts predominantly on sub-mesoscales while Holland and Batteen (1986) found that baroclinic mesoscale processes can be damped by Laplacian lateral heat diffusion. As a result the use of biharmonic lateral diffusion should allow mesoscale eddy generation via barotropic and/or baroclinic instability mechanisms. Coefficient values are given in Appendix A.

E. WIND FORCING

The incorporation of wind forcing into the PE model is described in Chapter III. Consistent with the wind band forcing used by McCreary *et al.* (1987) and Batteen *et al.* (1989) all wind forcing is imposed in the interior only and tapered to zero near the southern and northern open boundaries.

F. SURFACE THERMAL FORCING

The total heat flux across the surface is initially set to zero in all experiments. The downward flux of solar radiation, (S_0), is calculated as a function of the solar insolation at the top of the atmosphere (S_A^*) and cloud cover (n) using

$$S_0^* = 0.95(0.74 - 0.6n)S_A^* \quad [16]$$

(Haney *et al.*, 1978) The net longwave radiation (Q_B) and sensible (Q_S) and latent heat (Q_E) fluxes are computed from bulk formulas based on cloud cover, wind strength ($|V_A|$), sea surface temperature (T_S), saturation vapor pressure (e_S), and atmospheric vapor pressure (e_A) for a range of air temperatures (Haney *et al.*, 1978) using

$$Q_B = 0.985\sigma(T_S)^4[0.39 - 5.0(e_A)^{\frac{1}{2}}](1 - 0.6n^2) \quad [17]$$

$$Q_S = \rho_A C_H C_P |V_A| (T_S - T_A) \quad [18]$$

$$Q_E = \rho_A C_H L |V_A| (0.622/p_A)(e_S - e_A). \quad [19]$$

Vapor pressures are calculated using the Clausius Clapyron equation

$$e_S = 10^{9.405 - \frac{2353.0}{T_A}} \quad [20]$$

and using relative humidity (r)

$$e_A = r e_S. \quad [21]$$

Values of constants are given in Appendix A. The resulting air temperature, which corresponds to a value of $Q_N = Q_B + Q_S + Q_E = S_0$, is then used in the model for all experiments. Any subsequent surface heat flux forcing is therefore a secondary effect of the changes to sea surface temperature due to the forcing mechanisms being investigated, i.e., forcing due to the wind and/or thermal structure of the ocean.

G. BOUNDARY CONDITIONS

The eastern boundary of the domain, which represents the coast of West Australia, is modeled as a straight vertical wall and has a no-slip condition imposed. The northern, southern and western borders are open boundaries which use a modified version of the radiation boundary conditions of Camerlengo and O'Brien (1980).

III. INITIALIZATIONS, FORCING AND EXPERIMENTAL DESIGN

A. INITIALIZATIONS

1. Ocean Thermal Structure

The ocean temperature structure used to initialize the experiments is considered in two parts with the warmer, less saline North West Shelf waters considered separately from the Indian Ocean waters.

a. Indian Ocean

The initial temperature data used for the Indian Ocean is presented in Table 1 below for each layer of the model.

Table 1. INITIAL TEMPERATURE (°C) FOR INDIAN OCEAN

Latitude	Layer									
	1	2	3	4	5	6	7	8	9	10
22°S	24.0	22.9	21.6	19.2	14.5	09.4	05.9	03.5	02.0	01.0
24	23.3	22.3	20.9	18.6	14.3	09.4	05.9	03.5	02.0	01.0
26	22.6	21.7	20.3	18.0	14.1	09.3	05.9	03.5	02.0	01.0
28	22.0	21.0	19.7	17.4	13.9	09.3	05.9	03.5	02.0	01.0
30	21.3	20.4	19.0	16.7	13.6	09.2	05.8	03.5	02.0	01.0
32	20.6	19.8	18.4	16.1	13.4	09.2	05.8	03.5	02.0	01.0
34	19.9	19.1	17.7	15.5	13.2	09.1	05.8	03.5	02.0	01.0

The temperature data was derived from Levitus (1982). After interpolating between data points, a vertically integrated temperature for each layer was calculated and applied to the constant z levels. For computational ease, the data was further smoothed and a linear gradient fitted to each layer over its meridional extent. Zonal homogeneity was assumed at all levels as the data shows little variability apart from in the region of the Leeuwin Current. Slight differences between the final values used for the Indian Ocean forcing in this study (Table 1) and those of Weaver and Middleton (1989), since the same data source is used, are likely due to slightly different vertical integration and smoothing techniques. A meridional cross section of the domain showing the Indian Ocean temperature initialization is given in Figure 4.

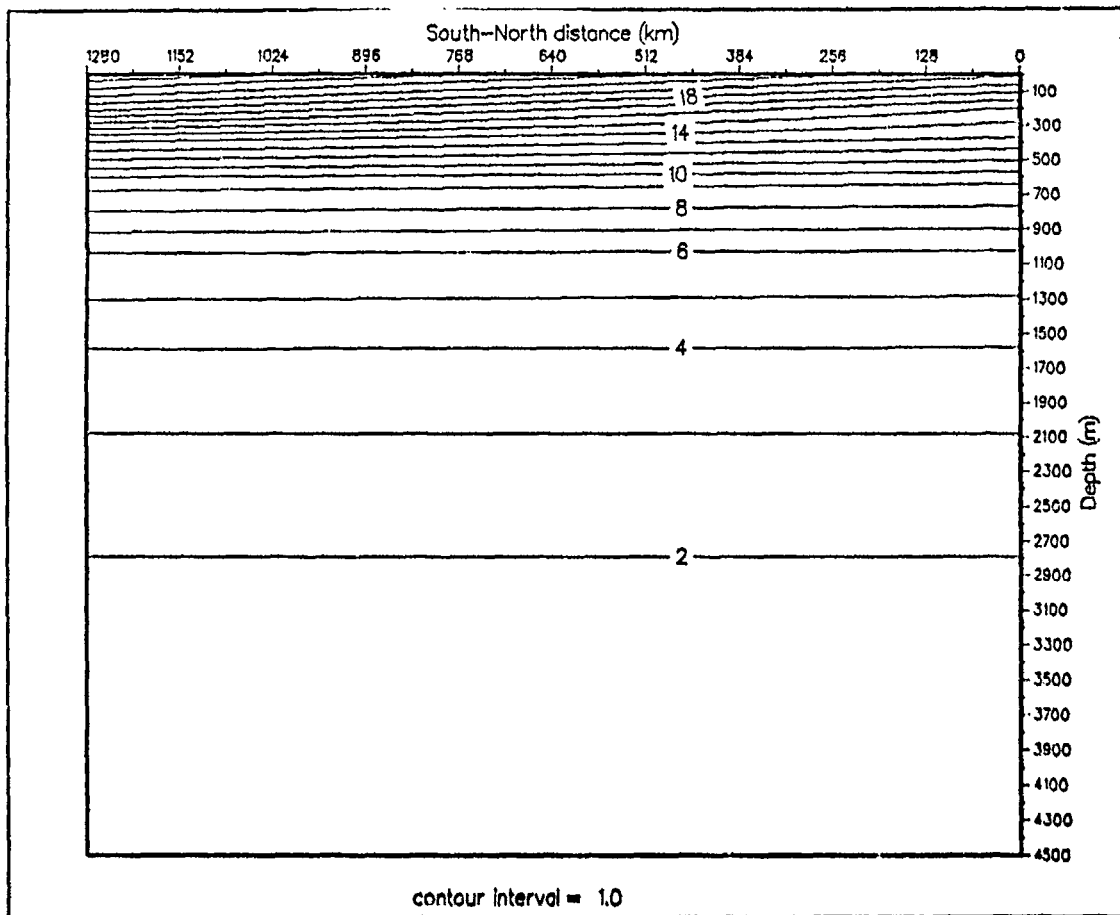


Figure 4. Indian Ocean temperature initialization: Meridional cross-section showing initial thermal structure for Indian Ocean forcing.

Salinity values from Levitus (1982) have a range of only 35.6 ± 0.2 psu over most of the domain in the upper five layers. This range is considered narrow enough to discount salinity variability so that no compensation is made for the assumption that density is a function of temperature alone.

b. North West Shelf

To investigate the impact of NW Shelf waters separately from the Indian Ocean, the NW Shelf waters are initialized separately in the model. As for the Indian Ocean, the data was again derived from Levitus (1982) and vertically integrated and smoothed. Due to the marked contrast in salinity between the water masses of the Indian Ocean and the NW Shelf, the NW Shelf waters are given an equivalent temperature which compensates for variations from a mean salinity of 35.6 psu.

The NW Shelf water is restricted to the upper five layers only so that the lower layers are initialized as for the Indian Ocean. When included in the experiments, the NW Shelf water is treated as a raft of warm water in the inshore equatorward corner of the model and is linearly smoothed into the surrounding Indian Ocean waters. The initial temperature structure of the NW Shelf water is shown in Figure 5, where a meridional cut is taken through the inshore waters showing both the NW Shelf water and the surrounding Indian Ocean temperature structure. The values used to initialize the NW Shelf waters are presented in Table 2.

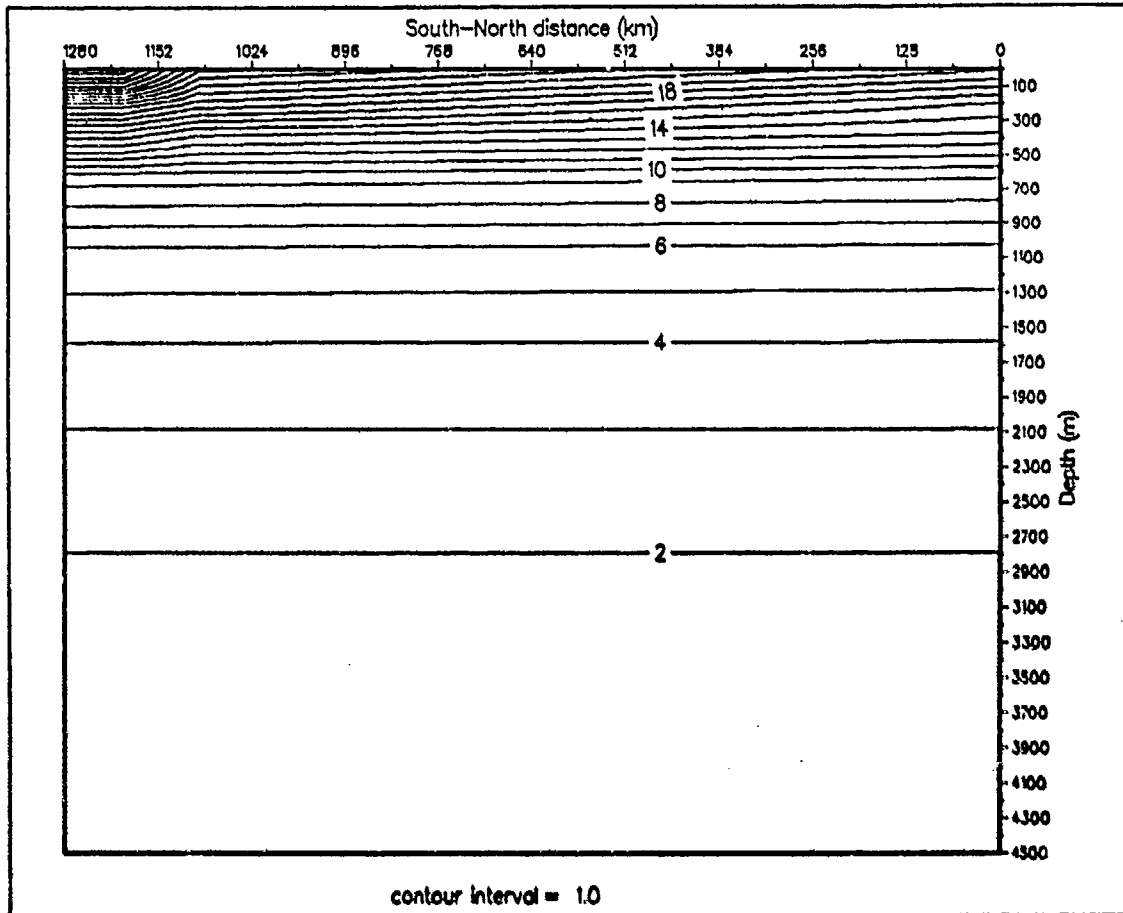


Figure 5. NW Shelf temperature initialization: Meridional cross-section showing initial thermal structure for NW Shelf and Indian Ocean forcing.

Table 2. INITIAL TEMPERATURE (°C) FOR NORTH WEST SHELF

Layer	Temperature
1	29.5
2	28.5
3	26.0
4	20.5
5	15.7

2. Wind Forcing

Monthly wind stress component data was taken from Godfrey and Ridgeway (1985) and converted back to the cross-shore and alongshore components of the wind velocity using:

$$u_*^2 = \left[\left(\frac{\tau_y}{\rho} \right)^2 + \left(\frac{\tau_x}{\rho} \right)^2 \right]^{\frac{1}{2}} \quad [22]$$

and

$$\theta = \tan^{-1} \left(\frac{\tau_y}{\tau_x} \right), \quad [23]$$

so that

$$u = \frac{u_*}{C_D} \cos \theta \quad [24]$$

$$v = \frac{u_*}{C_D} \sin \theta \quad [25]$$

Here, the same choices as used by Godfrey and Ridgeway (1985) for the drag coefficient ($C_D = 1.3 \times 10^{-3}$, after Nelson, 1977) and $\rho = 1.23 \times 10^{-3}$ are used. The values for wind stress and the corresponding components of the wind are given in Tables 3 and 4 respectively.

Table 3. MONTHLY COMPONENTS OF WIND STRESS (dynes cm^{-2})

		Jan	Mar	May	Jul	Sep	Nov
20° - 25°S	τ_x	0.0	-0.1	-0.2	-0.6	-0.1	0.0
	τ_y	0.7	0.6	0.2	0.1	0.6	1.0
25° - 30°S	τ_x	0.0	-0.1	0.0	0.1	0.1	0.0
	τ_y	1.2	1.0	0.3	0.1	0.5	1.1
30° - 35°S	τ_x	0.0	-0.1	0.4	1.5	0.8	0.1
	τ_y	0.8	0.7	0.2	0.0	0.4	0.7

Adapted from Godfrey and Ridgeway (1985)

Table 4. MONTHLY COMPONENTS OF WIND VELOCITY (cm s^{-1})

		Jan	Mar	May	Jul	Sep	Nov
20° - 25°S	u	0	-99	-289	-592	-99	0.0
	v	644	592	289	99	592	769
25° - 30°S	u	0	-77	0	204	108	0
	v	843	767	421	204	538	807
30° - 35°S	u	0	-91	460	942	650	91
	v	688	640	230	0	325	640

Even though Table 4 shows large temporal and spatial variability for the wind stress, a simpler but still representative initialization of the wind velocity was used for this study. The meridional variability was included by dividing the domain into three wind forcing regions consistent with the latitudinal divisions of 25°S and 30°S in Table 4. The wind stress field for May was selected as representative of the Leeuwin Current generation period as it is near the middle of the observed period of maximum poleward flow (autumn and winter). Examination of wind velocities in Table 4 also shows that the May figures are a reasonable approximation to the mean values for the period March to July. The wind forcing used in the model is shown in Figure 6.

3. Atmospheric Thermal Forcing

The choice of a representative air temperature for the zero initial surface heat flux, described earlier, is made complicated by the large latitudinal range of the domain. Mean values over the entire domain for cloud amount, sea surface temperature and rel-

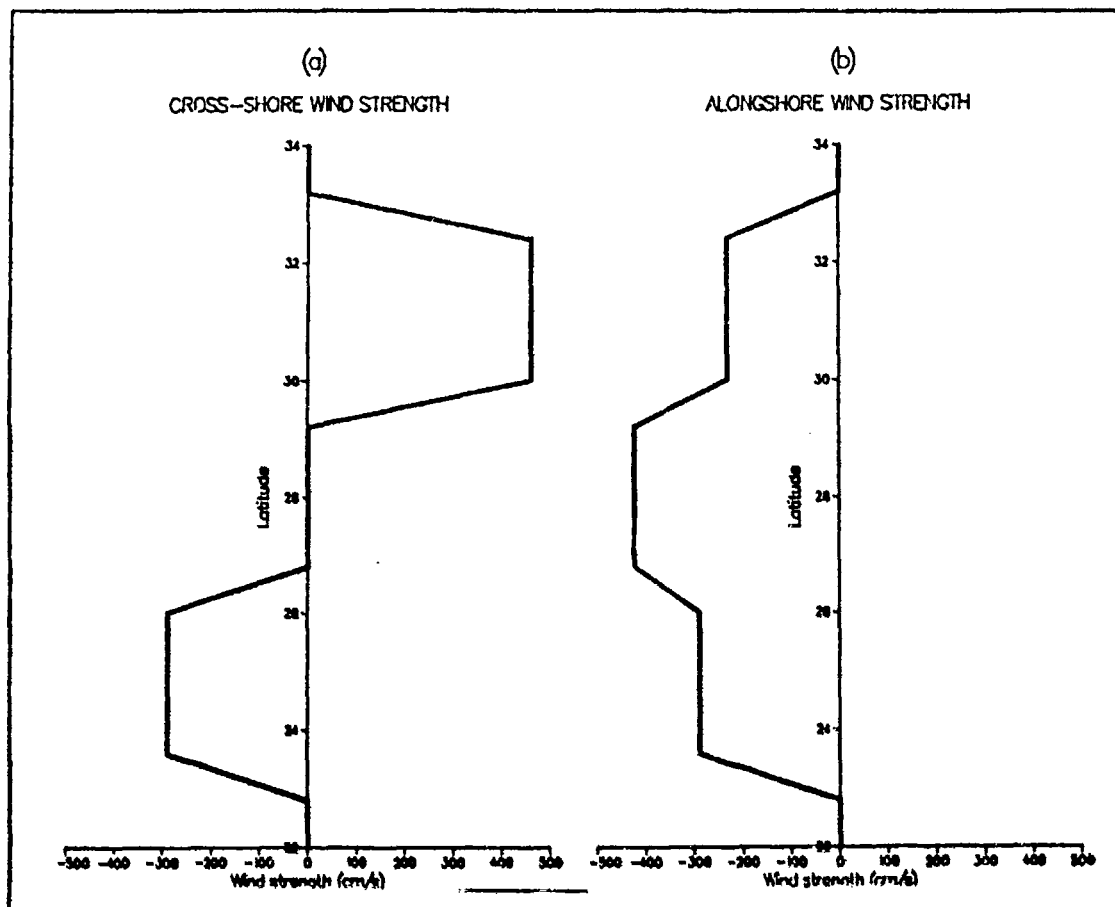


Figure 6. Wind Forcing: Cross-shore (a) and Alongshore (b) components of wind forcing used in the model, which is a generic (northern hemisphere) eastern boundary current model. Positive values of wind strength correspond to onshore and poleward wind velocities.

ative humidity (from USSR Ministry of Defense, 1979), and insolation at the top of the atmosphere (from List 1963) are listed in Table 5. The sensitivity of the heat budget to seasonal variations in wind strength was tested using the wind velocity data for May to July. Since the air temperature required for a zero initial heat flux (using the wind strengths in Table 5) is 297.7 K for May and 298.3 K for July, a value of 298.0 K was used in the model.

Table 5. HEAT BUDGET PARAMETERS

Cloud cover	0.65
Sea surface temperature	21.5 ° C
Relative humidity	0.65
Insolation at top of atmosphere	595.5 $cal\ cm^{-2}\ day^{-1}$
Wind strength (May)	400 $cm\ s^{-1}$
Wind strength (July)	589 $cm\ s^{-1}$

B. EXPERIMENTAL DESIGN

1. Forcing by an Initialized Current (Case 1)

A preliminary experiment, designed to test the model and confirm its ability to produce and resolve mesoscale features, was conducted. The model was initialized using a current field based on observations reported by Thompson (1984) and run for 40 days. The vertical structure was defined using a surface poleward flow of 50 $cm\ s^{-1}$ decaying exponentially to zero current at 150 m. A sinusoid was used to define the undercurrent which has maximum strength of 30 $cm\ s^{-1}$ at 300 m. The horizontal structure is Gaussian with maximum flow initialized 40 km offshore. The initial background temperature field used were based on the climatology of Levitus (1982) and decreases exponentially from 25°C at the surface to 2°C at 4500m. The initializations for Case 1 are shown in Figure 7.

2. Forcing by the Indian Ocean Density Field (Case 2)

The first of the forcing mechanisms to be investigated is the Indian Ocean thermal gradient. In this experiment, the model is initialized with the temperature data from Table 1 and allowed to run for 160 days. The length of this time period was chosen to include both the generation of the current and any eddies which may form on the flow.

3. Inclusion of North West Shelf Waters (Case 3)

To investigate the role of the NW Shelf water, the background Indian Ocean thermal field is retained to maintain the forcing as in Case 2. The warmer water, as detailed in Table 2, is then added to the inshore, equatorward corner of the model to simulate the influx of NW Shelf water, consistent with satellite imagery. The model is then run for 160 days.

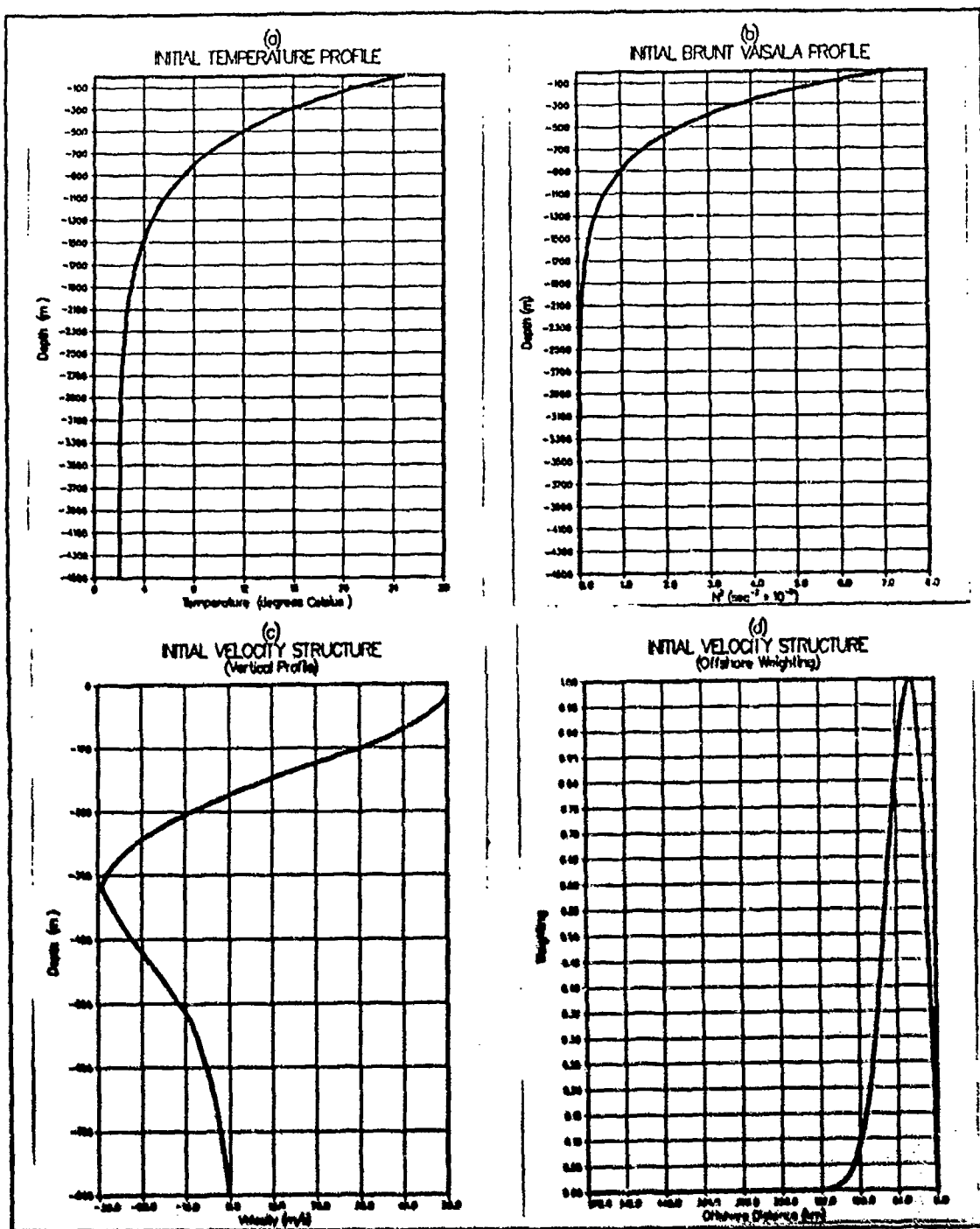


Figure 7. Case 1. Forcing by Initialized Current: Initializations of (a) Temperature, (b) Brunt Vaisala Frequency, (c) Vertical Velocity Structure and (d) Offshore Velocity Structure.

4. The Role of Wind Forcing (Case 4)

The forcing of the Leeuwin Current by wind is investigated over 160 days using the wind velocity data for May in Table 4. The Indian Ocean thermal structure is maintained thus allowing comparison between cases 2 and 4 to isolate the effects of the wind.

5. Combined Thermal and Wind Forcing (Case 5)

In the final experiment, all three proposed forcing mechanisms, i.e., the Indian Ocean thermal field, the influx of NW shelf waters and wind stress are combined and the model run for 240 days. In addition to generating the current and eddies, the longer period should allow the flow to evolve towards a statistically steady state, allowing a more detailed analysis of the instability to be conducted. As the Leeuwin Current is a strongly seasonal feature (Godfrey and Ridgeway, 1985; Pearce and Cresswell, 1985), it is considered unrealistic to run the model on longer without including seasonal variations to the forcing mechanisms.

IV. ANALYSIS TECHNIQUES

A. ENERGY ANALYSIS

An energy analysis based on that of Han (1975) and Semtner and Mintz (1977) was made to gain a better understanding of the energy transfers in the unstable flow. The energy calculations are presented using the Semtner and Mintz (1977) notation:

$\overline{(\quad)}$	time average
$(\quad)'$	time deviation
$\tilde{(\quad)}$	horizontal space average
$(\quad)'$	horizontal space deviation

1. Kinetic Energy

The kinetic energy (K) is calculated by:

$$K = \frac{u^2 + v^2}{2} \quad [26]$$

and presented in a time series plot. After reaching a quasi-steady state in which the total kinetic energy is nearly constant, the time mean and time eddy kinetic energy are calculated by:

$$\bar{K} = \frac{\bar{u}^2 + \bar{v}^2}{2} \quad [27]$$

$$K'' = \frac{\overline{u'^2} + \overline{v'^2}}{2} \quad [28]$$

2. Available Potential Energy

Available potential energy (P) is calculated by:

$$P = \alpha g \left[\frac{1}{2} (\bar{T}^*)^2 \left(\frac{\partial \tilde{T}}{\partial z} \right)^{-1} \right] \quad [29]$$

and plotted in a time series to determine when a quasi-steady state is reached and statistics can be collected. The temporal mean and eddy available potential energy are then calculated by:

$$\bar{P} = \alpha g \left[\frac{1}{2} (\bar{T}^*)^2 \left(\frac{\partial \bar{T}}{\partial z} \right)^{-1} \right] \quad [30]$$

$$P' = \alpha g \left[\frac{1}{2} (\bar{T}^*)^2 \left(\frac{\partial \bar{T}}{\partial z} \right)^{-1} \right]. \quad [31]$$

3. Energy Transfers

The transfers between the energy types are defined, after Semtner and Mintz (1977) by:

$$\{\bar{K} \rightarrow \bar{P}\} = -\alpha g [\bar{T} \bar{w}] \quad [32]$$

$$\{P' \rightarrow K'\} = \alpha g [\bar{T}^* \bar{w}'] \quad [33]$$

$$\{\bar{K} \rightarrow K'\} = \bar{v} \cdot \left(\nabla \cdot \bar{v}' \bar{v}' + \frac{\partial}{\partial z} \bar{w}' \bar{v}' \right) \quad [34]$$

$$\{\bar{P} \rightarrow P'\} = \alpha g \left[\bar{T}^* \nabla \cdot \bar{v}' \bar{T}^* \left(\frac{\partial \bar{T}}{\partial z} \right)^{-1} \right]. \quad [35]$$

The model output consists of velocity components and temperature at daily intervals at each grid point and neither the vertical velocity nor any advection terms calculated by the model are stored. As the calculation of the energy transfers requires both vertical velocity and numerous advection terms, these were recalculated in the same manner as in the model but using the stored values of u , v and T as the input data. Thus, although the energy transfers are recalculated from model output, they are done consistent with the initial calculations of vertical velocity and advection terms by the model.

4. Energy Transfer Diagrams

Using the energy transfers calculated above and the temporal mean and eddy kinetic and available potential energy values, an energy transfer diagram may be constructed for those periods in which the total energies are nearly constant. Semtner and Mintz (1977) applied their energy transfer analysis to currents which had become unstable, generated eddies and then reached a quasi-steady state. In this study, the steady energetic state prior to eddy generation will be examined and the energy transfer plots

and diagrams used to argue for the instability mechanism which leads to the initial eddy generation in each case.

B. SPECTRAL ANALYSIS

A spectral analysis technique discussed by Lopes da Costa (1989) is used to estimate the dominant wavelengths at which eddy growth occurs. The time evolution of the eddy fields can be seen on 3-dimensional time series plots of spectral density versus alongshore wavenumber. The alongshore wavenumber is selected based on an assumption of a meridional anisotropic preference for the eddy development. The model configuration of 65 alongshore temperature grid points and 64 velocity points is ideal in allowing data over the entire domain to be used in computing the discrete Fourier transform based on 64 points.

Features used in the spectral package include pre-whitening, which allows a relative energy maxima to be determined more easily when the general spectrum is high in the wavenumber region of interest and no clear peak is apparent. The pre-whitening procedure consists of differentiating the series in the space domain and using the transfer function to integrate in the wavenumber domain after the estimation of the spectral energy densities.

Leakage due to the finite length of the series is reduced using either a cosine taper or Hanning window. The loss of variance due to the windowing is then compensated for by scaling the calculated one sided spectral density by a factor of 2.0 for the Hanning window or 1.1 for the cosine taper. Lopes da Costa (1989) concludes that, in general, the combination of a cosine taper and no pre-whitening best conserves total variance. A Hanning window either with or without pre-whitening is found to give better results if the wavenumber with the maximum spectral density is to be determined, without regard to the total variance.

As the energy is calculated using the techniques described earlier in this chapter, the conservation of variance is disregarded in favor of the determining the wavenumber with maximum energy and a Hanning window used without pre-whitening in this study. For a more detailed explanation of the spectral analysis package, the reader is referred to Lopes da Costa (1989).

C. STABILITY ANALYSIS

The stability analysis used in this study is based on Batteen *et al.* (1989) who investigated the dynamics of the eddy generation observed in the PE model. The potential

for instability is determined by examining the potential vorticity (q) of the flow and also its cross-shore derivative ($\frac{\partial q}{\partial x}$). The potential vorticity is calculated by:

$$q = (f + \zeta) \frac{\partial T}{\partial z} - \frac{\partial T}{\partial x} \frac{\partial v}{\partial z} \quad [36]$$

where

$$\zeta = \frac{\partial v}{\partial x} - \frac{\partial u}{\partial y} \quad [37]$$

For a flow which has a basic state changing slowly in space and time Kamenkovich *et al.* (1986) give the necessary conditions for baroclinic instability as: $\frac{\partial q}{\partial x}$ change sign, and $\bar{v} \frac{\partial q}{\partial x}$ be positive somewhere in the flow. They also give sufficient conditions for the instability mechanisms. For baroclinic instability, the source of energy is the vertical shear in the mean flow, ($\frac{\partial \bar{v}}{\partial z}$) and the scale of the generated disturbances is of the order of the Rossby radius of deformation. For barotropic instability, the energy source is the horizontal shear in the mean flow ($\frac{\partial \bar{v}}{\partial x}$) and the disturbances grow at a scale less than the Rossby radius.

The sufficient condition for baroclinic instability (Kamenkovich *et al.*: 1986) of a minimum vertical shear is not required for this study as the mean flow is strongly meridional. Olivier (1987) showed that on a β plane, energy can be released in a meridional flow without being acted upon by β ; hence any vertical shear which is greater than the dissipation level in the model may produce instability.

The individual components of the analysis, namely energy transfers, spectral analysis and the instability analysis should all complement each other. From the energy transfer analysis, the location and magnitude of baroclinic and barotropic transfers can be found. Those waves which are unstable and, in particular, the fastest growing wave can be determined from the internal Rossby radii and the spectra can confirm whether those waves do indeed exist.

V. RESULTS AND DISCUSSION

A. LEEUWIN CURRENT GENERATION

To determine the success of the model in generating the Leeuwin Current, the data from the model will be compared with observational data collected during LUCIE. A simple statistical test will be used to test the hypothesis that the mean velocity components and temperature from the model could come from a population having the mean and variance of the observed data. The comparison between model and observation data will be done at three locations, one in each of the different wind forcing regions used in the model. The three locations are chosen to best coincide with deep water LUCIE stations and cover almost the entire latitudinal extent of the domain. Figure 8 shows the location of the LUCIE stations used in the comparison.

The contribution of each of the forcing mechanisms in each region of the model is determined by choosing a grid point representative of the current in that region for analysis. The points chosen are 45 km offshore of the model's eastern boundary. Based on satellite imagery (e.g., Figure 2), a position 45 km from the shelf break is on the western side of the core of the current and in a region of eddy generation. Analysis of the model data at these points should show a generally poleward flow with variability due to instability in the current. Time series plots and summary tables of velocity components and temperature will be presented to show the effect of the forcing mechanisms at a range of depths. The positions of the points at which the time series are plotted are also shown in Figure 8.

For ease of comparison between model results and observational data, the alongshore velocity components have been given the same sign convention, one consistent with the model and the northern hemisphere. Despite the application of the model results to the Leeuwin Current, the change is easier performed on tables of observations than on plotting and analysis routines which access the model output directly.

Grid point (60,11), designated A, is selected for analysis of the model output at the equatorward end of the domain. It is poleward of the region initialized with the warm water representing the NW Shelf waters and latitudinally central to the wind forcing regime for that region of the model. The comparison at the equatorward end of the model domain will use data from grid point (58,14), designated B. This is the closest point in the model to the station designated B2 by Boland *et al.* (1989) from LUCIE. The shal-

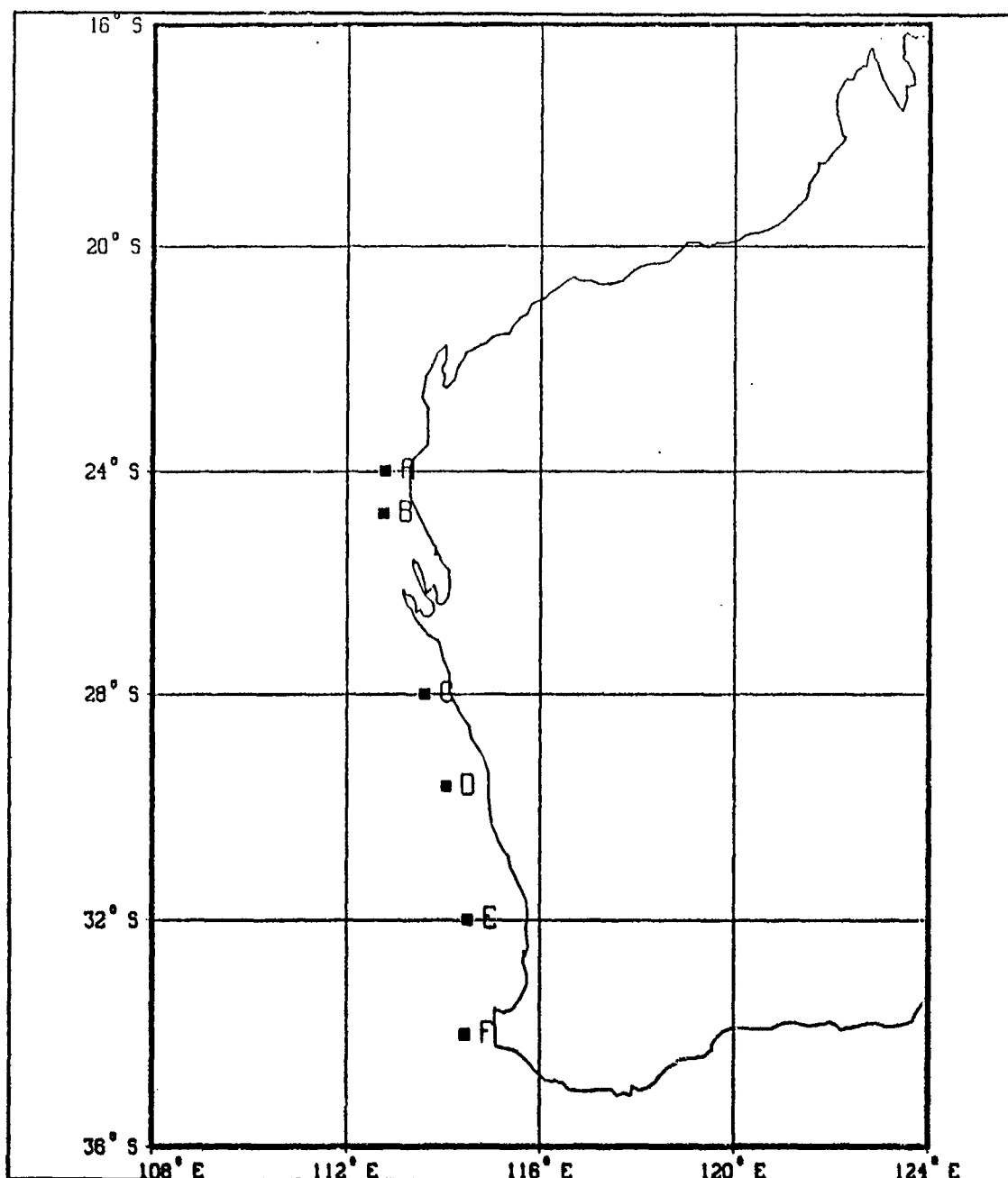


Figure 8. Location of points used for data analysis and comparison: Points A, C and E are selected for analysis of the contributions by the different forcing mechanisms to the Leeuwin Current. Points B, D and E coincide with LUCIE stations and will be used for comparison with model results. Refer to Figure 1 for geographic locations.

low waters (~ 80 m depth) in which the LUCIE array B2 was deployed make it barely suitable for use; however, since it is the only observational data available, it will be used to give at least some indication of the model's accuracy in that region.

Grid point (60,33), designated C, is chosen as representative of the current in the middle region of the model and will be used to discuss the effects of the different forcing mechanisms in that region. A mean of grid points (62,40) and (63,40) corresponds to the Dongara array designated D4 during LUCIE and will be used for comparisons. Data from these grid points is designated D in this study. Array D4 is chosen over the other Dongara arrays for comparison as it furthest offshore, thus minimizing the effects of bottom topography. No shallow water comparison is made with the current meter data available over the shelf, as a shelf is not included in the model.

Finally, in the poleward third of the domain, grid point (60,55), designated E, is selected as representative of the current in that region, being away from boundaries, latitudinally central and on the western side of the core of the current. In selecting Cape Mentelle arrays M3 and M4 for the comparison at the poleward end of the domain, the same reasoning is used as for the deep water Dongara stations. The model data is derived from an average of grid points (62,64) and (63,64) and is designated F. The positions of points A through F is shown in Figure 8.

1. Equatorward End of Domain

The model results at selected depths for grid point A are presented in Table 6. Figures 9, 10, and 11 show the time series for each Case at depths of 10 m, 100 m and 300 m. The velocity scale is unchanged over the series of plots to emphasize the magnitude of the fluctuations for each case. The tabulated data together with the figures will be used to examine the effect of each of the forcing mechanisms in the equatorward region of the model. Only Cases 2 through 5 are considered. Case 1, addressed in Chapter V. B. 1, was run as a test case for the model and does not include any forcing by the mechanisms under investigation.

Table 6. MODEL RESULTS. POINT A

		Case 2		Case 3		Case 4		Case 5	
		Mean	S.Dev.	Mean	S.Dev.	Mean	S.Dev.	Mean	S.Dev.
10 m	<i>u</i>	1.1	0.3	13.5	18.0	-2.6	1.4	7.6	15.3
	<i>v</i>	2.1	1.5	17.6	16.6	4.5	1.5	10.3	14.8
	<i>T</i>	23.1	0.1	26.4	1.8	22.2	0.3	24.1	1.6
50 m	<i>u</i>	0.8	0.4	11.0	13.3	-1.7	1.2	7.6	11.7
	<i>v</i>	1.6	1.5	13.7	13.2	3.4	1.6	9.3	12.8
	<i>T</i>	22.3	0.0	25.2	1.5	22.1	0.2	23.7	1.4
100 m	<i>u</i>	0.6	0.3	7.3	10.5	-1.6	1.0	5.5	8.9
	<i>v</i>	0.9	1.4	9.0	10.3	2.6	1.5	6.8	11.1
	<i>T</i>	21.1	0.0	23.8	1.0	21.1	0.1	22.6	1.1
300 m	<i>u</i>	-0.2	0.2	2.6	5.2	-1.0	0.7	4.3	5.2
	<i>v</i>	-1.1	1.2	-3.7	4.0	-0.5	1.3	-1.5	7.0
	<i>T</i>	15.0	0.1	16.0	0.3	15.0	0.1	16.1	0.3
500 m	<i>u</i>	-0.1	0.2	0.3	2.8	-0.3	0.2	1.8	3.3
	<i>v</i>	-0.9	0.8	-6.0	3.4	-0.6	1.0	-5.5	3.8
	<i>T</i>	10.1	0.0	10.5	0.1	10.1	0.0	10.6	0.1

a. Case 2. Forcing by Indian Ocean Density Field

The Indian Ocean density field, as defined by its temperature structure, is sufficient to establish a surface geostrophic flow with onshore and poleward components. The onshore flow is weak and decreases with depth, reversing direction and becoming offshore above 300 m. The alongshore flow shows a similar trend, being poleward in the upper layers, reversing with depth and showing little variability over the 160 days of the run.

b. Case 3. Forcing by Indian Ocean and NW Shelf

The addition of NW Shelf water to the Indian Ocean forcing leads to a much stronger and highly variable flow. The strength of the onshore and the poleward components of the flow increases markedly. The much warmer temperatures in Case 3 compared with Case 2 highlights the advection of the warmer NW Shelf water poleward. In the vertical structure, the depth at which the flow reverses appears, by interpolation, to be slightly deeper and the equatorward undercurrent is also increased in strength compared with Case 2. In view of the proximity of point A to the source of the shelf

water, the domination of the geostrophic flow in Case 2 by the shelf water is expected so that further downstream, these effects should be decreased.

c. Case 4. Forcing by Indian Ocean and Winds

At the equatorward end of the domain, the winds have offshore and equatorward components (Table 3); hence their effect on the surface current, according to Ekman theory, should be to transport mass poleward and offshore respectively. Table 6 shows that the cross-shore flow reverses in the upper 100 m from the onshore flow of Case 2, and the flow is now offshore at all five chosen levels. The alongshore component of the current is stronger in the poleward direction, consistent with the coastal Ekman theory. This increase in strength of the poleward component of the flow into the prevailing wind has been observed in current meter data collected at the southern end of the NW Shelf by Holloway and Nye (1985). Below 100 m, the equatorward undercurrent is still present but has weakened slightly from Case 2. A temperature decrease from 23.1 °C to 22.2°C in the near surface layer (10 m) is consistent with upwelling due to the equatorward alongshore component of the wind.

Comparing the magnitude of the variations in velocity components and temperature due to the addition of NW Shelf water (Case 3) and wind forcing (Case 4), the effect of the winds is clearly less significant than the NW Shelf waters. The wind forcing would appear to be a significant feature only during those periods when the NW Shelf waters are not present, possibly immediately before the influx of the warmer waters. From the monthly components of wind stress (Table 3), one observes that the wind stress between 20°S and 25°S in November and January has no zonal component. This is the period during which the Leeuwin Current is weakest and often non-existent (Godfrey and Ridgeway, 1985). The change in the wind stress to a strengthening offshore component and weaker alongshore component coincides with the seasonal generation of the Leeuwin Current. Although this study shows the effect of the winds to be second order to the NW Shelf waters, they may play a significant role in determining the timing of the poleward surge of the warmer NW Shelf waters, which, once established, dominates the flow regime.

d. Case 5. Forcing by Indian Ocean, NW Shelf and Winds

The flow resulting from the combined effect of the three forcing mechanisms shows that their net effect is dominated by the inclusion of the NW Shelf water and that the combined flow is weakly non-linear. In Case 3, the addition of the NW Shelf waters to the Indian Ocean waters (Case 2) led to a large increase in the strength of both the onshore and poleward components of the flow. In Case 4, the effect of the wind forcing

was to create an offshore flow, whilst increasing slightly the strength of the poleward flow. Upper layer temperatures were much higher in Case 3 and slightly lower in Case 4. The combined forcing produces a current which is closer in character to Case 3 than Case 4. The flow is onshore and poleward in the upper layers with an equatorward undercurrent at and below 300 m. Temperatures are increased at all levels from Case 2. The flow in Case 5 clearly shows the contributions of the NW Shelf waters and the wind forcing on the current generated in Case 2. Since their combined effect cannot be calculated by a simple linear addition of the individual effects, it is likely that the forcing mechanisms are weakly non-linear in the equatorward third of the domain.

e. Comparison with Observations

A comparison between the statistics from Case 5 at a depth of 65 m and the observations at the LUCIE Carnarvon station at the same depth is shown in Table 7. The hypothesis that the mean values of the model data μ_1 are equal to the means of the observational data μ_2 is tested. Using the procedure of Walpole and Myers (1985) with a significance level of $\alpha = 0.01$, corresponding to a critical region of $z = \pm 2.575$, the z statistics for u , v , and T were calculated by:

$$z = \frac{(\bar{x}_1 - \bar{x}_2)}{\sqrt{(\frac{\sigma_1^2}{n_1}) + (\frac{\sigma_2^2}{n_2})}}$$

where \bar{x}_1 and \bar{x}_2 are the means of the two populations, σ_1^2 and σ_2^2 their variances, and n_1 and n_2 the number of data points.

The calculated z statistics for u , v , and T are -1.55, 1.43 and 8.54 respectively. Thus, the means of the velocity components from the model are not statistically different from observations at a significance level of 0.01, although the temperature data is.

Comparing the results from points A and B, 63 km apart, the sensitivity of the statistical comparison to the grid point chosen from the model is clearly apparent. Had a position a mere few grid points away from point A been selected for the comparison, the mean values for u , v , and T of 7.0, 8.6, and 23.4 respectively would have been well outside the critical values for the 0.01 significance level. The strong gradient in the mean values between the two points, which are on the western side of the core of the current, indicates the model generated current may have either a strong shear or large variability. The sensitivity to the point chosen for comparison also reduces the

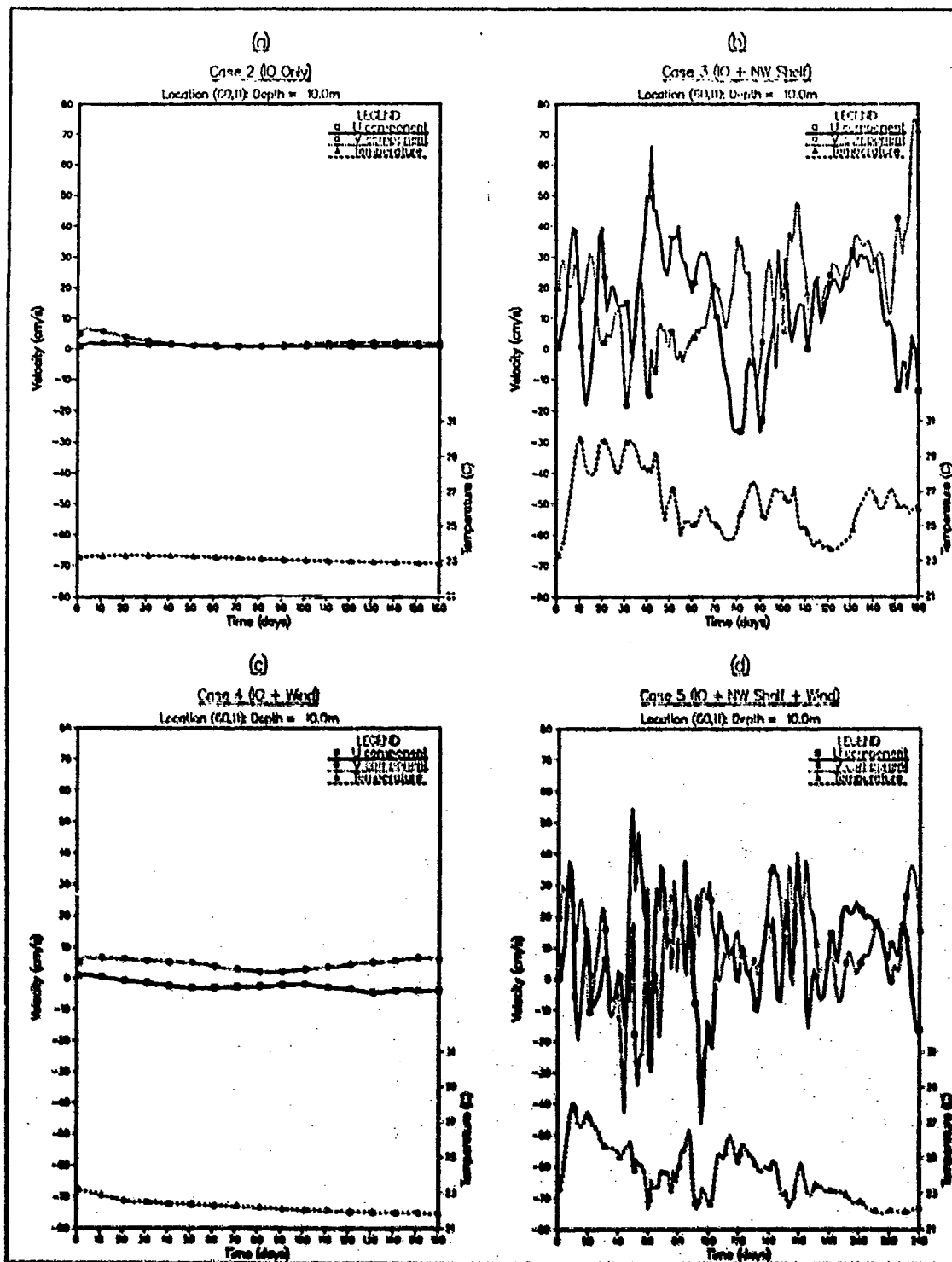


Figure 9. Velocity & temperature time series: Time series of (a) Case 2; (b) Case 3; (c) Case 4; and (d) Case 5 at point A (Figure 8) at depth 10 m.

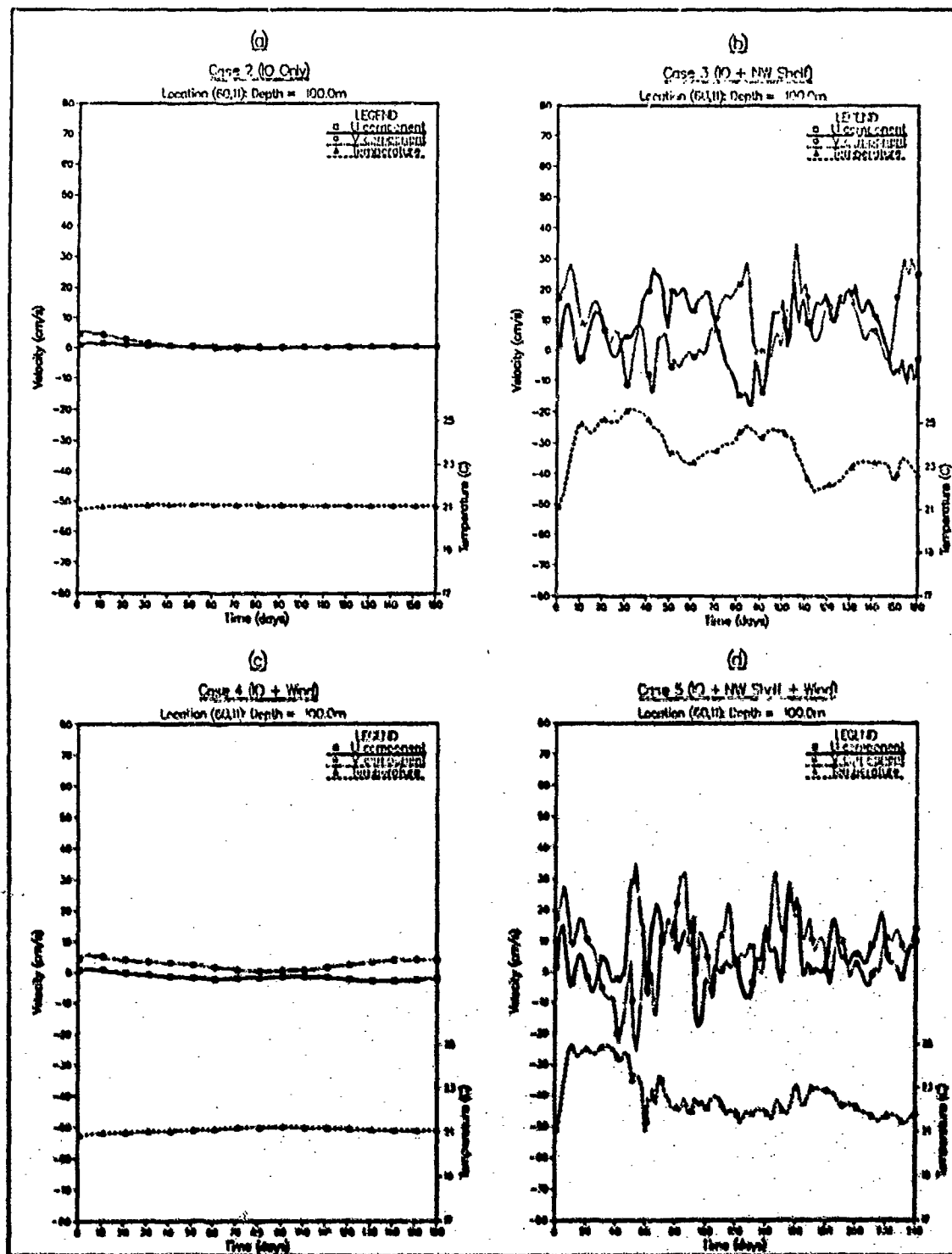


Figure 10. Velocity & temperature time series: Time series of (a) Case 2; (b) Case 3; (c) Case 4; and (d) Case 5 at point A (Figure 8) at depth 100 m.

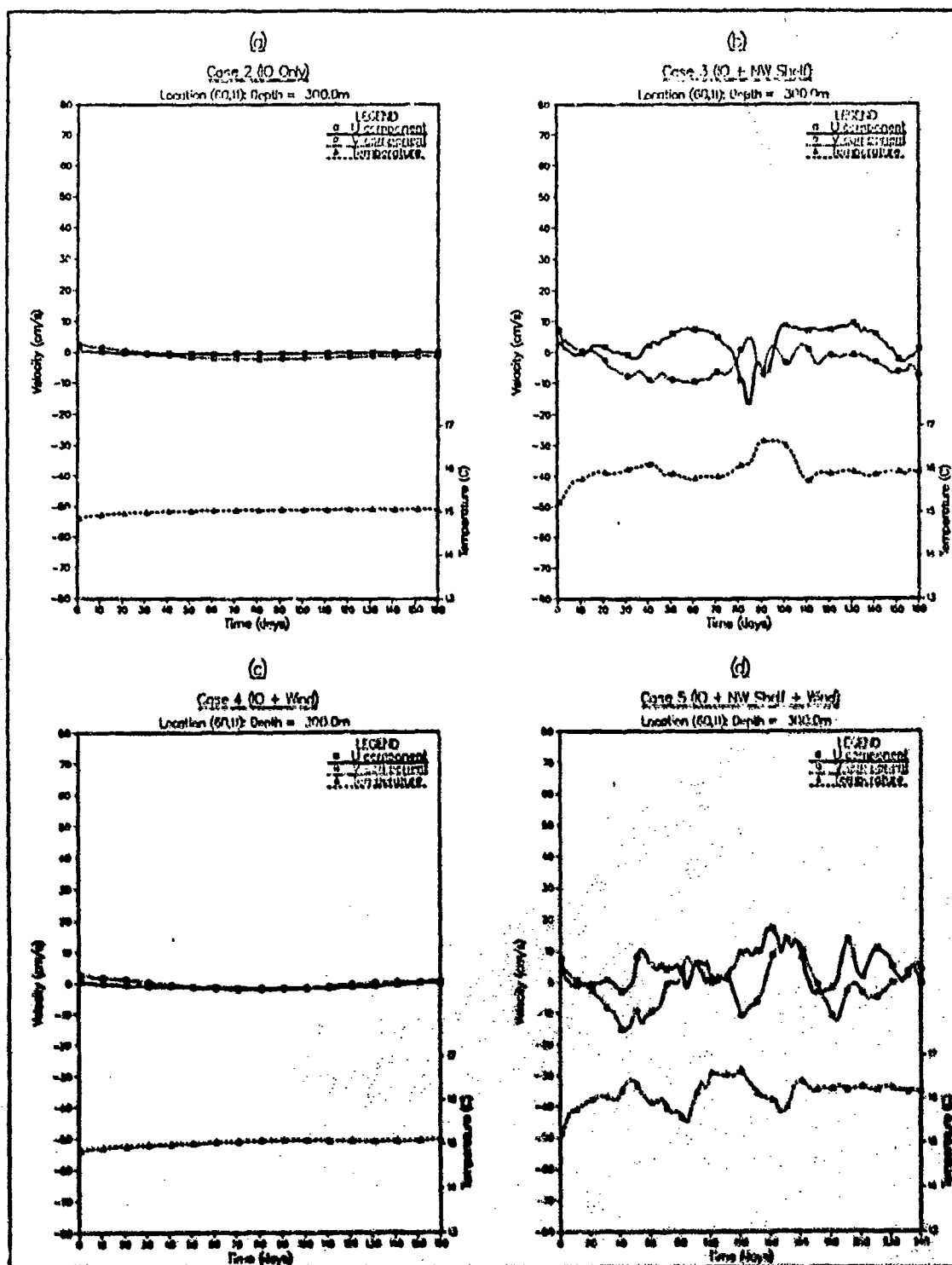


Figure 11. Velocity & temperature time series: Time series of (a) Case 2; (b) Case 3; (c) Case 4; and (d) Case 5 at point A (Figure 8) at depth 300 m.

significance of the statistical results. One may conclude only that the model produces a current with similar characteristics to the Leeuwin Current as observed at the Carnarvon array during LUCIE.

Table 7. MODEL/OBSERVATIONS COMPARISON (B VERSUS CARNARVON)

		U		V		T	
		Mean	S.Dev.	Mean	S.Dev.	Mean	S.Dev.
65 m	Model	-1.5	13.5	7.4	12.4	23.1	0.9
	Observations	0.2	6.3	5.7	8.9	22.3	1.5

2. Center of Domain

Table 8 contains model results for selected depths for point C, (Figure 7) chosen as representative of the center of the domain. This table, along with Figures 12, 13 and 14, will be referred to in discussing the effects of the different forcing mechanisms over the middle third of the domain (covering approximately latitudes 26° to 30°).

Table 8. MODEL RESULTS. POINT C

		Case 2		Case 3		Case 4		Case 5	
		Mean	S.Dev.	Mean	S.Dev.	Mean	S.Dev.	Mean	S.Dev.
10 m	u	1.6	0.8	7.0	6.3	-0.7	4.1	-13.2	14.9
	v	7.9	3.5	8.5	11.4	8.6	5.4	8.4	16.6
	T	22.1	0.1	22.3	0.4	21.7	0.1	22.2	0.5
50 m	u	1.3	0.7	6.7	5.2	0.5	3.9	-11.4	13.8
	v	6.3	3.6	6.9	10.2	7.8	5.2	7.6	15.5
	T	21.3	0.2	21.6	0.4	21.5	0.3	22.0	0.6
100 m	u	0.9	0.5	6.2	4.7	0.4	3.5	-10.4	12.4
	v	4.2	3.8	5.0	9.0	6.3	5.0	6.0	13.9
	T	20.1	0.2	20.5	0.3	20.3	0.3	21.3	0.8
300 m	u	0.0	0.4	4.9	4.4	0.5	2.4	-8.3	8.9
	v	-2.8	4.0	-4.0	6.6	0.3	5.1	-3.0	10.4
	T	14.9	0.2	15.2	0.2	14.9	0.2	15.8	0.6
500 m	u	-0.1	0.4	3.0	3.4	0.5	1.5	-5.0	6.4
	v	-3.4	2.5	-7.1	4.3	-1.1	4.7	-6.3	7.9
	T	10.3	0.1	10.5	0.2	10.2	0.1	10.5	0.4

a. Case 2. Forcing by Indian Ocean Density Field

The features of the surface flow field observed at the equatorward end of the domain, i.e., onshore and poleward flow, are much stronger in the center region of the model. In the upper 100 m, the onshore flow is at least 50% stronger, and the poleward flow approximately four times that observed at point A at the same levels. This is consistent with the alongshore pressure gradient generating a geostrophic onshore flow which then forces the poleward boundary current. The alongshore current is expected to increase in strength at the poleward end of the domain as it is continually augmented by more inflow. The variability in the velocity components is also larger in the middle of the domain than at the equatorward end. This suggests that eddies forming in the flow generated by the alongshore pressure gradient are more likely at the poleward end of the domain where the flow is stronger. Temperatures are colder at point C than at point A, which is consistent with the temperature initialization.

b. Case 3. Forcing by Indian Ocean and NW Shelf

The inclusion of the NW Shelf waters strongly increases the strength of the onshore flow but has little effect on the mean poleward flow. The most significant change due to the Shelf waters is in the variability which is much larger at all levels. This increased variability is most pronounced on the alongshore velocity component. Temperatures are slightly increased at all levels due to the advection of the warmer waters poleward. The magnitude of the temperature increase is far less than that observed at point A. This is seen as evidence of increased mixing with the Indian Ocean water and of a larger net flux of heat to the atmosphere during the longer passage of the NW Shelf waters away from their origin. The effect of the NW Shelf waters is most pronounced on the equatorward undercurrent which increases in strength by far more than the poleward flow. While the increase in strength of the undercurrent is seen as a better indicator of the overall effects of the inclusion of NW Shelf water, the surface flow is a better indicator of the variability due to the NW Shelf waters.

c. Case 4. Forcing by Indian Ocean and Winds

The wind stress used by the model in the central third of its domain is equatorward with no cross shore component (Table 3). On a western boundary, this equatorward stress is expected to force an offshore flow and bring cooler waters to the surface. The results in Table 8 show the offshore flow at 10 m and a reduced onshore flow at 50 m and 100 m, evidence of the expected effect of the wind forcing. At 300 m

and 500 m, which are below the thermocline, the cross-shore flow is onshore whereas in Case 2 the u component of velocity is negligible. This onshore flow below the thermocline is seen as further evidence of a wind forced upwelling regime as it provides a continuity balance for the offshore flow nearer the surface.

In considering the effect at point C of the wind forcing, one must account for both the local forcing and the current advected into the region by wind forcing upstream. As seen earlier, the wind forcing strengthened the poleward component of the flow at point A. The local forcing, having no cross-shore component, does not directly contribute to any alongshore transport. Thus, the increase in strength of the poleward component of the flow is due to upstream wind forcing instead of local forcing.

d. Case 5. Forcing by Indian Ocean, NW Shelf and Winds

The current generated at point C by the combination of the three forcing mechanisms (Case 5) appears to be highly non-linear. Each of the flow characteristics (u , v , T) reacts to the combined forcing in a far different manner than it does to each forcing mechanism in isolation.

This is seen most clearly in the cross-shore (u) component of velocity. From a weak onshore flow at 10 m, 50 m and 100 m in Case 2, which is strengthened in Case 3 and opposed in Case 4, the combined forcing produces a mean flow which is very strongly offshore and highly variable. Examination of Figures 12 and 13 shows a nearly sinusoidal trend to the velocity components which is suggestive of eddies moving slowly past point C.

Despite the large departure from the results of Cases 2, 3, and 4 for the cross-shore component of velocity, the alongshore component for Case 5 varies little from the values recorded in the earlier experiments. The standard deviation is much higher, reflecting the variations due to eddies. However, the mean, particularly at 10 m, 50 m and 100 m, is not significantly different in Case 5 to the mean in each of the previous cases.

One important feature of the combined forcing is the time of onset of the variability. As can be seen in Figures 12, 13 and 14, Case 2 has little variability. With the inclusion of wind forcing in Case 4, low frequency fluctuations are apparent from about day 80 onward. In Case 3, the variability occurs earlier and at a higher frequency and finally in Case 5 the instability in the flow is apparent almost immediately.

e. Comparison with Observations

Model results and observational data are presented in Table 9 for comparison. A two sided test using a z statistic was again used to test the hypothesis that the

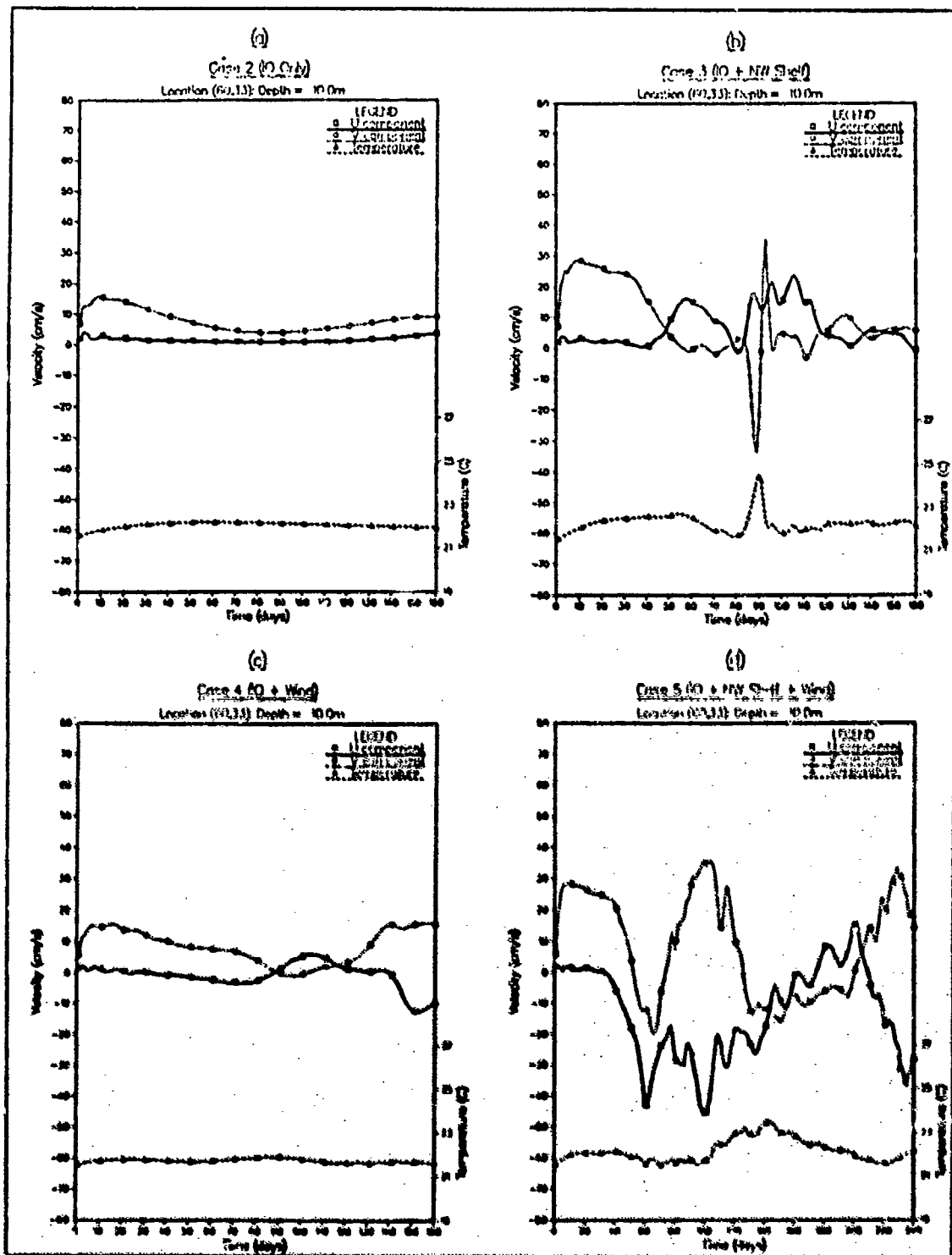


Figure 12. Velocity & temperature time series: Time series of (a) Case 2; (b) Case 3; (c) Case 4; and (d) Case 5 at point C (Figure 8) at depth 10 m.

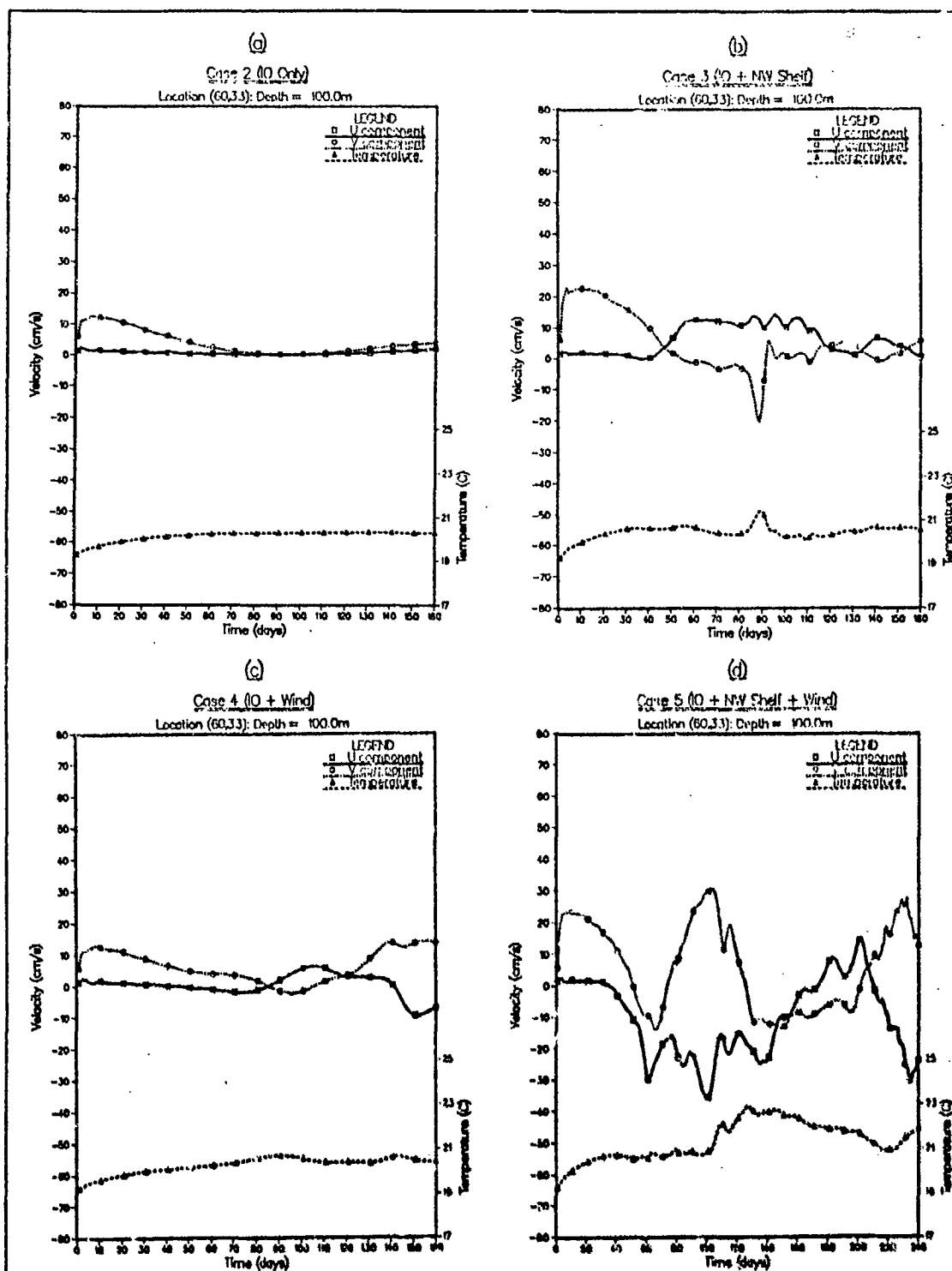


Figure 13. Velocity & temperature time series: Time series of (a) Case 2; (b) Case 3; (c) Case 4; and (d) Case 5 at point C (Figure 8) at depth 100 m.

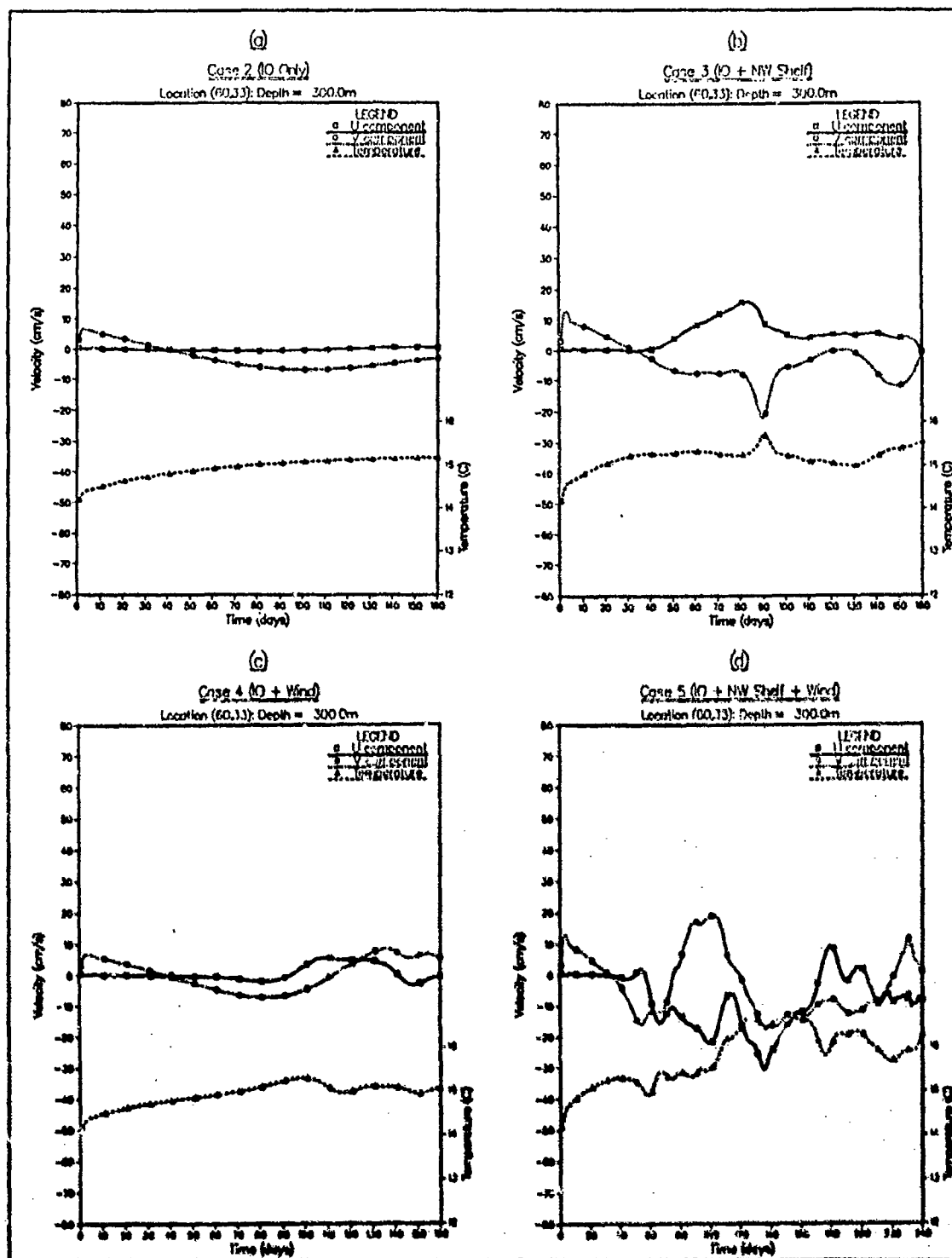


Figure 14. Velocity & temperature time series: Time series of (a) Case 2; (b) Case 3; (c) Case 4; and (d) Case 5 at point C (Figure 8) at depth 300 m.

means of the model and observational data are from the same population. Using the same significance level of 0.01, corresponding to a critical z region of ± 2.575 , the test showed that model results differed markedly from observations for both u and T . The v component had z statistics of 2.4 (71 m), 0.34 (121 m), 0.11 (246 m) and 9.27 (446 m), indicating good model results for the poleward flow.

Whilst the u component of velocity from the model at point D differs so markedly from the observed values at the Dongara array, a comparison of data from Tables 8 and 9 shows that the large onshore velocities observed during LUCIE are produced by the model a few grid points away at point C. This further highlights the difficulties in choosing a single point from the grid of a model which has a flat bottom and shear walls for comparison with observations. This would be further exacerbated if, as suggested by Weaver and Middleton (1989), the local shelf geography and topography are important factors determining the flow characteristics.

Table 9. MODEL/OBSERVATIONS COMPARISON (D VERSUS DONGARA)

		U		V		T	
		Mean	S.Dev.	Mean	S.Dev.	Mean	S.Dev.
71 m	Model	1.3	4.6	25.1	17.2	21.9	0.7
	Observations	-15.4	28.7	30.3	34.6	20.9	0.9
121 m	Model	1.3	4.7	23.5	14.7	21.2	0.6
	Observations	-5.5	14.3	24.3	20.7	19.4	1.5
246 m	Model	0.8	4.1	0.1	10.7	17.3	0.4
	Observations	-2.4	7.7	0.2	11.1	14.4	0.9
446 m	Model	0.3	4.1	-12.7	6.5	12.1	0.2
	Observations	-1.1	5.3	-5.9	11.2	9.4	0.2

3. Poleward End of domain

The results from the model at point E are presented in Table 10 along with time series plots at 50 m, 100 m, and 300 m shown in Figures 15, 16 and 17, respectively. The effects of the different forcing mechanisms in the poleward third of the domain, covering approximately latitudes 30° to 34° , should be an extrapolation of the results in Tables 6 and 8 and are discussed earlier.

Table 10. MODEL RESULTS. POINT E

		Case 2		Case 3		Case 4		Case 5	
		Mean	S.Dev.	Mean	S.Dev.	Mean	S.Dev.	Mean	S.Dev.
10 m	u	3.1	2.3	4.2	13.9	1.2	5.2	-5.1	17.0
	v	8.9	8.2	14.7	14.8	8.1	11.4	12.7	16.8
	T	20.8	0.3	21.5	0.8	21.0	0.3	21.7	0.6
50 m	u	2.8	2.2	3.7	11.8	1.7	5.2	-4.2	15.9
	v	7.8	7.6	13.0	12.8	8.6	10.4	13.1	15.5
	T	20.1	0.4	20.8	0.8	20.6	0.6	21.4	0.8
100 m	u	2.4	2.0	2.9	9.9	1.0	5.0	-4.2	14.3
	v	6.1	6.7	10.1	11.0	6.7	9.1	10.9	13.9
	T	19.0	0.4	19.7	0.8	19.3	0.6	20.7	1.1
300 m	u	1.1	1.4	-0.3	7.9	-2.2	5.5	-5.7	10.5
	v	-0.8	4.7	-2.5	8.1	-1.4	5.6	0.8	10.9
	T	14.5	0.3	15.0	0.5	14.5	0.4	15.5	0.8
500 m	u	0.6	1.2	-1.5	6.9	-2.2	4.0	-6.0	7.6
	v	-4.4	3.7	-7.7	6.6	-4.4	4.0	-4.8	8.4
	T	10.4	0.2	10.5	0.3	10.3	0.2	10.7	0.3

a. Case 2. Forcing by Indian Ocean Density Field

As theorized earlier, the strength of the onshore and poleward components of the velocity generated by the model are stronger at the poleward end of the model (point E) than at either of points A and C. By interpolation, the flow reversal below the stronger surface flow appears to be deeper at point E than at point C and the undercurrent is stronger at 500 m. The onshore velocity component is stronger at point E than at either points A or C, and, as expected, temperatures are generally lower at the poleward end of the domain.

b. Case 3. Forcing by Indian Ocean and NW Shelf

The effects of the inclusion of NW Shelf waters are similar at the poleward end of the domain as elsewhere. The poleward flow in the upper levels (10 m, 50 m and 100 m) increases in magnitude and variability and the equatorward component of the undercurrent is also stronger.

Temperatures increase at all levels due to the advection of the NW Shelf water poleward. The magnitude of the temperature increases is less at the poleward end than at the equatorward end of the domain.

c. Case 4. Forcing by Indian Ocean and Winds

The wind forcing at the poleward end of the model is mainly onshore with a weak equatorward component (Table 3). The effects of wind forcing at point E is a combination of the remote upstream forcing, which contributes to the flow advected to the poleward end of the region, and the local forcing. The local forcing, having onshore and equatorward components should produce equatorward and offshore transport. The local forcing is clearly the stronger of the two as the onshore and poleward flows of Case 2, which should be augmented by upstream advection, are both reduced at point E. This is evidence of the local offshore and equatorward Ekman transport weakening the magnitude of the flow. With no offshore velocity component there are no upwelling effects seen and the temperature actually increases slightly over than of Case 2. The variability due to the inclusion of wind forcing is much higher at E than at either points A or C. This may be due to the higher wind stress at the poleward end of the domain than further equatorward. A second factor may be the downstream location of point E which makes it more susceptible to eddies which are advected into the region. Finally, the eddies may be more prevalent purely as a function of the increase in strength of the current at the poleward end of the domain.

d. Case 5. Forcing by Indian Ocean, NW Shelf and Winds

At point E, non-linearity and very high variability are major characteristics of the flow generated by the combined forcing mechanisms. The alongshore component of the flow, whilst highly variable, is very similar in strength to Case 3. This indicates that the wind forcing, whilst stronger in absolute terms than at points A or C, has the least effect of the three forcing mechanisms at the poleward end of the domain. This is borne out by Figures 15 and 16 in which the general characteristics of plot (d) are more similar to (b) than either (a) or (c).

The effect of each forcing mechanism on the timing and frequency of instability is also seen in Figures 15 and 16. In Case 2 (b) the instability is low frequency and slow to develop. In Case 4 (d) it develops earlier but again at low frequency and with low amplitude fluctuations. The NW Shelf water in Case 3 (c) leads to earlier, higher frequency and larger amplitude deviations while in Case 5 (d) the instability is apparent almost immediately. These results are consistent with the results at point C. There the instability occurs earlier in Case 5, i.e., when the three forcing mechanisms are

combined. The results at point A are less clear due to the immediate proximity of the NW Shelf water.

e. Comparison with Observations

The two-sided hypothesis test described earlier was again used to test the hypothesis that the model and observational data are from the same population. A significance level of 0.01 was again used and the velocity components calculated by the model easily met the criteria. The calculated z statistics for the u components are 0.08 (43 m), 0.0 (90 m and 160 m), 2.38 (230 m) and 0.32 (320 m) compared to the critical value of 2.575. For the v component the z statistics are 0.76 (43 m), 0.48 (90 m), 0.26 (160 m), 0.83 (230 m) and 1.43 (320 m). Temperature values are consistently high in the model and differ from observations by up to three degrees. Comparison of model results at the inshore comparison point and the representative point chosen further offshore shows a strong cross-shore temperature gradient. The discrepancy between temperatures from the model and observations corresponds to a two grid point misalignment of the data from each source.

Table 11. MODEL/OBSERVATIONS COMPARISON (F VERSUS CAPE MENTELLE)

		U		V		T	
		Mean	S.Dev.	Mean	S.Dev.	Mean	S.Dev.
43 m	Model	0.1	1.1	30.5	25.2	21.5	0.6
	Observations	0.2	12.0	28.8	22.6	20.5	1.0
90 m	Model	0.0	1.1	24.7	21.1	20.7	0.7
	Observations	0.0	12.7	23.8	24.0	24.6	2.6
160 m	Model	-0.0	0.8	13.8	17.2	19.1	1.0
	Observations	-0.0	9.3	13.4	20.0	16.9	2.1
230 m	Model	-0.1	0.7	4.5	15.2	17.5	0.9
	Observations	-1.0	6.9	3.2	20.3	14.4	2.0
320 m	Model	-0.0	0.7	-6.0	14.6	15.1	0.5
	Observations	0.1	5.6	-3.8	22.2	12.1	0.9

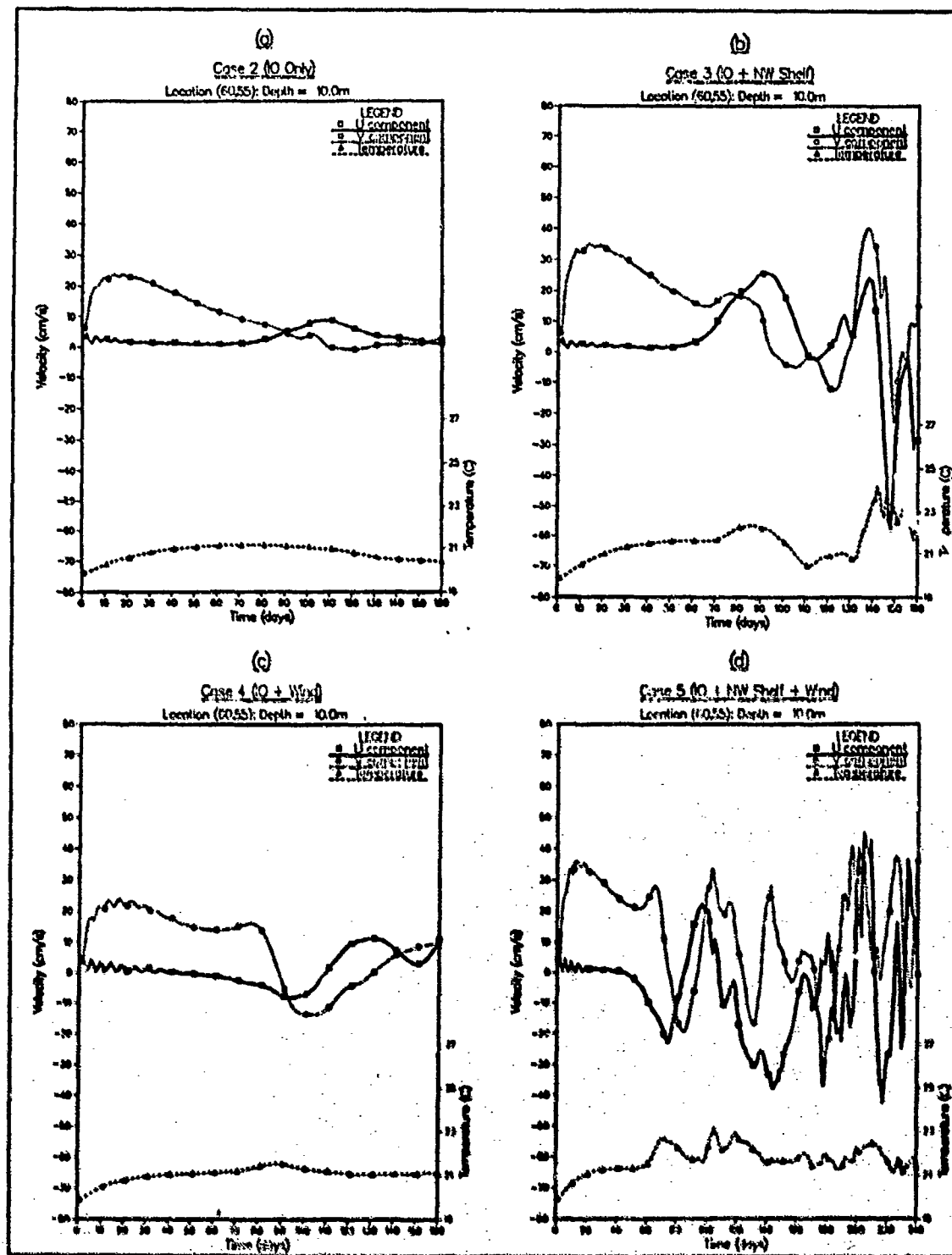


Figure 15. Velocity & temperature time series: Time series of (a) Case 2; (b) Case 3; (c) Case 4; and (d) Case 5 at point E (Figure 8) at depth 10 m.

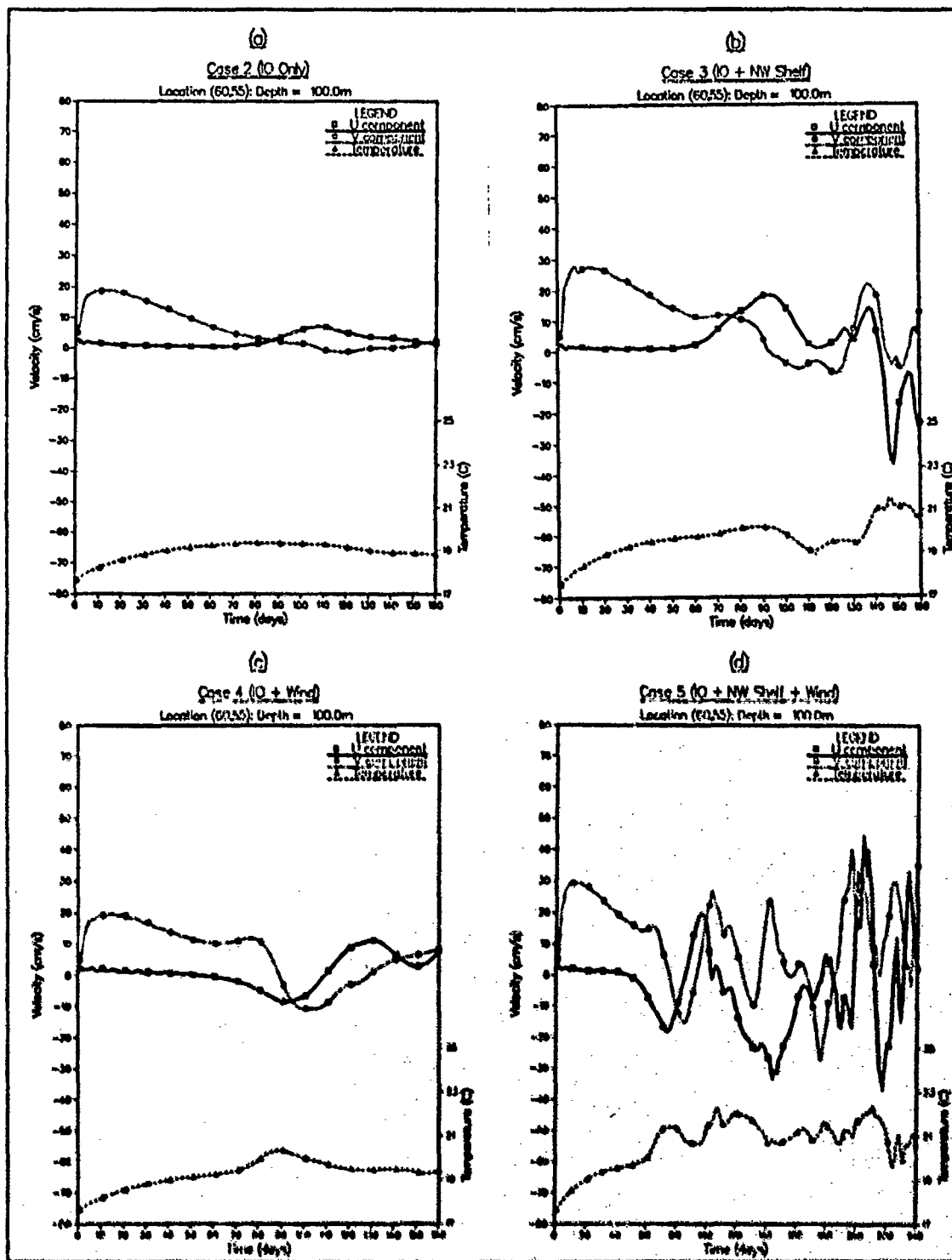


Figure 16. Velocity & temperature time series: Time series of (a) Case 2; (b) Case 3; (c) Case 4; and (d) Case 5 at point E (Figure 8) at depth 100 m.

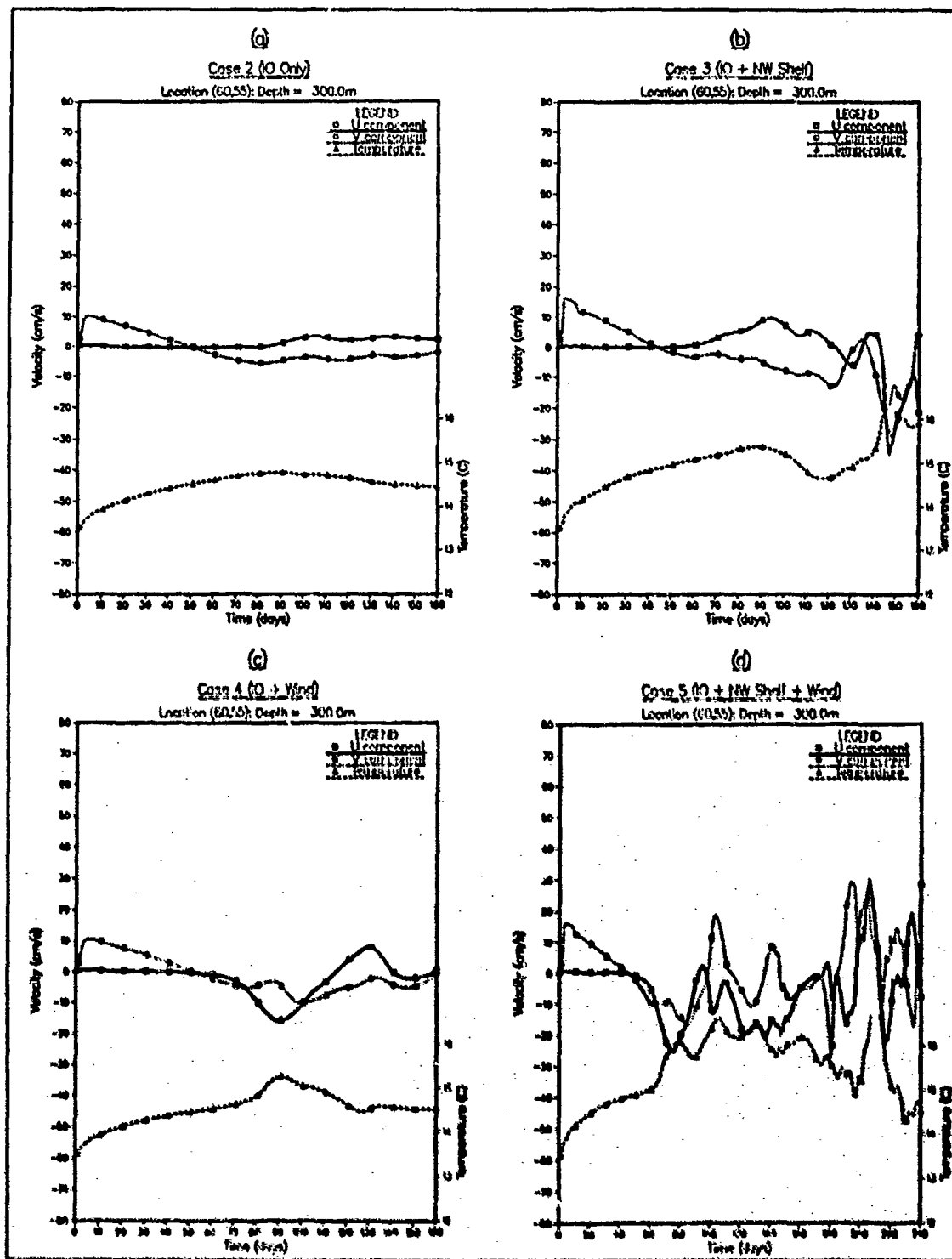


Figure 17. Velocity & temperature time series: Time series of (a) Case 2; (b) Case 3; (c) Case 4; and (d) Case 5 at point E (Figure 8) at depth 300 m.

B. INSTABILITY IN THE LEEUWIN CURRENT

1. Case 1. Forcing by Initialized Current

Case 1 was run primarily as a test of the model and analysis software. The results are presented for completeness and to acquaint the reader with the analysis. The results will also act as a reference for the later studies. Figure 18 shows the surface dynamic height anomaly field, calculated from a reference level of 2000 m. Dynamic height anomaly plots will subsequently be referred to as pressure fields. The pressure field shows instabilities developing rapidly in the current with perturbations apparent by day 10. By day 30 rings have formed and detached from the jet. The rings then move offshore from days 30 to 40.

The surface fields of velocity components and temperature are presented at 10 day intervals for the duration of the run (40 days) in Figures 19 through 21. The cross-shore velocity field is generally the best indicator of eddy formation and by day 10 it is apparent that instabilities are leading to eddy formation along the entire meridional extent of the domain. By day 20 the eddies have increased in size and move offshore. This trend of growth and offshore movement continues to the end of the run at 40 days.

a. Energy Analysis

The energy analysis described in Chapter 4 may be used to determine the temporal mean and eddy kinetic energy and available potential energy from statistics collected during periods of near constant total energy. Plots of the energy transfers during these periods give the dominant transfers and the regions in which they are most active. The total kinetic energy and available potential energy over the entire domain and for all layers is plotted in a time series and shown in Figure 22. The period during which the energy analysis may be applied to determine the dominant instability mechanisms is the first 10 days. Since a separate layer by layer analysis showed that the upper five layers contain most of the energy, subsequent analysis will be confined to those layers.

Figure 23 shows the energy transfers summed over the upper five layers for the first 10 days. Subplots (a), (b) and (c) are plotted at the same contour interval to allow for easy comparison, and (d) is the cross-shore velocity component field at day 10, the end of the period under analysis. Subplot (a) shows the large transfer from mean available potential energy (\bar{P}) to eddy available potential energy (P') along the entire inshore extent of the domain. The baroclinic transfer from P' to eddy kinetic energy (K') is shown in subplot (b), and the barotropic transfer from mean kinetic energy (\bar{K}) to K' in (c). Comparisons of (b) and (c) and each of them in turn with (d), show that the

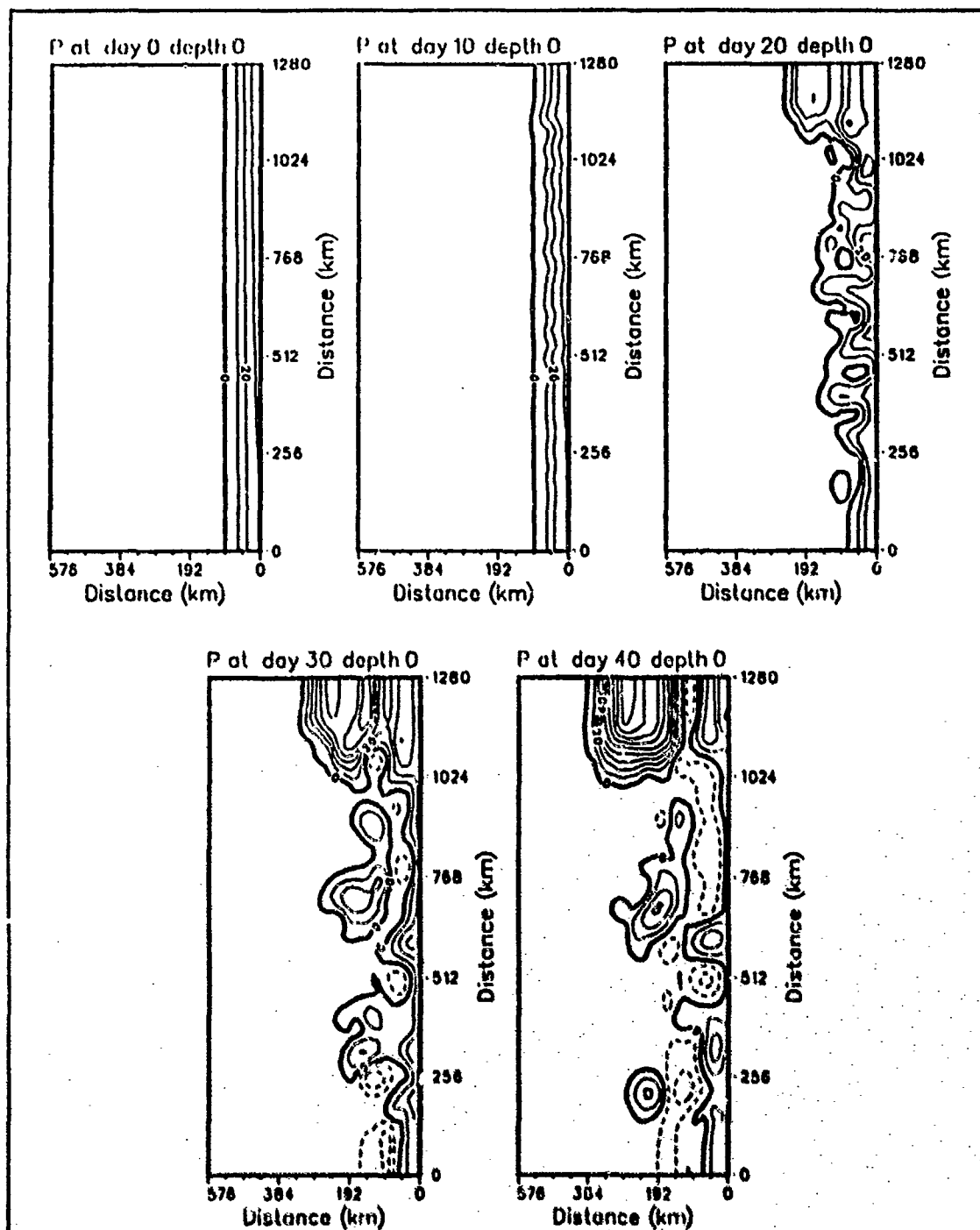


Figure 18. Case I. Surface pressure field, days 0 - 40: Dynamic height anomaly (cm) at surface relative to a reference level of 2000 m. Contour interval is 5 cm.

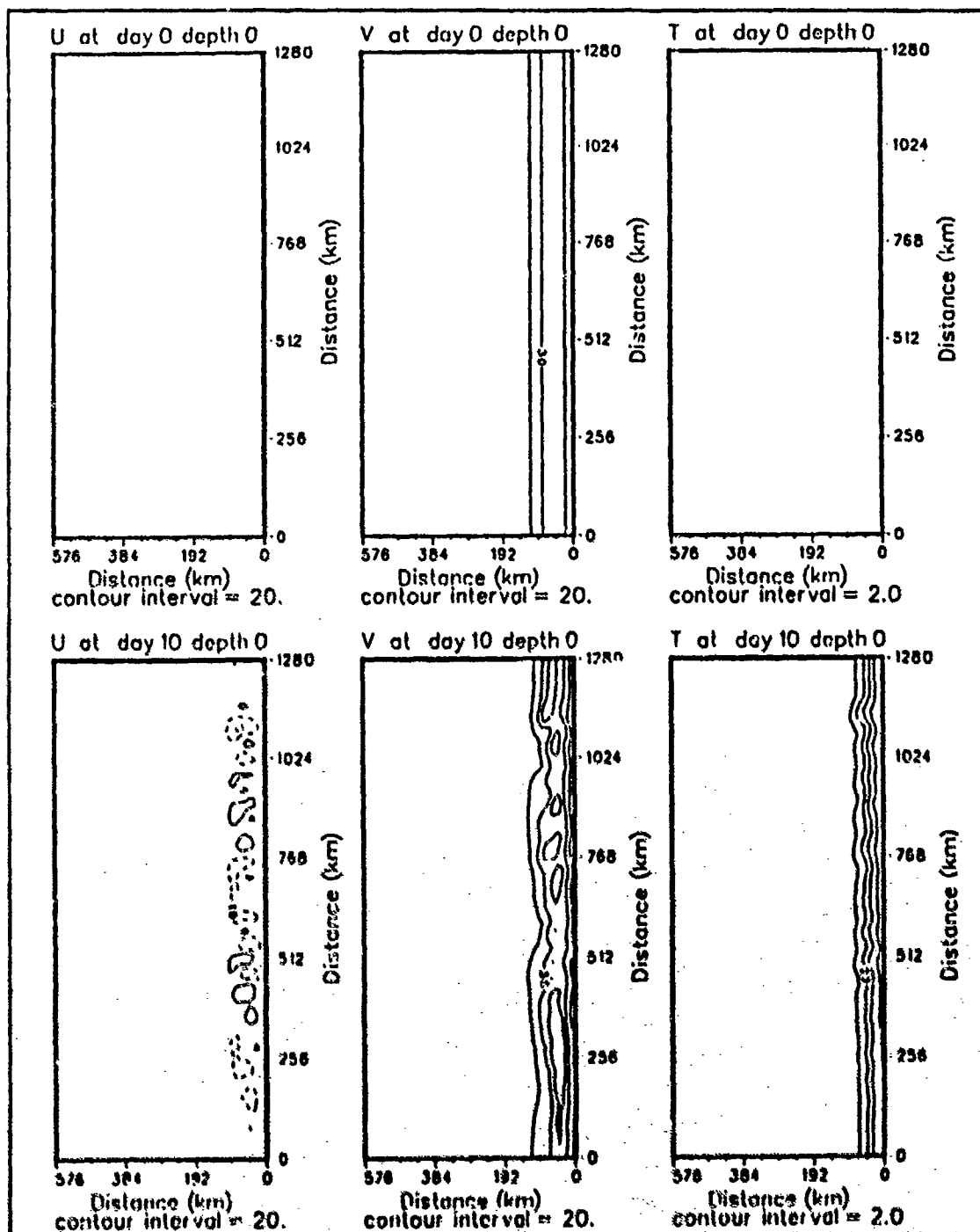


Figure 19. Case 1. Surface velocity and temperature fields, days 0 - 10: Cross-shore velocity component (cm s^{-1}), alongshore velocity component (cm s^{-1}) and temperature ($^{\circ}\text{C}$) at surface.

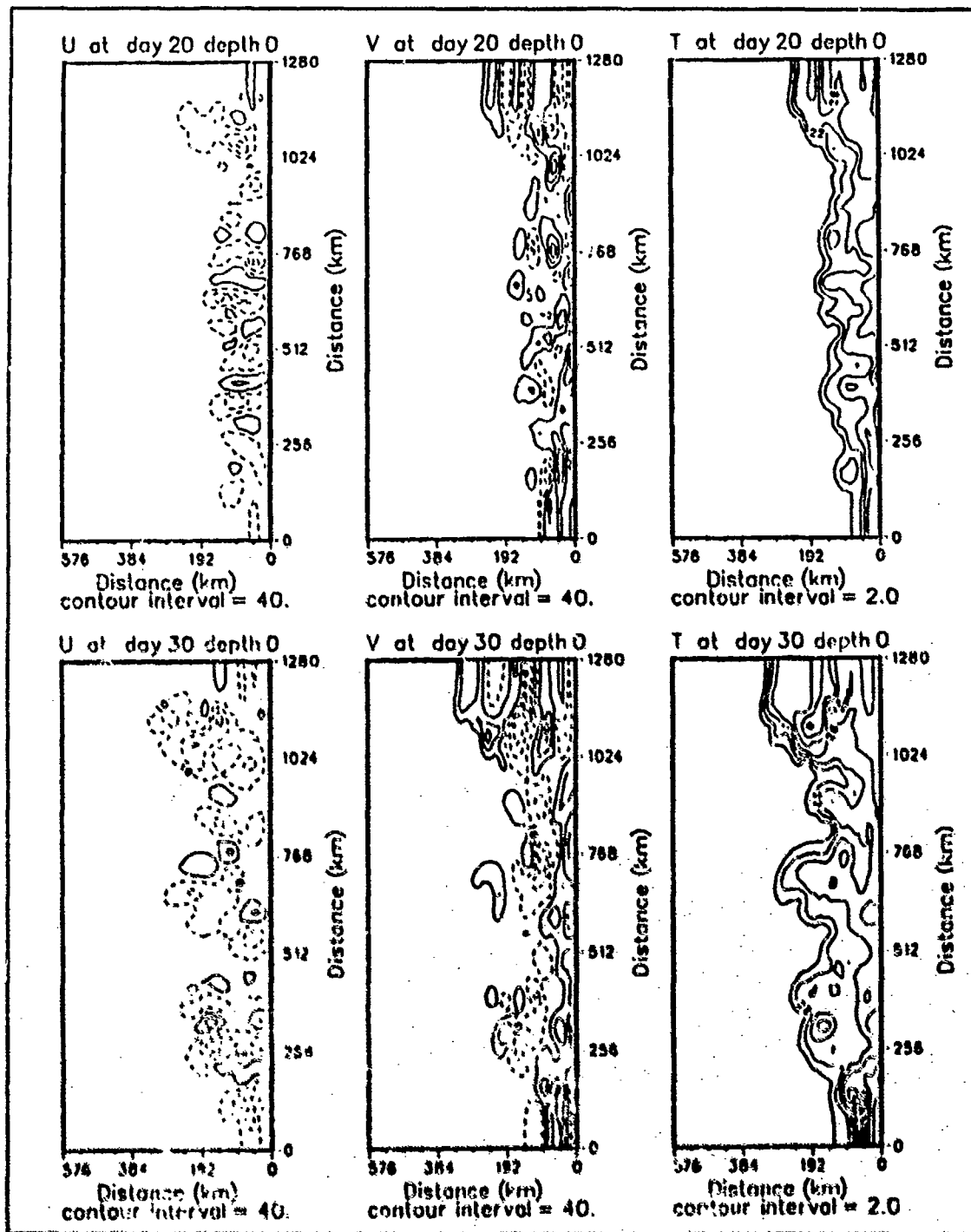


Figure 29. Case 1. Surface velocity and temperature fields, days 20 - 30: As for Figure 19. Note: contour interval for the velocity components is now 40 cm s^{-1}

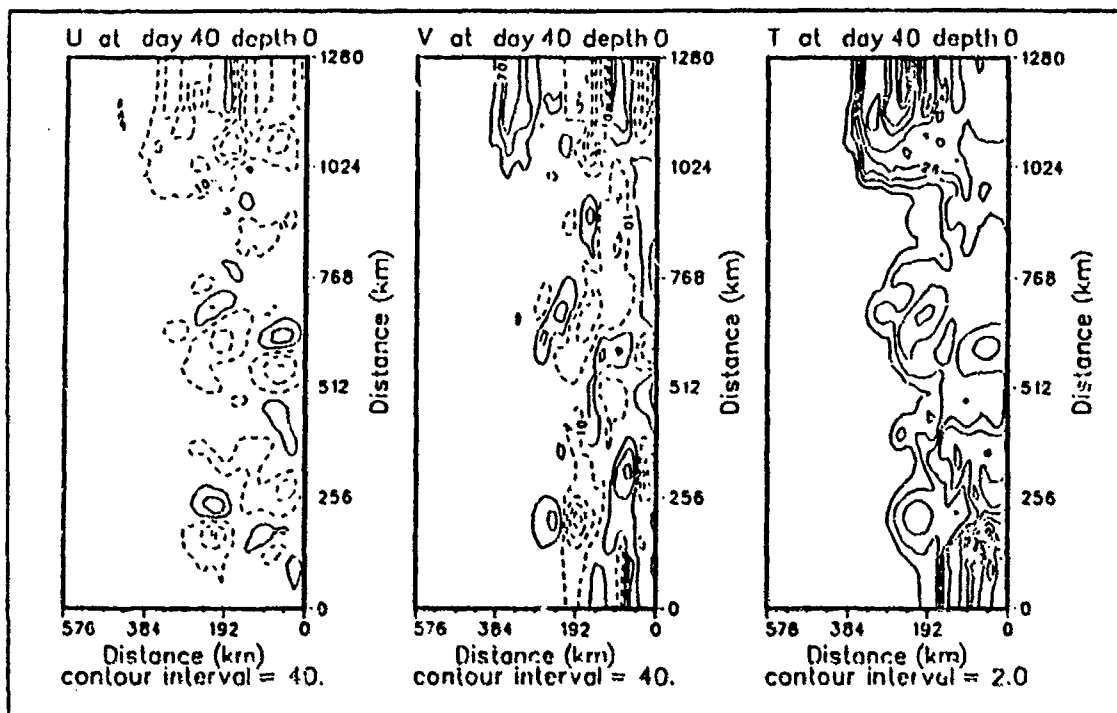


Figure 21. Case I. Surface velocity and temperature fields, day 40: As for Figure 20.

instability appears to be mixed baroclinic and barotropic, with the barotropic apparently stronger and more widespread. The choice of contour interval may be masking other regions of instability which fail to reach a contour level so a more detailed analysis is required. The extensive regions of negative barotropic and available potential energy transfers need to be accounted, since a domain wide average may result in cancellation of effects and not show the eddy generation mechanisms.

After identifying the region of instability, the energy analysis was re-run over the more constrained region of the inshore 10 grid points, corresponding to an offshore distance of 90 km, between 120 km and 1160 km alongshore. The energy transfer diagram for the first 10 days over the narrow inshore region is shown in Figure 24. It shows that the regions of positive barotropic transfer are dominant over the negative barotropic transfers, resulting in a net transfer from \bar{K} to K' . The energy available for barotropic instability comes from the horizontal shear in the flow (Kamenkovich *et al.*, 1986) so increased barotropic contribution should be apparent if the energy transfers are calculated over the shear zone offshore of the core of the

poleward jet (Figure 19). Similarly, in the core of the poleward jet, where the under-current and hence vertical shear are greatest, baroclinic instability is expected to be dominant. To test these hypotheses, the region described above is divided into two smaller regions, each covering five cross-shore grid points. The inshore region is in the core of the current and the offshore region closer to the horizontal shear zone. The energy transfer diagrams for each region are in Figures 25 and 26, respectively. Comparing the transfers for each domain, the regions of dominant baroclinic and barotropic instability can be isolated. The results clearly show that in a region of mixed instability, the baroclinic growth will be dominant in regions of high vertical shear and the barotropic dominant in regions where horizontal shear is strongest.

b. Spectral Analysis

The spectral techniques described in Chapter 4 are now applied to Case 1. Figures 27 through 30 show the spectral density as a function of alongshore wavenumber at 10 day intervals. As seen in Figure 23 earlier, the u component of velocity is a better indicator of eddy formation than either the v component or temperature. Although spectra for each variable are on the plots, the discussion will focus on the u velocity component. At day 10, the dominant growth is at wavenumbers $k = 0.002, 0.01$ and 0.015 corresponding to wavelengths of 500 km, 100 km and 66 km respectively. By day 20 the energy has increased by an order of magnitude and a slight spectral shift is evident. The maximum energy is now at wavenumbers $k = 0.007, 0.01$ and 0.015 . The amplitude of the spectra remains nearly constant from days 20 to 40. Figure 31 shows the time series of Figures 27 to 30. The aspect of the plots makes it possible for peaks to 'hide' other features and the linear amplitude scale suppresses all but the dominant wavenumbers. Comparing Figures 27 and 31, the peaks at day 10 cannot be seen on the linear scale as they are nearly 2 orders of magnitude smaller than the maximum values on the plot. Figure 31 shows three dominant peaks at approximately 400 km, 135 km and 90 km. By day 40 the peak at a wavelength of 135 km is the strongest. A combination of the figures allows both the wavenumbers associated with the initial growth to be determined from the 2-dimensional plots and the general trend or shifts at maximum amplitude to be determined from the 3-dimensional plots.

c. Instability Analysis

Finally, the necessary and sufficient conditions for the sources of instability are investigated. For baroclinic instability Kamenkovich *et al.* (1986) gives the necessary conditions as:

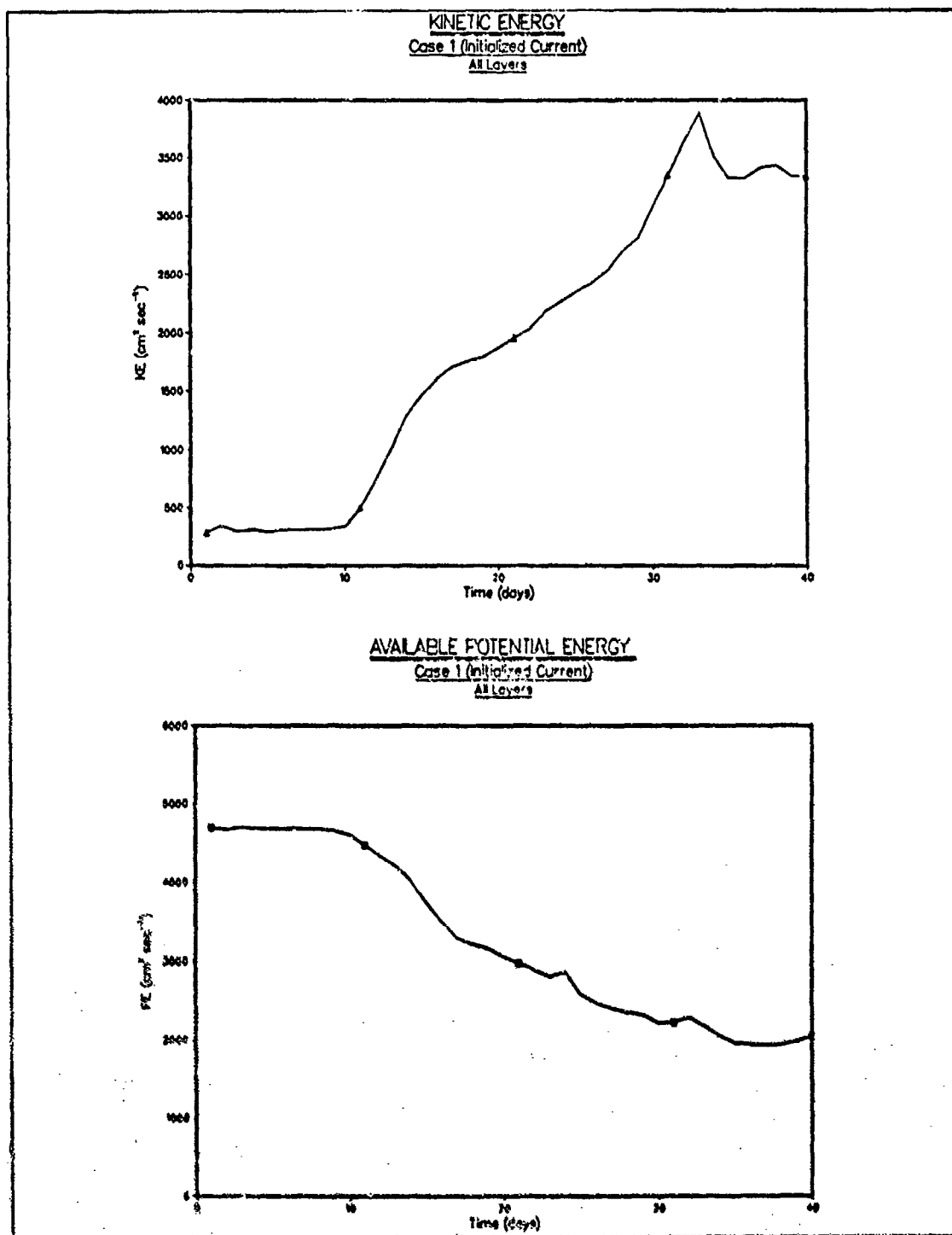


Figure 22. Case 1. Energy time series: Total kinetic and available potential energy ($\text{cm}^2 \text{s}^{-1}$) summed over all layers and the entire domain.

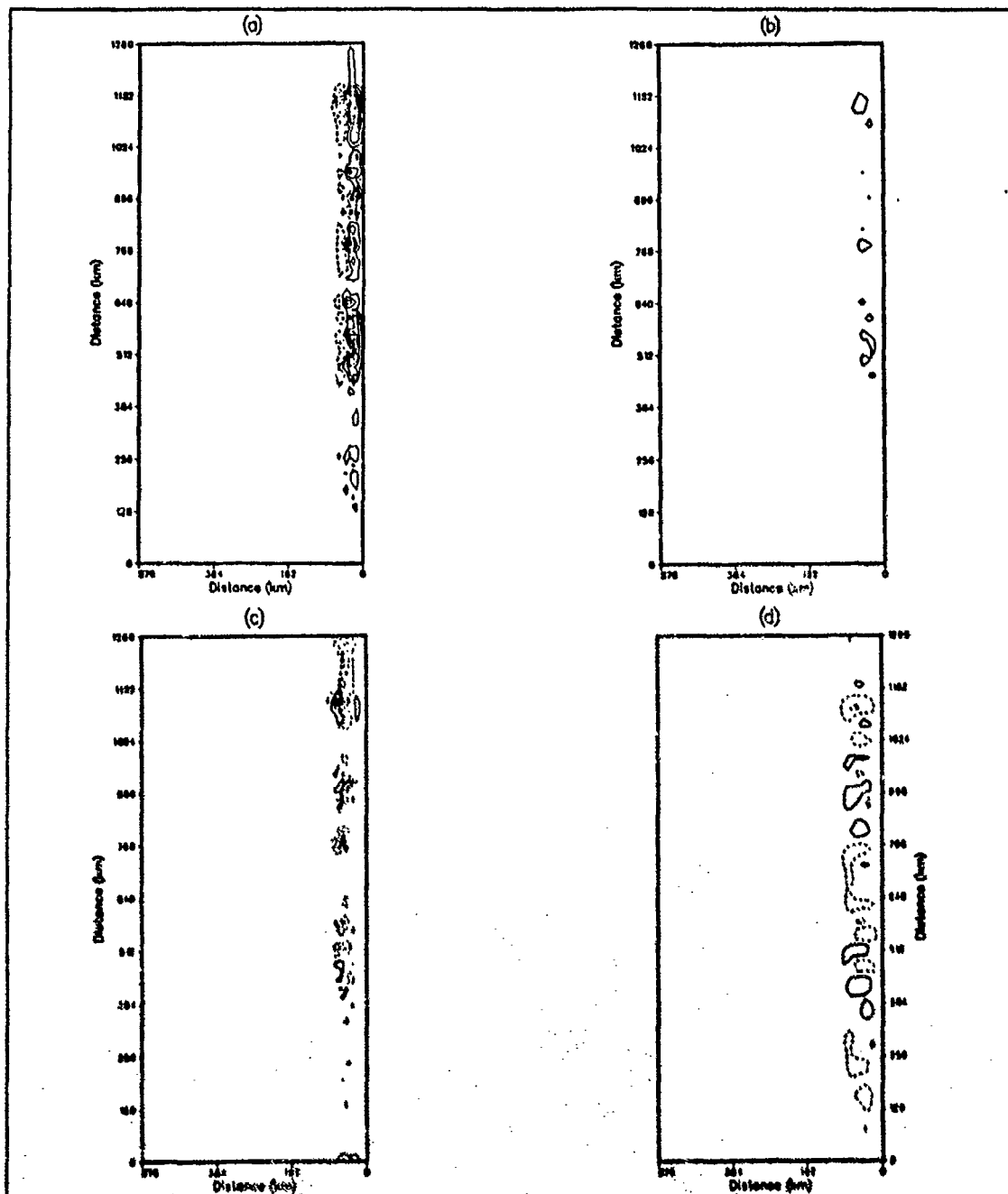


Figure 23. Case 1. Energy transfers: Transfers of energy from (a) \bar{P} to P' , (b) P' to K' and (c) \bar{K} to K' in units of $\text{ergs cm}^{-3} \text{s}^{-1}$ with contour interval of $2 \times 10^3 \text{ ergs cm}^{-3} \text{s}^{-1}$. Transfers are averaged over days 1-10 and summed over the upper five layers. Subplot (d) is the cross-shore velocity component at day 10. Contour interval is 20.0 cm s^{-1} .

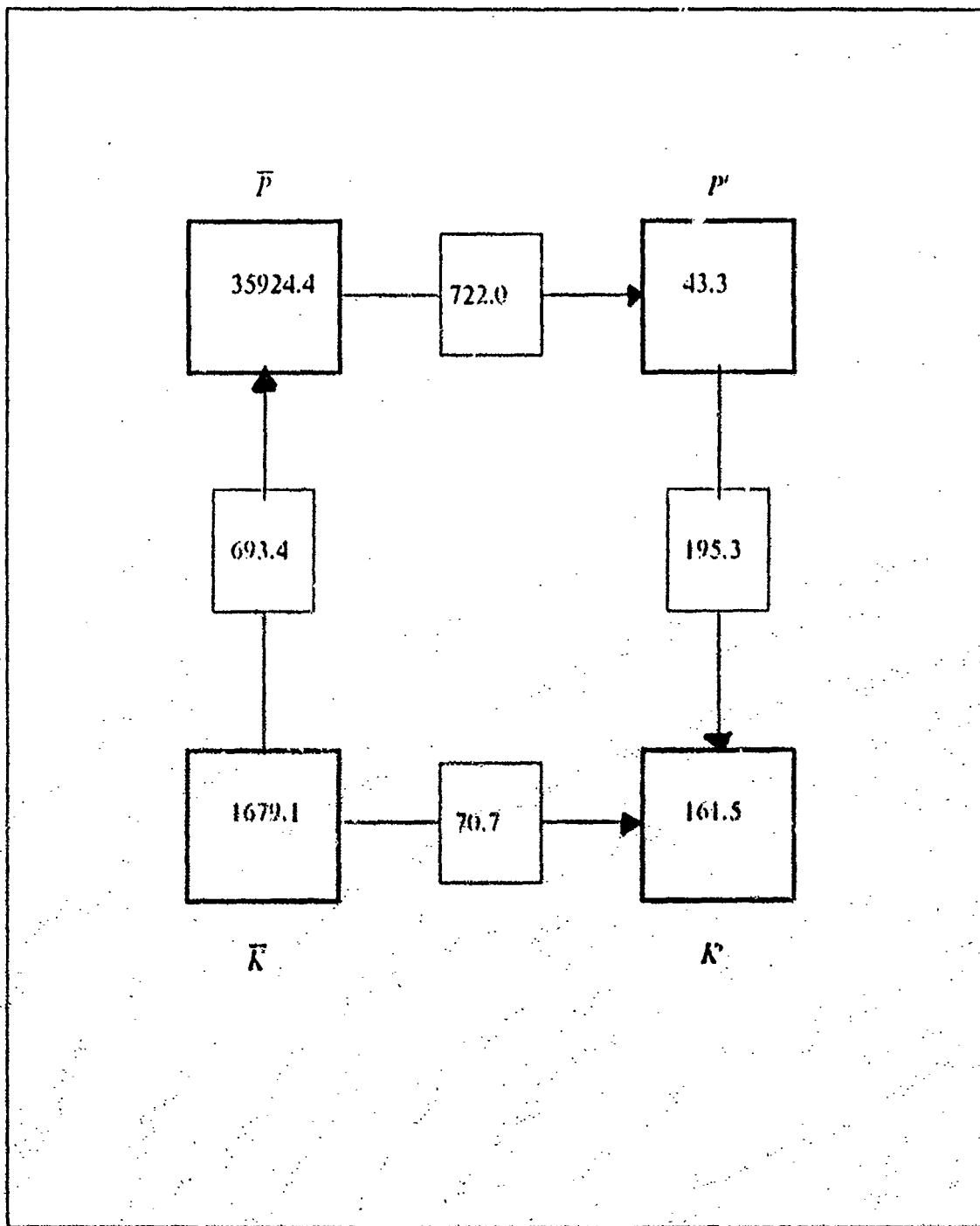


Figure 24. Case 1. Energy transfer diagram: The energy transfer diagram for the region extending 90 km offshore. Units for \bar{P} , \bar{K} , P' and K' are ergs cm^{-3} , and transfers are in units of $\text{ergs cm}^{-3} \text{s}^{-1} \times 10^{-4}$.

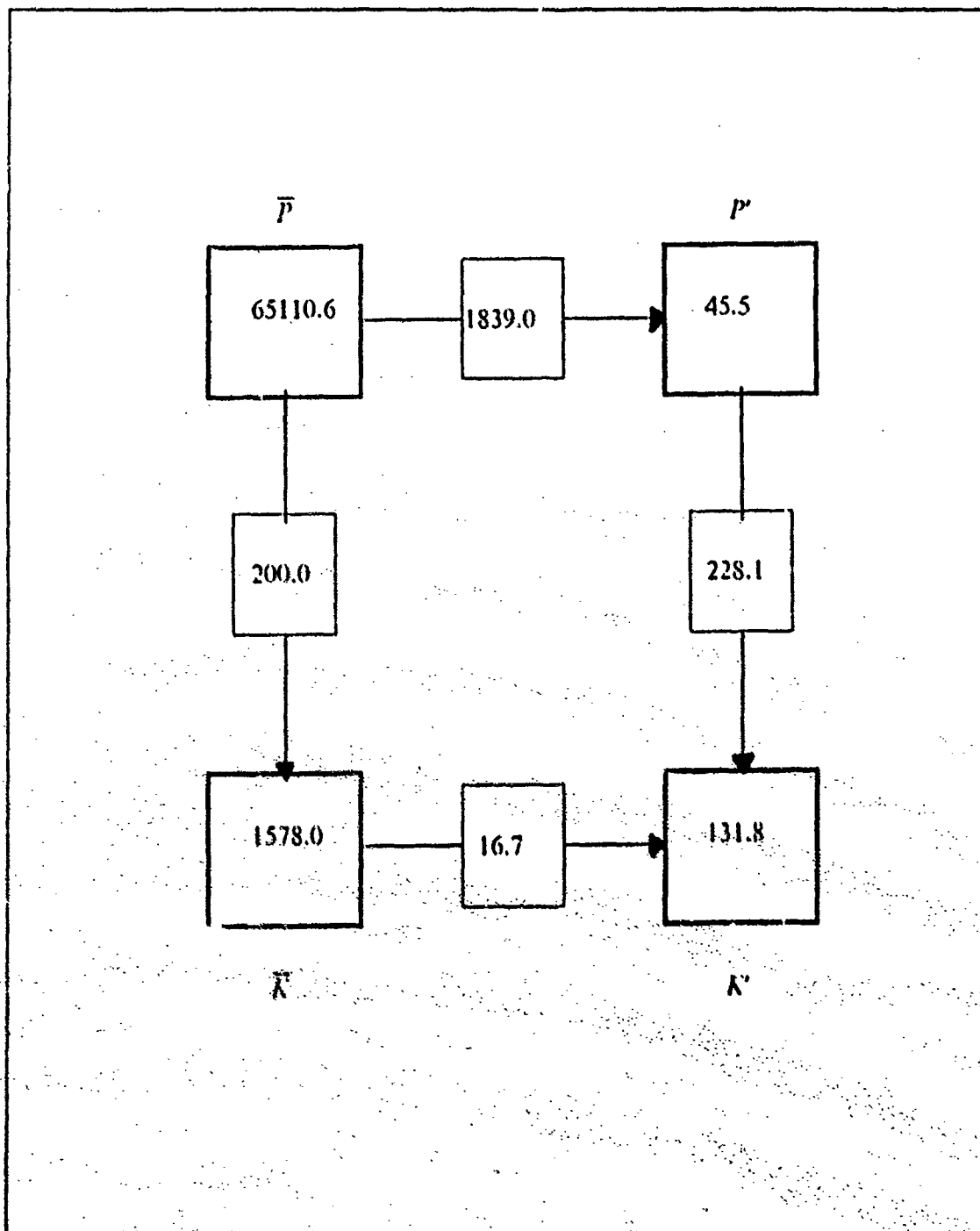


Figure 25. Case 1. Energy transfer diagram: As for Figure 24 for the region extending 45 km offshore which is the inshore half of the region in Figure 24.

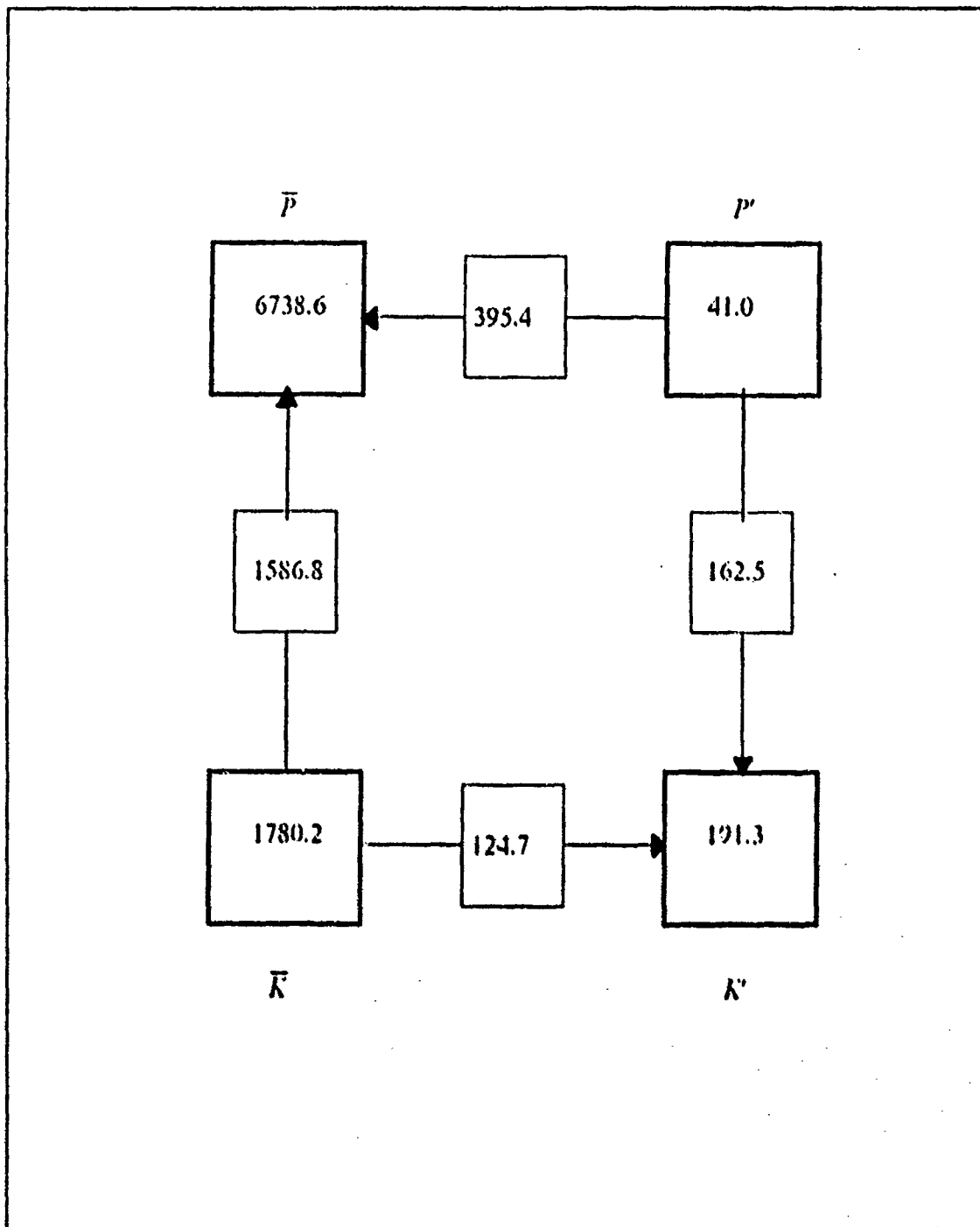


Figure 26. Case 1. Energy transfer diagram: As for Figure 24 for the region extending from 45 km to 90 km offshore which is the offshore half of the region in Figure 24.

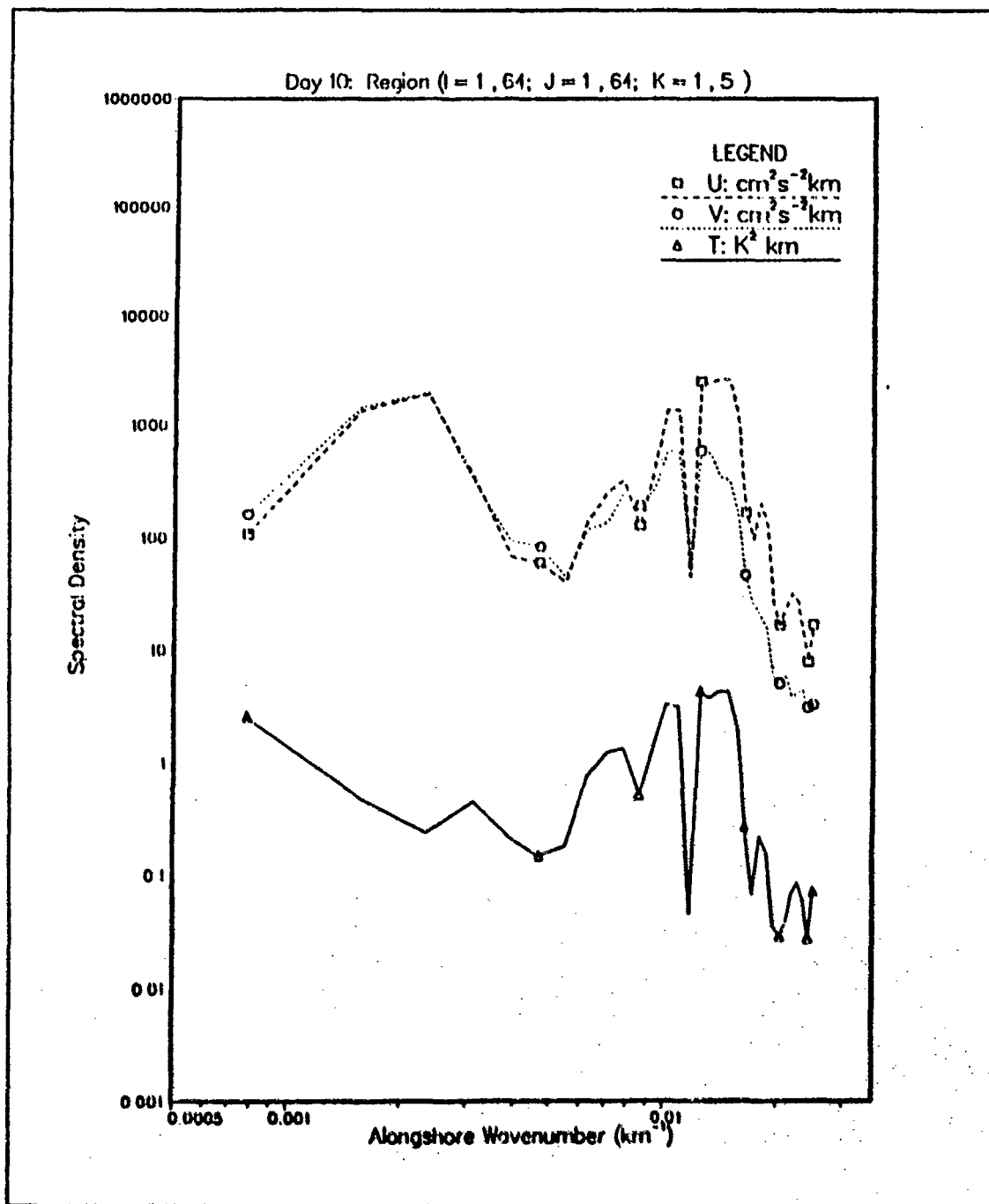


Figure 27. Case 1. Spectral density at day 10: Spectral density versus alongshore wavenumber at day 10. The wavenumber has been scaled by $\frac{1}{2\pi}$ and so is an inverse wavelength. A logarithmic scale is used for the spectral energy.

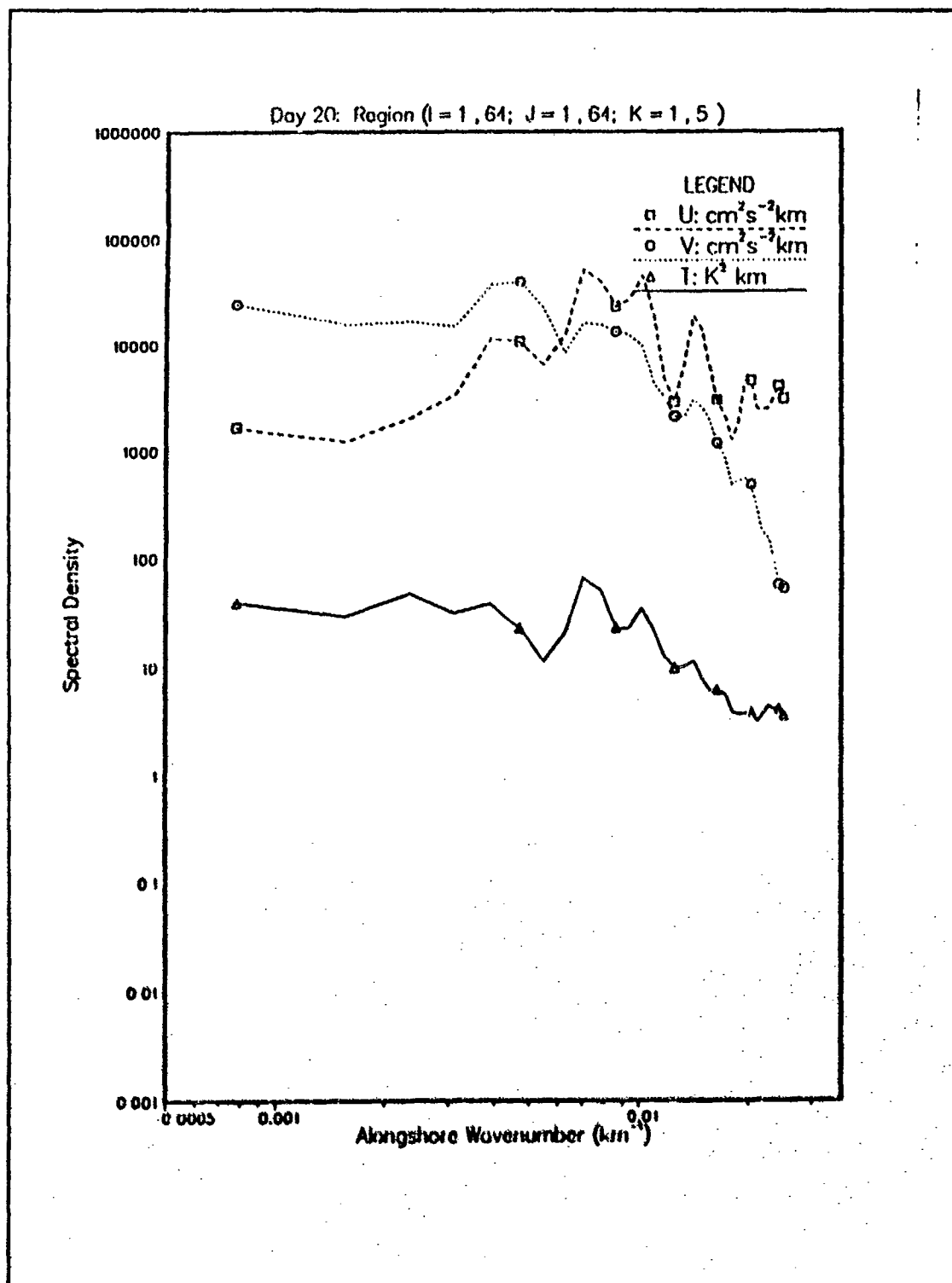


Figure 28. Case I. Spectral density at day 20: As for Figure 27 but at day 20.

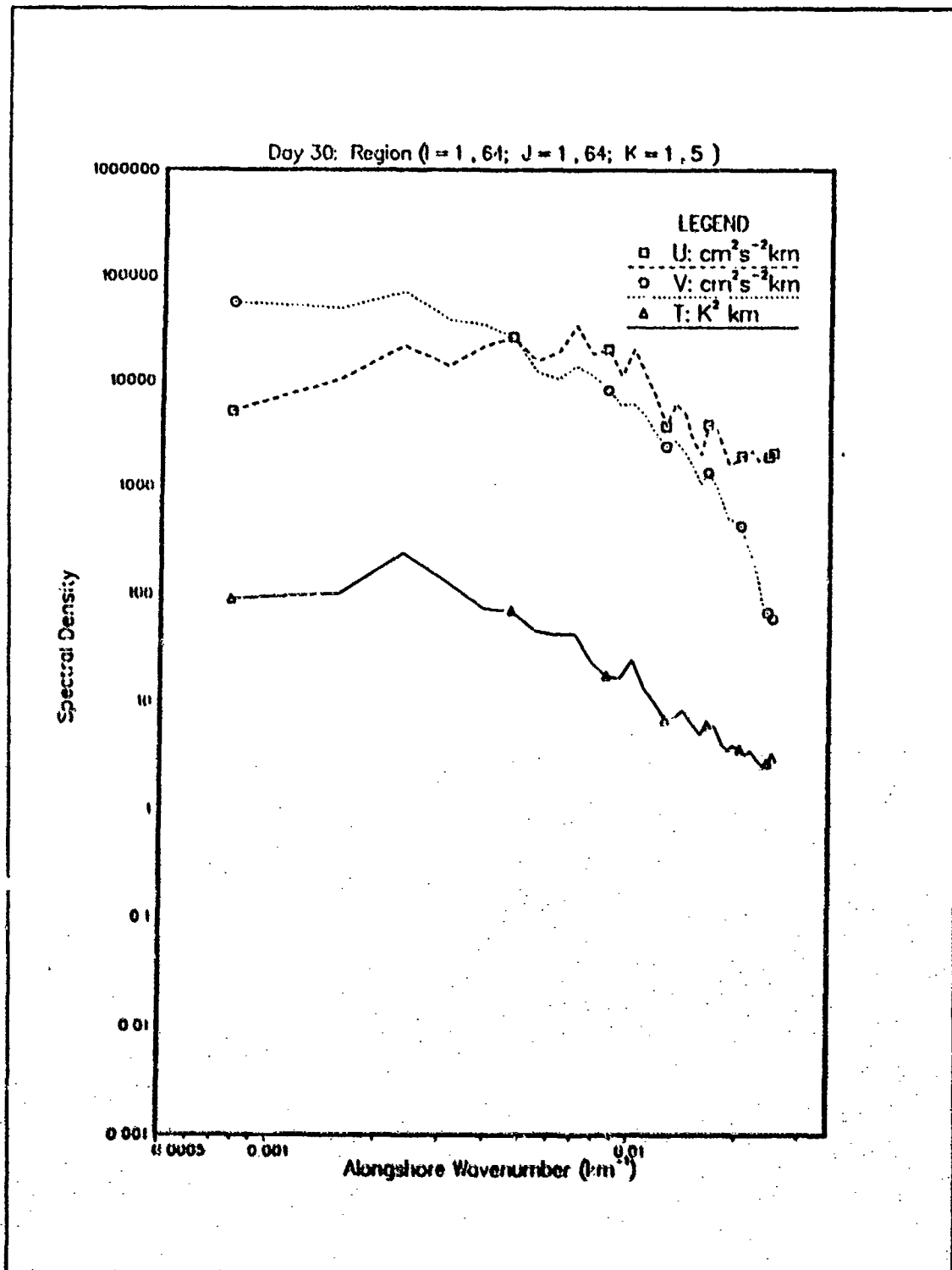


Figure 29. Case 1. Spectral density at day 30: As for Figure 27 but at day 30.

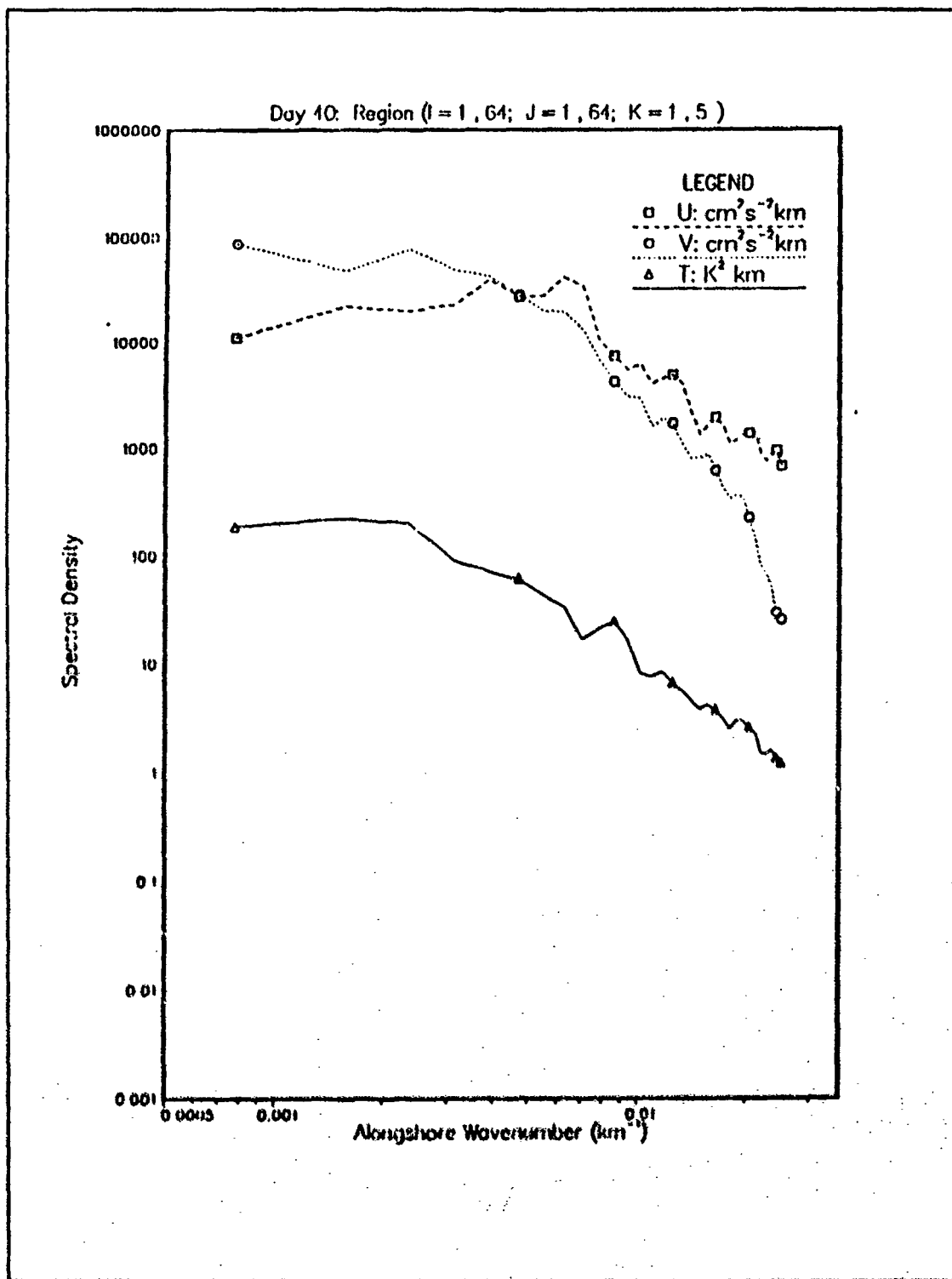


Figure 30. Case 1. Spectral density at day 40; As for Figure 27 but at day 40.

Region ($l = 1, 64$; $J = 1, 64$; $K = 1, 5$)

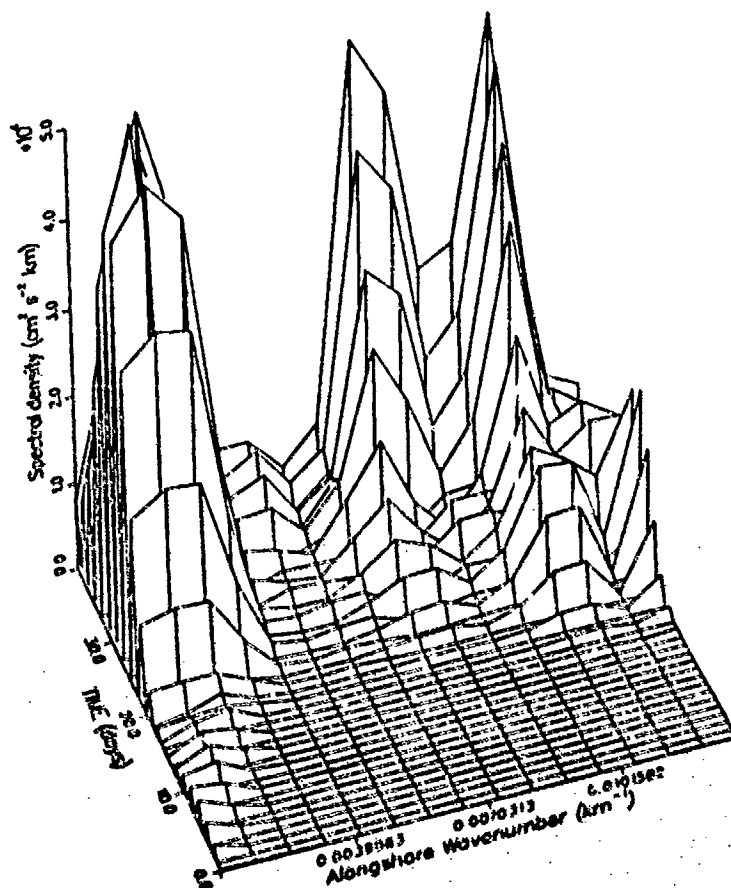


Figure 31. Case 1. Spectral density time series: The time series of spectral density from days 0 to 40 corresponding to Figures 27 to 30. The amplitude of the spectral energy is now on a linear scale.

$\frac{dq}{dx}$ changes sign, and

$\bar{v} \frac{dq}{dx}$ is positive

somewhere in the domain. The energy source for the instability is a vertical velocity shear (baroclinic) or horizontal velocity shear (barotropic). Figure 32(a) shows the alongshore and time averaged horizontal gradient of potential vorticity ($\frac{dq}{dx}$), and Figure 32(b) the alongshore and time averaged alongshore velocity. Both are averaged over the model's entire meridional extent and over the first 10 days. The conditions for baroclinicity are satisfied as $\frac{dq}{dx}$ changes sign near 35 km offshore and the product of \bar{v} and $\frac{dq}{dx}$ is positive over much of the region. The source of the baroclinic energy is readily seen from the strong vertical shear. The strong horizontal shears further offshore provide an energy source for the barotropic instability. The $\frac{dq}{dx}$ and mean alongshore flow fields therefore support the earlier findings that a mixed instability mechanism is responsible for the initial eddy generation. Baroclinic instability is dominant inshore near the core of the current while barotropic instability is stronger further offshore on the edge.

The Rossby radius of deformation, calculated from the temperature profile at day 10, is $R_d = 21.9$ km. The wavelength of the fastest growing wave associated with this radius is given by $2\pi R_d$ and calculated as 138 km. From the spectral analysis in Figure 31 the dominant scales for growth are near 400 km, 135 km and 90 km. The 400 km peak is attributed to a basin scale wave and the 135 km peak to the fastest growing baroclinically unstable wave. Possible explanations for the peak near 90 km are second baroclinic mode instability or growth of the barotropically unstable wave.

d. Conclusions

Case 1 was initialized with a poleward surface jet and equatorward undercurrent with characteristics similar to the observed LECUWIN Current (Thompson, 1984). Instability developed in the first 10 days and mesoscale eddies develop rapidly in the core of the current and its offshore boundary. The instability mechanism is mixed with baroclinic instability dominant, particularly inshore. The contribution due to barotropic instability is a maximum on the offshore edge of the jet. Plots of the cross-shore derivative of potential vorticity and alongshore velocity show that the necessary and sufficient conditions for instability are satisfied. The length scale at which maximum growth occurs is 135 km, associated with the first baroclinic mode and a Rossby radius of approximately 22 km.

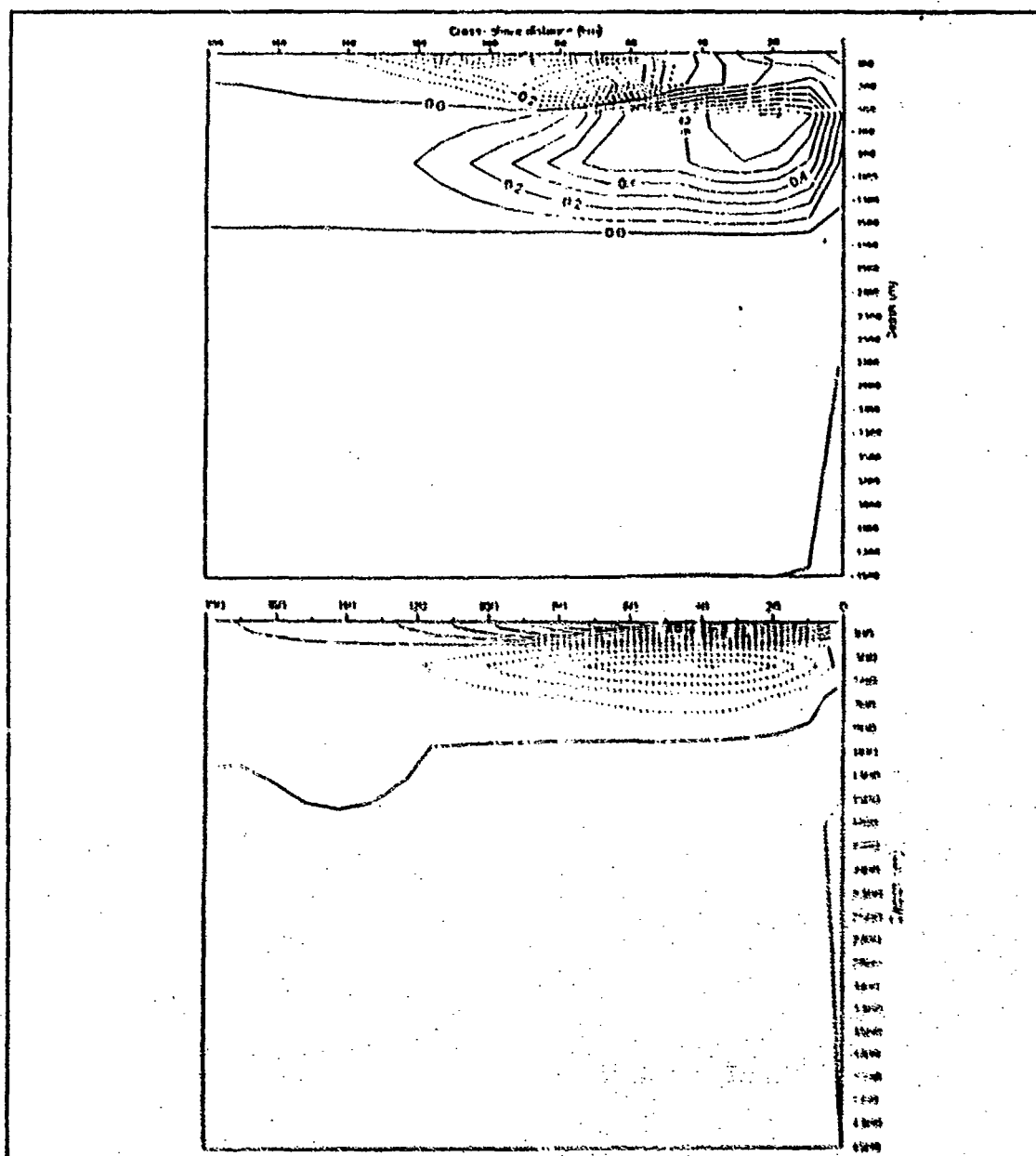


Figure 32. Case 1. Cross sections of dq/dy and alongshore velocity: (a). Vertical cross section of the alongshore and time averaged cross-stream derivative of potential vorticity, multiplied by the grid size ($^{\circ}\text{C m}^{-1} \text{s}^{-1}$), and scaled by 10^5 . Contour interval is $0.1^{\circ}\text{C m}^{-1} \text{s}^{-1}$. (b). Vertical cross section of the alongshore and time averaged alongshore velocity component (cm s^{-1}). Contour interval is 5.0 cm s^{-1} . Time averaging for (a) and (b) is over days 1-10. Dashed contours denote negative values.

Most importantly, the analysis tools are consistent and in general agreement with each other. These techniques may now be applied to the climatologically forced currents of Cases 2 through 5.

2. Case 2. Forcing by Indian Ocean Density Field

Surface pressure fields at 10 day intervals are shown in Figures 33 to 35, and the corresponding time series of surface velocity components and temperatures in Figures 36 to 44. The fields show the geostrophic onshore flow which feeds the poleward current. At day 30 (Figure 37) a uniform onshore flow and an alongshore flow which strengthens toward the pole are seen. The first evidence of eddy generation is seen at day 70 at the poleward inshore end of the domain (Figure 39) and the eddy development is seen thereafter. The eddies intensify, grow, and move offshore, advecting warmer surface temperatures with them.

a. Energy Analysis

The time series of kinetic energy and available potential energy are presented in Figure 45. The available potential energy decreases steadily throughout whereas the kinetic energy, initially large whilst the model adjusts geostrophically to the forcing, is nearly steady from days 70 to 90. Since this corresponds to the period of eddy generation, the energy transfers are calculated for that period.

Figure 46 shows: (a), the transfer between mean and eddy available potential energy; (b), baroclinic transfer; and (c), barotropic transfer for the period days 70-90. Also shown, in Figure 46(d), is the cross-shore velocity component at day 90. The transfers are clearly strongest in the region of the eddy development. A comparison of plots (b) and (c), which have the same contour interval, indicates that barotropic instability is more important than baroclinic in providing the eddy kinetic energy. The magnitude of the transfers was calculated for a sub-domain of 63 km cross-shore and 100 km alongshore centered on the position of the eddy at day 90. The energy transfer diagram is shown in Figure 47. The transfer diagram supports the contour plot and shows barotropic instability to be stronger than baroclinic in the immediate vicinity of the eddy development.

b. Spectral Analysis

Figures 48 through 51 show energy increasing at a wavelength near 150 km (alongshore wavenumber of $\sim 0.0065 \text{ km}^{-1}$) during the period of eddy development (days 70-100). Whilst the initial development is not apparent in the 160 day spectral time series for Case 2 (Figure 52), the peak energy at the end of the experiment is also at a

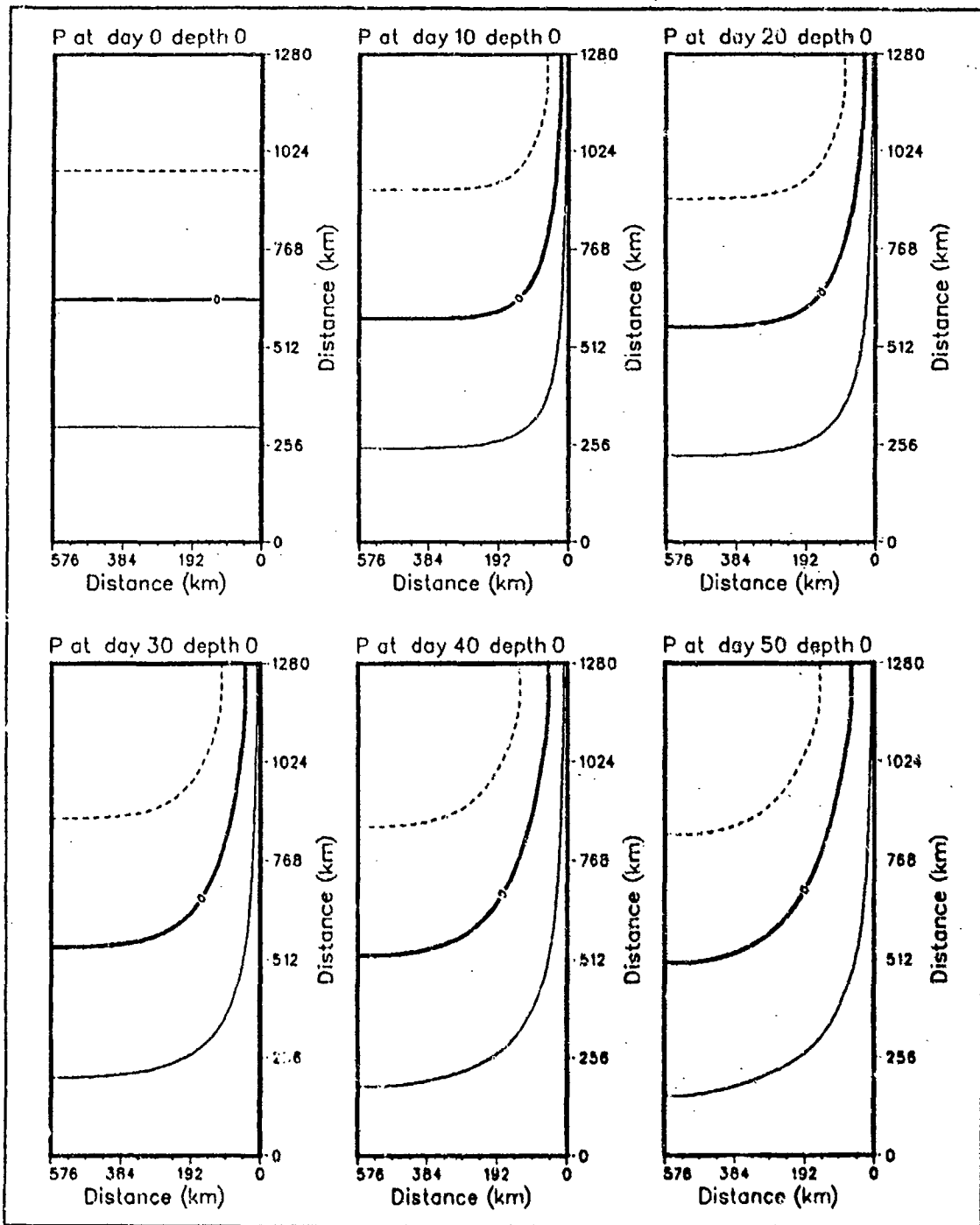


Figure 33. Case 2. Surface pressure field, days 0 - 50: Dynamic height anomaly (cm) at surface relative to a reference level of 2000 m. Contour interval is 5 cm.

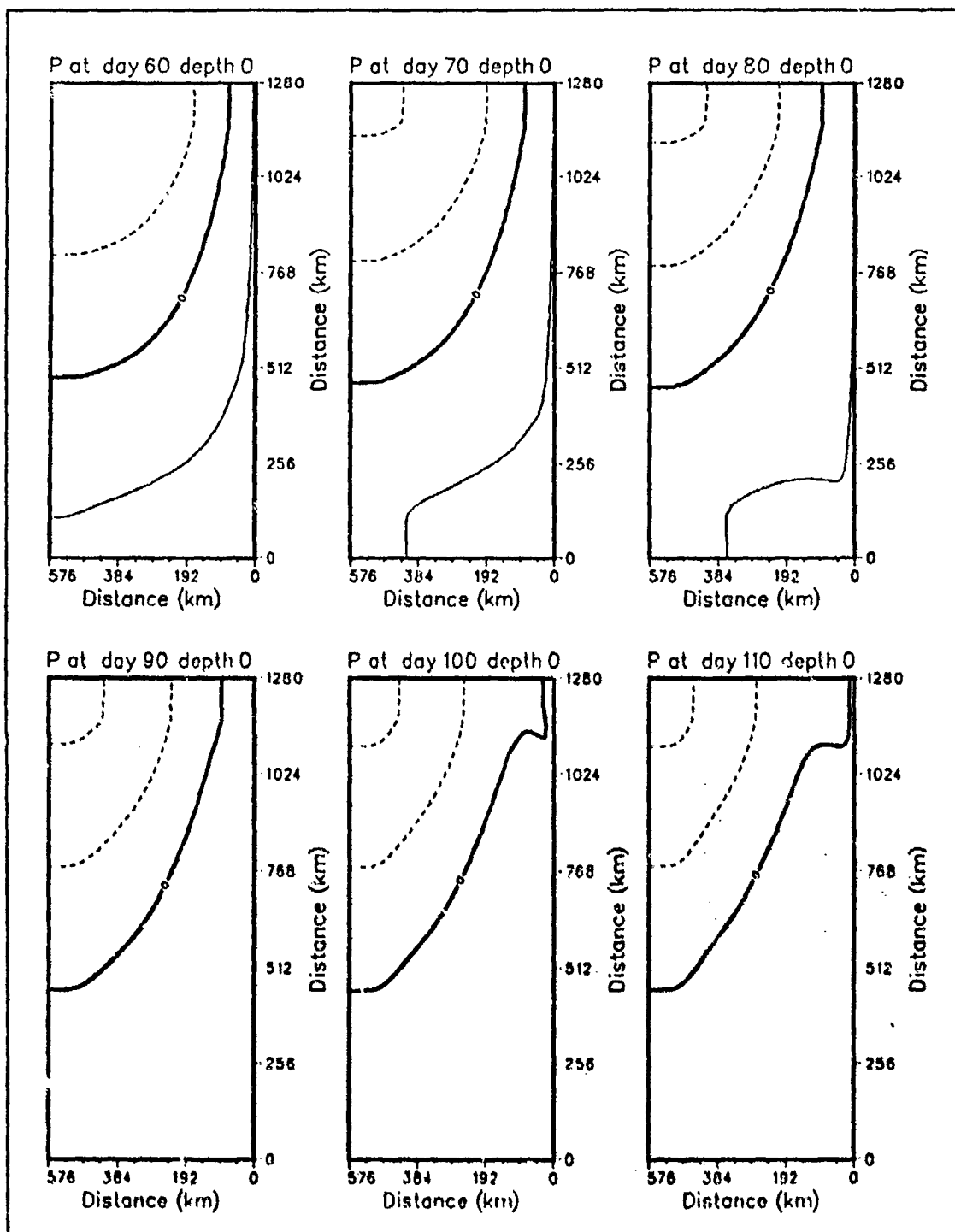


Figure 34. Case 2. Surface pressure field, days 60 - 110: As for Figure 33.

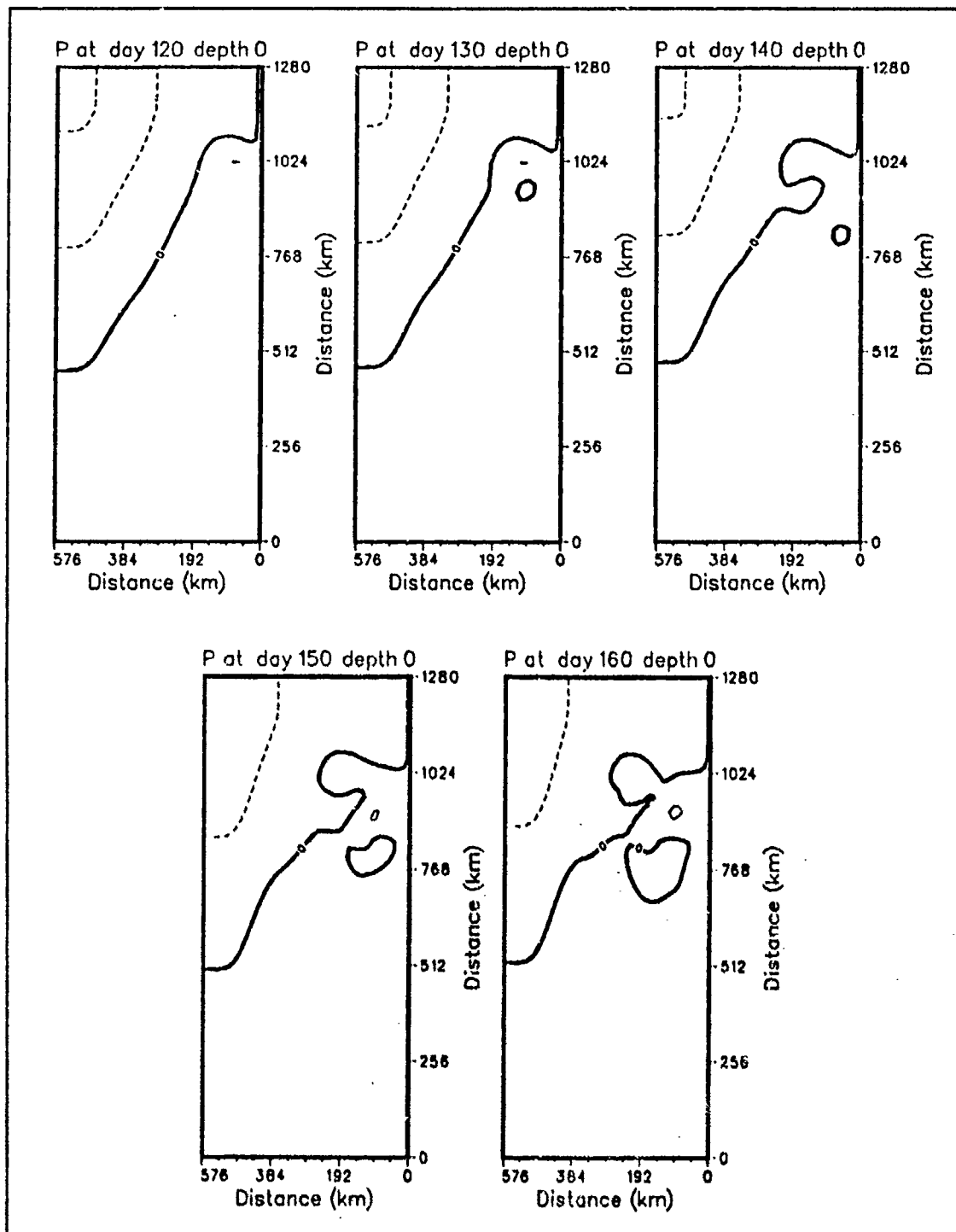


Figure 35. Case 2. Surface pressure field, days 120 - 160: As for Figure 33.

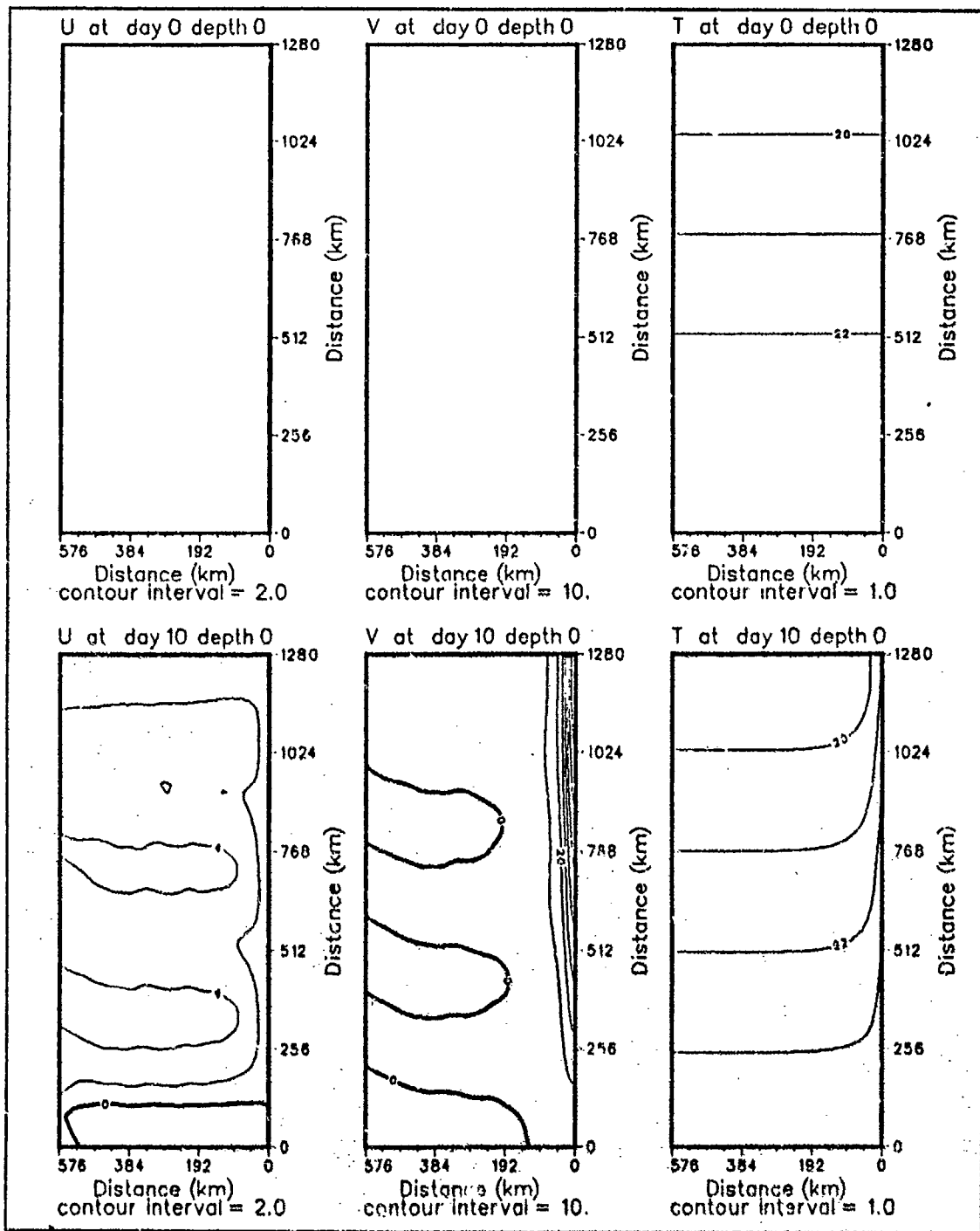


Figure 36. Case 2. Surface velocity and temperature fields, days 0 - 10: Cross-shore velocity component (cm s^{-1}), alongshore velocity component (cm s^{-1}) and temperature ($^{\circ}\text{C}$) at surface.

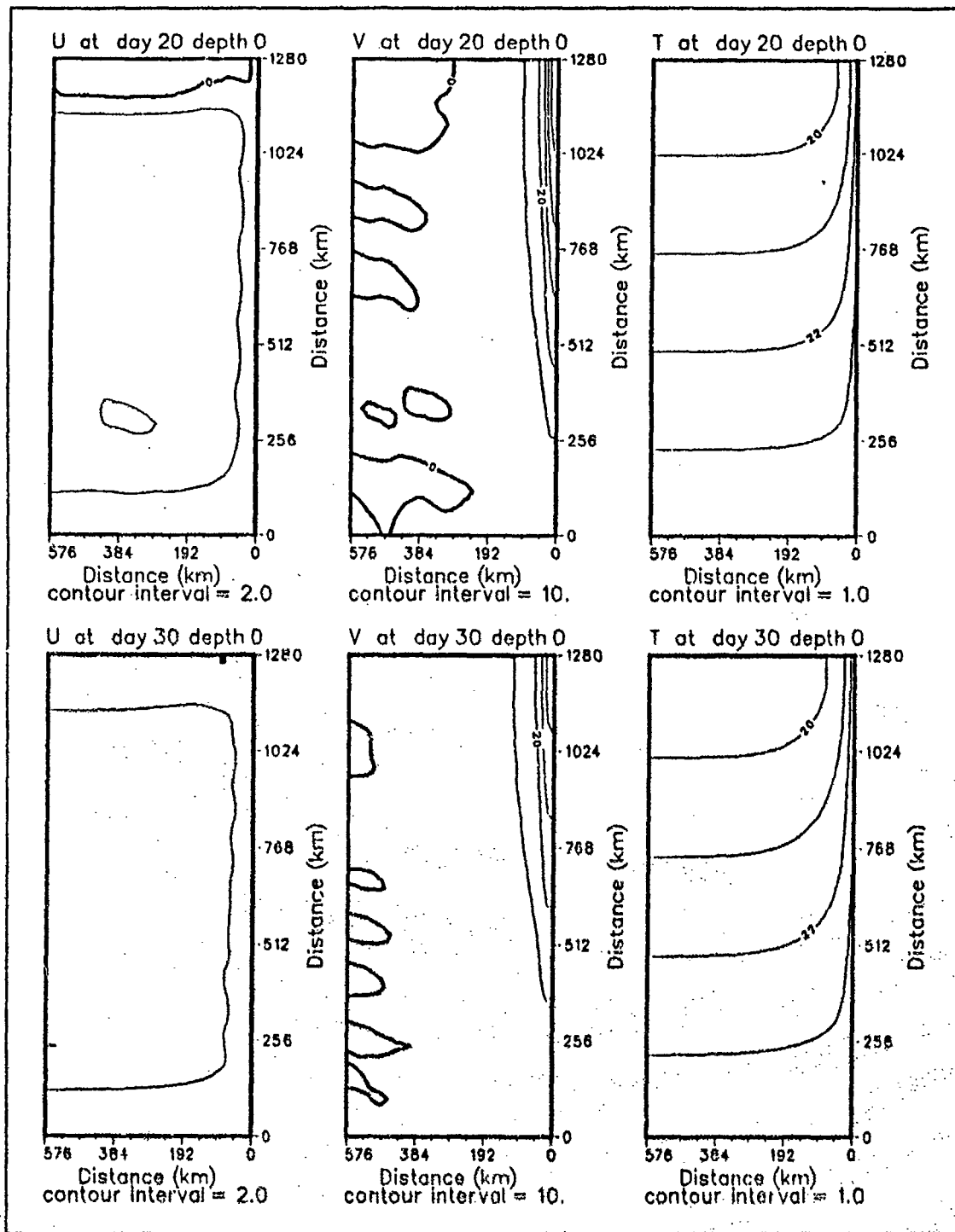


Figure 37. Case 2. Surface velocity and temperature fields, days 20 - 30: As for Figure 36.

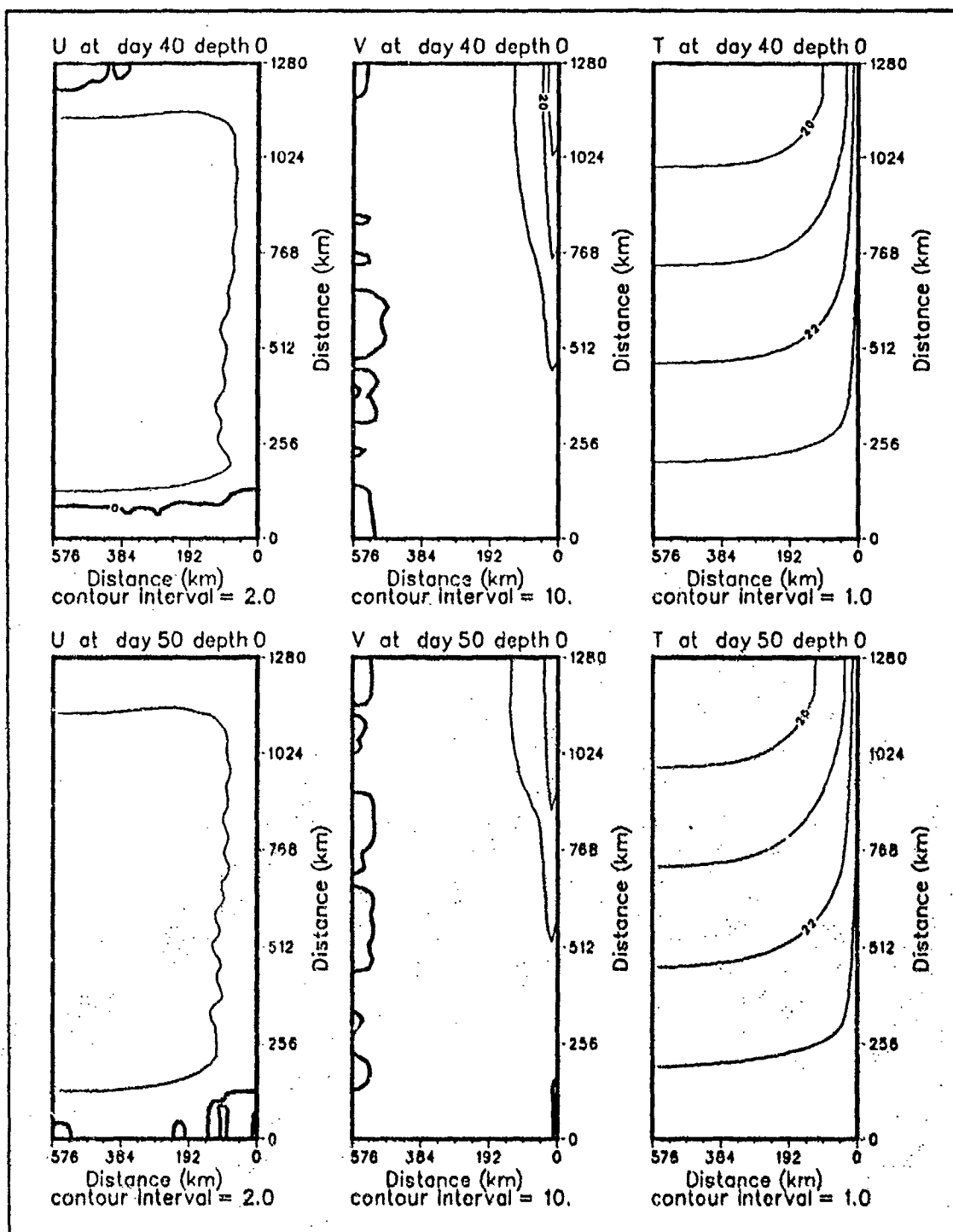


Figure 38. Case 2. Surface velocity and temperature fields, days 40 - 50: As for Figure 36.

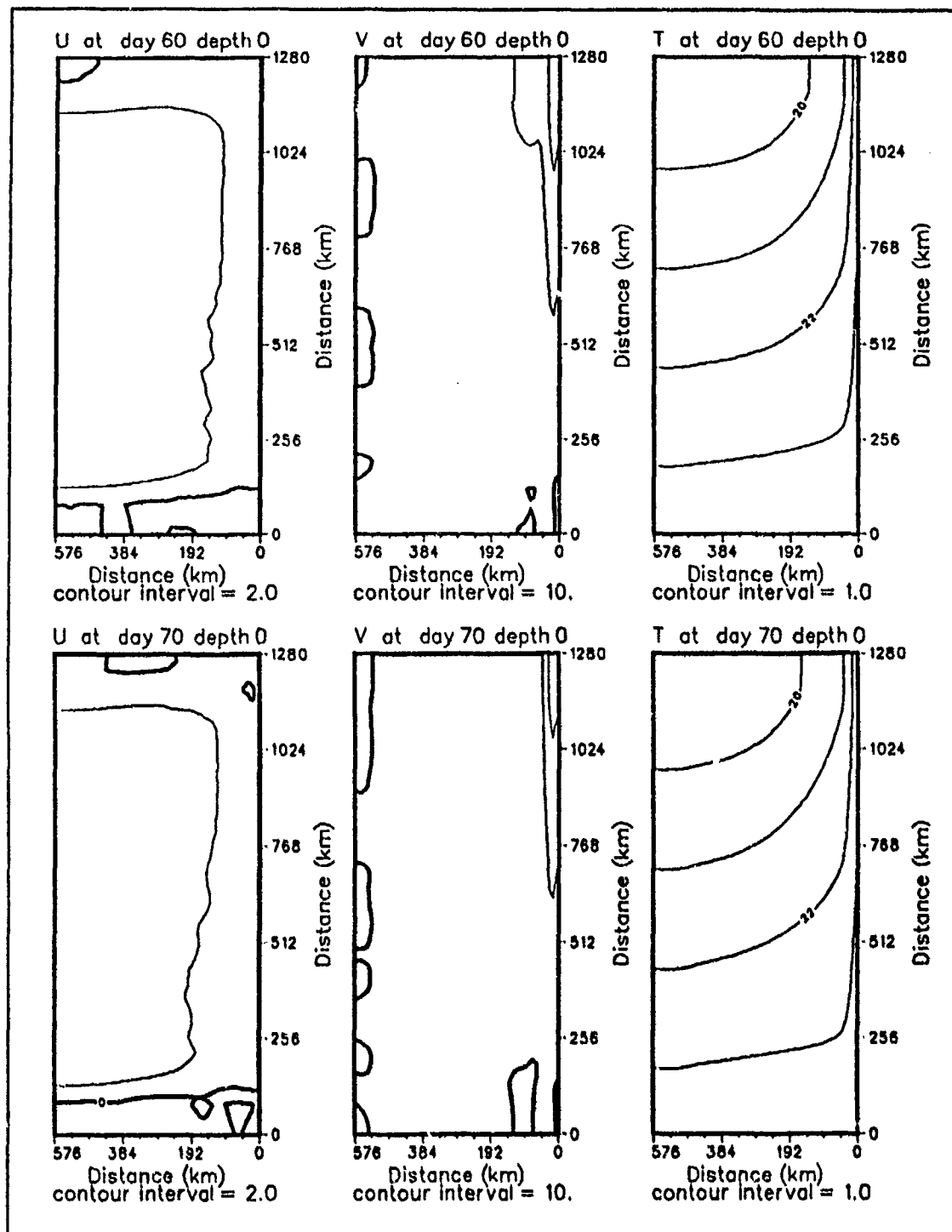


Figure 39. Case 2. Surface velocity and temperature fields, days 60 - 70: As for Figure 36.

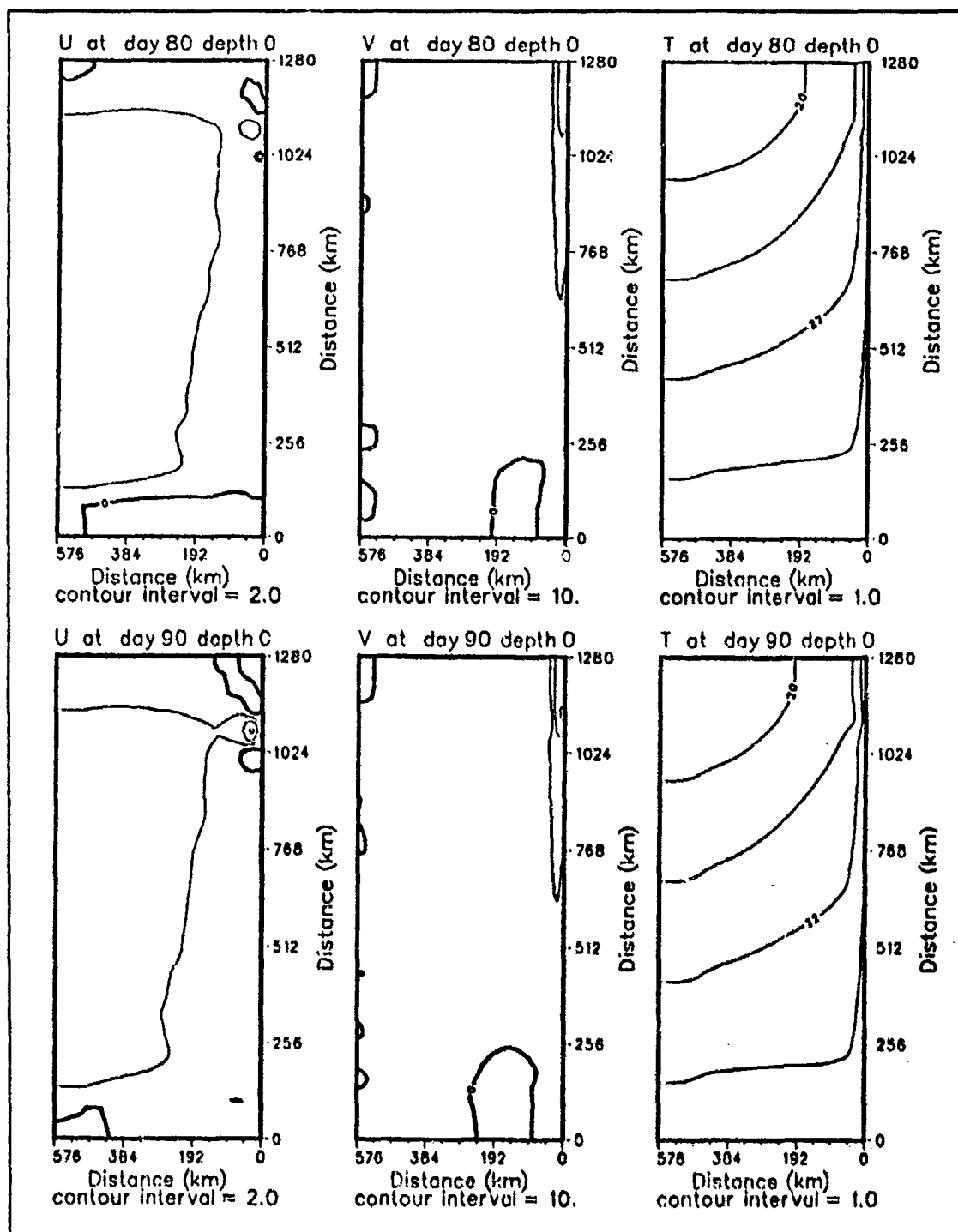


Figure 40. Case 2. Surface velocity and temperature fields, days 80 - 90: As for Figure 36.

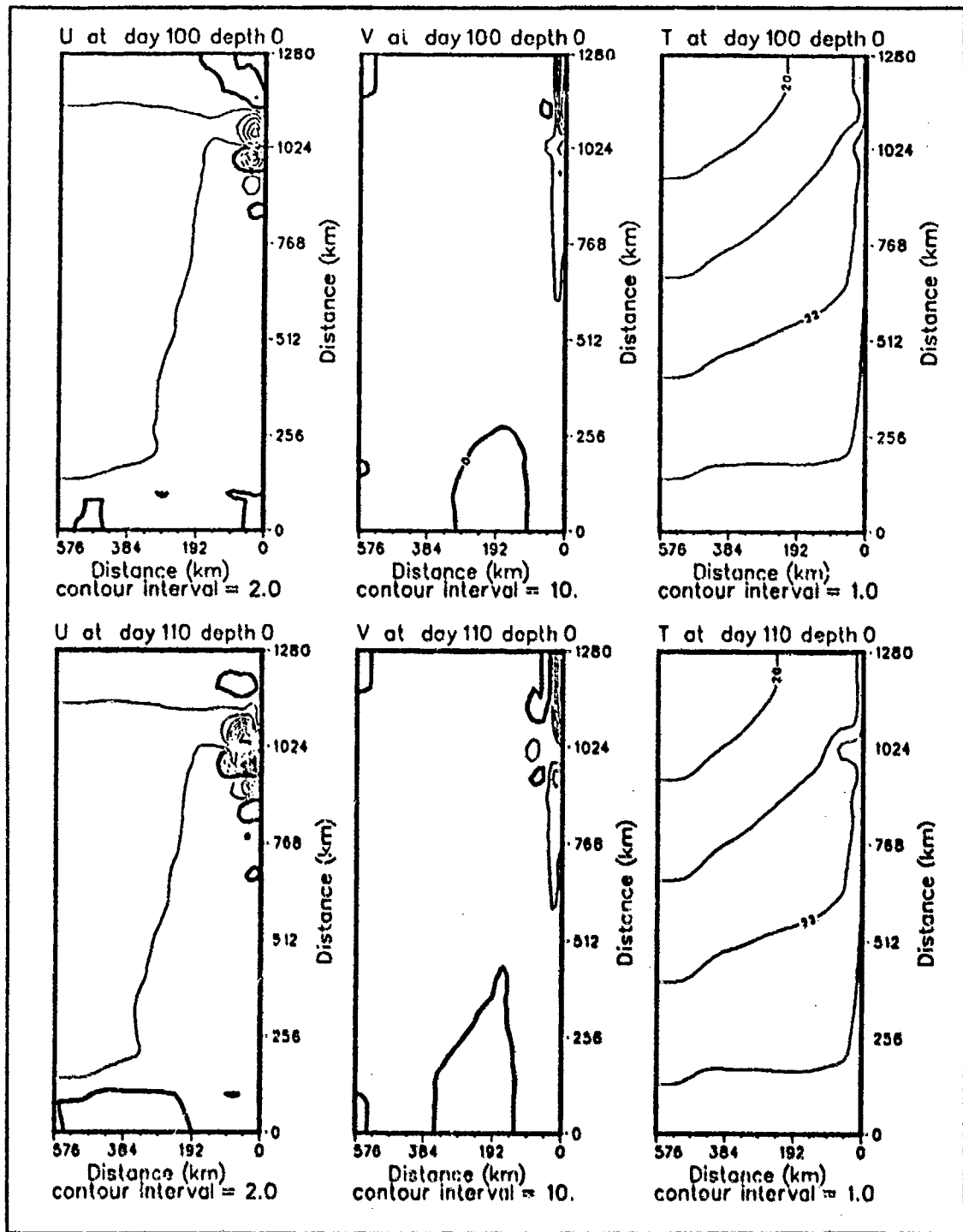


Figure 41. Case 2. Surface velocity and temperature fields, days 100 - 110: As for Figure 36.

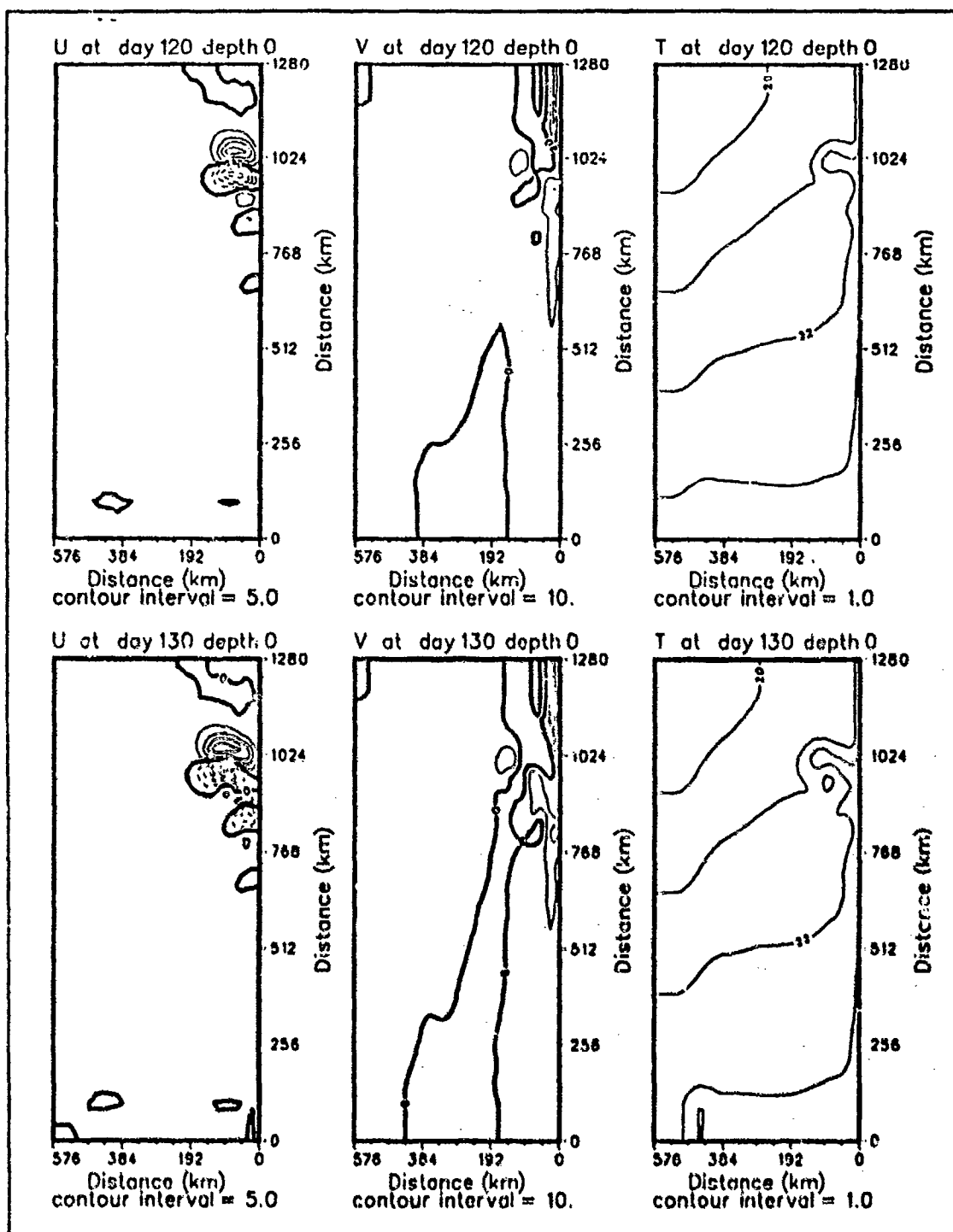


Figure 42. Case 2. Surface velocity and temperature fields, days 120 - 130: As for Figure 36. Note: u contour interval is now 5 cm s^{-1} .

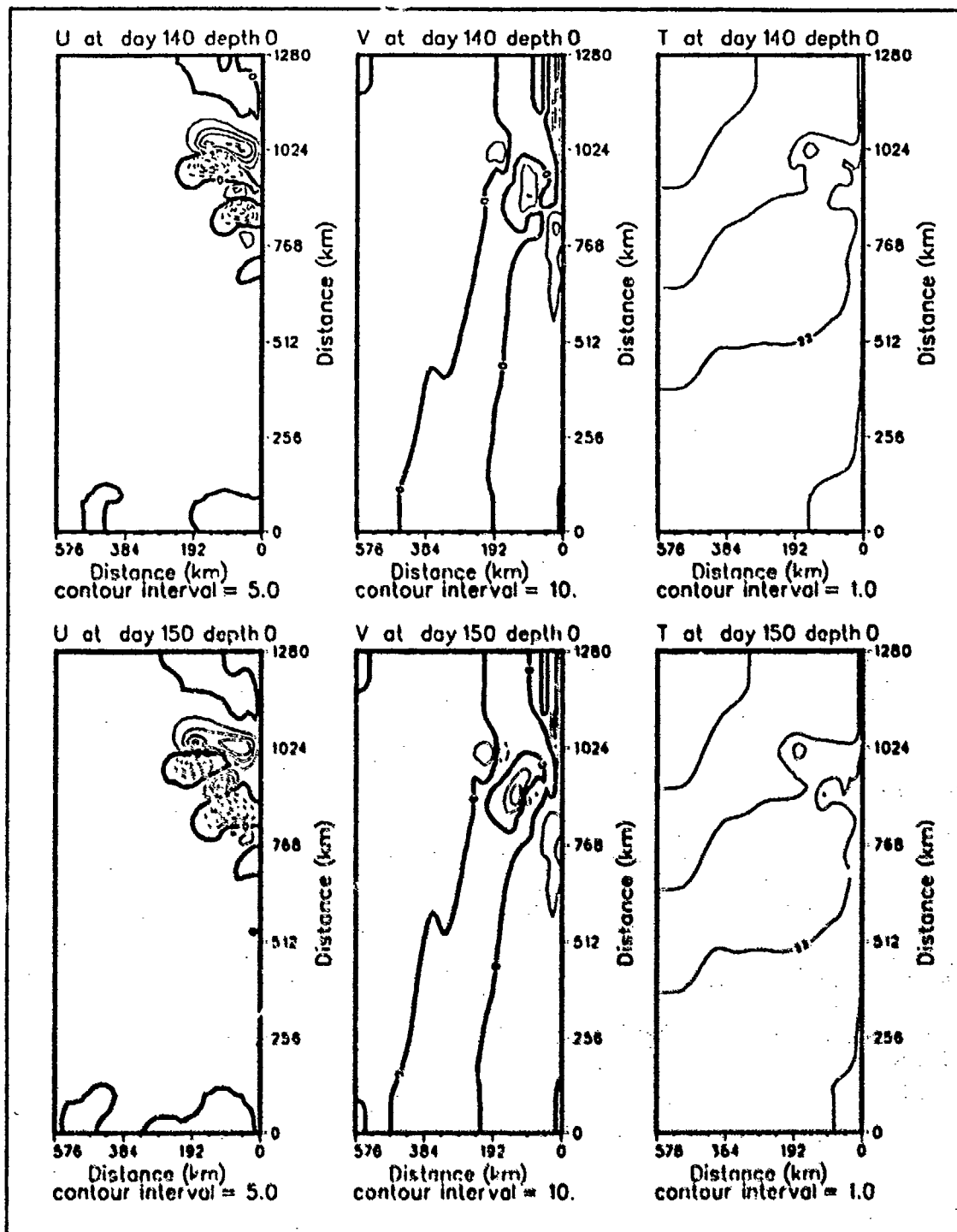


Figure 43. Case 2. Surface velocity and temperature fields, days 140 - 150: As for Figure 42.

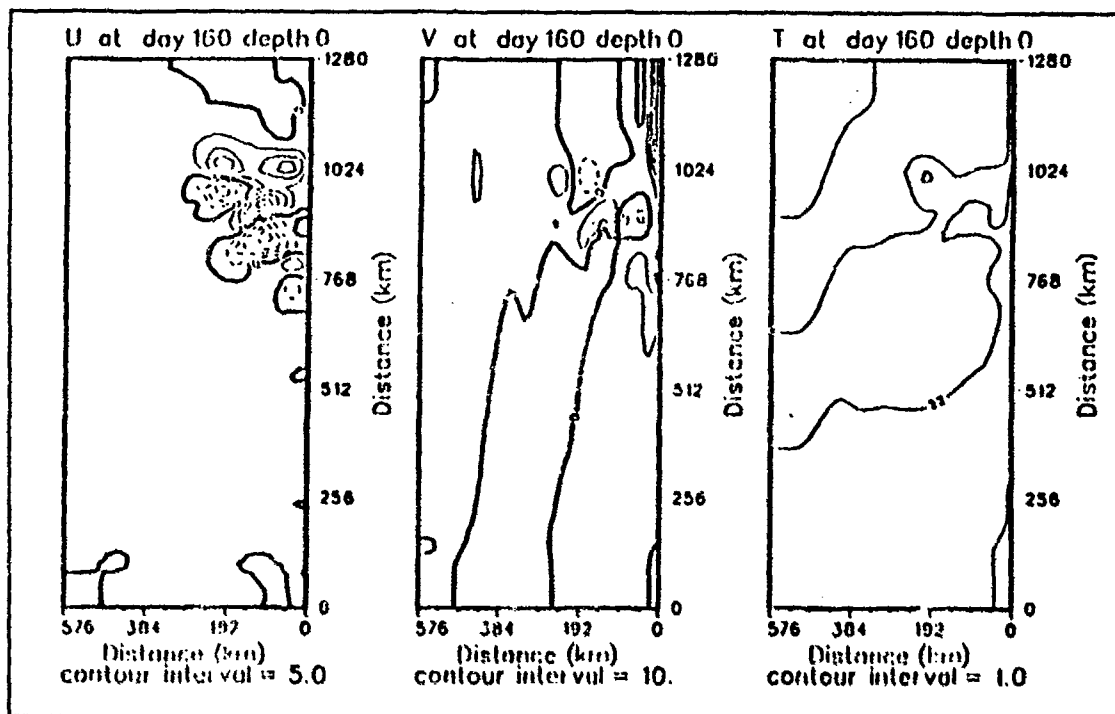


Figure 44. Case 2. Surface Velocity and Temperature Fields, day 160: As for Figure 42.

wavelength near 150 km. Hence, both the development and subsequent growth of eddies appears to be at the same wavelength scale.

c. Instability Analysis

The necessary and sufficient conditions for instability in Case 2 are investigated using Figure 53, which plots cross sections through the eddy generation region of: (a) the cross-stream derivative of potential vorticity and (b) the alongshore velocity, averaged over days 70 to 90. The cross-stream derivative changes sign at several locations and its product with the alongshore mean flow is positive in the domain, satisfying the necessary conditions for baroclinic instability. The necessary conditions for an energy source for instability are satisfied by the vertical and horizontal shears in the flow.

The internal Rossby radius of deformation was calculated for the region of initial instability, using the method given in Chapter IV, as 27.6 km. As baroclinic instability favors wave growth at $2\pi R_d$, and barotropic growth a shorter scale, (Kamenkovich *et al.*, 1986), the dominant wavelength scale of ~ 150 km is consistent with the mixed instability observed in this case.

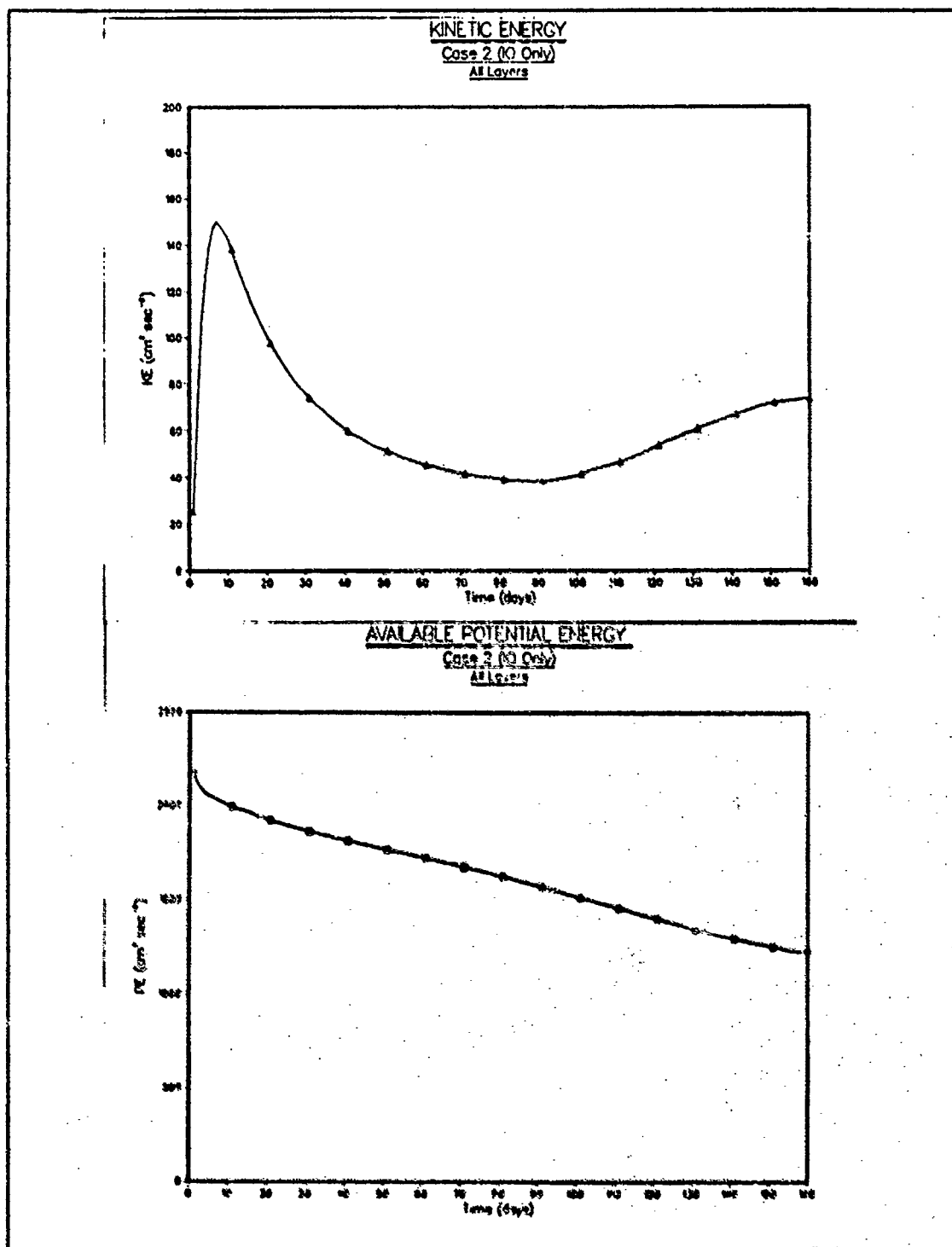


Figure 45. Case 2. Energy time series: Total kinetic and available potential energy ($\text{cm}^3 \text{s}^{-3}$) summed over all layers and the entire domain.

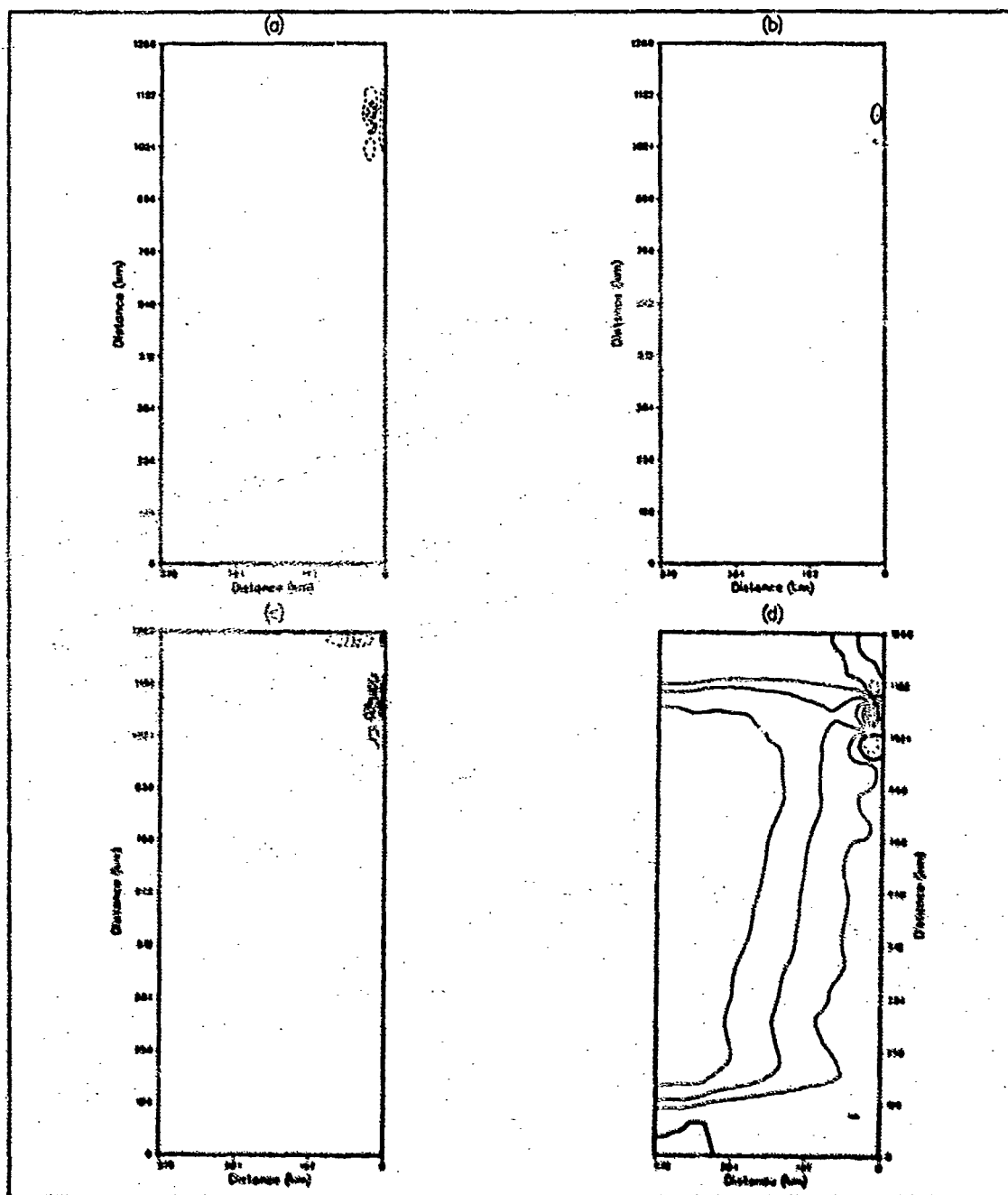


Figure 46. Case 2. Energy transfers: Transfers of energy from (a) \bar{P} to P' , (b) P' to K' and (c) \bar{K} to K' in units of $\text{ergs cm}^{-2} \text{s}^{-1}$. Transfers are averaged over days 70-90 and summed over the upper five layers. Contour interval is $1.6 \times 10^{-2} \text{ergs cm}^{-2} \text{s}^{-1}$. Subplot (d) is the cross-shore velocity component at day 90 at a contour interval of 1.0 cm s^{-1} .

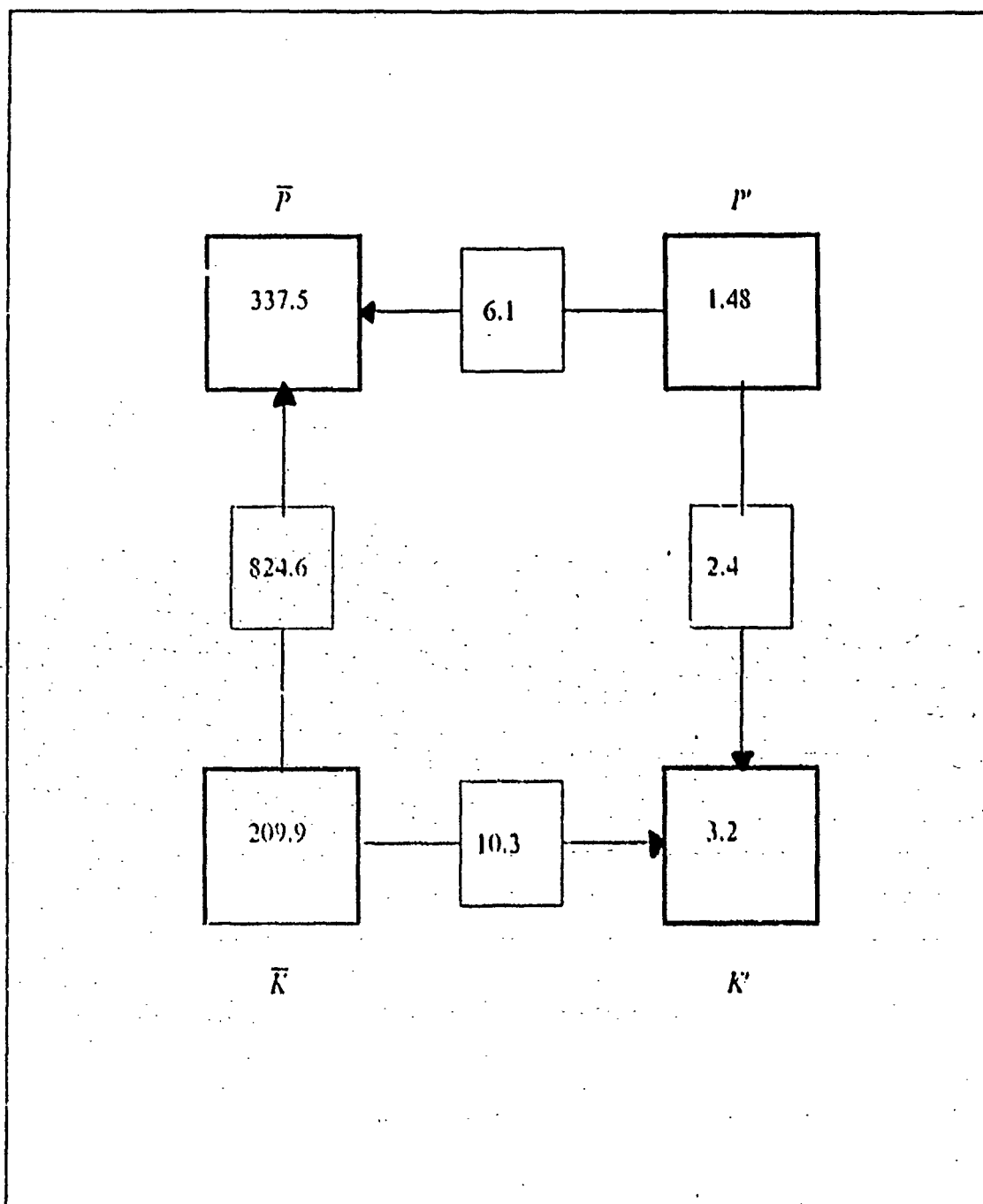


Figure 47. Case 2. Energy transfer diagram: The energy transfer diagram for the upper five layers for the region between alongshore distances 1020 km to 1120 km, extending 90 km offshore. Units for \bar{P} , \bar{K} , P' and K' are ergs cm^{-3} , and transfers are in units of $\text{ergs cm}^{-3} \text{s}^{-1} \times 10^{-6}$.

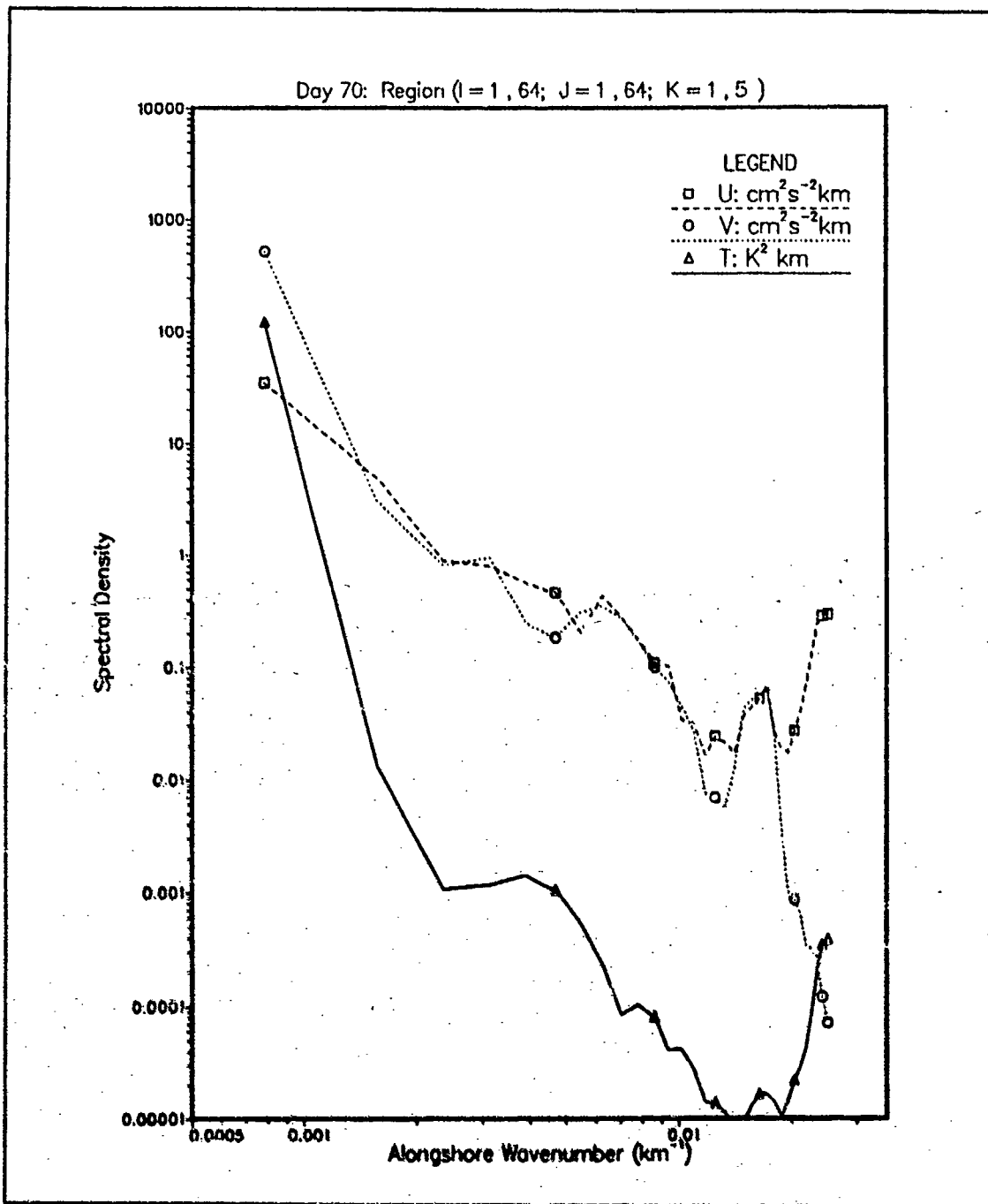


Figure 48. Case 2. Spectral density at day 70: Spectral density versus alongshore wavenumber at day 70. The wavenumber has been scaled by $\frac{1}{2\pi}$ and so is an inverse wavelength. A logarithmic scale is used for the spectral energy.

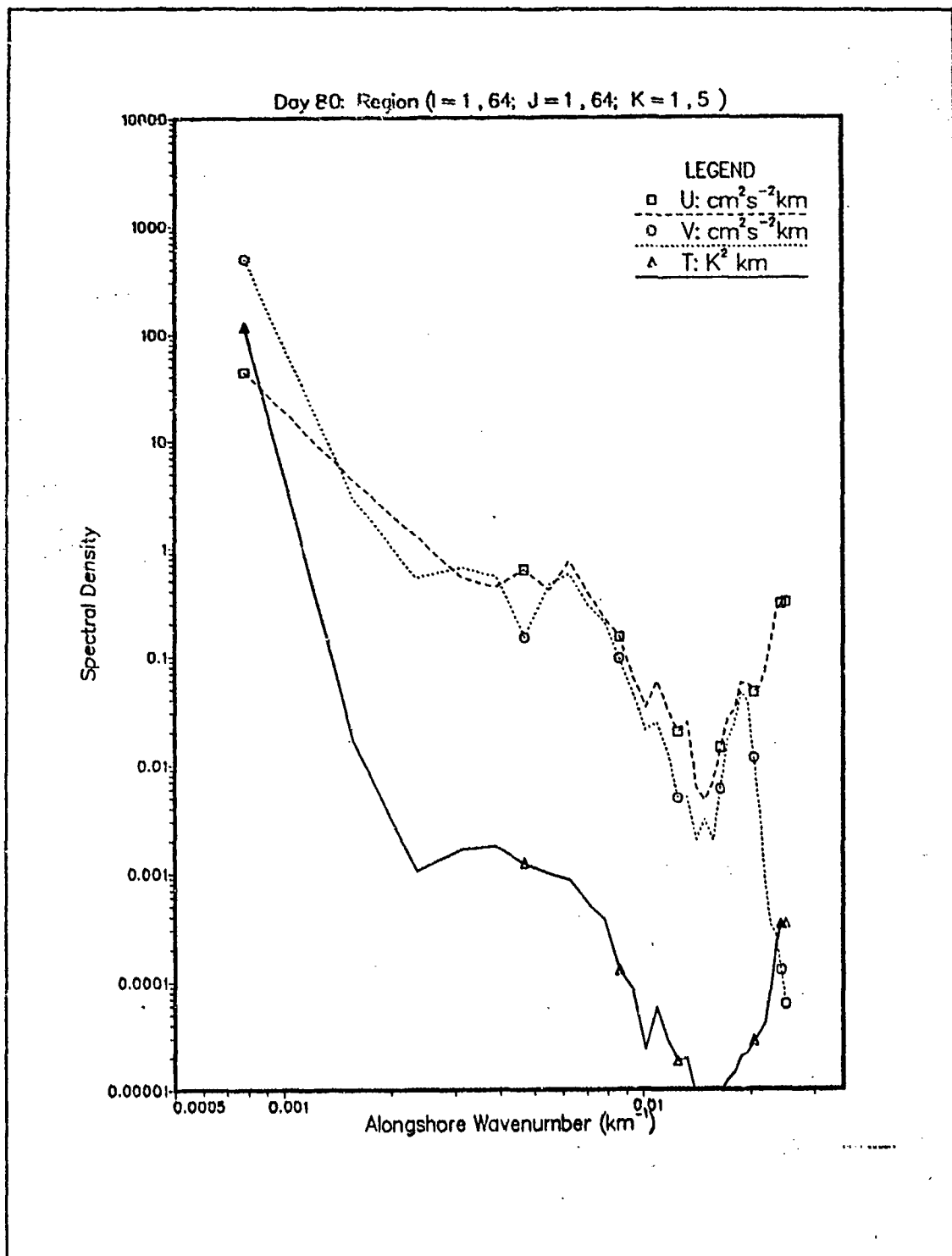


Figure 49. Case 2. Spectral density at day 80: As for Figure 48 but at day 80.

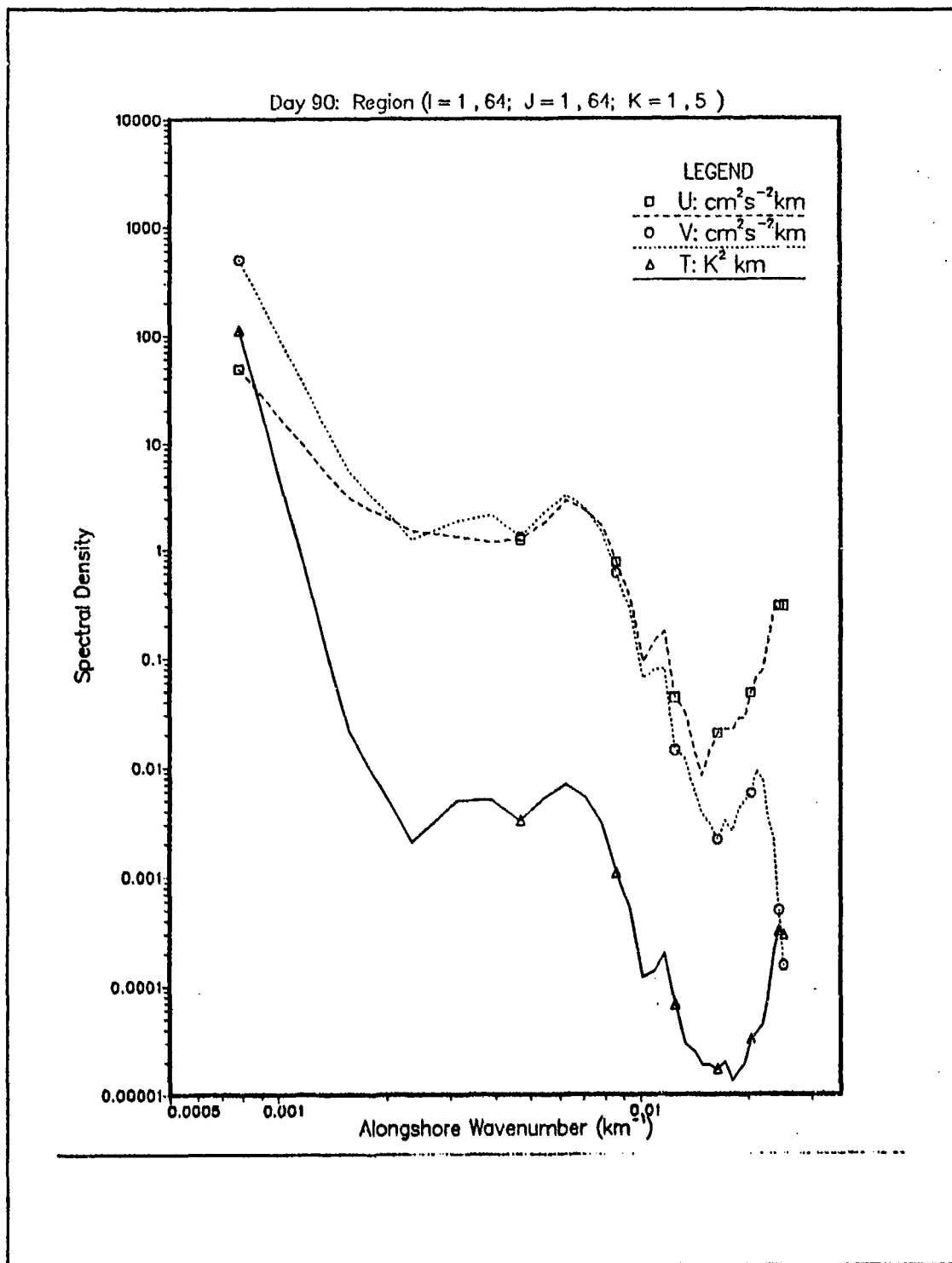


Figure 50. Case 2. Spectral density at day 90: As for Figure 48 but at day 90.

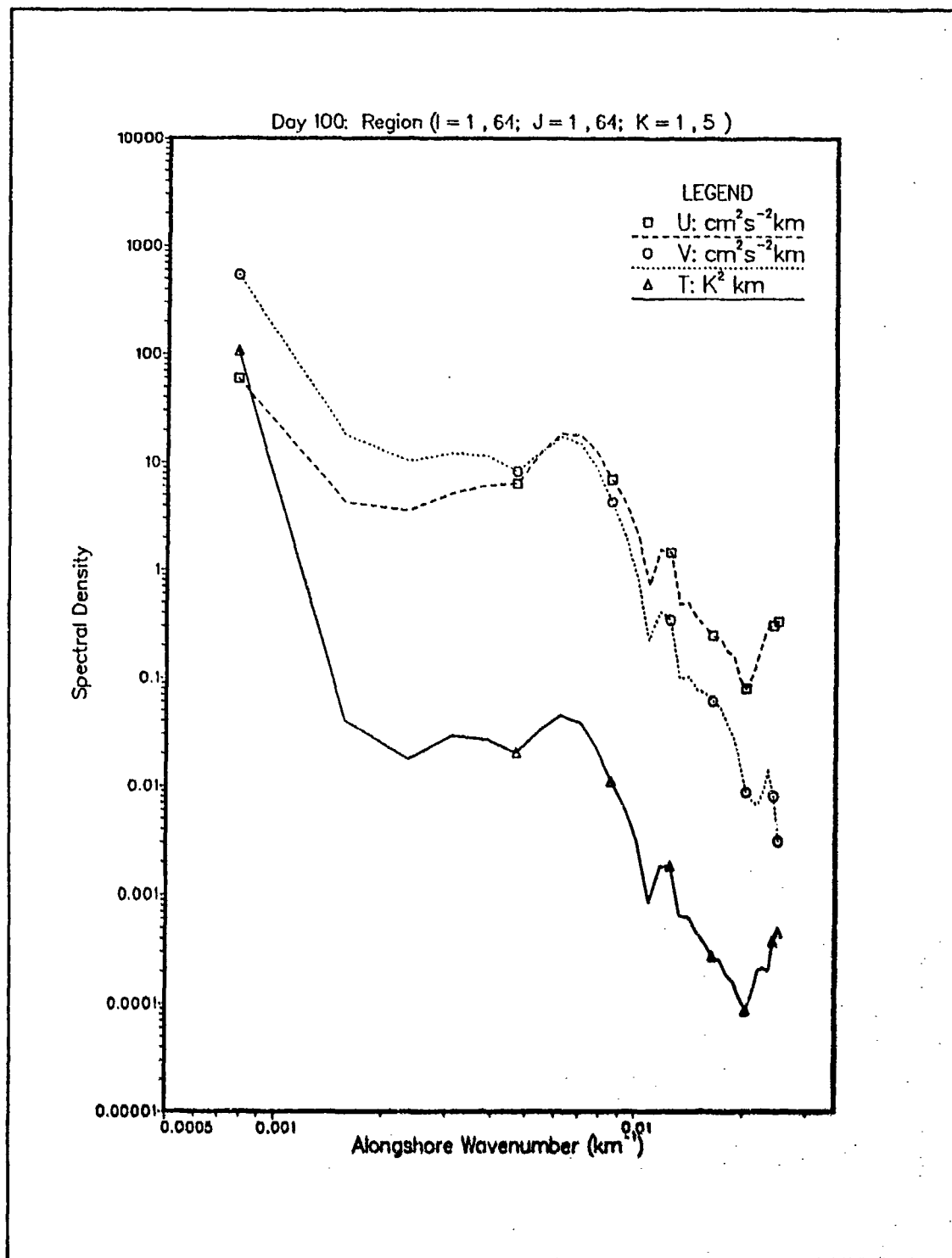


Figure 51. Case 2. Spectral density at day 100: As for Figure 48 but at day 100.

Region ($l = 1, 64$; $J = 1, 64$; $K = 1, 5$)

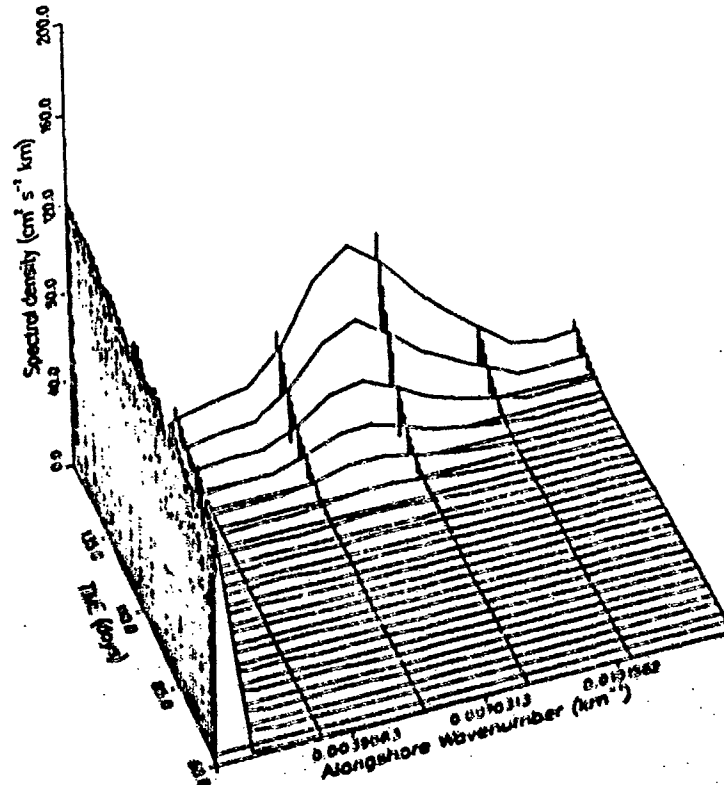


Figure 52. Case 2. Spectral density time series: The time series of spectral density from days 60 to 160. Note: the amplitude of the spectral energy is on a linear scale.

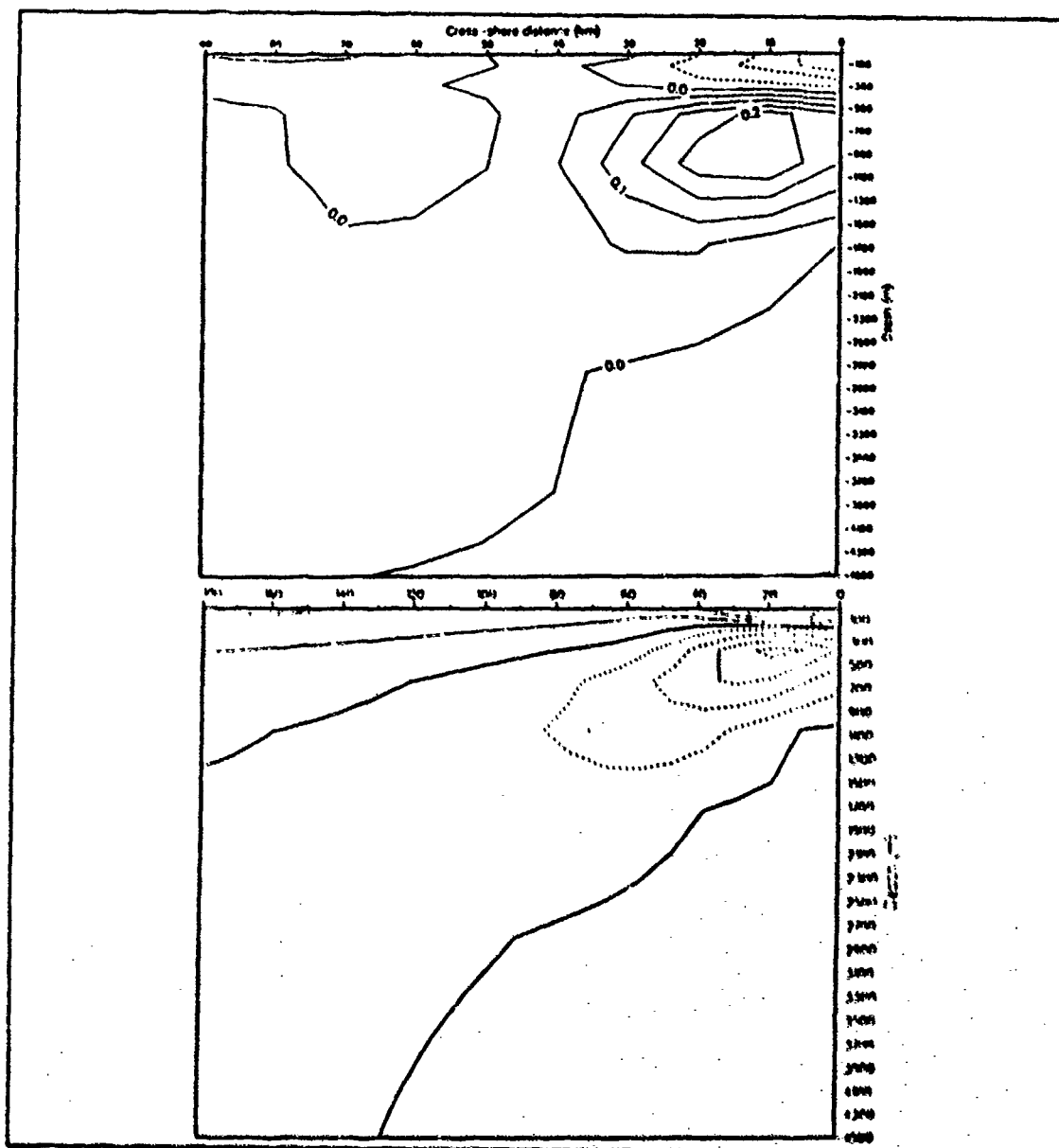


Figure 53. Case 2. Cross sections of dq/dx and alongshore velocity: (a). Vertical cross section of the time averaged (days 70-90) cross-stream derivative of potential vorticity, multiplied by the grid size ($^{\circ}\text{C m}^{-1} \text{s}^{-1}$), and scaled by 10^6 . Contour interval is $0.05 ^{\circ}\text{C m}^{-1} \text{s}^{-1}$. (b). Vertical cross section of the time averaged (days 70-90) alongshore velocity component (cm s^{-1}). Contour interval is 2.0 cm s^{-1} . Vertical cross-sections are at 1080 km alongshore. Dashed contours denote negative values.

d. Conclusions

The poleward surface flow and equatorward undercurrent driven by the Indian Ocean climatological temperature field is unstable and generates mesoscale eddies at the poleward end of the domain. Instability is mixed with barotropic dominant. The eddies form in the horizontal shear zone on the offshore side of the core of the current and have a dominant wavelength of around 150 km, a scale consistent with the Rossby radius of deformation of 27.6 km and the mixed instability mechanism.

3. Case 3. Forcing by Indian Ocean and NW Shelf

Figures 54 to 56 show the surface pressure fields at 10 day intervals for Case 3. The initialization of the NW Shelf water is seen at the inshore equatorward corner of the domain at day 0. The poleward flow is now much stronger than in Case 2 and instability develops more quickly. Whereas in Case 2 the instability developed at the poleward end of the domain, the initial eddy development occurs first at the equatorward end and spreads poleward with time. This can also be seen in the time series of velocity components and temperature in Figures 57 to 65. The NW Shelf water temperature initialization is seen at day 0 in Figure 57. An eddy forms on the boundary of the NW Shelf water by day 10 and additional eddies are seen developing downstream in subsequent plots. Closed contours on both the pressure and temperature plots from day 90 are indicative of anticyclonic rings forming near 512 km and 1024 km alongshore. These rings pinch-off the offshore meander, trap warm NW Shelf origin water, and then move offshore.

a. Energy Analysis

Time series of total kinetic and available potential energy over the entire domain are shown in Figure 66. Since, after the initial geostrophic adjustment by the model, the kinetic energy becomes quasi-steady during days 30 to 60 before steadily growing, again, days 30 to 40 were chosen for more detailed analysis. Over the same period, available potential energy is quasi-steady over days 30 to 40 and then decreases.

The energy transfer plots in Figure 67 show strong transfers between the mean and eddy available potential energy, and strong barotropic transfer, all at the equatorward end of the domain. A comparison between the u velocity component fields on days 30 and 40 in Figure 58 shows that eddy generation has occurred further poleward than shown in the transfers in Figure 67. The transfers shown in Figure 67 are much stronger than those leading to eddy development further downstream so that the downstream transfers fail to show at the contour interval used.

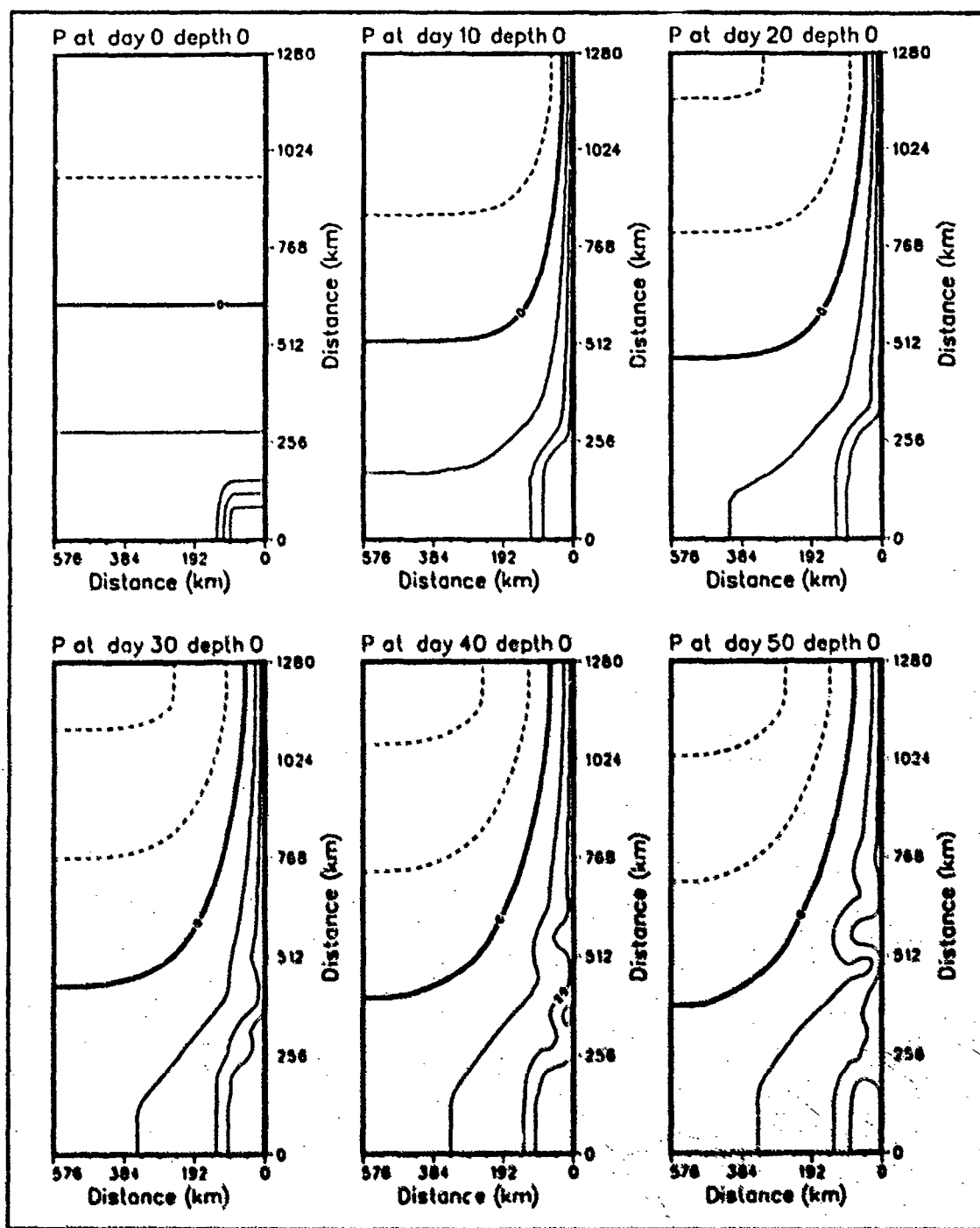


Figure 54. Case 3. Surface pressure field, days 0 - 50: Dynamic height anomaly (cm) at surface relative to a reference level of 2000 m. Contour interval is 5 cm.

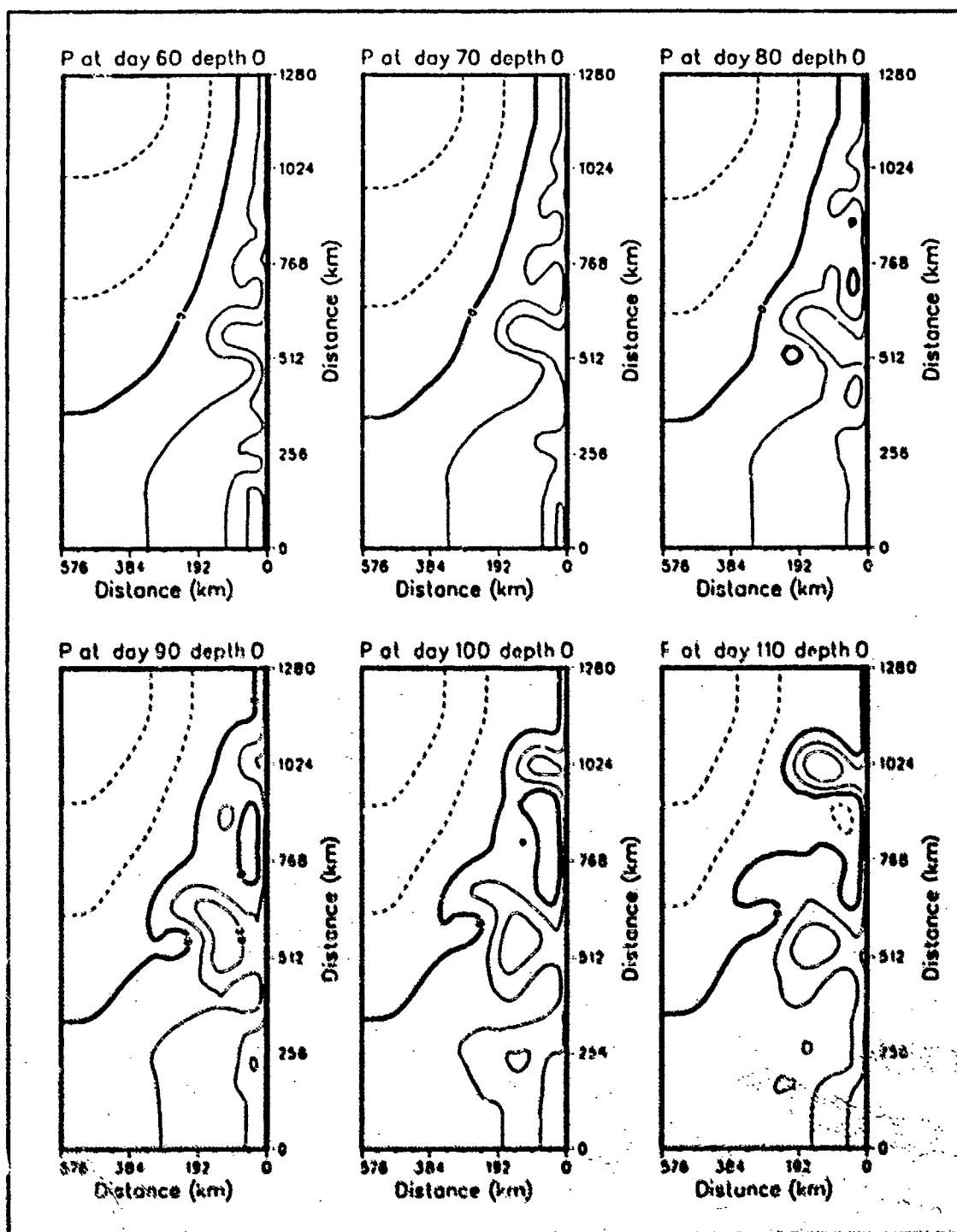


Figure 55. Case 3. Surface pressure field, days 60 - 110: As for Figure 54.

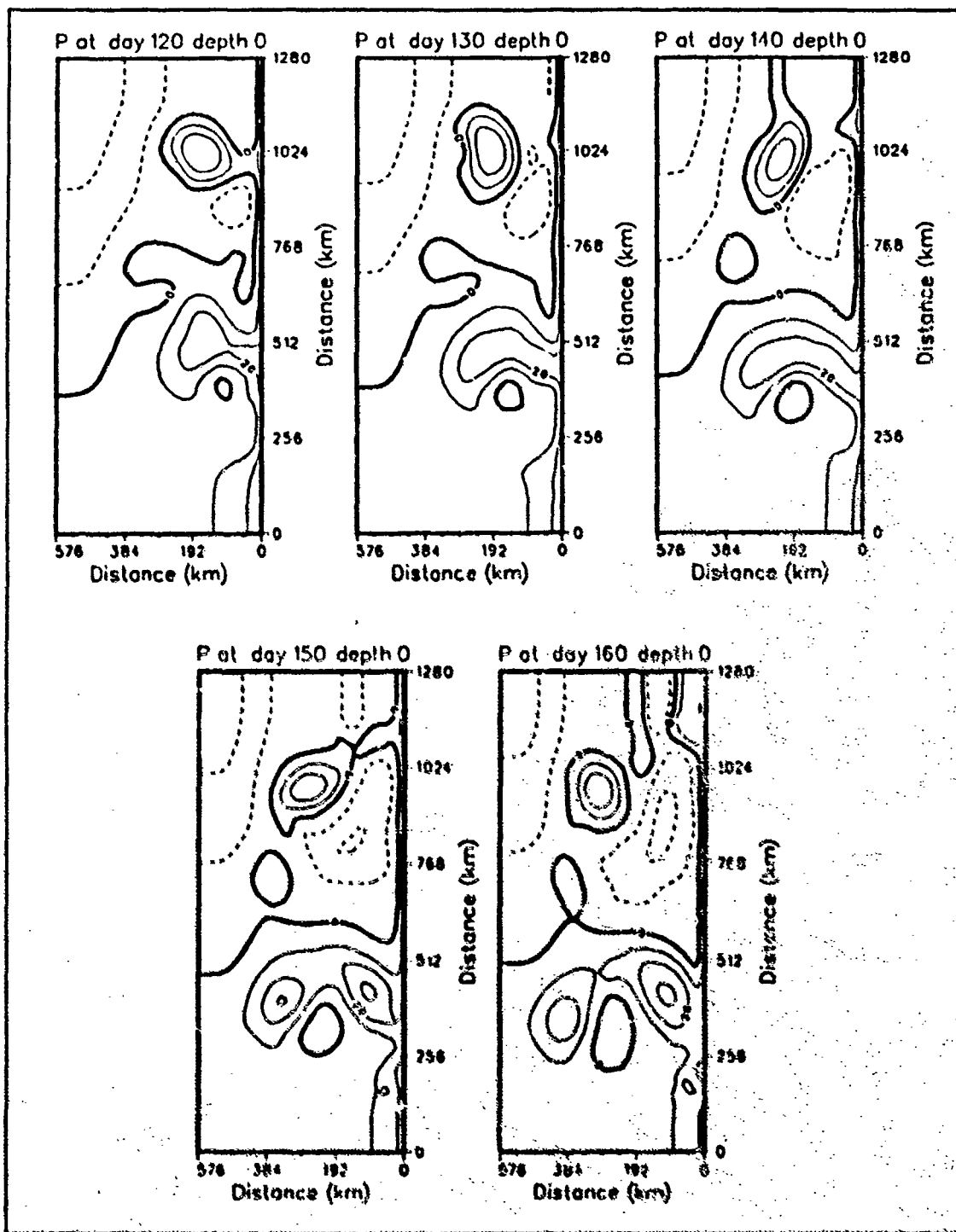


Figure 56. Case 3. Surface pressure field, days 120 - 160: As for Figure 54.

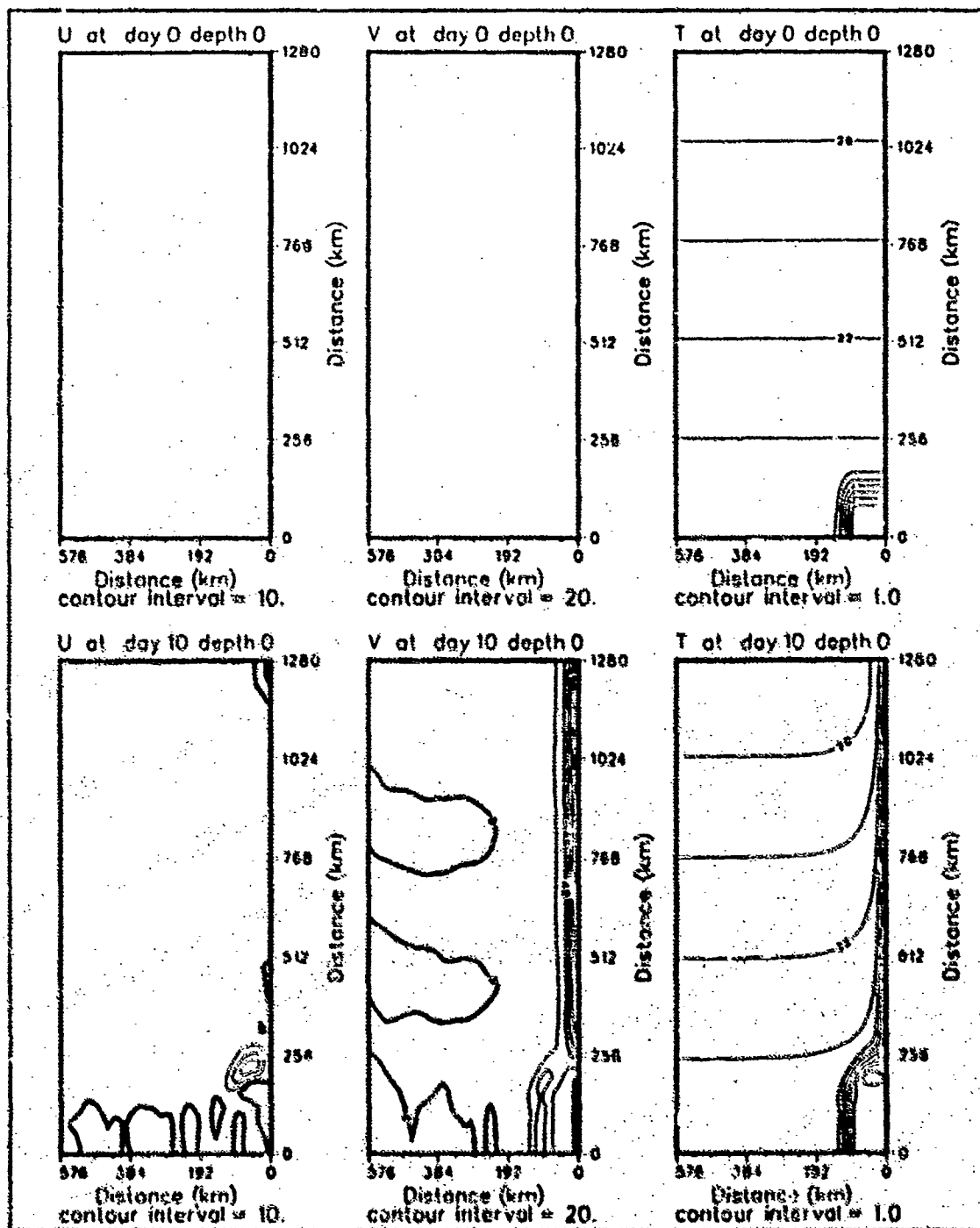


Figure 57. Case 3. Surface velocity and temperature fields, days 0 - 10: Cross-shore velocity component (cm s^{-1}), alongshore velocity component (cm s^{-1}) and temperature ($^{\circ}\text{C}$) at surface.

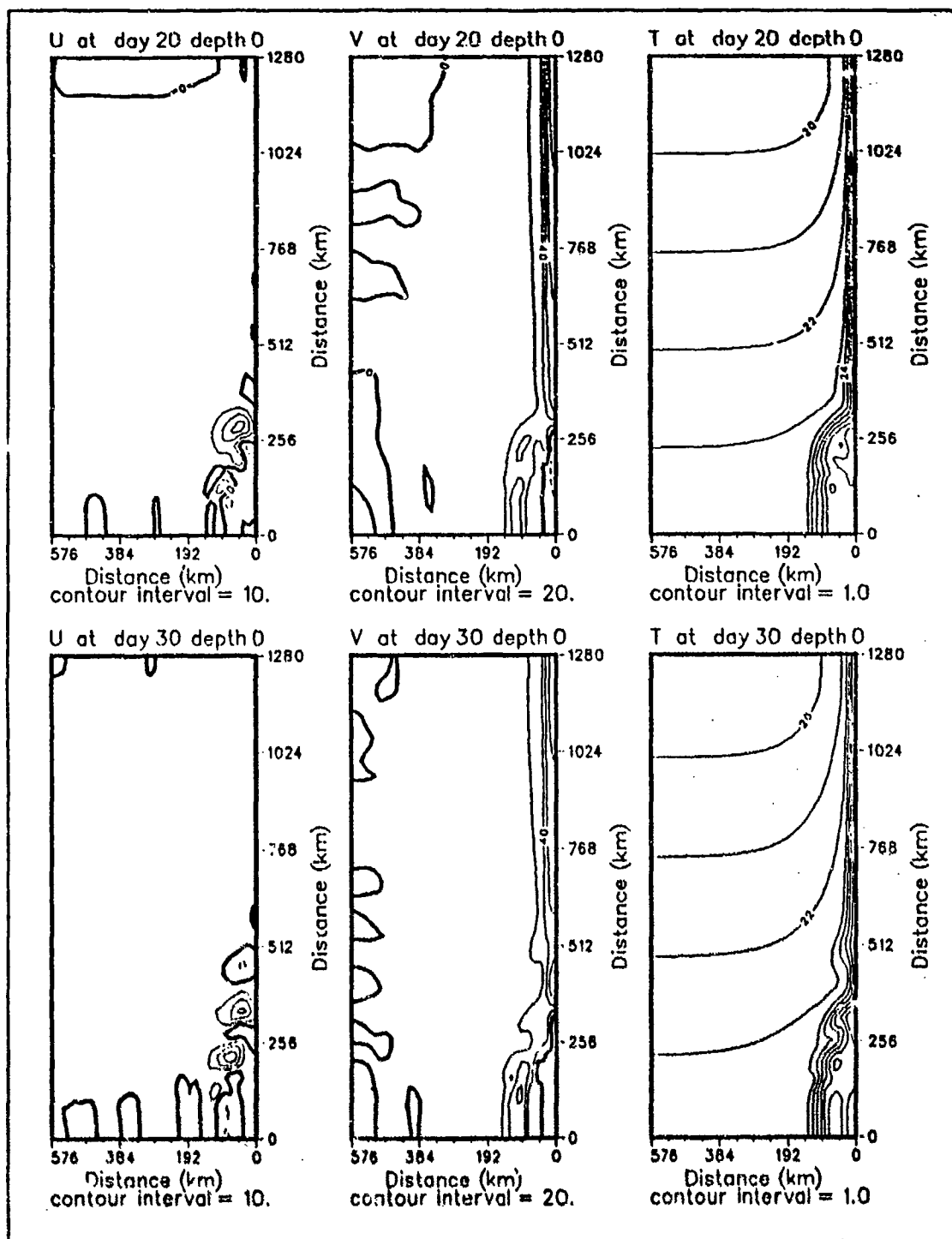


Figure 58. Case 3. Surface velocity and temperature fields, days 20 - 30: As for Figure 57.

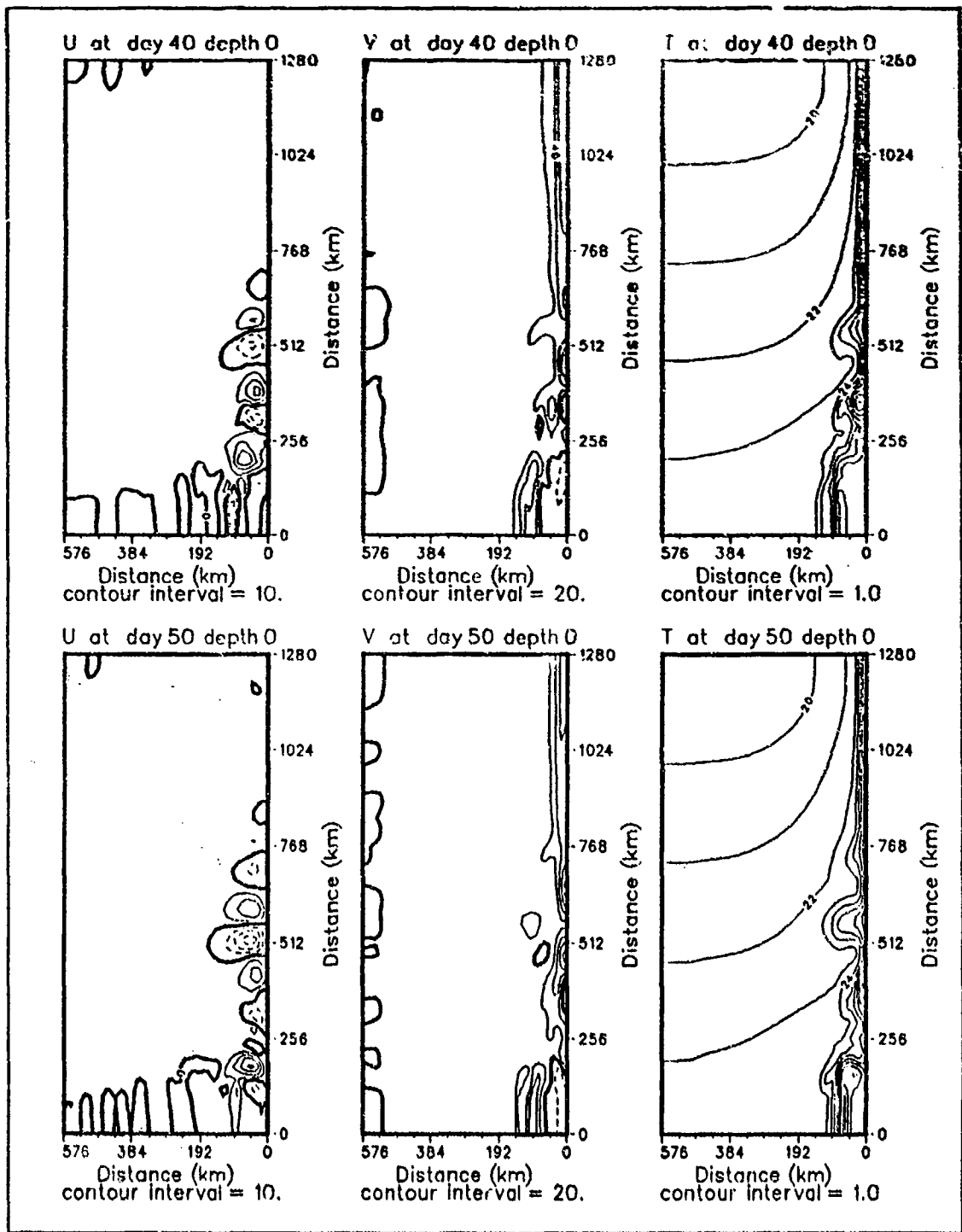


Figure 59. Case 3. Surface velocity and temperature fields, days 40 - 50: As for Figure 57.

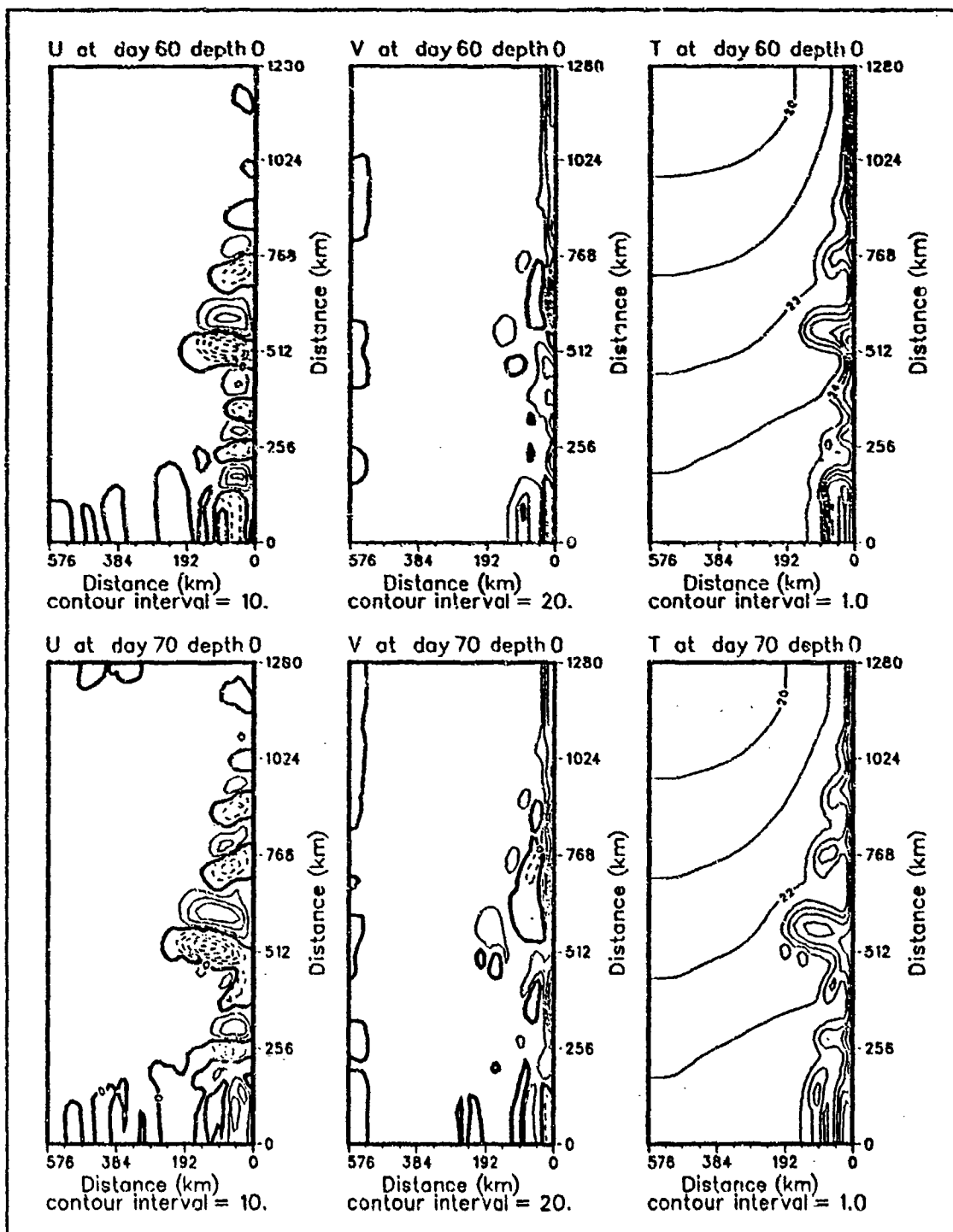


Figure 60. Case 3. Surface velocity and temperature fields, days 60 - 70: As for Figure 57.

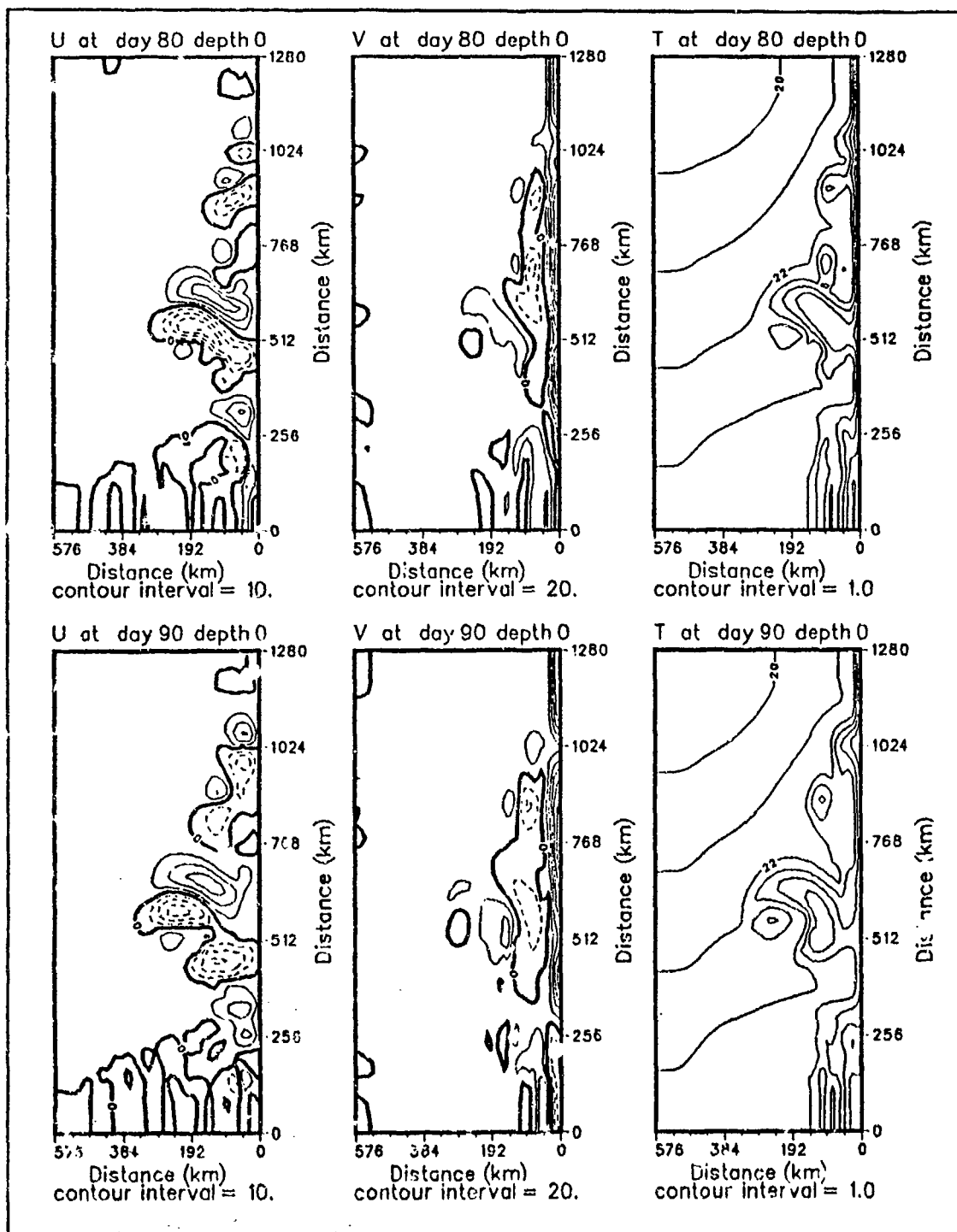


Figure 61. Case 3. Surface velocity and temperature fields, days 80 - 90: As for Figure 57.

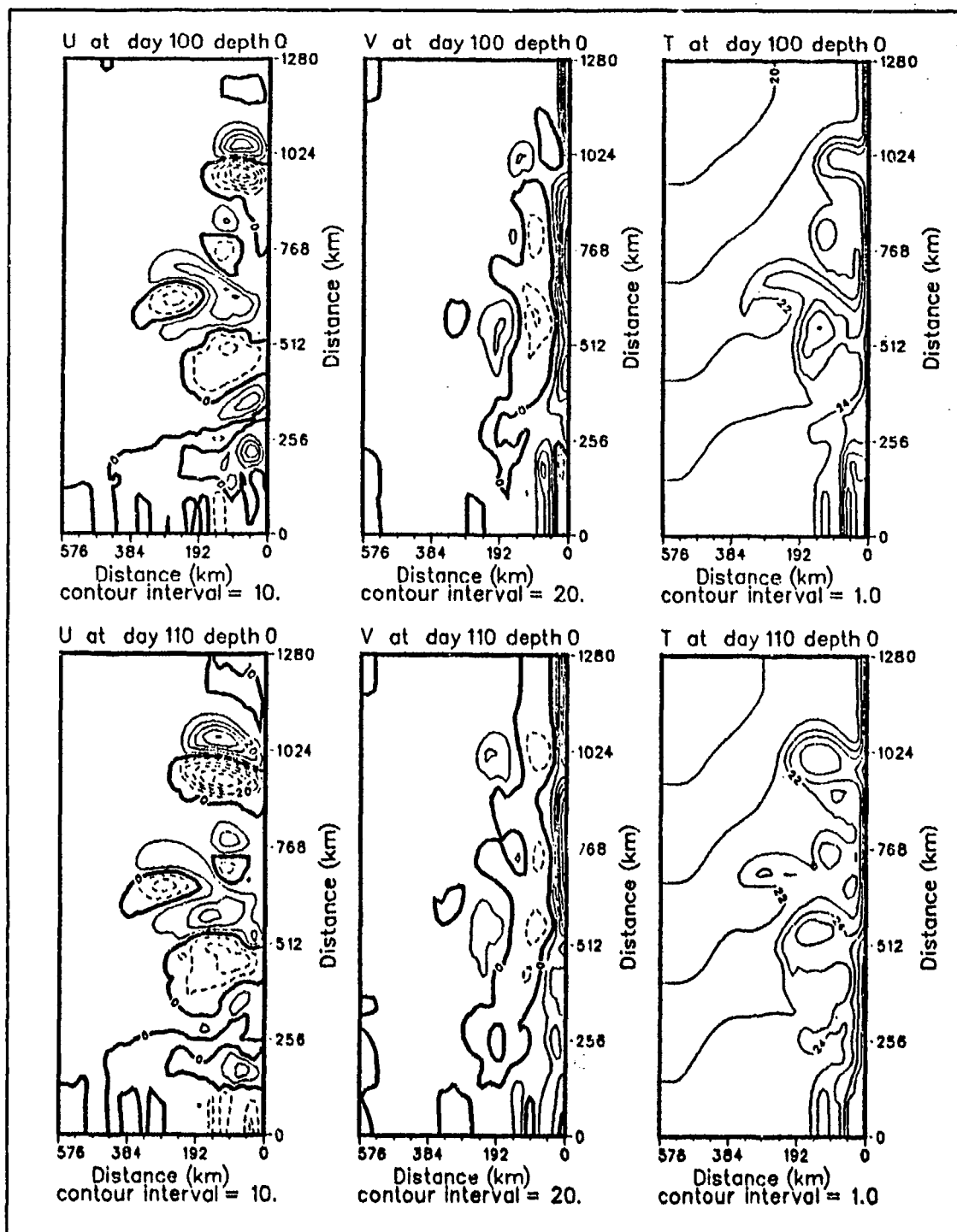


Figure 62. Case 3. Surface velocity and temperature fields, days 100 - 110: As for Figure 57.

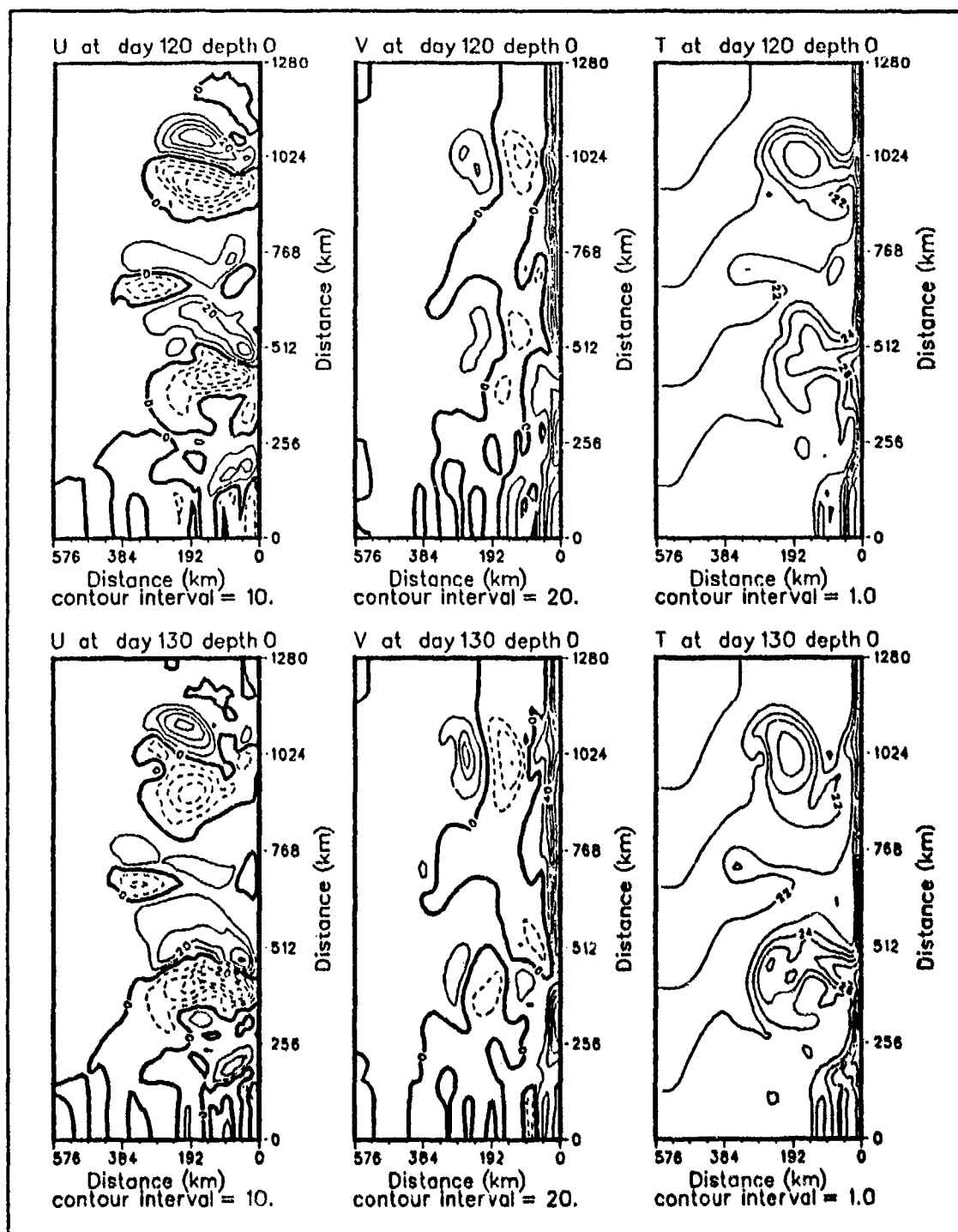


Figure 63. Case 3. Surface velocity and temperature fields, days 120 - 130: As for Figure 57.

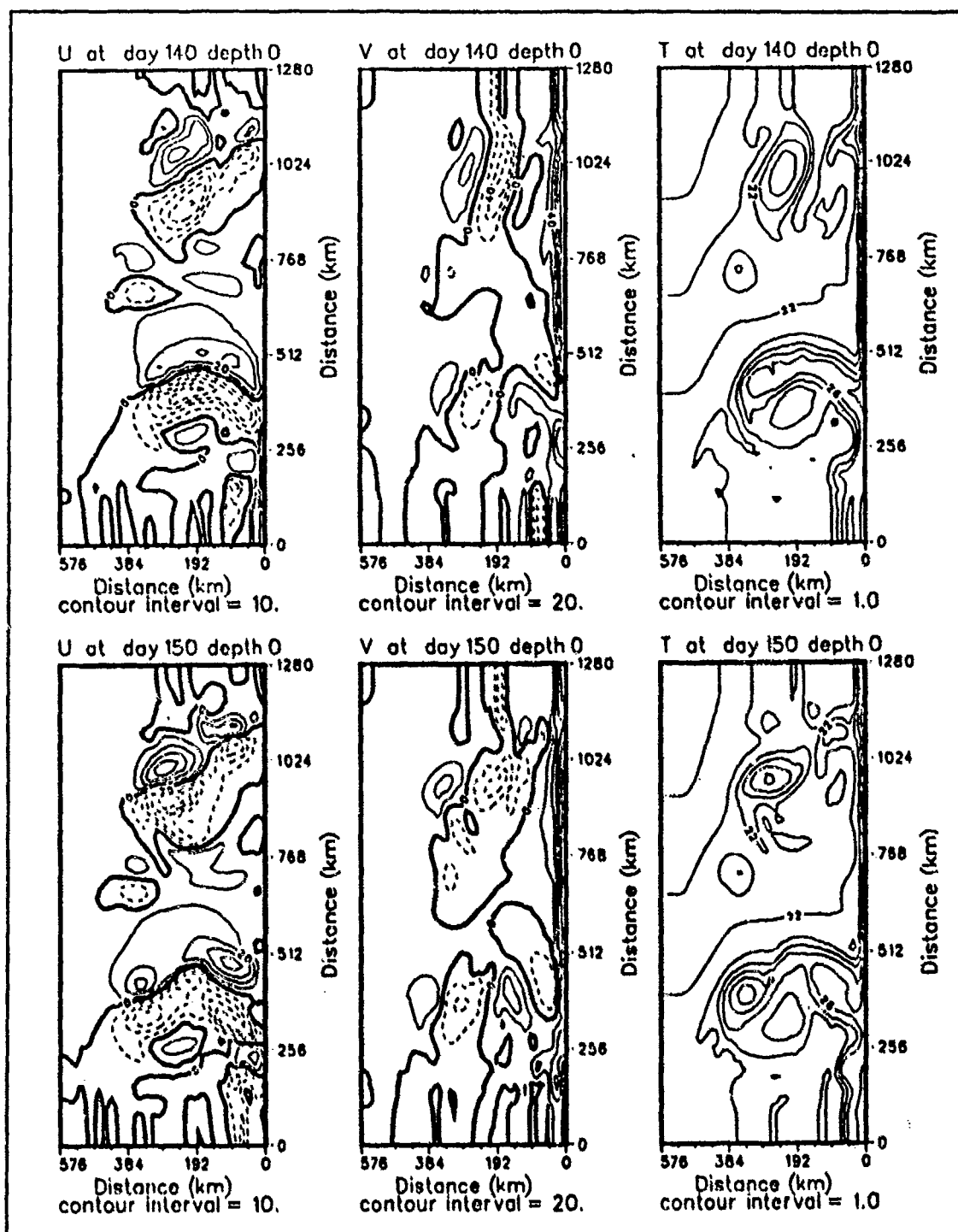


Figure 64. Case 3. Surface velocity and temperature fields, days 140 - 150: As for Figure 57.

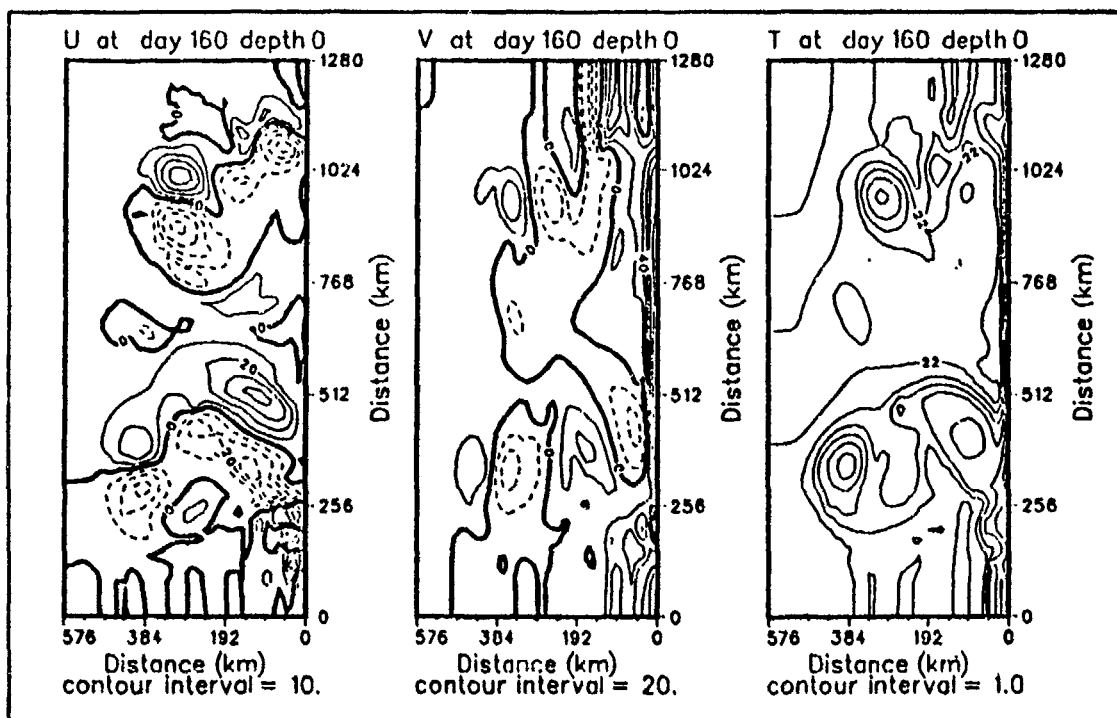


Figure 65. Case 3. Surface velocity and temperature fields, day 160: As for Figure 57.

An energy transfer diagram was calculated for a region extending 90 km offshore between 520 km and 700 km alongshore. The transfers, calculated over the upper five layers are shown in Figure 68. The baroclinicity is clearly important but the large negative barotropic transfer indicates no net barotropic contribution over the region. As in Case 1 the 90 km offshore domain is divided into regions to localize the baroclinic and barotropic contributions. Figure 69 shows that for the inshore 45 km, baroclinic instability is stronger as is the negative barotropic transfer. Over the region extending from 45 km to 90 km offshore the baroclinic contribution is weaker and stronger barotropic instability is observed.

b. Spectral Analysis

The spectral energy plots at days 30, 40, 50 for Case 3 are given in Figures 71, 72 and 73 respectively. The strong growth from days 30 to 40 is seen in the peak developing at a 180 km wavelength (alongshore wavenumber of $\sim 0.0055 \text{ km}^{-1}$). Smaller peaks are also apparent at 100 km (alongshore wavenumber of $\sim 0.01 \text{ km}^{-1}$) and 65 km (alongshore wavenumber of $\sim 0.015 \text{ km}^{-1}$) scales. From days 40 to 50 the three distinct

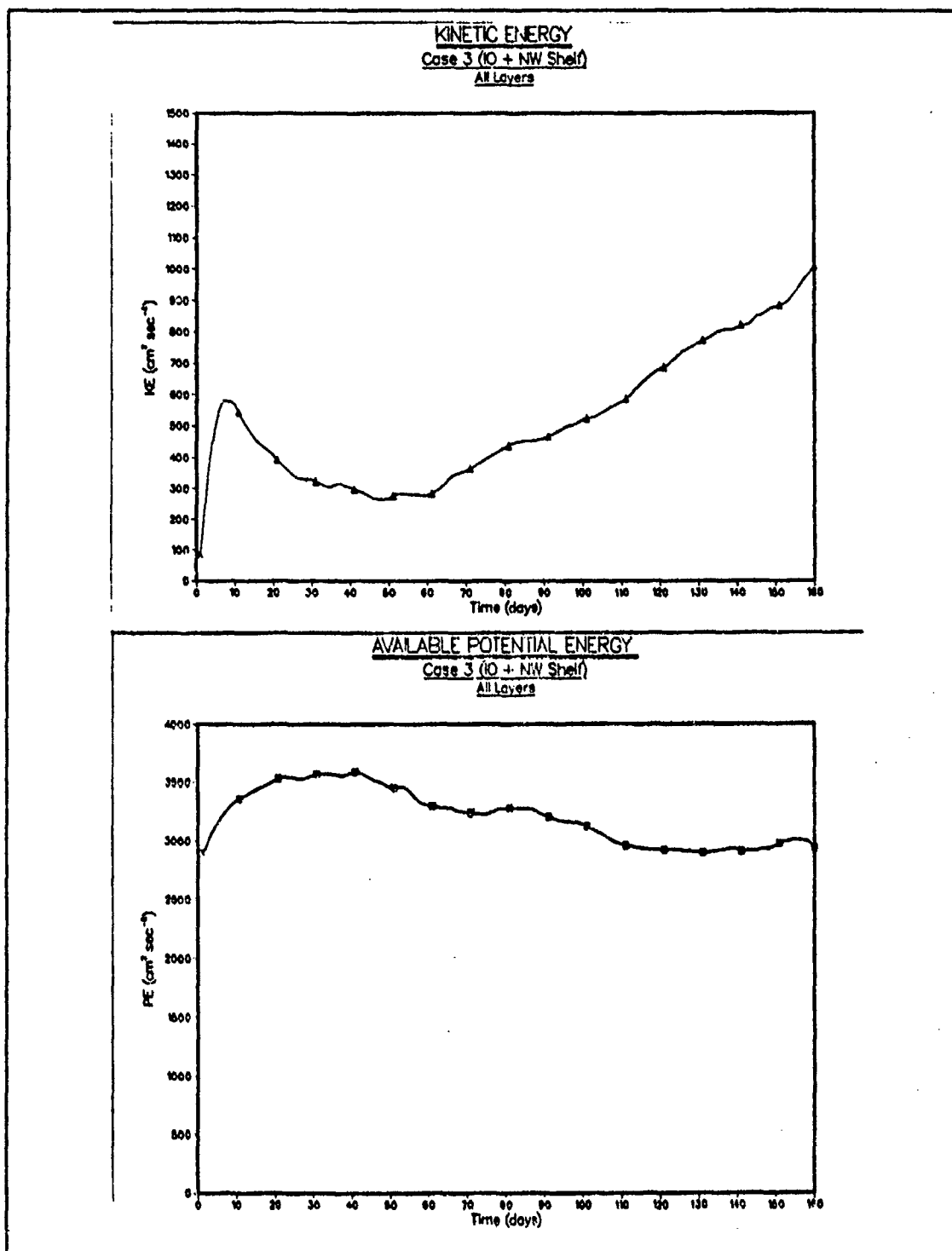


Figure 66. Case 3. Energy time series: Total kinetic and available potential energy ($\text{cm}^2 \text{s}^{-2}$) summed over all layers and the entire domain.

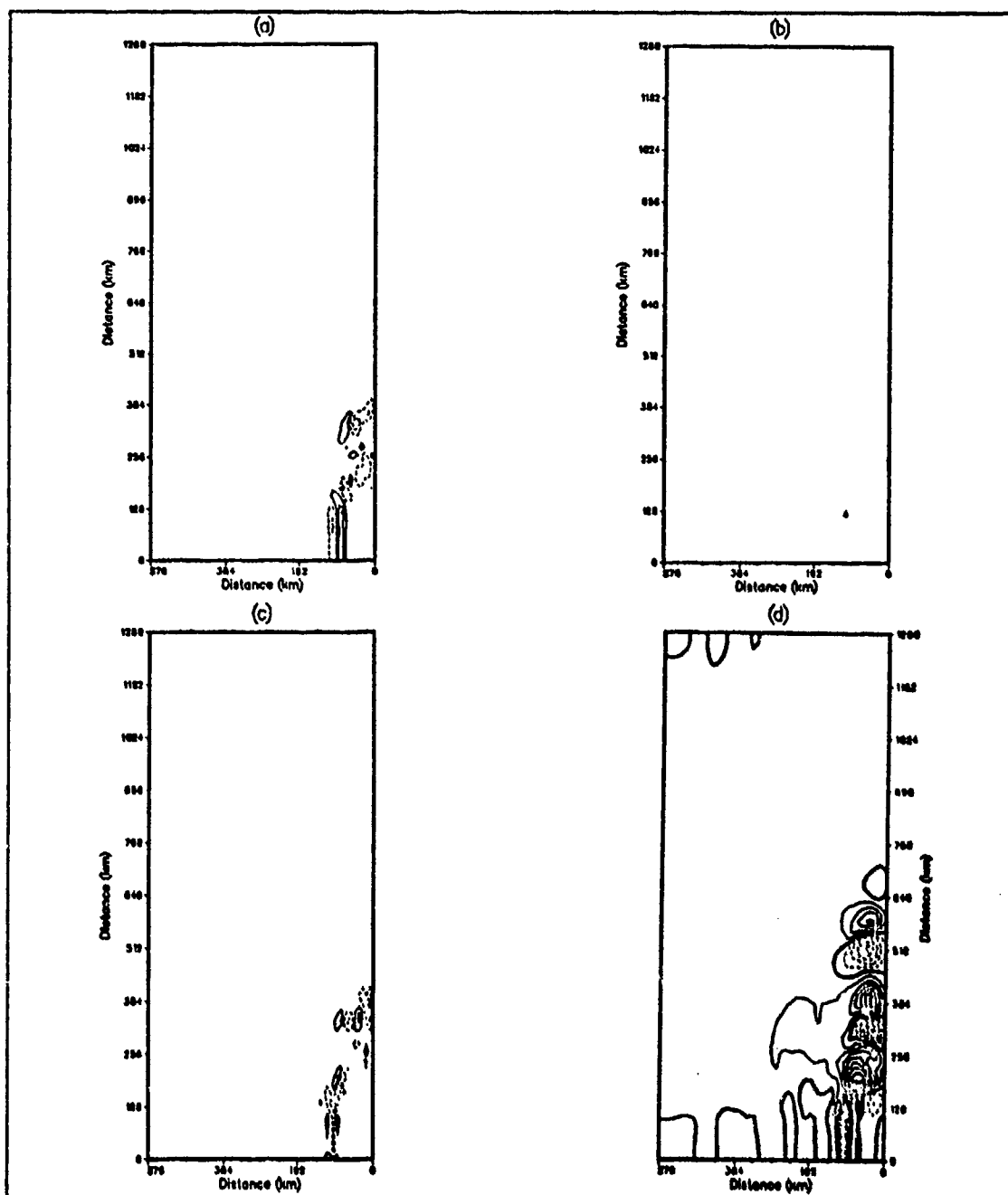


Figure 67. Case 3. Energy transfers: Transfers of energy from (a) \bar{P} to P' , (b) P' to K' and (c) \bar{K} to K' in units of $\text{ergs cm}^{-3} \text{s}^{-1}$. Transfers are averaged over days 30-40 and summed over the upper five layers. Contour interval is $4.0 \times 10^{-3} \text{ergs cm}^{-3} \text{s}^{-1}$. Subplot (d) is the cross-shore velocity component at day 40 at a contour interval of 5.0 cm s^{-1} .

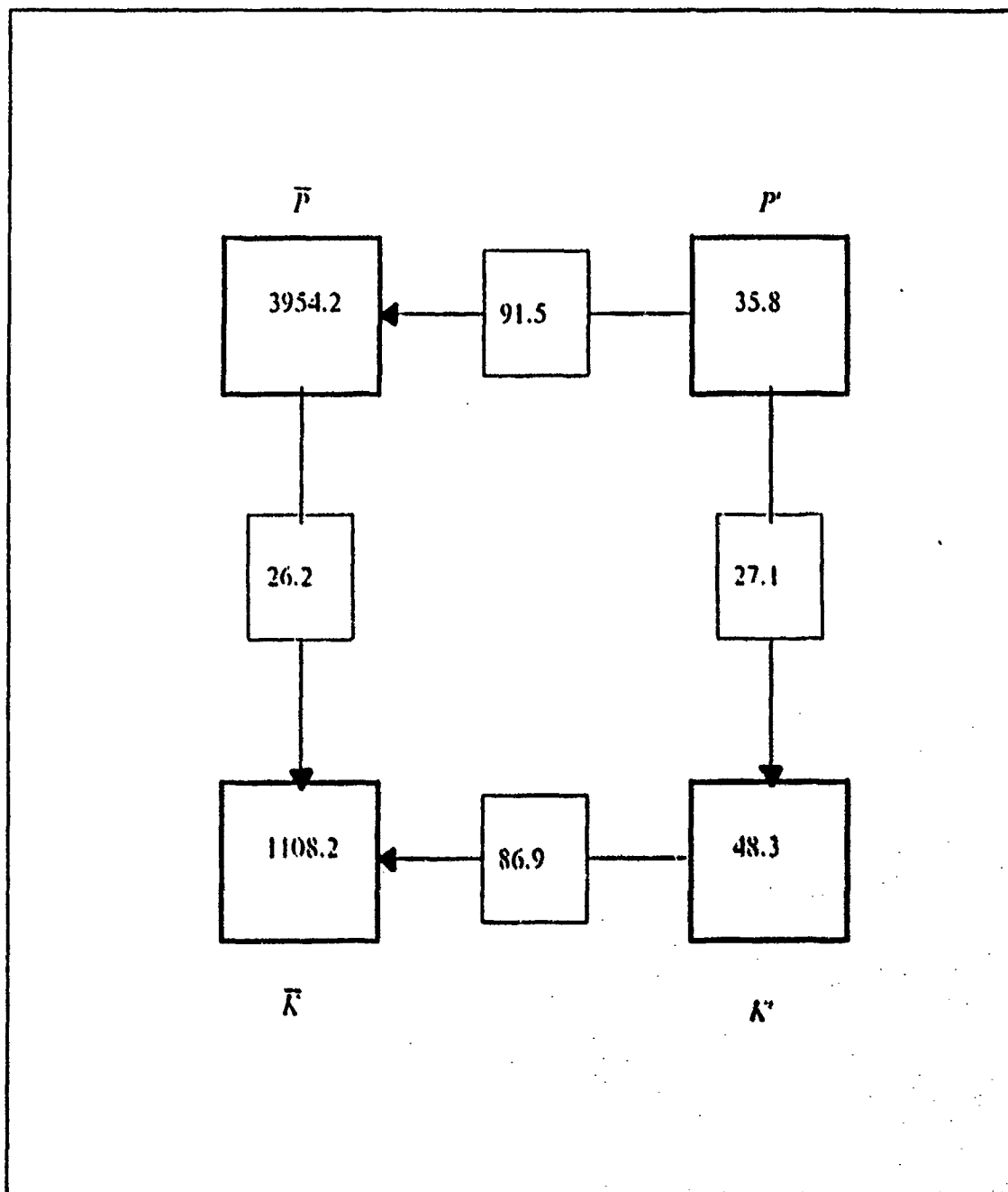


Figure 68. Case 3. Energy transfer diagram: The energy transfer diagram for the upper five layers for the region between 520 km and 700 km alongshore, extending 90 km offshore. Units for \bar{P} , \bar{K} , P' and K' are ergs cm^{-2} , and transfers are in units of $\text{ergs cm}^{-2} \text{s}^{-1} \times 10^4$.

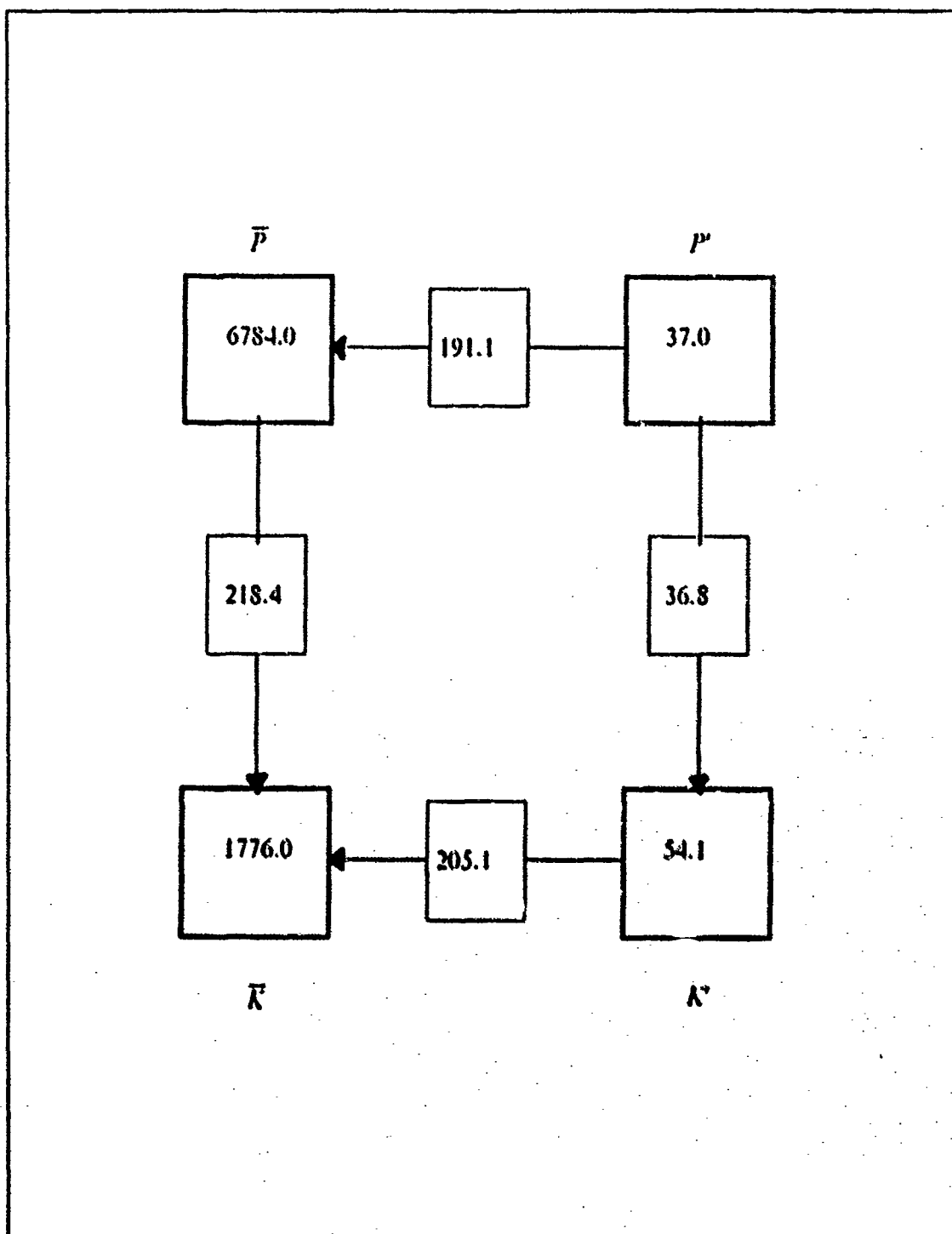


Figure 69. Case 3. Energy transfer diagram: As for Figure 68 for the same alongshore region but now extending only 45 km offshore.

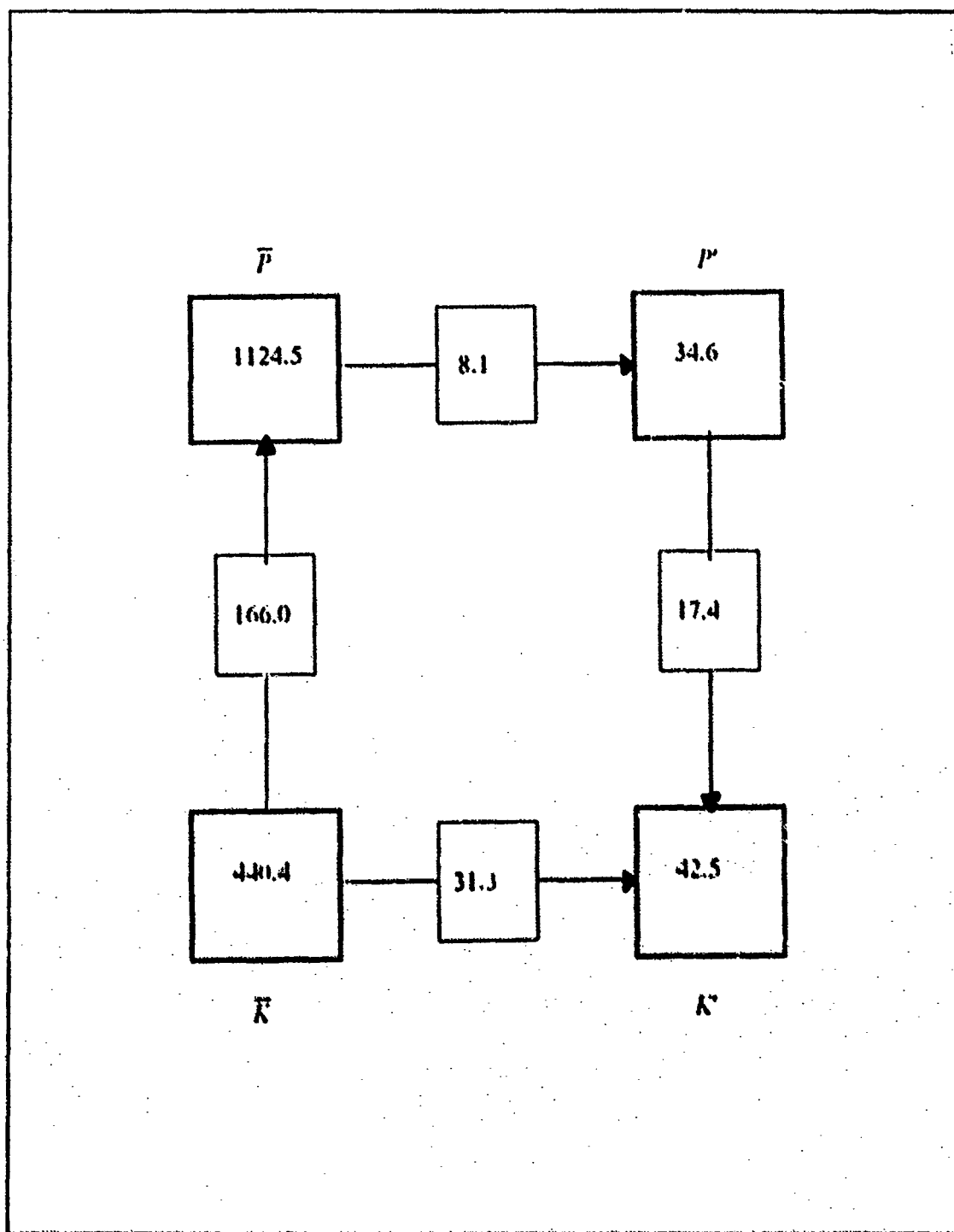


Figure 70. Case 3. Energy transfer diagram: Λ^* for Figure 68 for the same alongshore region but now extending from 45 km to 90 km offshore.

peaks are still apparent with maximum energy again at the 180 km scale. Whereas Case 2 had a single peak and barotropic growth was dominant, both Cases 1 and 3 have multiple spectral peaks during the eddy generation stage and strong baroclinicity is also a feature. It appears that when baroclinicity is strong, growth at multiple wavelengths occurs, possibly coinciding with other internal modes.

The spectral density for the entire 160 days of Case 3 is shown in Figure 74. The dominant scale of 180 km appears to broaden with time and a shift to larger scales is seen. To isolate the scales of generation and growth, a second spectral analysis was done over the inshore 90 km of the model, coinciding with the generation region. The spectral time series for the inshore region, corresponding to the current, is in Figure 75 and for the remainder of the domain in Figure 76. Inshore, the wavelength of the dominant growth in the vicinity of the current is near 180 km, (alongshore wavenumber of $\sim 0.0055 \text{ km}^{-1}$), and a secondary maxima occurs at 125 km. (alongshore wavenumber of $\sim 0.008 \text{ km}^{-1}$). Away from the core, Figure 76 shows that the 180 km wavelength is dominant and that a shift to longer wavelengths occurs with time.

Comparing the results of the spectral analysis from Cases 2 and 3, the effects of the addition of NW Shelf water may be determined. In the mainly barotropic Case 2, eddy generation and subsequent growth was at a wavelength of approximately 150 km. With the inclusion of the NW Shelf water, and its strong baroclinic contribution toward instability, the main growth occurs at 180 km. The NW Shelf waters appear to increase the scale at which the dominant eddy growth occurs by modifying the thermal structure in the inshore region.

c. Instability Analysis

Figure 77 is used to confirm that the necessary and sufficient conditions for the observed eddy generation are satisfied. In particular, the cross-shore derivative of potential vorticity changes sign inshore and its product with the mean alongshore flow is clearly positive at some location in the domain, which satisfies the necessary conditions for baroclinic instability. The vertical and horizontal shears in alongshore velocity, which provide an energy source for the eddy generation are apparent from Figure 77 (b).

The Rossby radius of deformation was calculated for the region of instability as 27.9 km. Comparing this value with that of Case 2 (27.6 km), little change has occurred to the radius of deformation despite the inclusion of the NW Shelf waters.

d. Conclusion

The current, driven by a combination of Indian Ocean and NW Shelf thermal forcing, is much more vigorous and unstable than Case 2, forced by the Indian

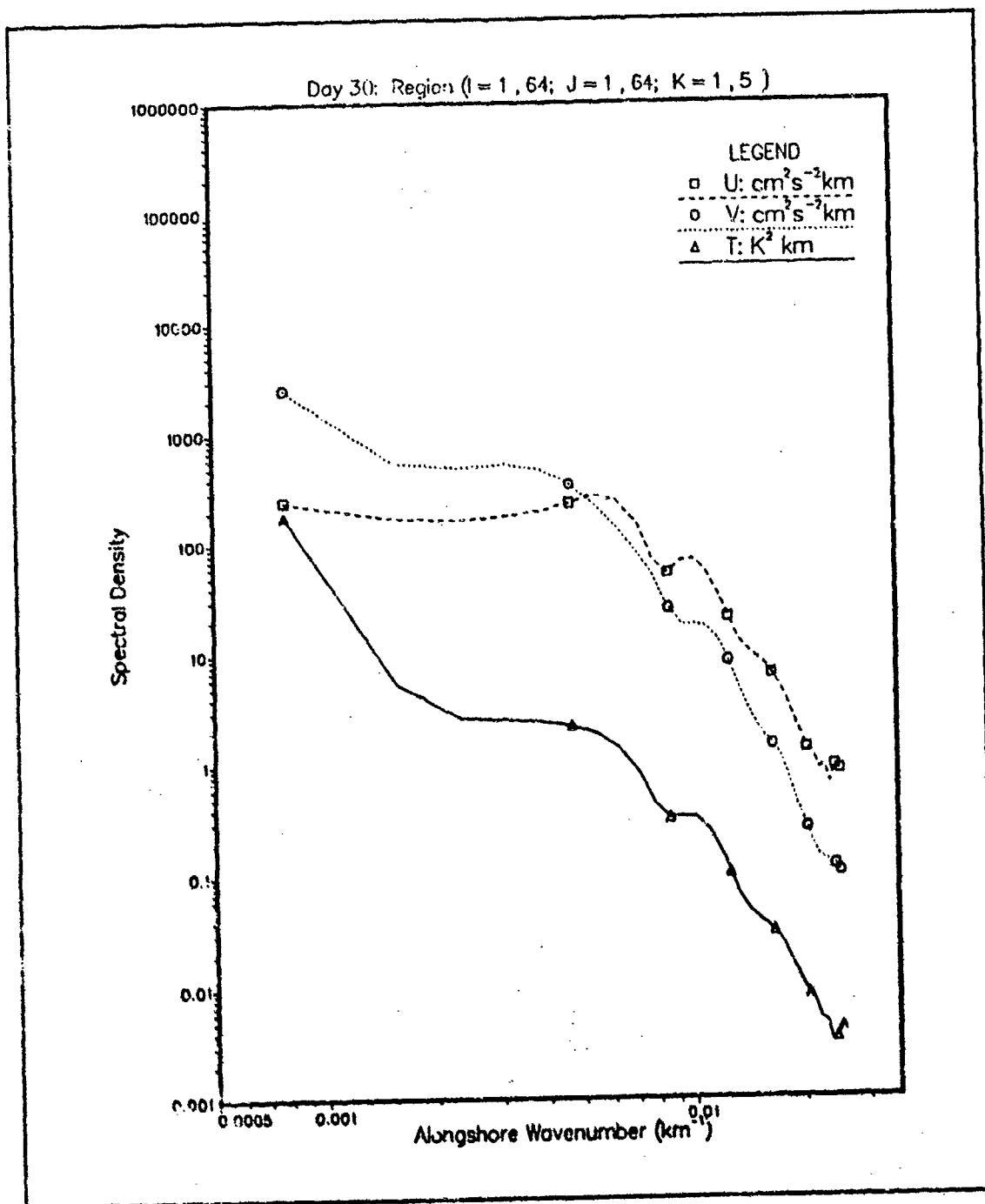


Figure 71. Case 3. Spectral density at day 30: Spectral density versus alongshore wavenumber at day 30. The wavenumber has been scaled by $\frac{1}{2\pi}$ and so is an inverse wavelength. A logarithmic scale is used for the spectral energy.

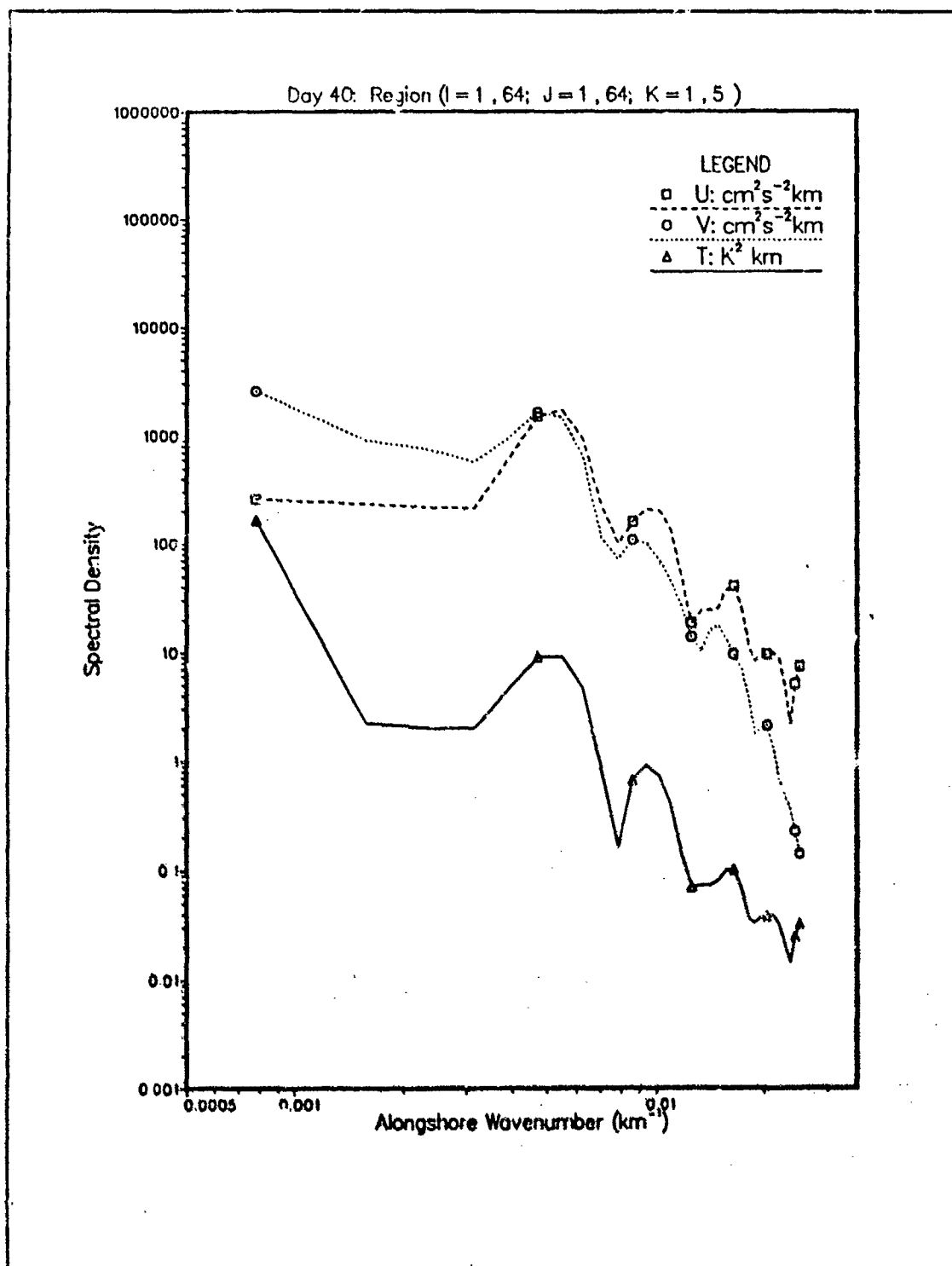


Figure 72. Case 3. Spectral density at day 40: As for Figure 48 but at day 40.

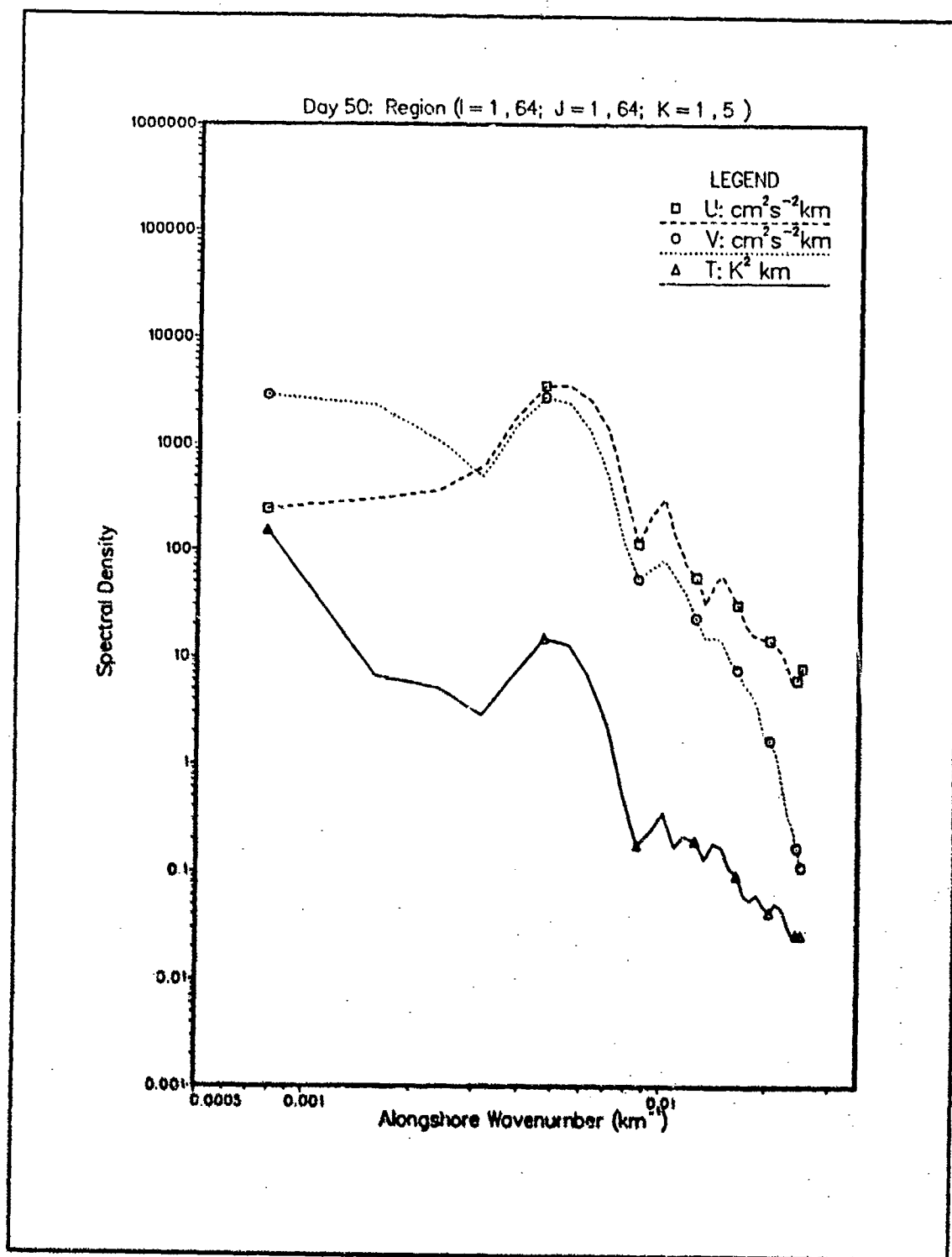


Figure 73. Case 3. Spectral density at day 50: As for Figure 48 but at day 50.

Region (I = 1,64; J = 1,64; K = 1,5)

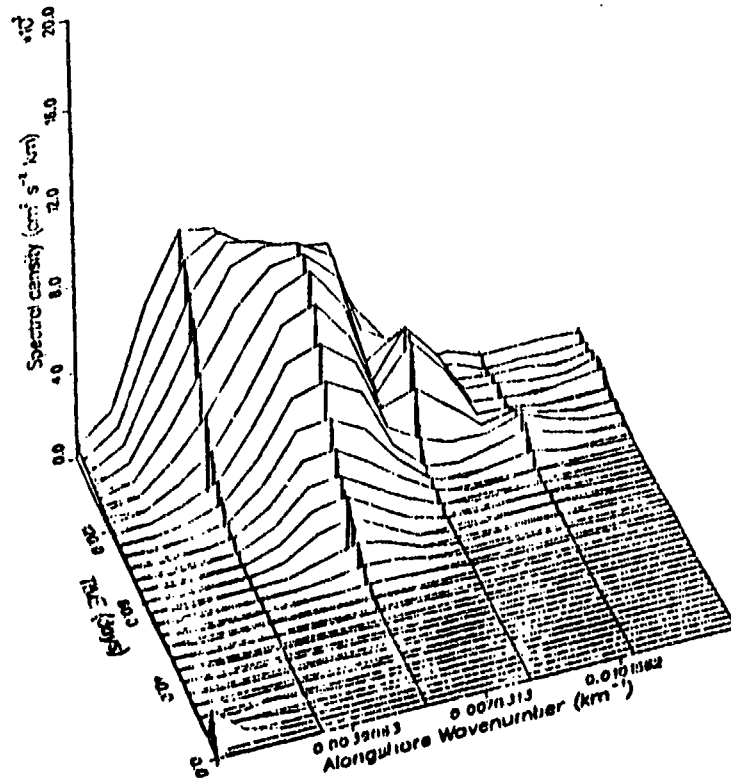


Figure 74. Case 3. Spectral density time series: The time series of spectral density from days 0 to 160 over the entire domain. Note: the amplitude of the spectral energy is on a linear scale.

Region (I = 55 , 64; J = 1 , 64; K = 1 , 5)

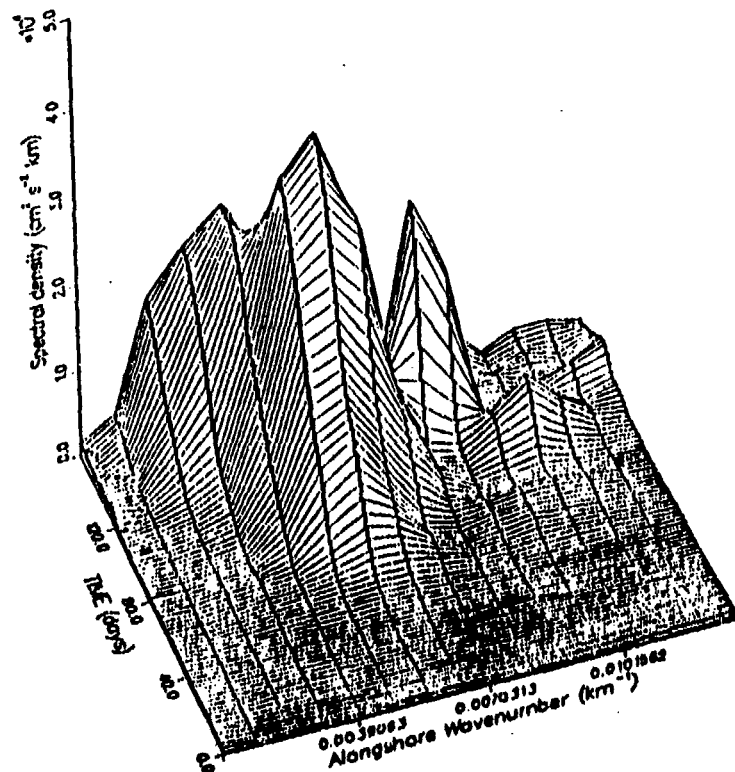


Figure 75. Case 3. Spectral density time series: As for Figure 74 but confined to a domain extending 90 km offshore.

Region (I = 1, 54; J = 1, 64; K = 1, 5)

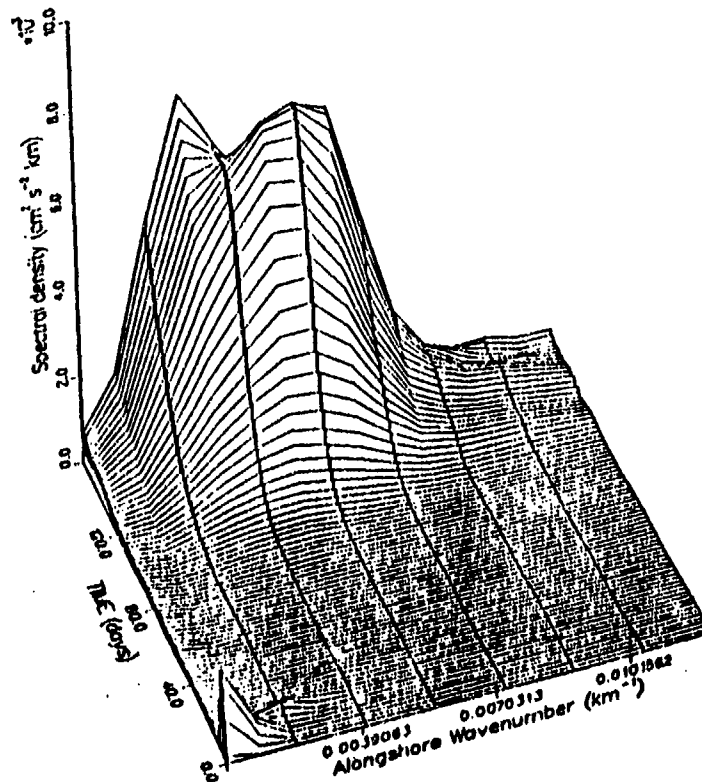


Figure 76. Case 3. Spectral density time series: As for Figure 74 but over the offshore region not covered by Figure 75.

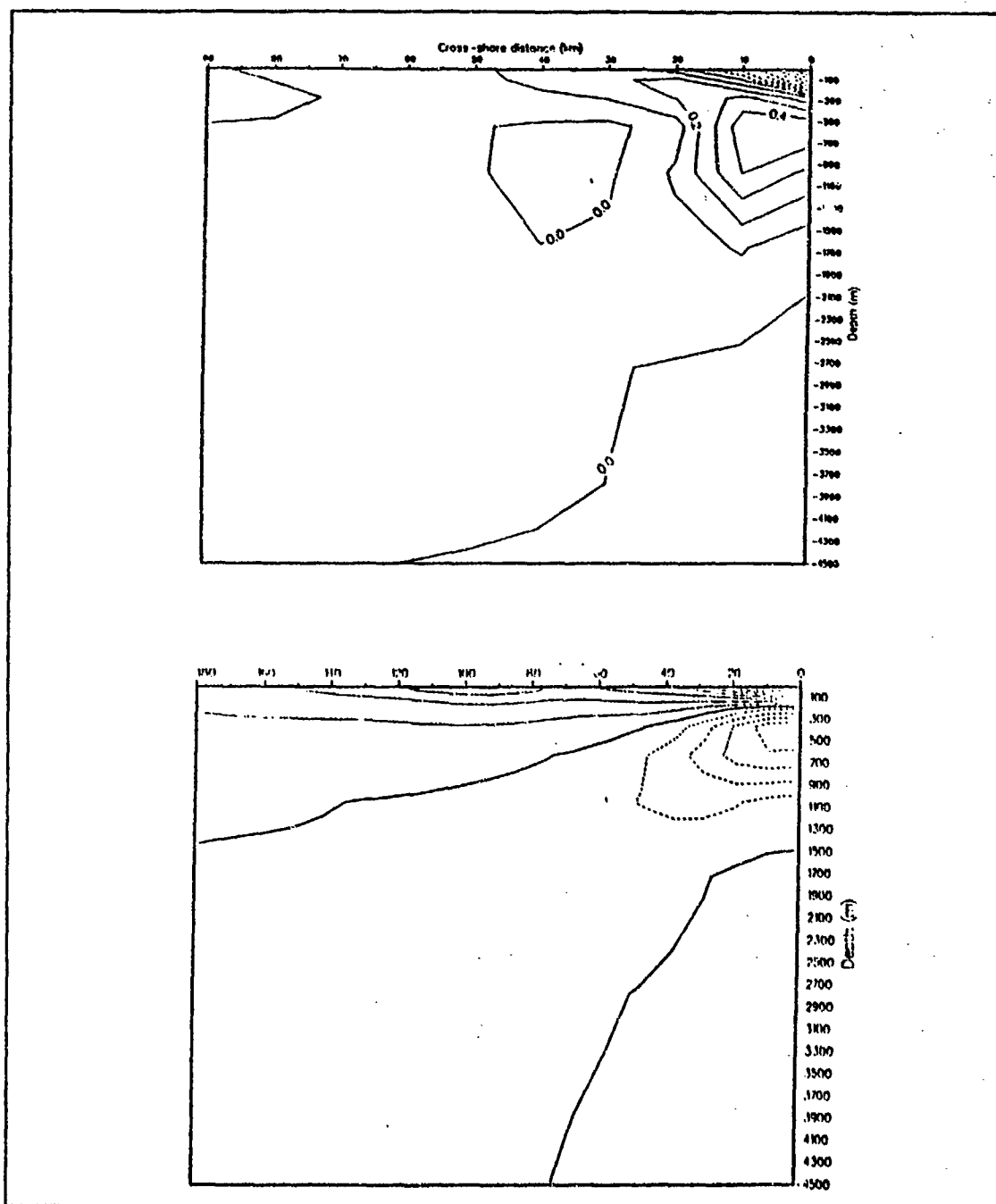


Figure 77. Case 3. Cross sections of dq/dx and alongshore velocity: As for Figure 53. Time averaging is now over days 30-40 and the cross-section at alongshore distance 600 km. Contour intervals are (a) $0.1\text{ }^{\circ}\text{C m}^{-1}\text{ s}^{-1}$ and (b) 5.0 cm s^{-1} .

Ocean alone. Barotropic instability is strong at the equatorward end, near the source of the NW Shelf waters. The addition of the NW Shelf waters adds strongly to the baroclinicity of the current inshore, although the Rossby radius remains virtually unchanged. The barotropic contribution at the offshore edge of the core of the current is also slightly increased by the presence of the NW Shelf waters. The dominant scale of eddy generation in the current is 180 km. This is consistent with the calculated Rossby radius of ~ 28 km. in the strongly baroclinic flow. Away from the current a spectral shift toward longer wavelengths is seen, consistent with the growth of eddies as they move offshore.

4. Case 4. Forcing by Indian Ocean and Winds

The time series of surface dynamic heights (pressure) is shown in Figures 78 to 80. The pressure fields are similar to those of Case 2 and indicate a generally weak poleward flow increasing in strength poleward where it is fed by onshore geostrophic inflow. More specific detail on the characteristics of the flow is discernable in the time series of surface velocity components and temperature in Figures 81 to 89. The major effect of the wind is seen offshore where the uniform onshore flow seen in Case 2 (Figures 36 to 44) is modified by the wind forcing. Inshore, the changes are more subtle. The strongest eddy development is again found at the poleward end of the domain, and is in almost the same location as in Case 2. Comparing Figures 40 and 78, the eddy is stronger in Case 4 and additional structure is observed inshore between alongshore distances 512 km and 768 km in Case 4 which can only be attributed to the wind forcing. Another feature seen for the first time in Case 4 is the elongated region of equatorward alongshore velocity, seen offshore of the poleward flow starting at the poleward end of the model at day 100 (Figure 79) and then spreading equatorward.

The temperature fields in Case 4 show far less structure than in Case 2. This is evidence of the upwelling effect of the wind forcing which, although weak, is sufficient to counter the poleward advection of warmer waters from the equatorward end of the domain.

a. Energy Analysis

The plots of kinetic energy and available potential energy in Figure 90 show both to be nearly constant from day 40 to day 60. As a result this period is chosen for a more detailed analysis of the instability mechanisms.

The energy transfer plots over days 40 to 60 for Case 4 are shown in Figure 91. As in previous cases, a large transfer between mean and eddy available potential energy is observed. Comparing subplots (b) and (c) in Figure 90, baroclinicity appears

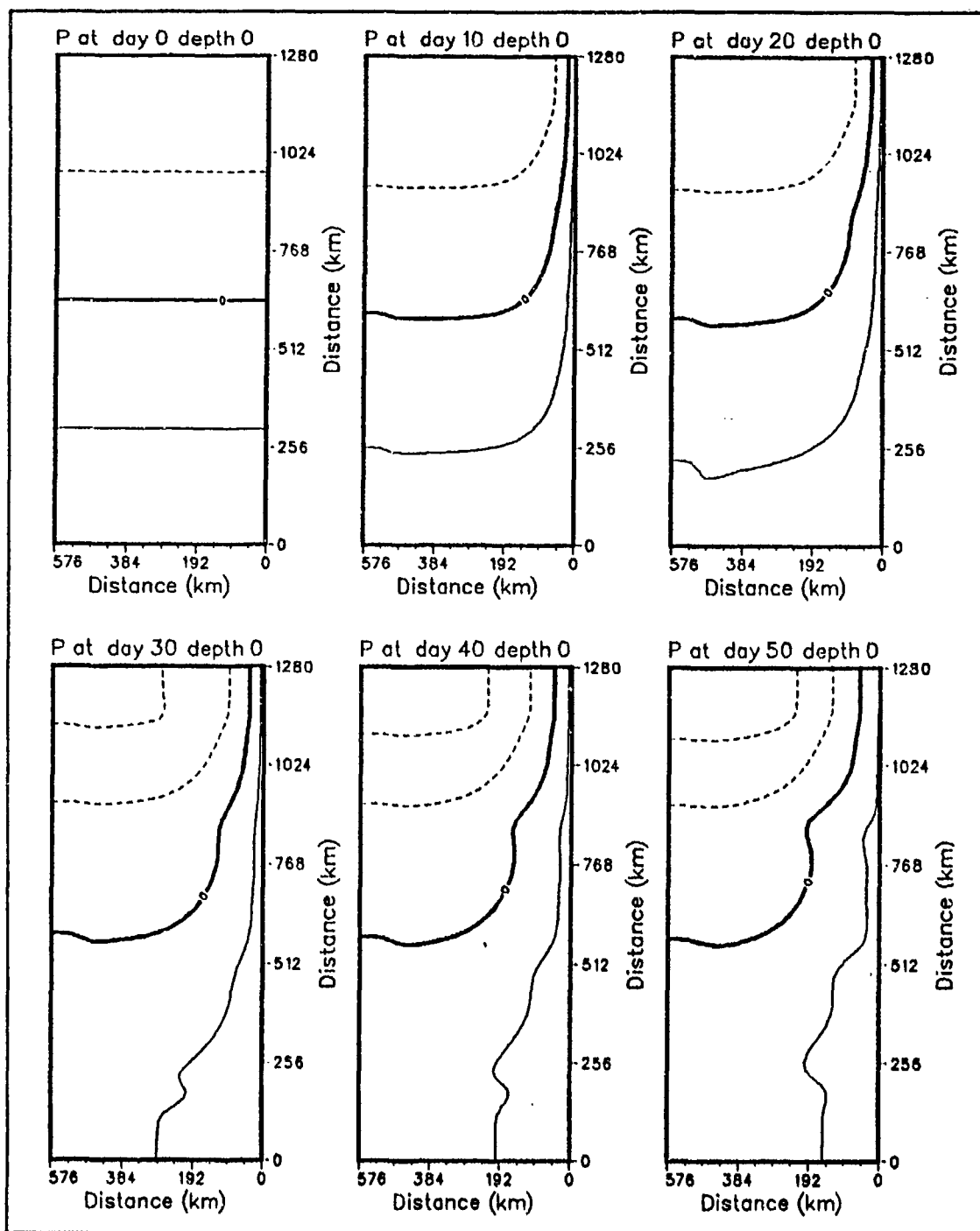


Figure 78. Case 4. Surface pressure field, days 0 - 50: Dynamic height anomaly (cm) at surface relative to a reference level of 2000 m. Contour interval is 5 cm.

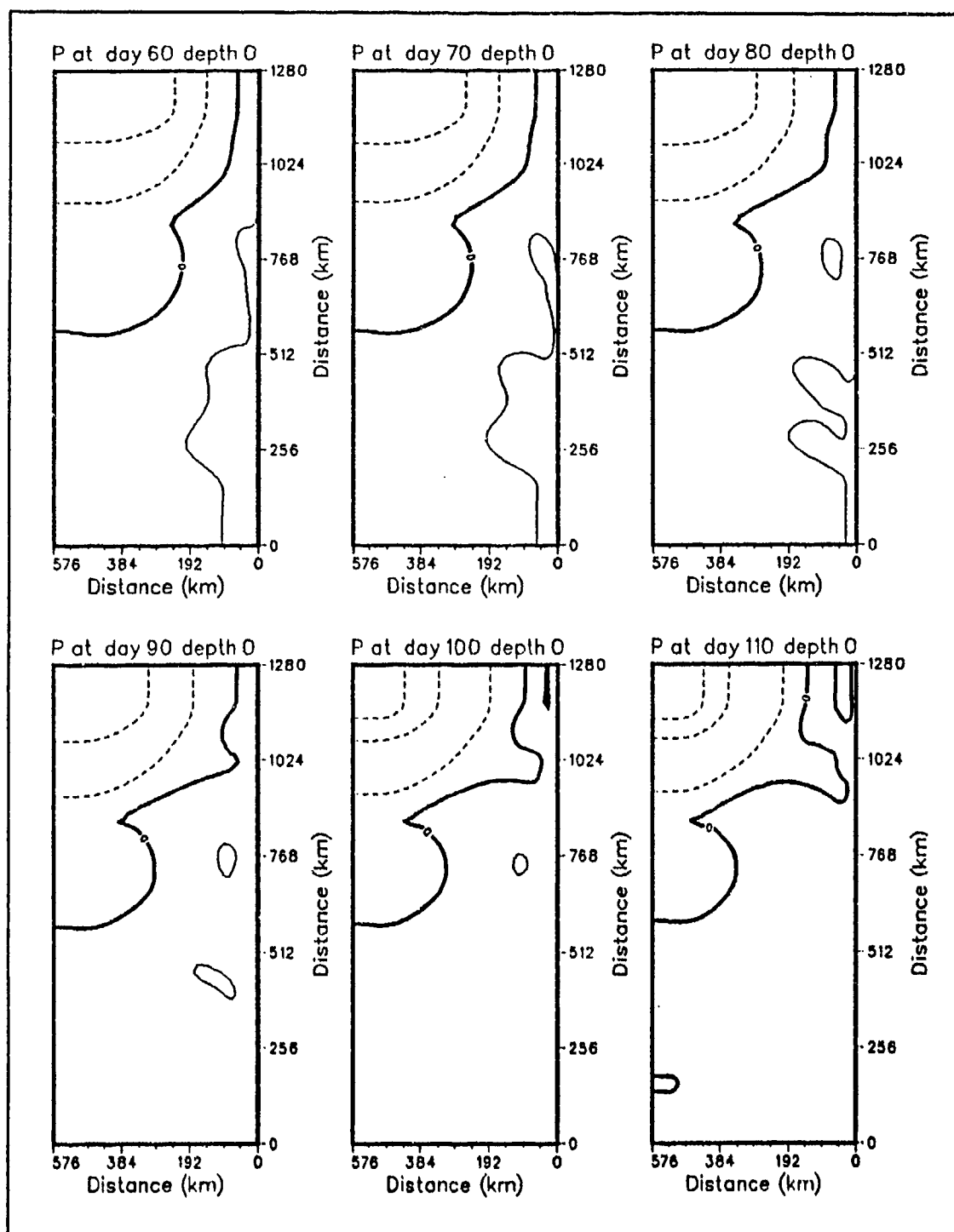


Figure 79. Case 4. Surface pressure field, days 60 - 110: As for Figure 78.

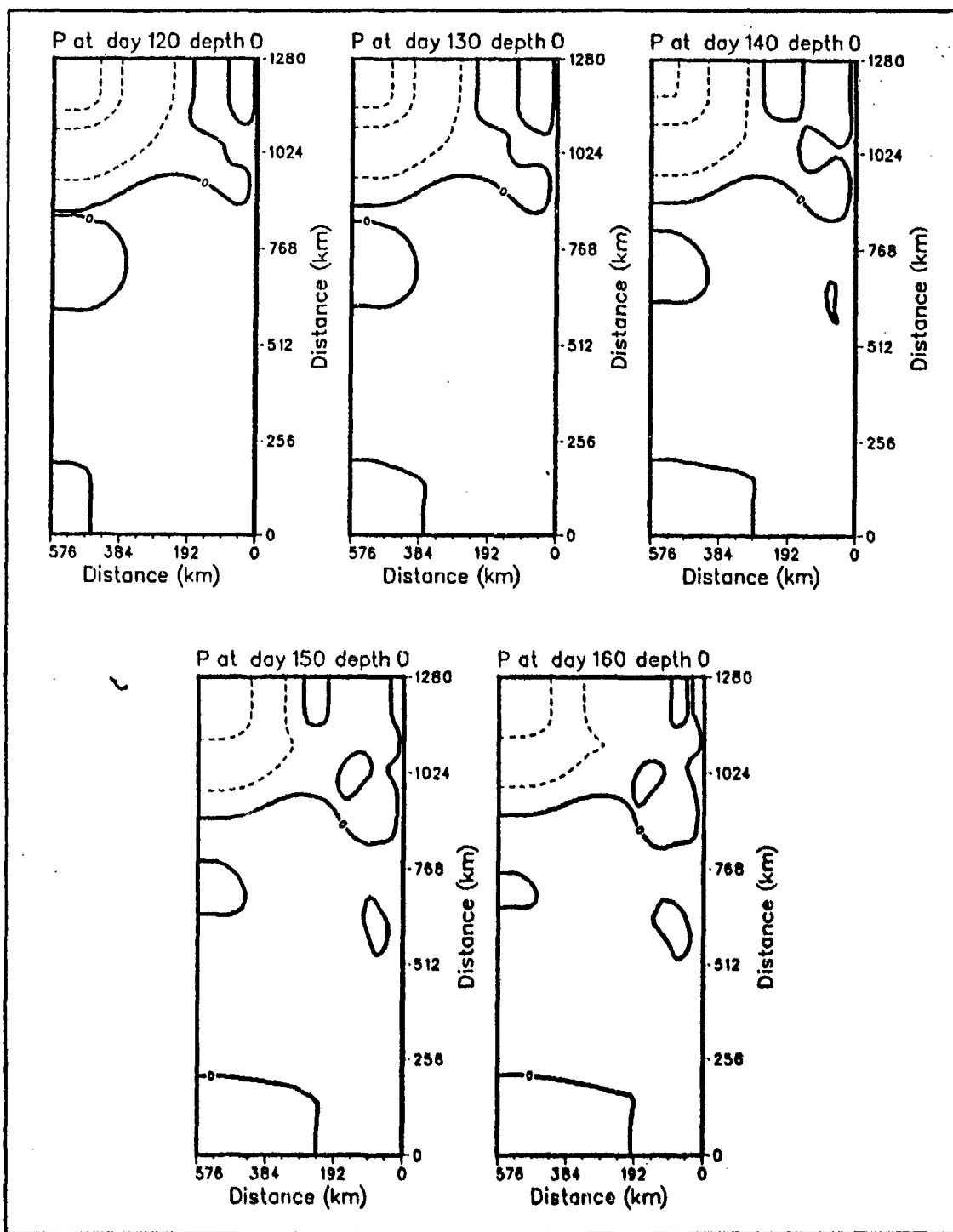


Figure 80. Case 4. Surface pressure field, days 120 - 160: As for Figure 78.

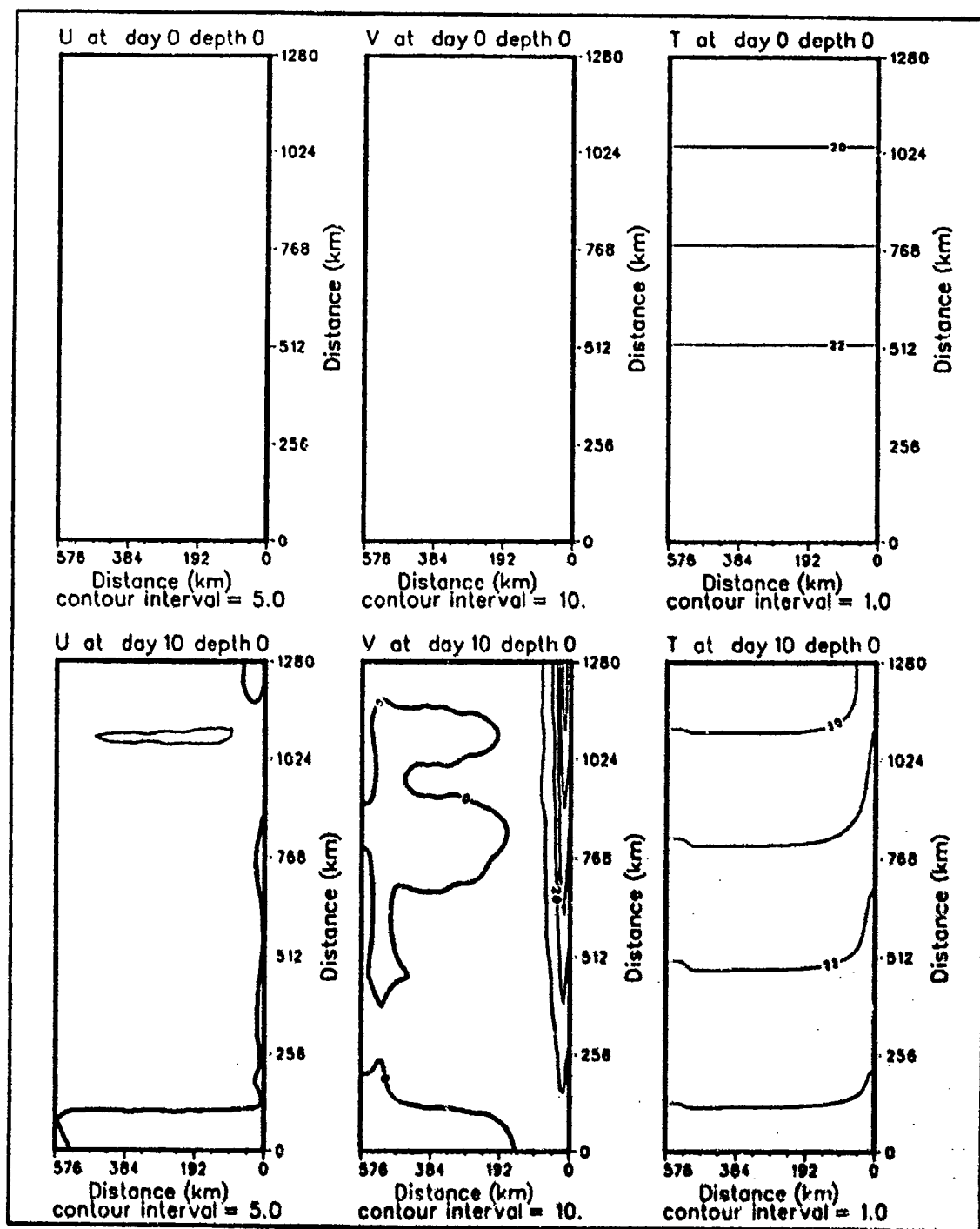


Figure 81. Case 4. Surface velocity and temperature fields, days 0 - 10: Cross-shore velocity component ($cm s^{-1}$), alongshore velocity component ($cm s^{-1}$) and temperature $^{\circ}C$ at surface.

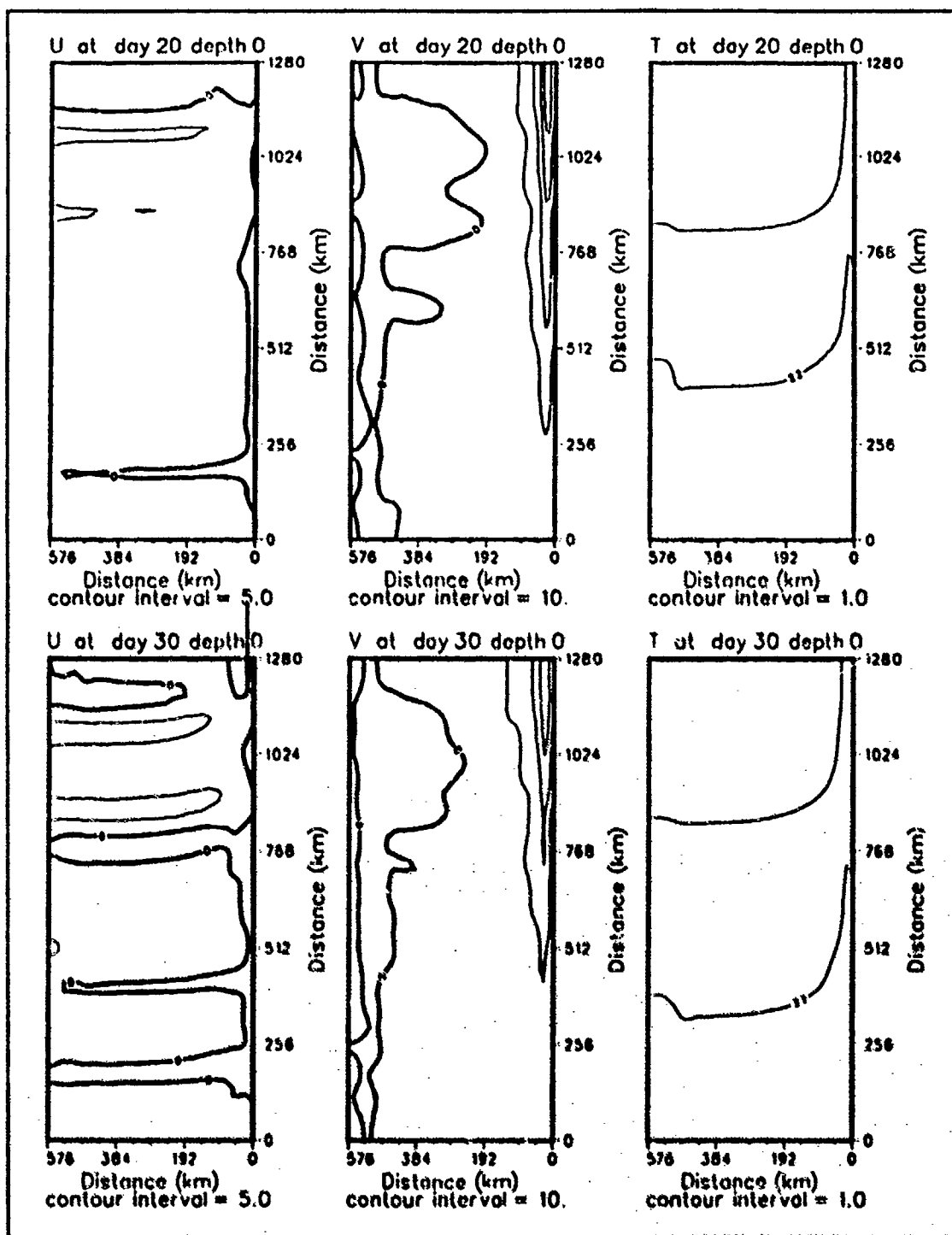


Figure S2. Case 4. Surface velocity and temperature fields, days 20 - 30: As for Figure 81.

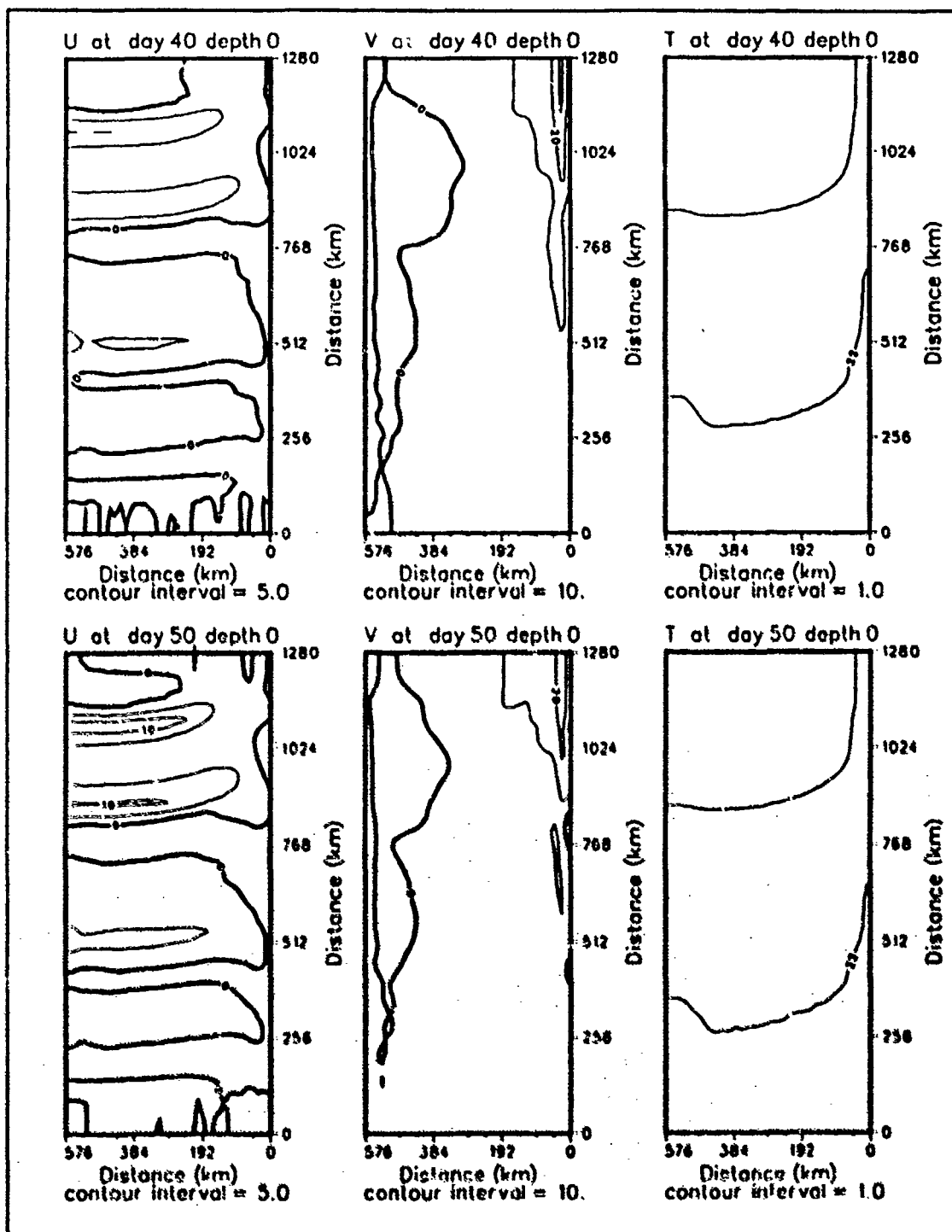


Figure 83. Case 4. Surface velocity and temperature fields, days 40 - 50: As for Figure 81.

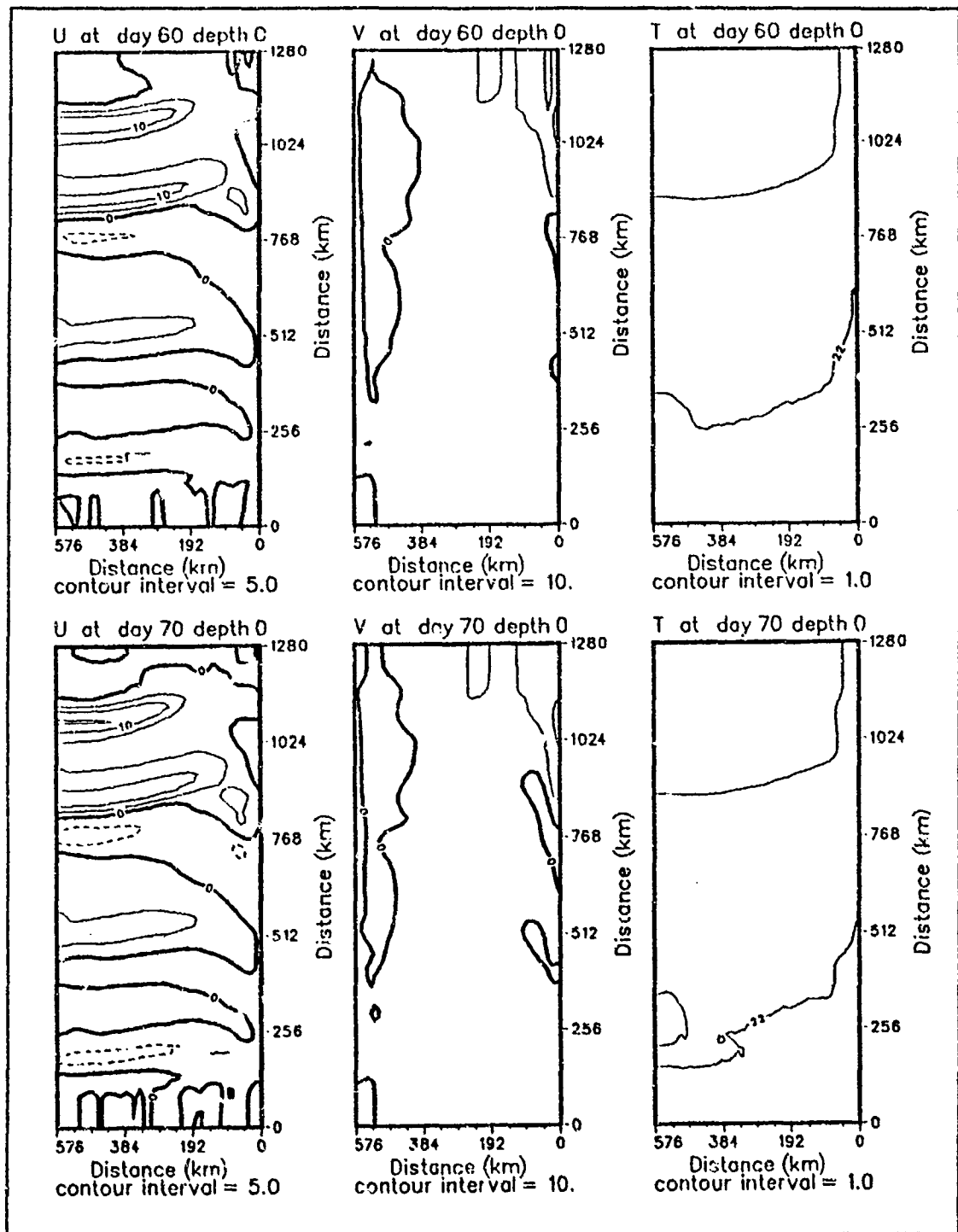


Figure 84. Case 4. Surface velocity and temperature fields, days 60 - 70: As for Figure 81.

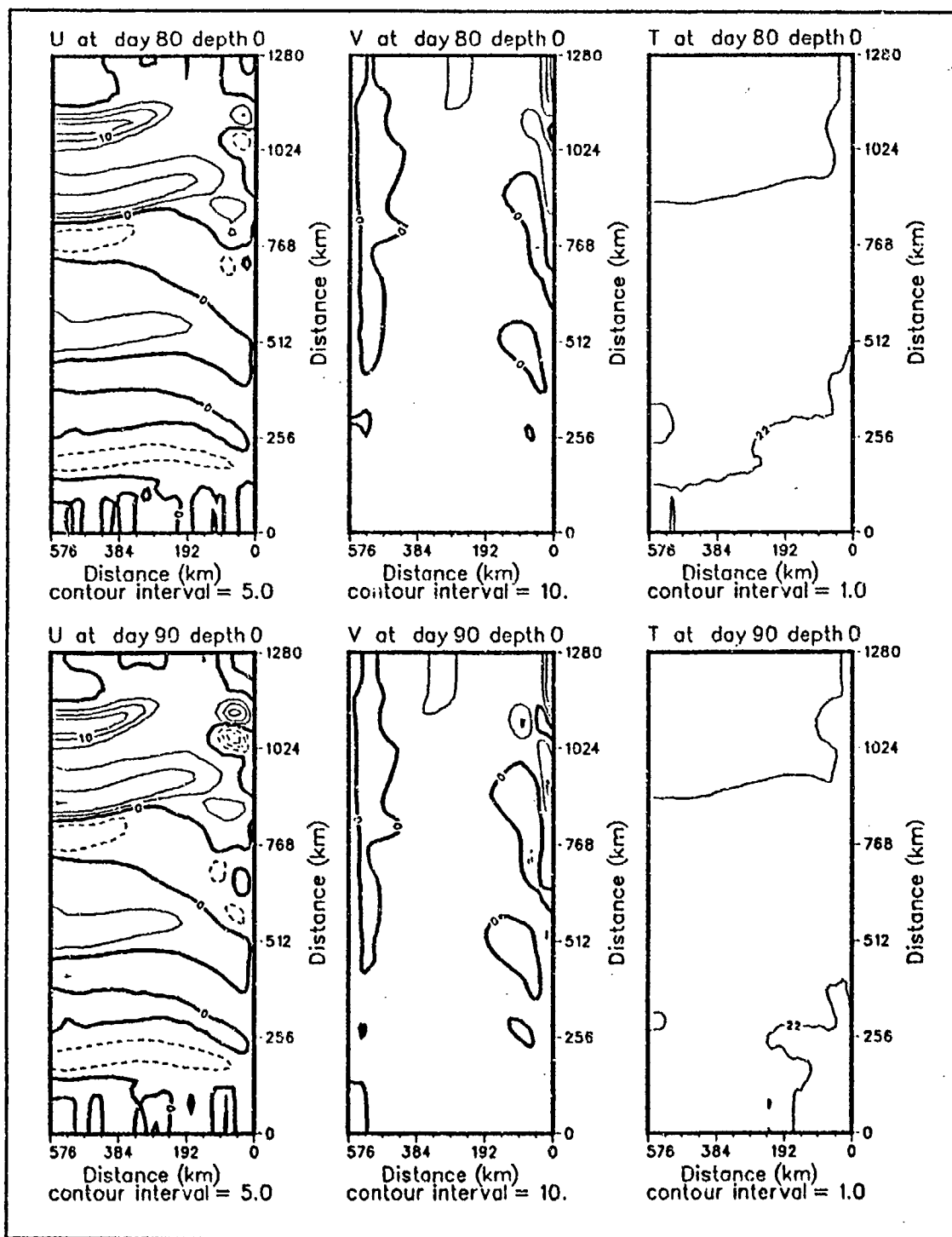


Figure 85. Case 4. Surface velocity and temperature fields, days 80 - 90: As for Figure 81.

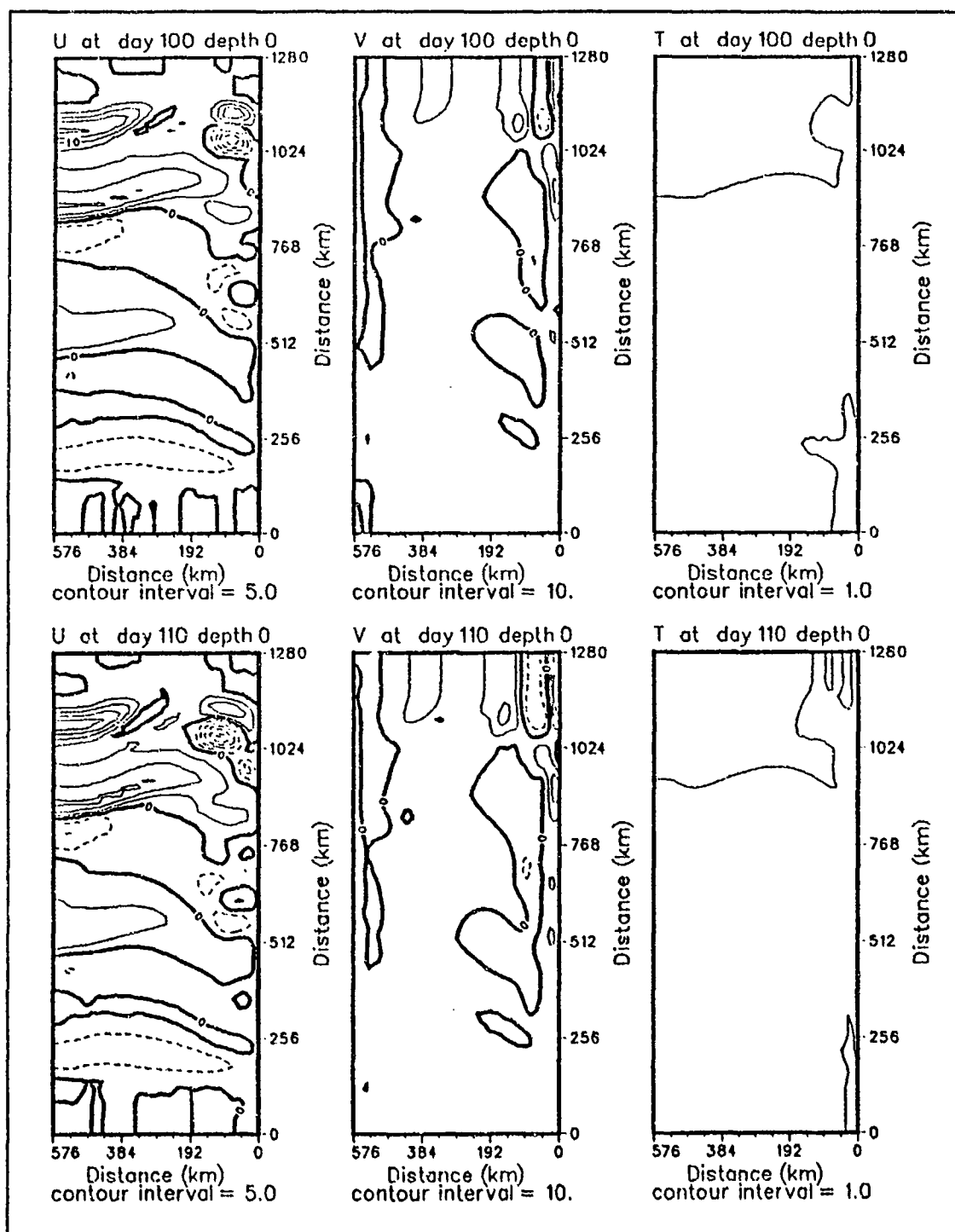


Figure 86. Case 4. Surface velocity and temperature fields, days 100 - 110: As for Figure 81.

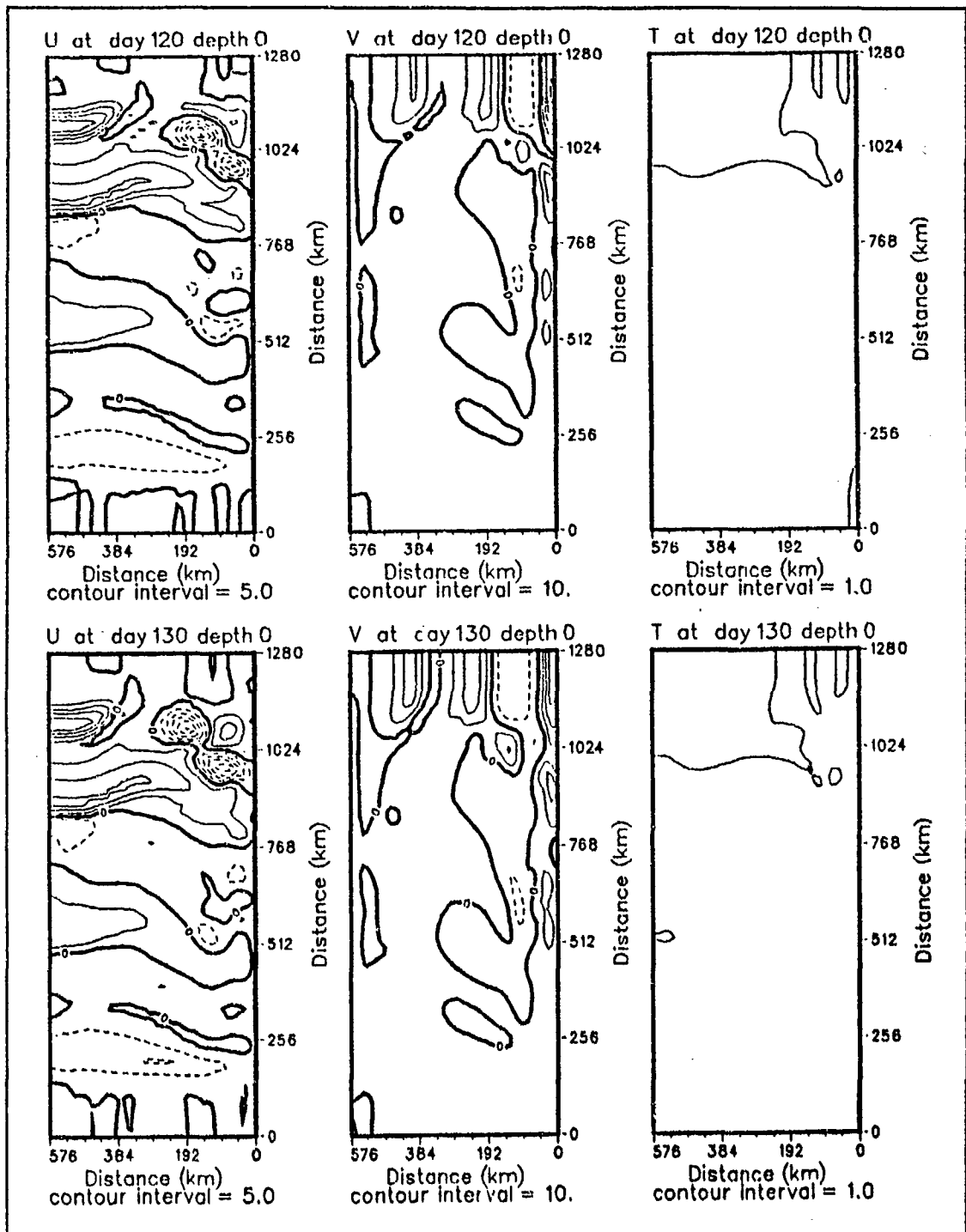


Figure 87. Case 4. Surface velocity and temperature fields, days 120 - 130: As for Figure 81.

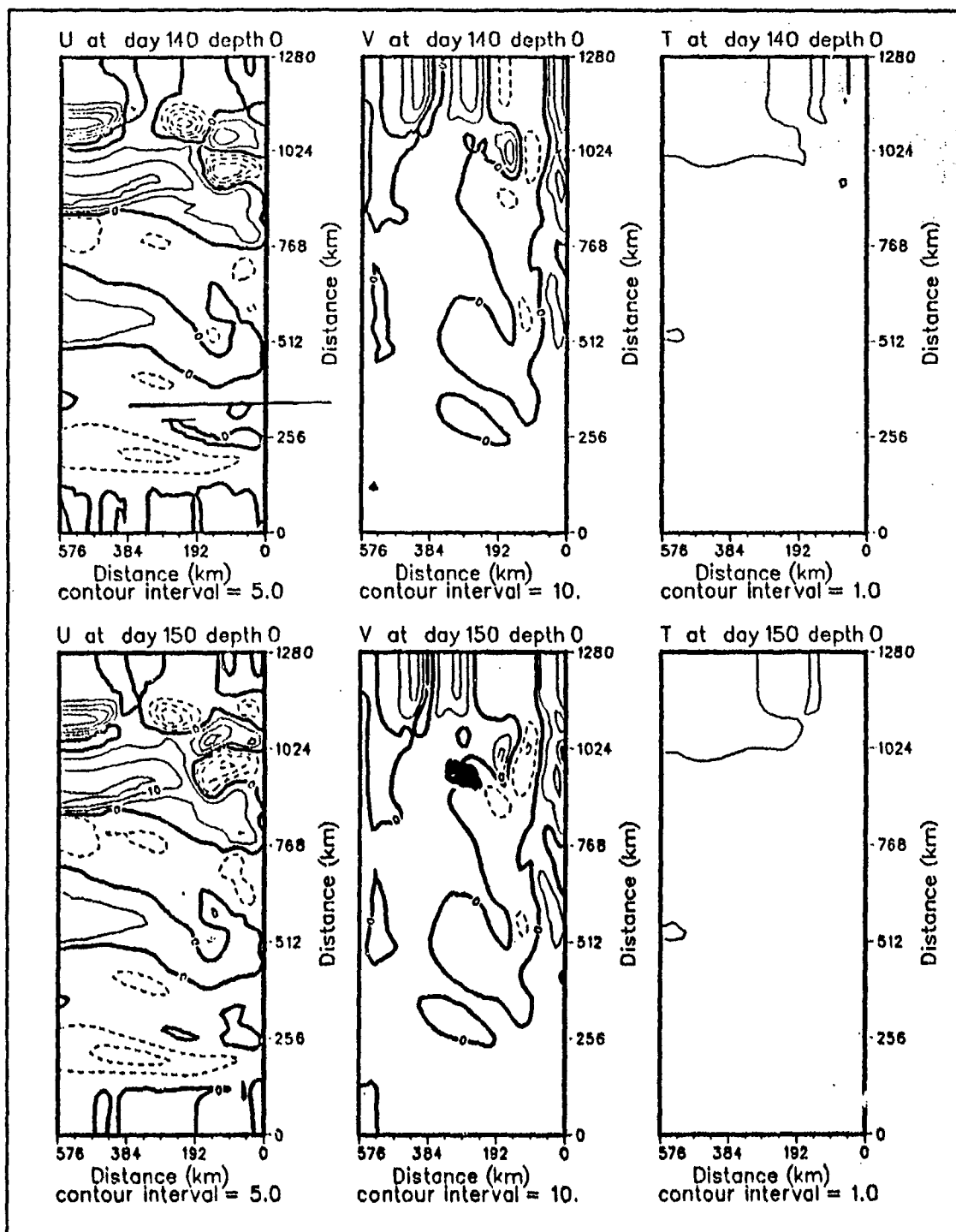


Figure 88. Case 4. Surface velocity and temperature fields, days 140 - 150: As for Figure 81.

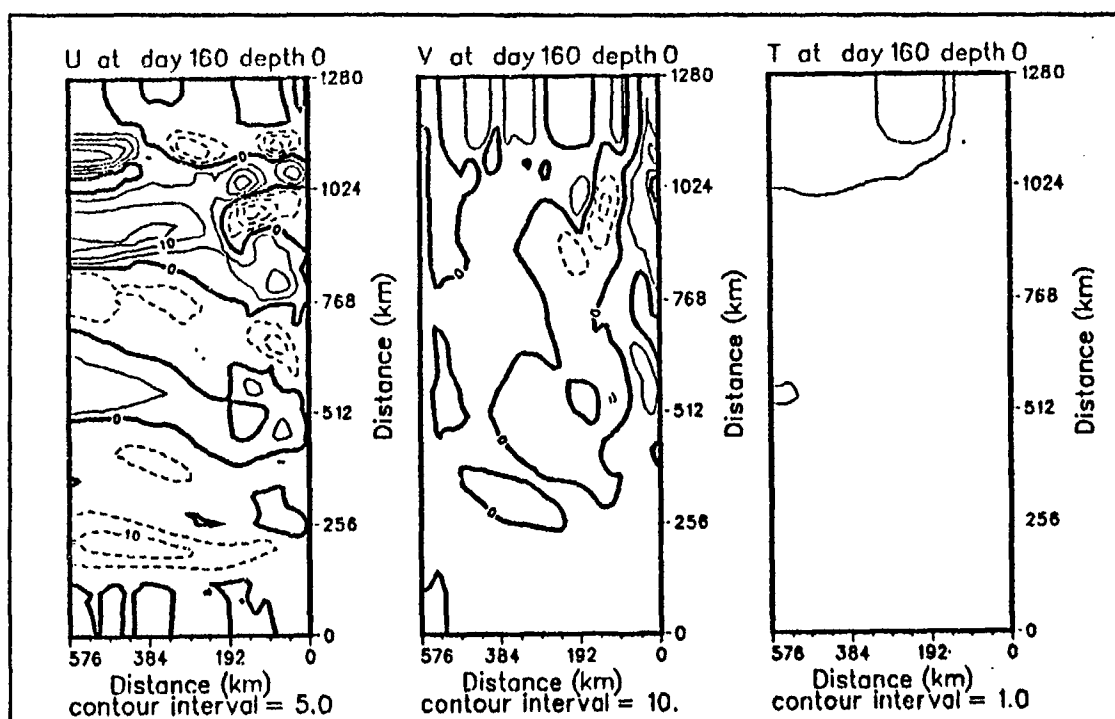


Figure 89. Case 4. Surface velocity and temperature fields, day 160: As for Figure 81.

to occur only inshore whilst barotropic transfers occur both inshore and away from the poleward current.

Two regions were chosen for closer analysis, one between alongshore distances 700 km and 880 km, extending 90 km offshore, and the second between alongshore distances 1000 km and 1180 km, between 180 km and 360 km offshore. From Figure 91, the two regions appear to have different instability mechanisms and they are in different dynamical regions. The first location is associated with the inshore current. The second region is away from the current and affected by the Indian Ocean thermal structure and wind forcing without the presence of the solid boundary. The energy transfer diagrams for each region are shown in Figures 92 (inshore) and 93 (offshore). Consistent with Figure 91, the inshore region is one of mixed instability but with the barotropic transfer dominant. In the offshore region the baroclinic transfer is weakly negative, so that all the instability must be due to barotropic transfer.

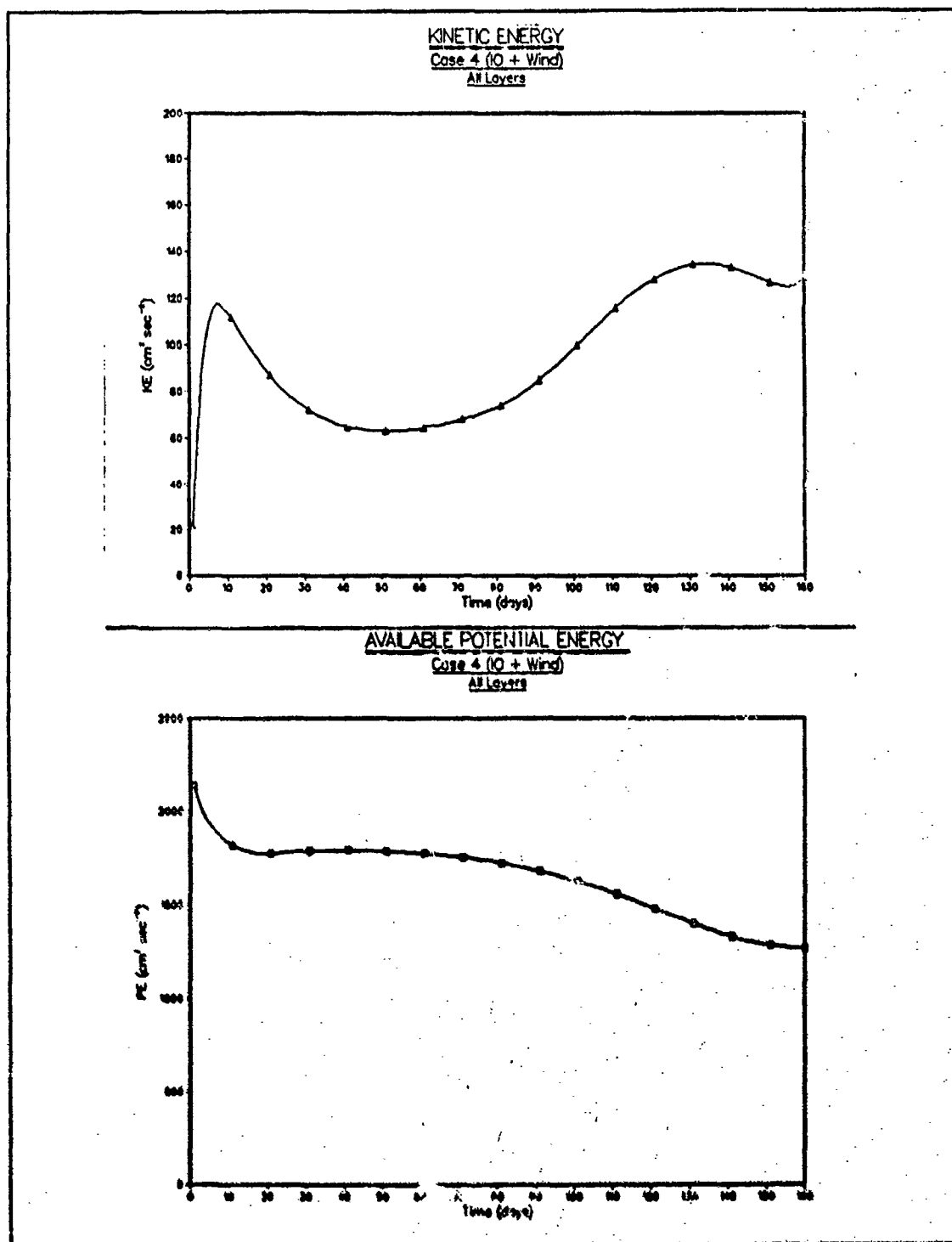


Figure 90. Case 4. Energy time series: Total kinetic and available potential energy summed over all layers and the entire domain. Units are $cm^2 s^{-2}$.

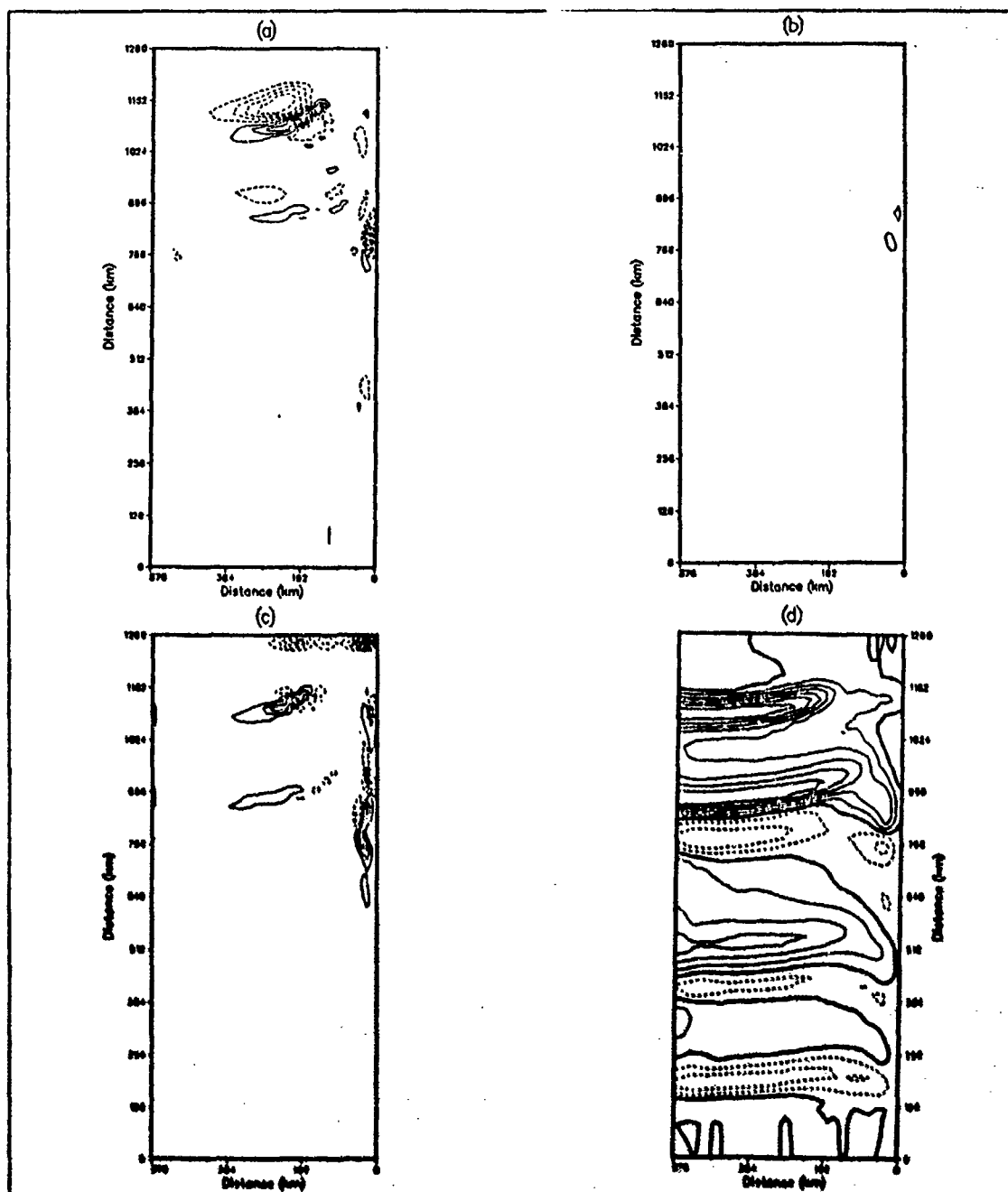


Figure 91. Case 4. Energy transfers: Transfers of energy from (a) \bar{P} to P' , (b) P' to K' and (c) \bar{K} to K' in units of $\text{ergs cm}^{-3} \text{s}^{-1}$. Transfers are averaged over days 40-60 and summed over the upper five layers. Contour interval is $1.6 \times 10^{-3} \text{ ergs cm}^{-3} \text{s}^{-1}$. Subplot (d) is the cross-shore velocity component at day 60. Contour interval for (d) is 2.0 cm s^{-1} .

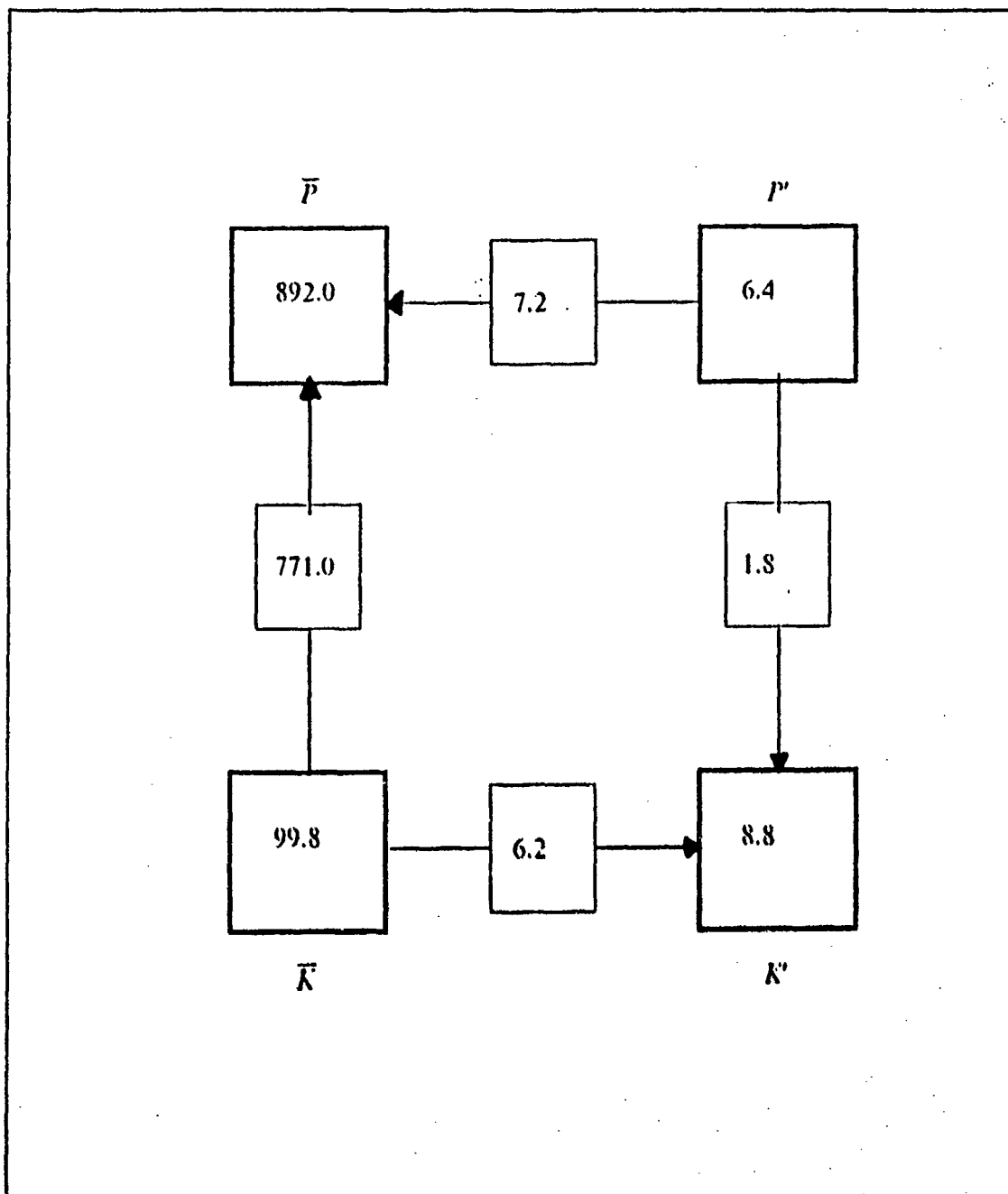


Figure 92. Case 4. Energy transfer diagram: The energy transfer diagram for upper five layers for the region between alongshore distances 700 km and 880 km, extending 90 km offshore. Units for \bar{P} , \bar{K} , P' and K' are ergs cm^{-3} , and transfers are in units of $\text{ergs cm}^{-3} \text{s}^{-1} \times 10^{-4}$.

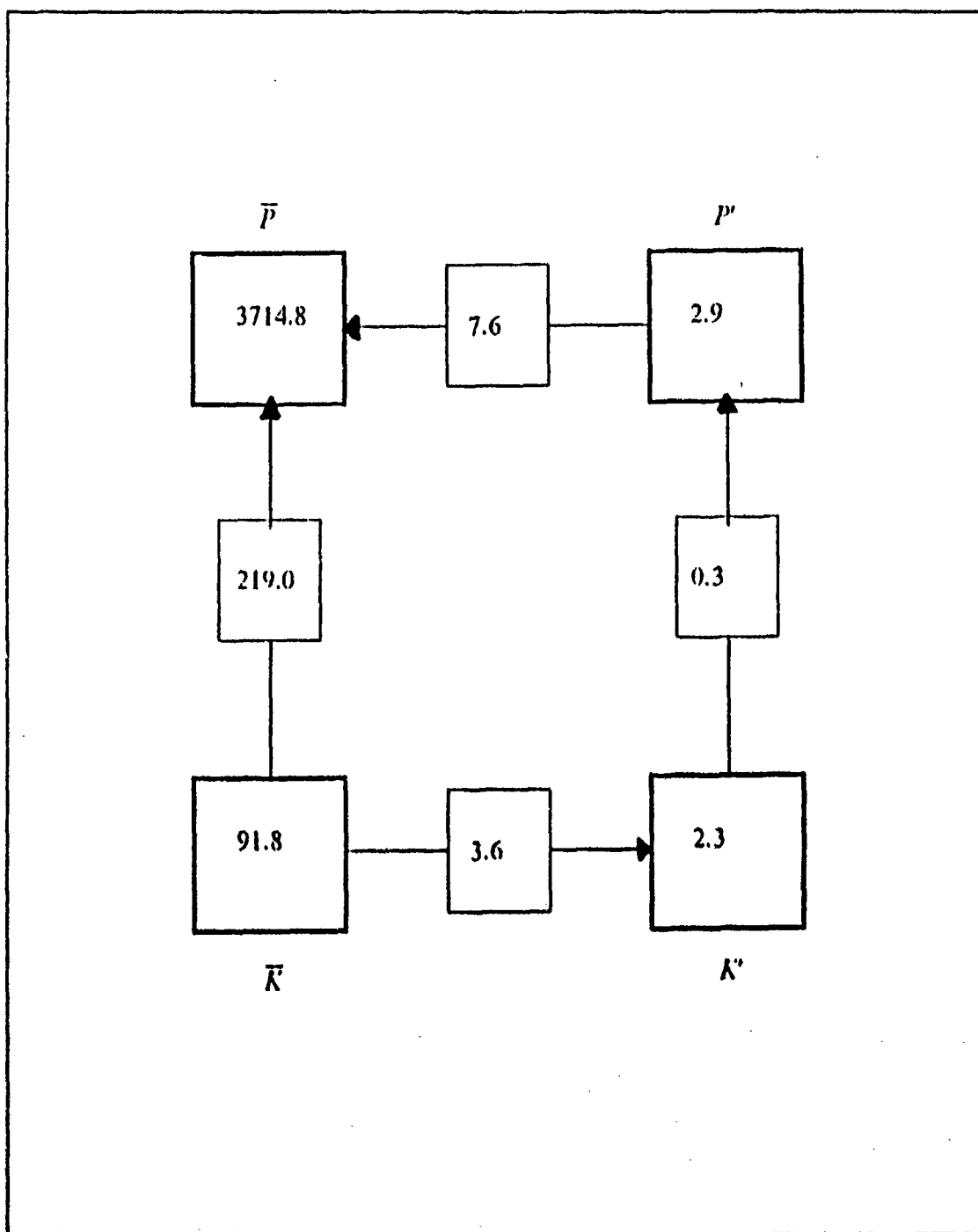


Figure 93. Case 4. Energy transfer diagram: As for Figure 92 for the region between 1000 km and 1180 km alongshore and extending from 180 km to 360 km offshore.

b. Spectral Analysis

Plots of spectral density against alongshore wavenumber for days 40, 50 and 60 are shown in Figures 94, 95 and 96 respectively. The plots show a number of distinct energy peaks, the major two being a broad peak between centered near 385 km (alongshore wavenumber of $\sim 0.0026 \text{ km}^{-1}$), and a narrower peak at a wavelength near 180 km. (alongshore wavenumber of $\sim 0.0055 \text{ km}^{-1}$).

As the energetics appear to be different in the inshore than in the offshore part of the model domain, the time series are presented in several figures. Figure 97 shows the spectra over the entire domain, Figure 98 over only the inshore 90 km corresponding to the current, and Figure 99 the offshore region not included in Figure 98. Over the entire model domain (Figure 97), two dominant wavelengths at which growth occurs are observed, one near 385 km and the second at approximately 180 km. In the inshore domain (Figure 98), both peaks are discernable but the 385 km wavelength is dominant and the 180 km wavelength is very weak. In the offshore region (Figure 99) both spectral peaks are strong but the longer wavelength is still the strongest.

A comparison may now be made with Case 2 in which a single dominant growth scale of around 150 km was observed. The addition of wind forcing, in the absence of the NW Shelf waters, leads to a new scale at which eddies develop in the current of approximately 385 km. Away from the poleward flow, the wind forcing leads to eddy growth due to barotropic instability at the shorter wavelength of 180 km.

c. Instability Analysis

Figures 100 and 101 are used to consider the necessary and sufficient conditions and may indicate why no baroclinic instability is observed offshore. Inshore (Figure 100 a), the change of sign in the cross-shore potential vorticity gradient occurs at depths of 400 m to 500 m, with the strongest gradient a distance of 20 km offshore. The corresponding alongshore cross-section has a negative alongshore velocity below 200 m, which, when combined with the cross-shore gradient of potential vorticity meets the second necessary condition of baroclinic instability, given earlier. Figure 100(b) also shows the vertical and horizontal shears in the alongshore flow which provide a source of energy for the instability. For the offshore region, Figure 101(a) shows the change of sign in the cross-shore gradient of potential vorticity extending across the region, generally between 200 m and 500 m. The cross-section of alongshore velocity (Figure 101 b) shows a positive (poleward flow) extending below 1000 m, hence the necessary conditions are satisfied. In considering the sufficient conditions however, the vertical and horizontal shears are both weak. For a purely meridional flow, no critical vertical

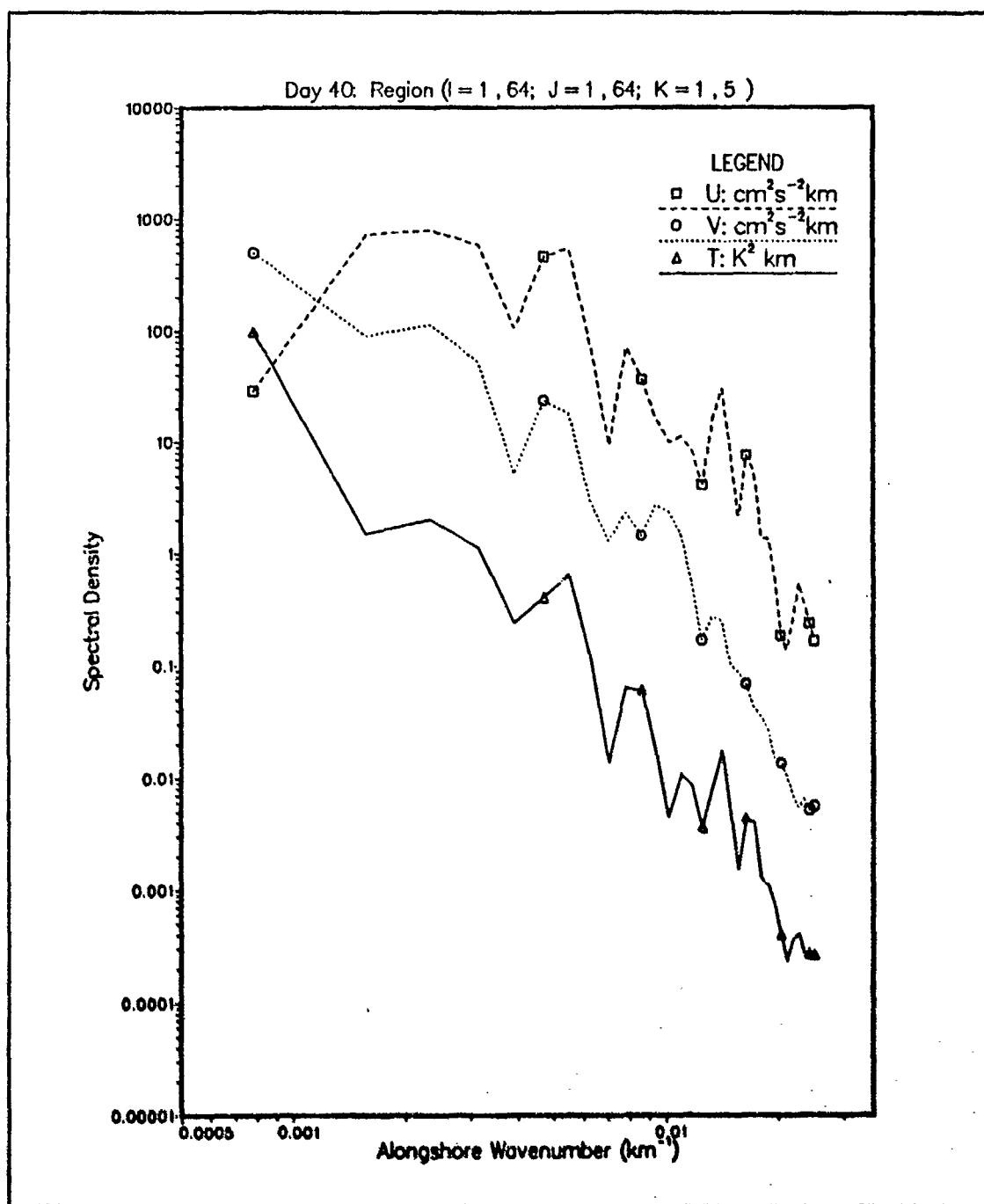


Figure 94. Case 4. Spectral density at day 40: Spectral density versus alongshore wavenumber at day 40. The wavenumber has been scaled by $\frac{1}{2\pi}$ and so is an inverse wavelength. A logarithmic scale is used for the spectral energy.

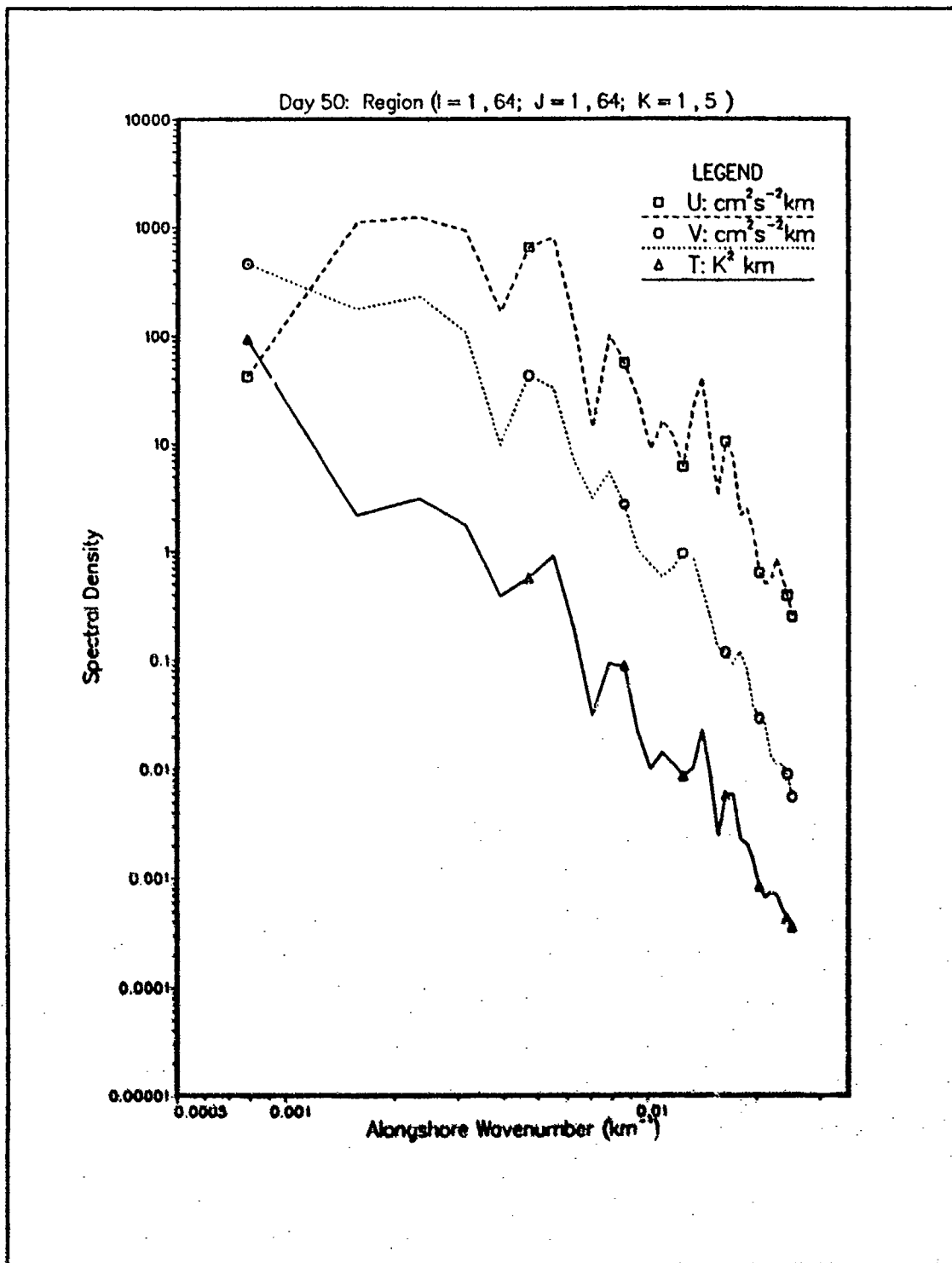


Figure 95. Case 4. Spectral density at day 50: As for Figure 94 but at day 50.

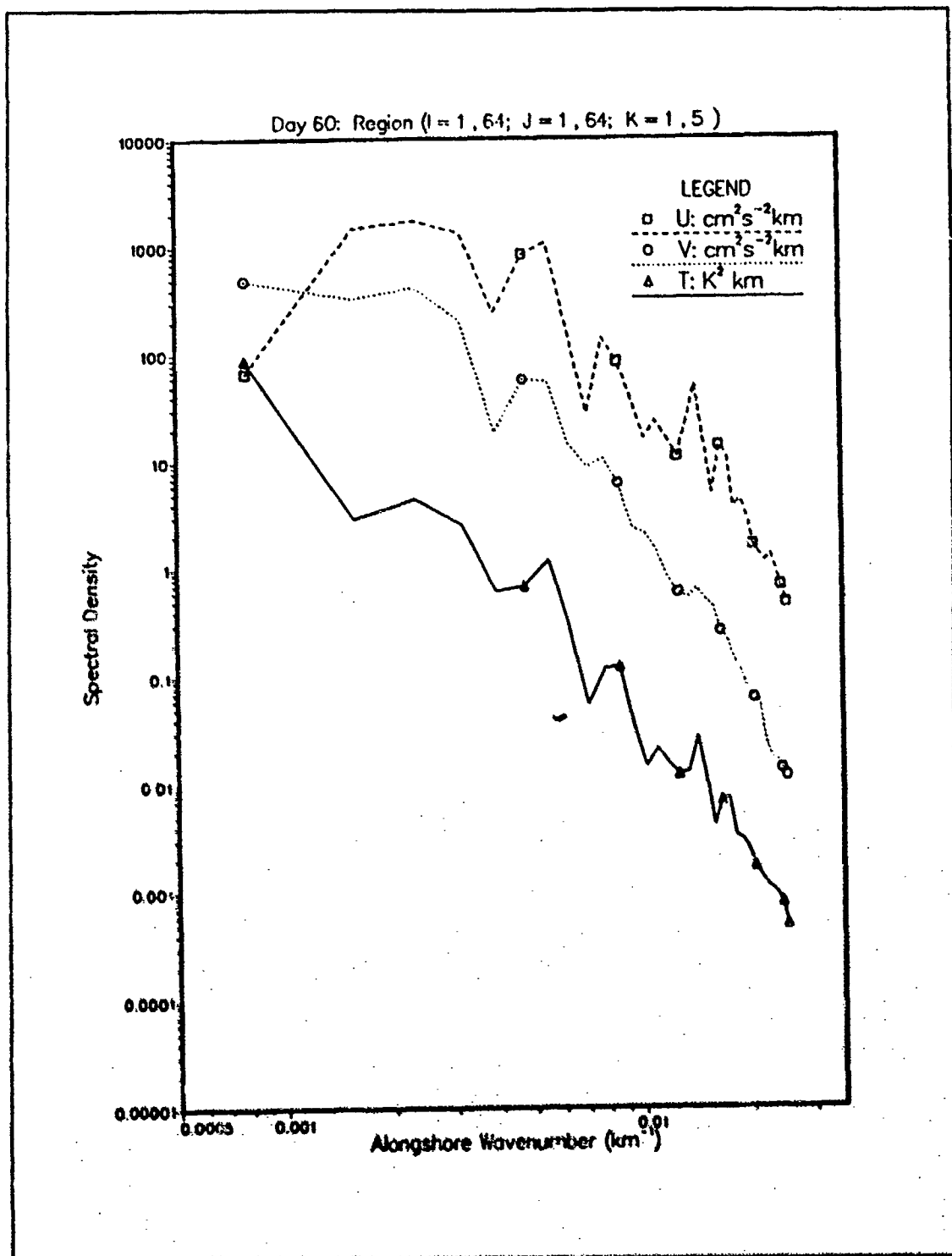


Figure 96. Case 4. Spectral density at day 60: As for Figure 94 but at day 60.

Region $(i = 1, 64; j = 1, 64; k = 1, 5)$

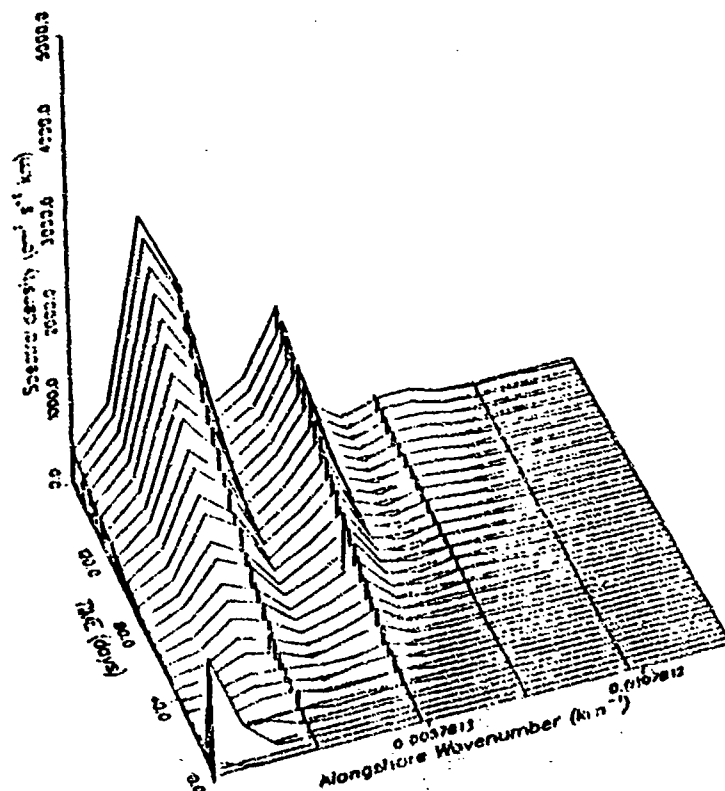


Figure 97. Case 4. Spectral density time series.: The time series of spectral density from days 0 to 160 over the entire domain. Note: the amplitude of the spectral energy is on a linear scale.

Region (I = 55 . 64; J = 1 . 64; K = 1 . 5)

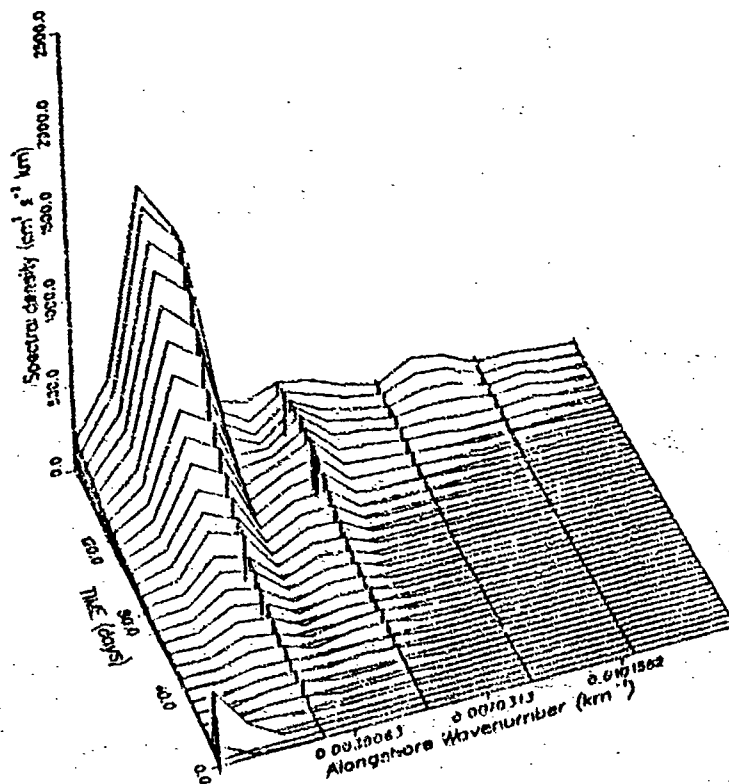


Figure 98. Case 4. Spectral density time series: As for Figure 97 but confined to a domain extending 90 km offshore.

Region ($I = 1.54$; $J = 1.64$; $K = 1.5$)

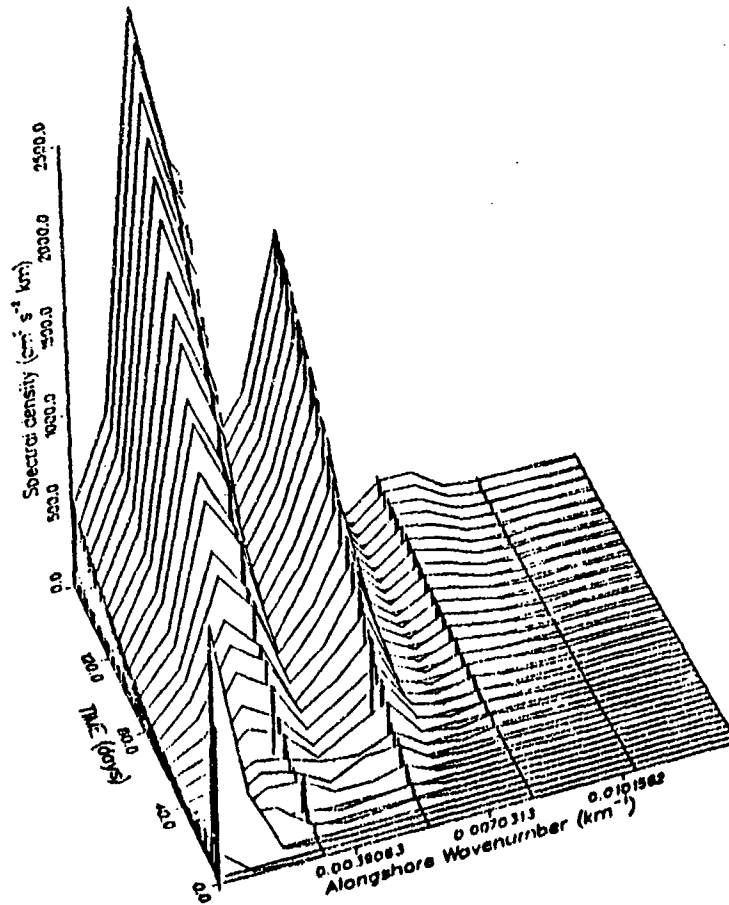


Figure 99. Case 4. Spectral density time series: As for Figure 97. The domain is that region not covered by Figure 97.

shear is required to overcome β (Olivier, 1987), and the sufficient condition for baroclinic instability should be satisfied. It is speculated that the cross-shore component of the mean flow (5 cm s^{-1} to 10 cm s^{-1} from Figures 83 and 84) is sufficiently strong to cause a stabilizing β contribution which the weak vertical shear does not overcome. The Rossby radius of deformation, calculated for the coastal current regime, using the temperature structure at day 50 is 58.4 km.

d. Conclusions

The combination of the Indian Ocean thermal structure and wind forcing in a climatological sense corresponds to the austral spring and summer, when the NW Shelf waters are not augmenting the Leeuwin Current. In this forcing regime, the flow is still unstable, but, without the NW Shelf waters to provide the baroclinicity, barotropic instability is stronger. The model generated eddies in the poleward coastal current are due to mixed instability, at a wavelength of approximately 385 km. This is consistent with growth at $2\pi R_d$ for the Rossby radius of 58.4 km. Offshore, away from the coastal current, wind forcing generates eddies due solely to barotropic instability at a scale of 180 km.

5. Case 5. Forcing by Indian Ocean, NW Shelf and Winds

The 240 day time series of dynamic height isopleths for the combined forcing by the Indian Ocean thermal structure, NW Shelf density structure and wind stress is shown in Figures 102 to 106. A comparison with the cases previously run shows the inshore region where the poleward current is strongest is most like Case 3. Offshore, the wind forcing is dominant and the pressure field is initially most like Case 4.

Figures 107 to 119 present the surface fields of velocity components and temperature for the same time sequence. As in Case 3, the proximity to the source of the NW Shelf water leads to a rapid development of eddies at the equatorward end of the domain. The generation region for the eddies spreads poleward and by day 50 instability is also apparent offshore at the poleward end of the model domain. By day 70 eddies have started to form inshore at the poleward end of the domain, near the location of the initial eddy development seen in Case 2 and Case 4.

Comparing Cases 3 and 5, the effect of the wind forcing on the surface temperatures can be seen. The generally lower temperatures in Case 5 are consistent with the effects of wind forcing seen in the earlier comparison between Cases 2 and 4. With weaker sea surface temperature gradients in Case 5, the formation and existence of rings, as seen in Case 3 is far less apparent. Rings are still formed in Case 5 but generally there are fewer closed contours of both temperature and dynamic height, indicating that an

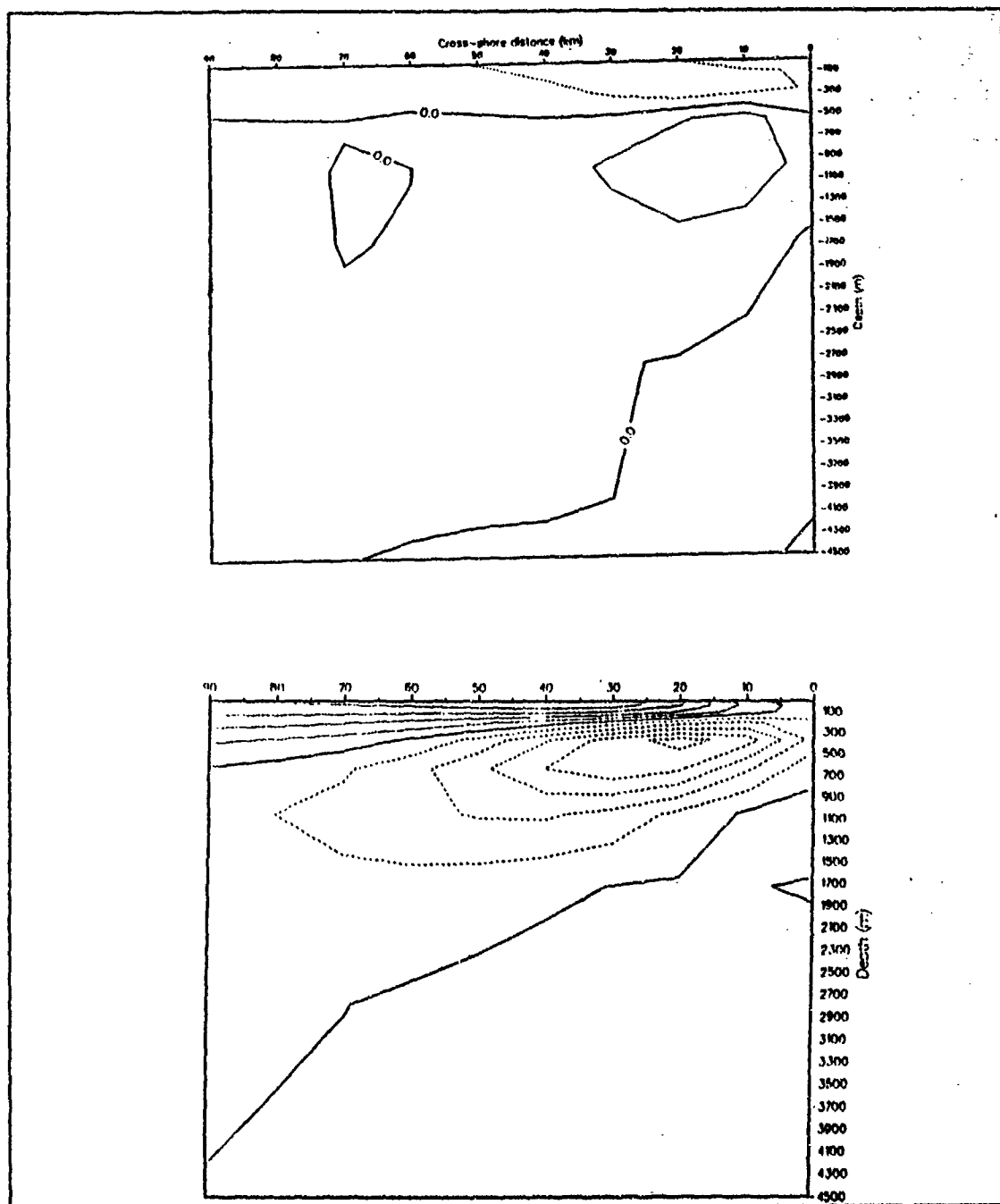


Figure 100. Case 4. Cross sections of dq/dx and alongshore velocity: As for Figure 53. Time averaging is over days 40-60 and the cross-section at alongshore distance 800 km. Contour intervals are (a) $0.1^{\circ}\text{C m}^{-1} \text{s}^{-1}$ and (b) 2.0 cm s^{-1} .

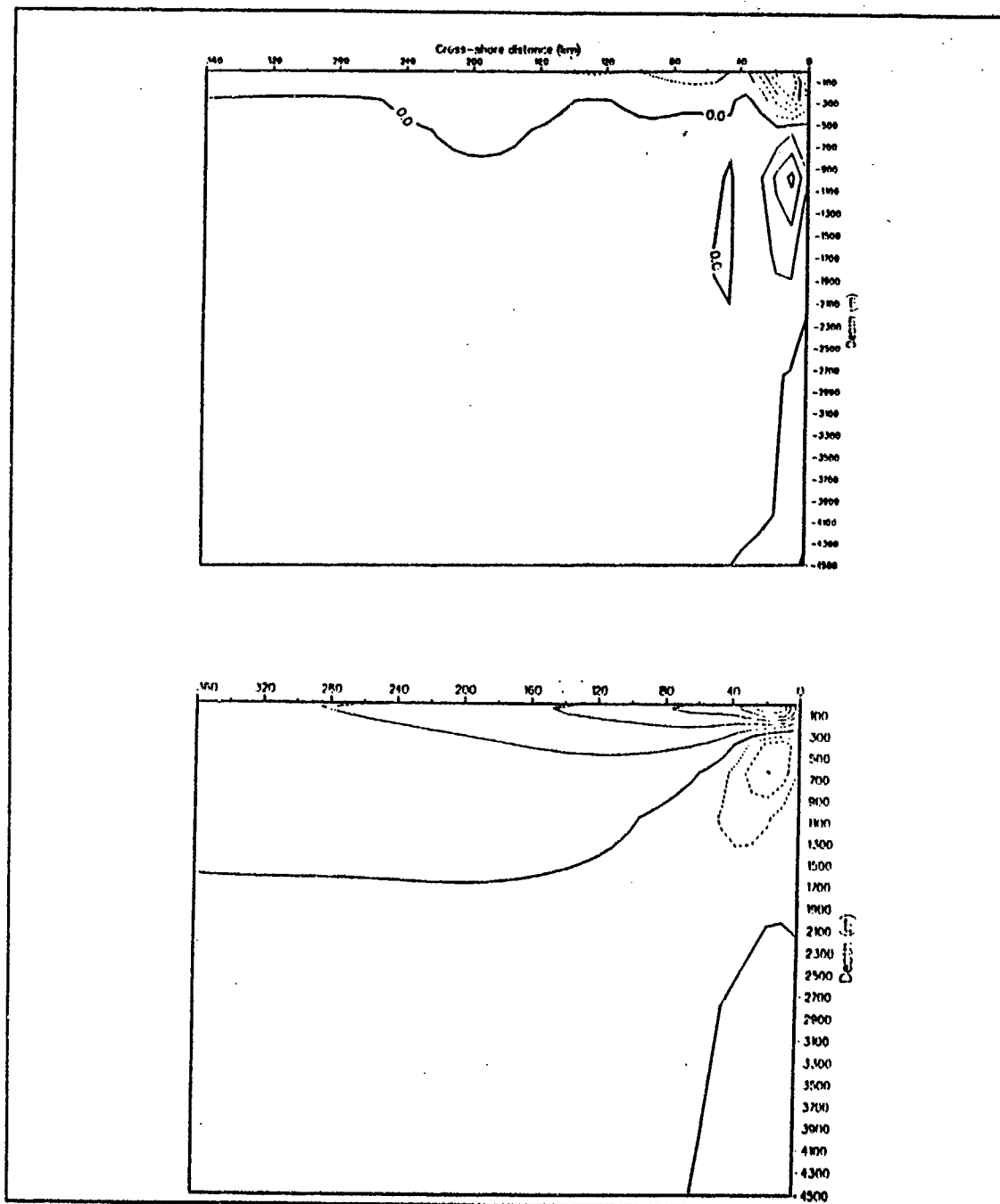


Figure 101. Case 4. Cross sections of dq/dx and alongshore velocity: As for Figure 53. Time averaging is over days 40-60 and the cross-section at alongshore distance 1100 km. Contour intervals are (a) $0.1\text{ }^{\circ}\text{C m}^{-1}\text{ s}^{-1}$ and (b) 4.0 cm s^{-1} .

important effect of the wind forcing is to weaken the eddies through a relaxation of the sea surface temperature gradient.

The narrow band of equatorward alongshore velocity, seen previously in Case 4 is seen again at the poleward end of the domain at day 80. It then grows with time and is associated with a trough on the pressure plots from day 140. At day 240 the alongshore flow at the poleward end of the model, offshore of the narrow coastal current, is generally equatorward. This is consistent with observations, with the wind driven West Australian Current flowing equatorward, and separated from the poleward flowing Leeuwin Current by an active trough. Whether this feature is due to the forcing mechanisms or whether the model has captured another observed feature of the current is undetermined. A possible explanation is that as the temperature structure is an initialization only and the wind forcing applied at each time step, the wind forcing is beginning to overwhelm the flow generated by the temperature initializations as time increases. This would explain why the feature is only observed in Cases 4 and 5, in which wind forcing is included.

a. Energy Analysis

Despite running the experiment out for 240 days, the kinetic energy and available potential energy in Case 5 are still not in a steady state. Examination of their time series in Figure 120 shows several plateau on which the energy analysis may be applied. The periods selected for more detailed analysis are days 30-40 and 60-70. The energy transfers will be calculated for each period and the regions of energy generation during that period analyzed for their instability mechanisms.

Figure 121 applies to days 30 to 40 and is very similar to Figure 46 discussed earlier in Case 2. The influence of the NW Shelf water source region overwhelms the energy transfers further downstream which are contributing to eddy generation. A comparison between the cross-shore velocity fields at days 30 and 40 (Figures 108,109 respectively) is used to determine the region of eddy generation. Figure 122 is the energy transfer diagram for the upper five layers in a region extending 90 km offshore between alongshore distances 460 km and 640 km. The instability has a mixed baroclinic and barotropic energy source with baroclinicity dominant. A comparison of Figures 68 and 122 highlights the effect of the wind forcing on eddy generation in that region of the model. The domains in Cases 3 and 5 are offset by 60 km but the wind forcing appears to have made a significant contribution to the barotropic instability in the region.

Energy transfers for the period from day 60 to day 70 are shown in Figure 123. Once again, the strength of transfers near the source of the NW Shelf water dom-

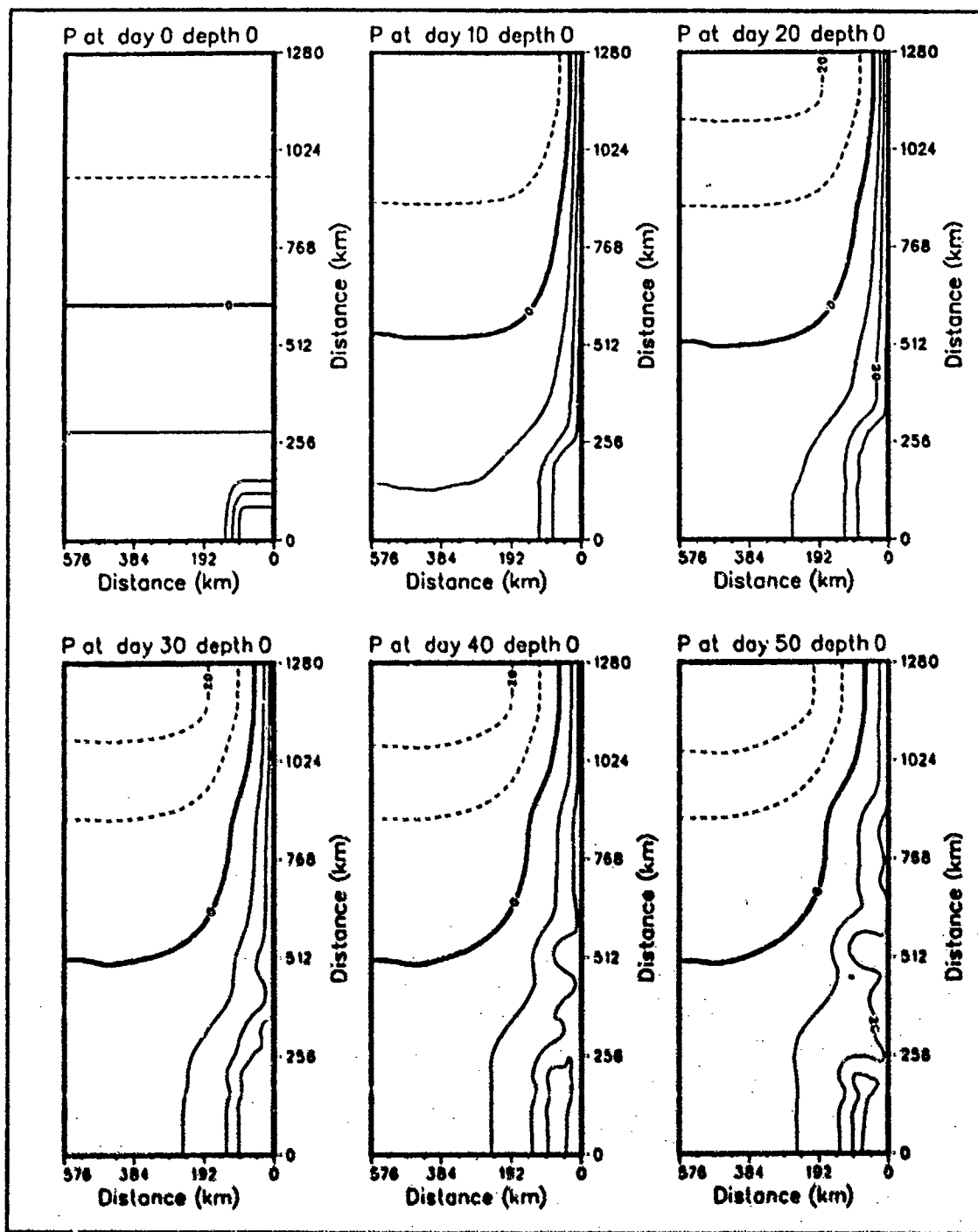


Figure 102. Case 5. Surface pressure field, days 0 - 50: Dynamic height anomaly (cm) at surface relative to a reference level of 2000 m. Contour interval is 5 cm.

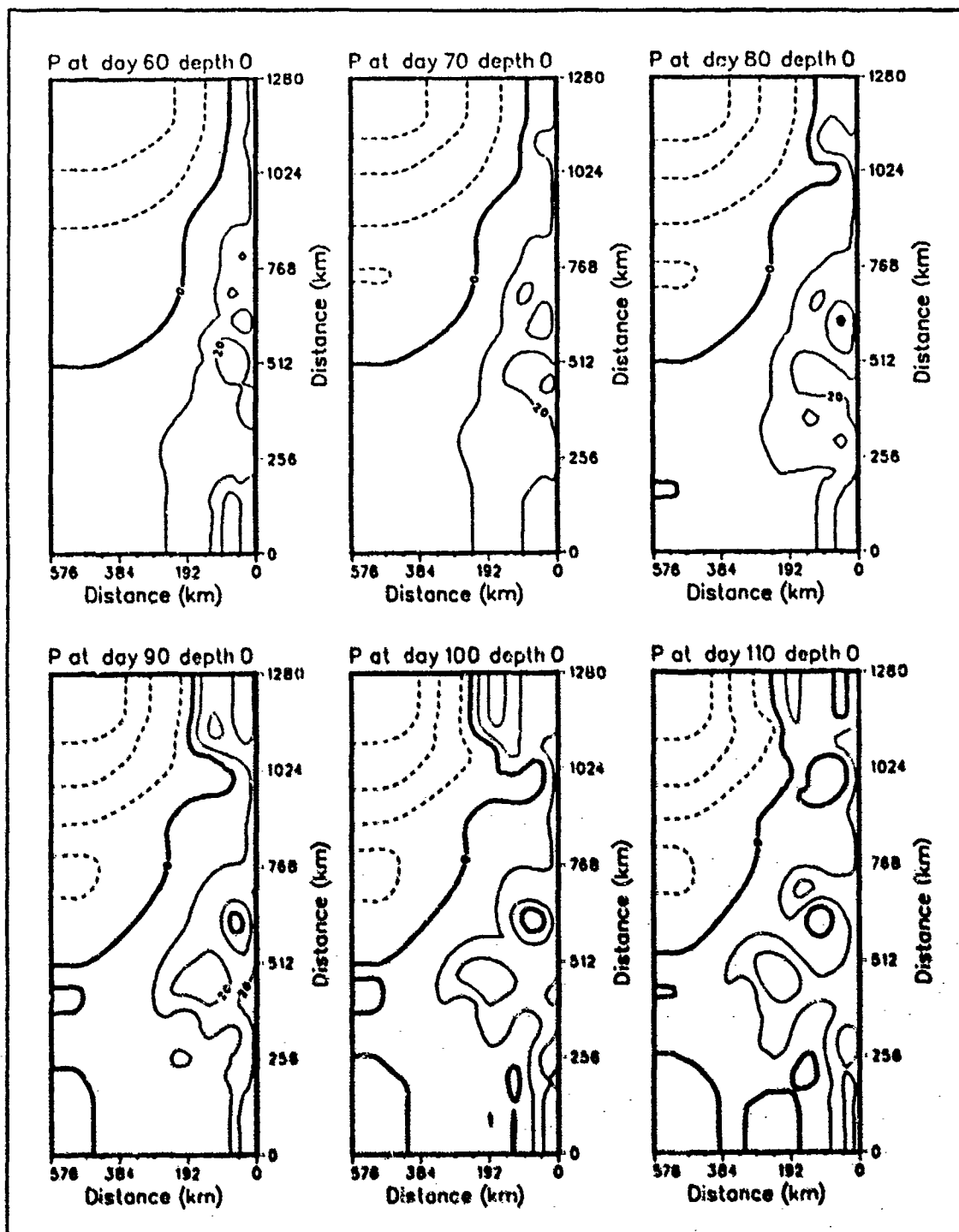


Figure 103. Case 5. Surface pressure field, days 60 - 110: As for Figure 102.

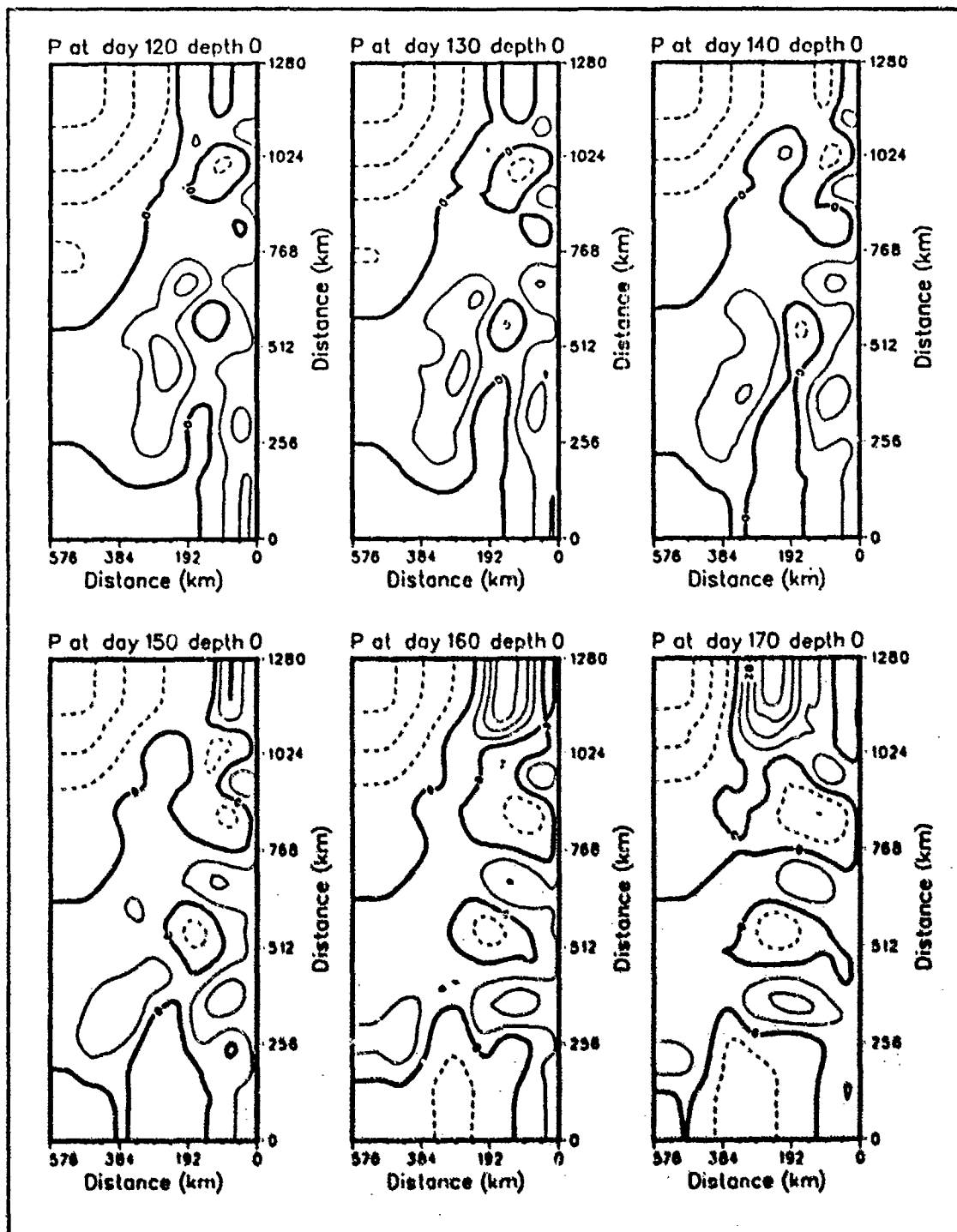


Figure 104. Case 5. Surface pressure field, days 120 - 170: As for Figure 102.

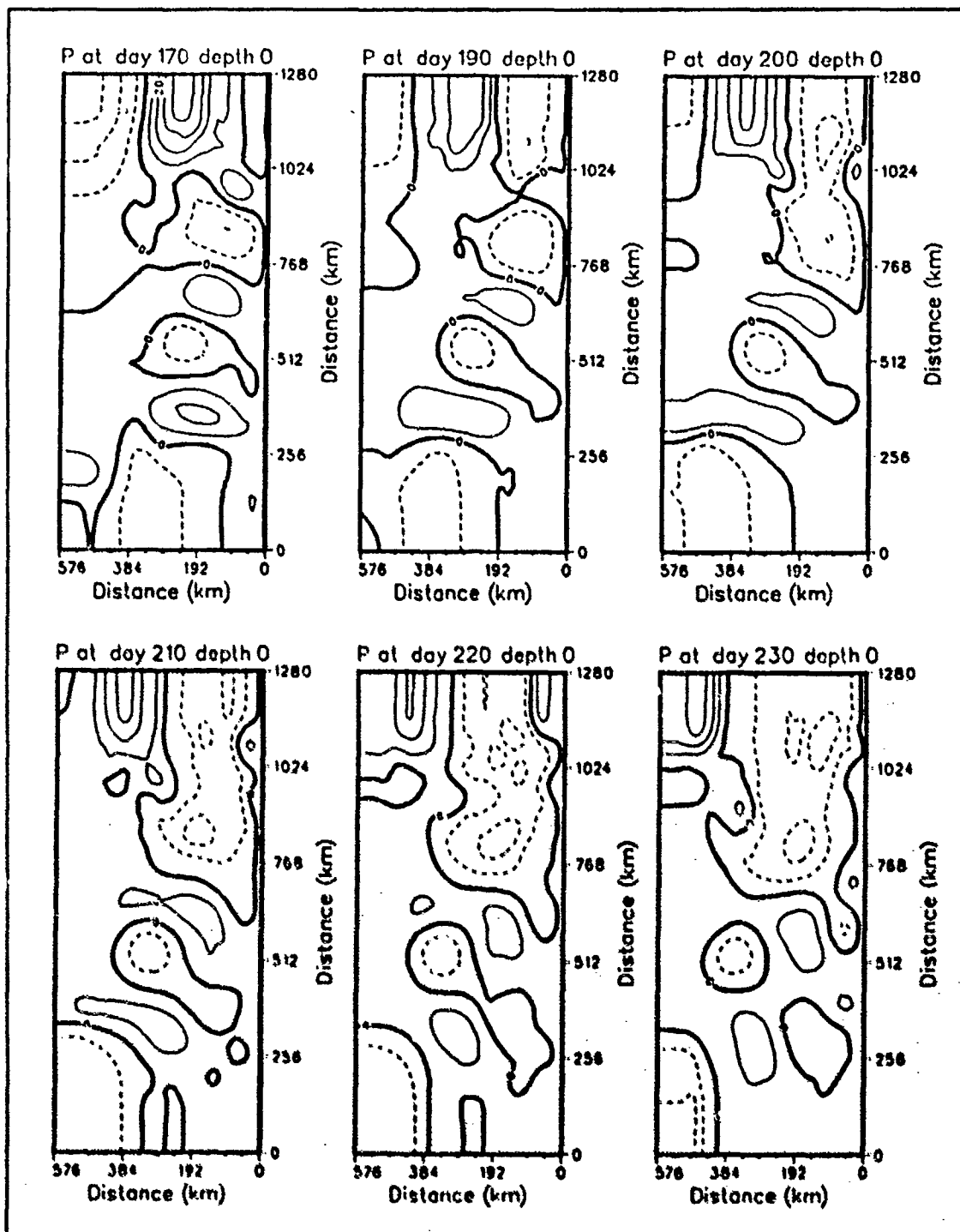


Figure 105. Case 5. Surface pressure field, days 180 - 230: As for Figure 102.

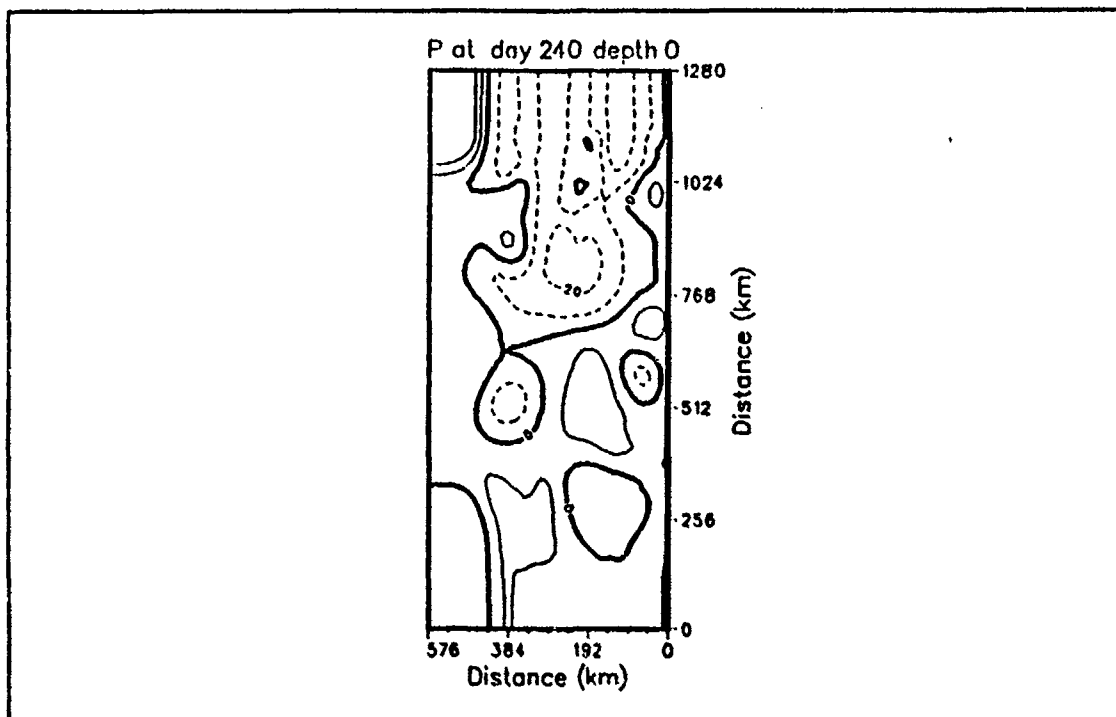


Figure 106. Case 5. Surface pressure field, day 240: As for Figure 102.

inate the contouring and nothing is seen at the poleward end of the region, which is where, according to Figure 110, the eddies are developing. The corresponding energy transfer diagram is in Figure 124. Both baroclinic and barotropic instability are present with barotropic effects dominant. As baroclinicity in this study has generally been associated with the presence of NW Shelf water, the effects of NW Shelf water should be weaker at the poleward end of the current. This is confirmed by the cool temperatures and weak temperature gradients in Figure 110. In the generation discussion earlier in this chapter it was determined that the effects of the geostrophic current driven by the Indian Ocean temperature field are dominant in this region. Figure 47 showed the instability due to the Indian Ocean to be mainly barotropic while Case 4 showed the addition of wind forcing contributed to barotropic instability. The strong barotropic instability in Figure 124 is therefore consistent with earlier findings.

b. Spectral Analysis

The plots of spectral density against alongshore wavenumber for days 30 to 70 covering the two periods of instability are presented in Figures 125 to 129. The spectral peak associated with growth from day 30 (Figure 125) to day 40 (Figure 126) is

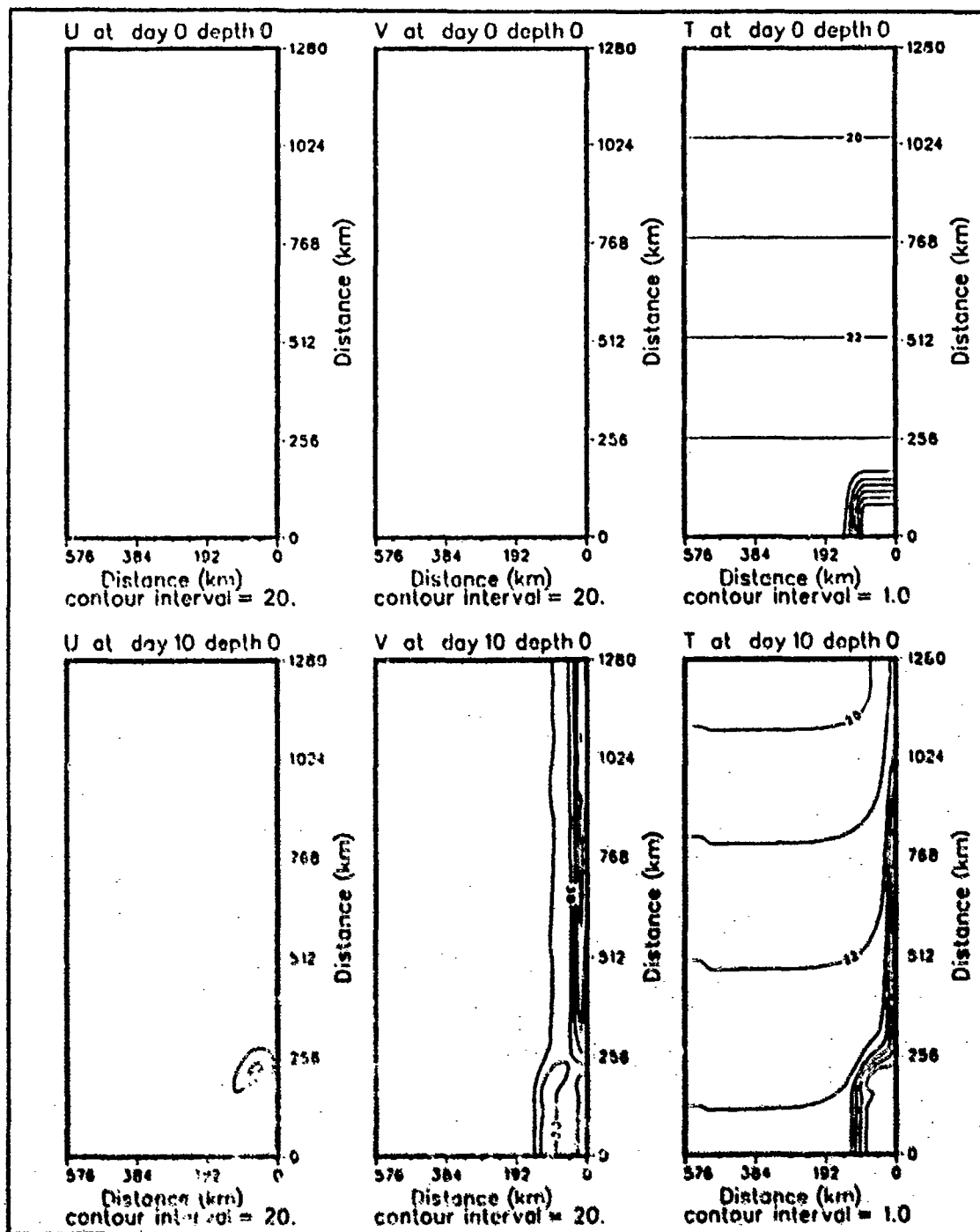


Figure 107. Case 5. Surface velocity and temperature fields, days 0 - 10: Cross-shore velocity component ($cm s^{-1}$), alongshore velocity component ($cm s^{-1}$) and temperature ($^{\circ}C$) at surface.

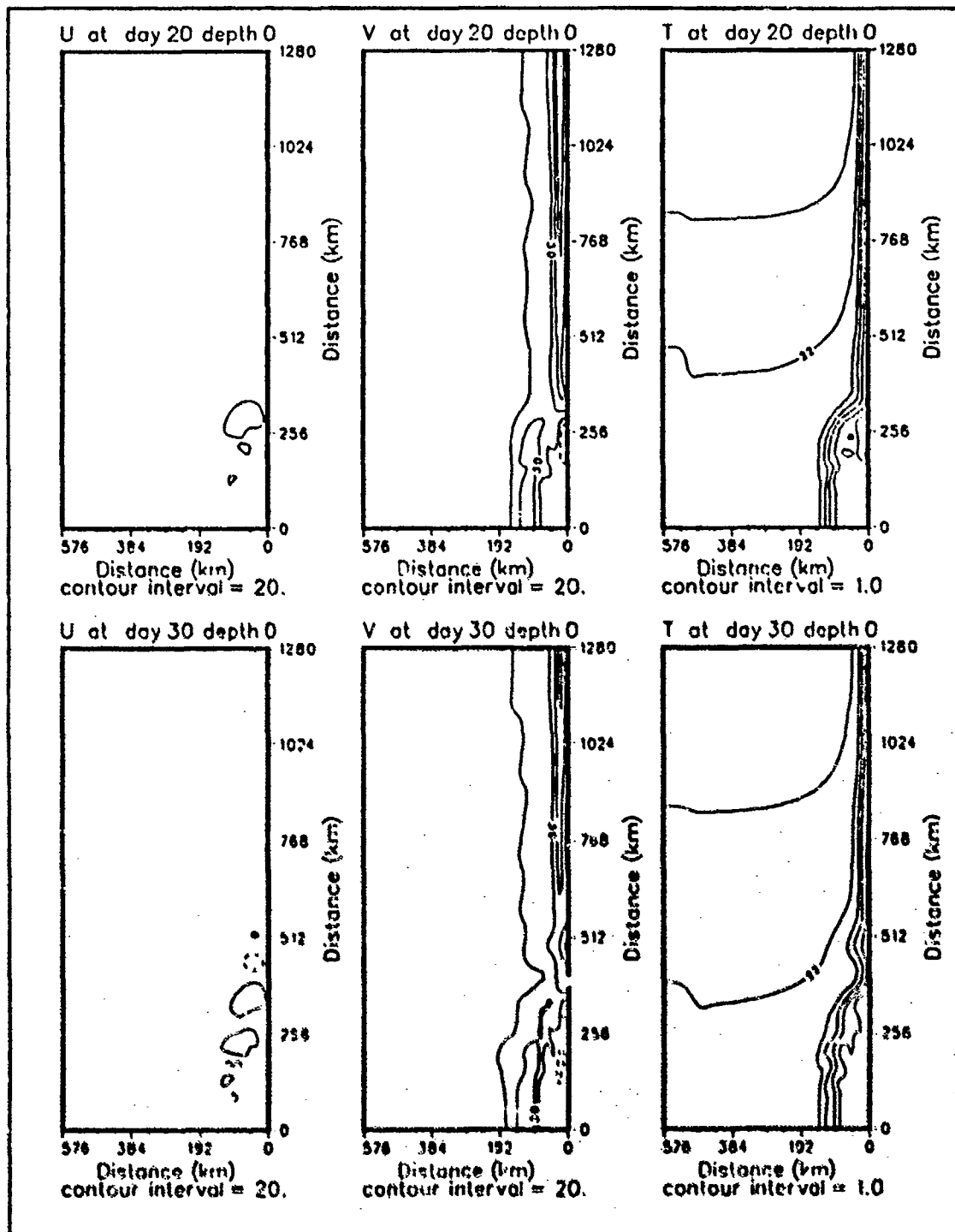


Figure 108. Case 5. Surface velocity and temperature fields, days 20 - 30: As for Figure 107.

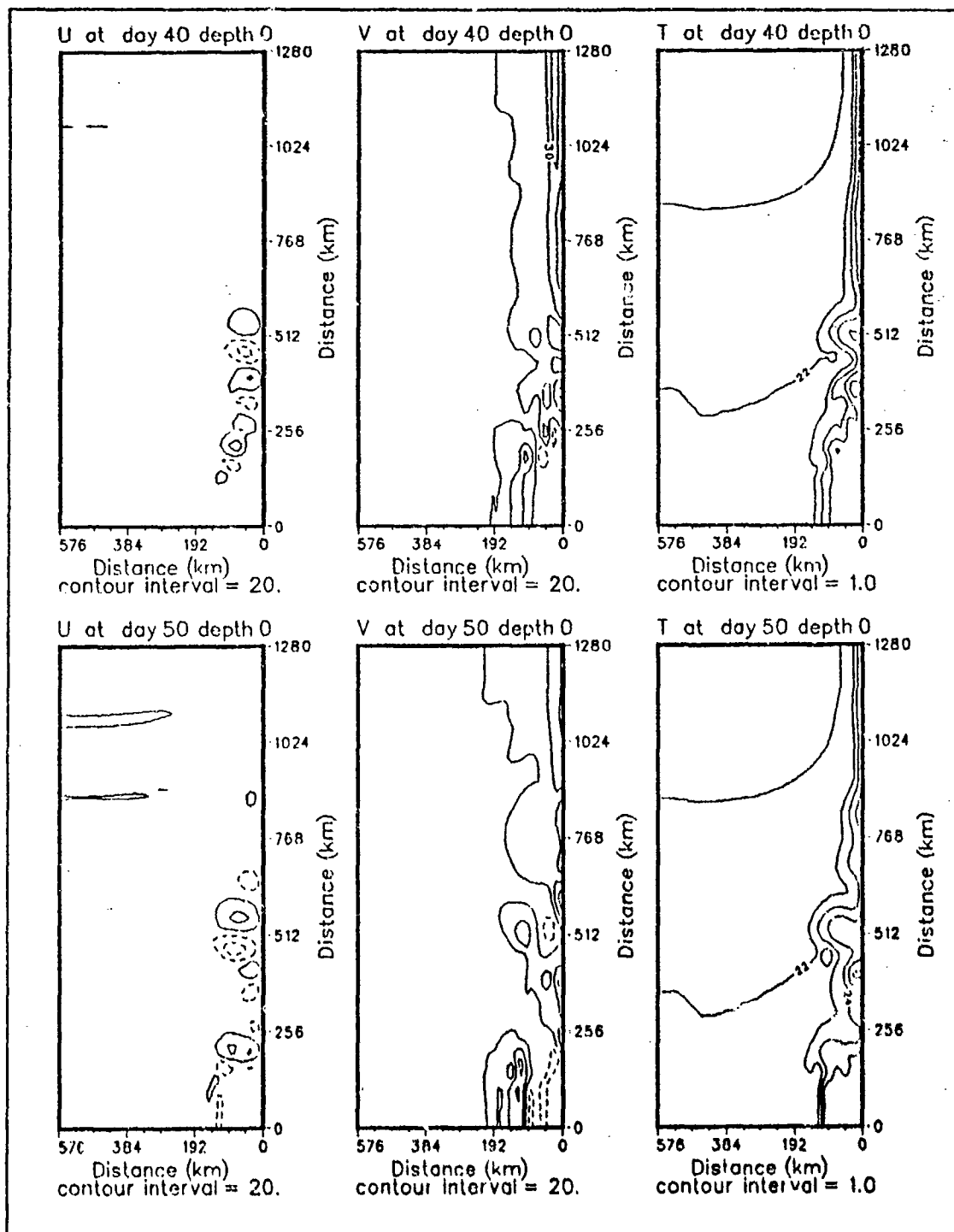


Figure 109. Case 5. Surface velocity and temperature fields, days 40 - 50: As for Figure 107.

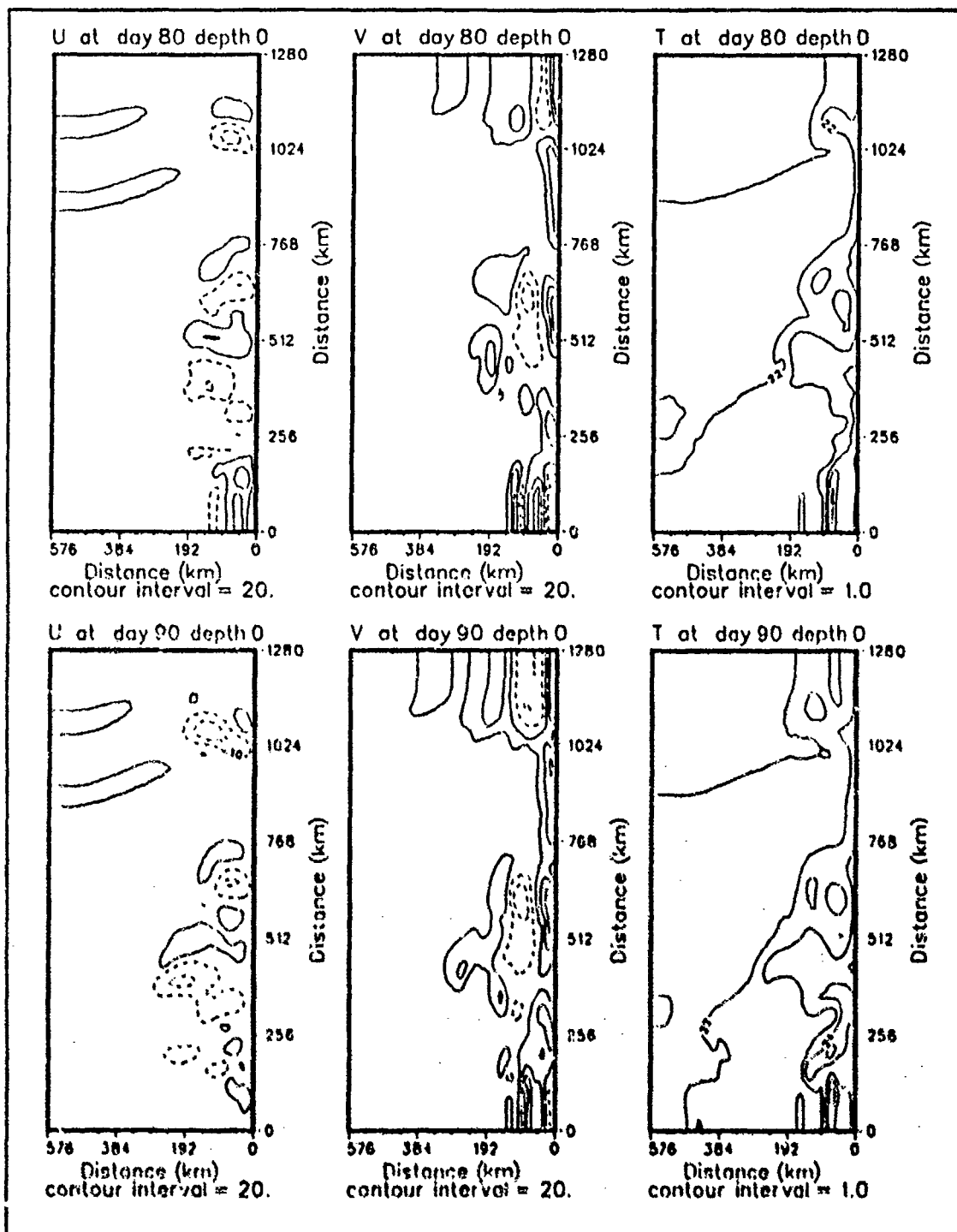


Figure 111. Case 5. Surface velocity and temperature fields, days 80 - 90: As for Figure 107.

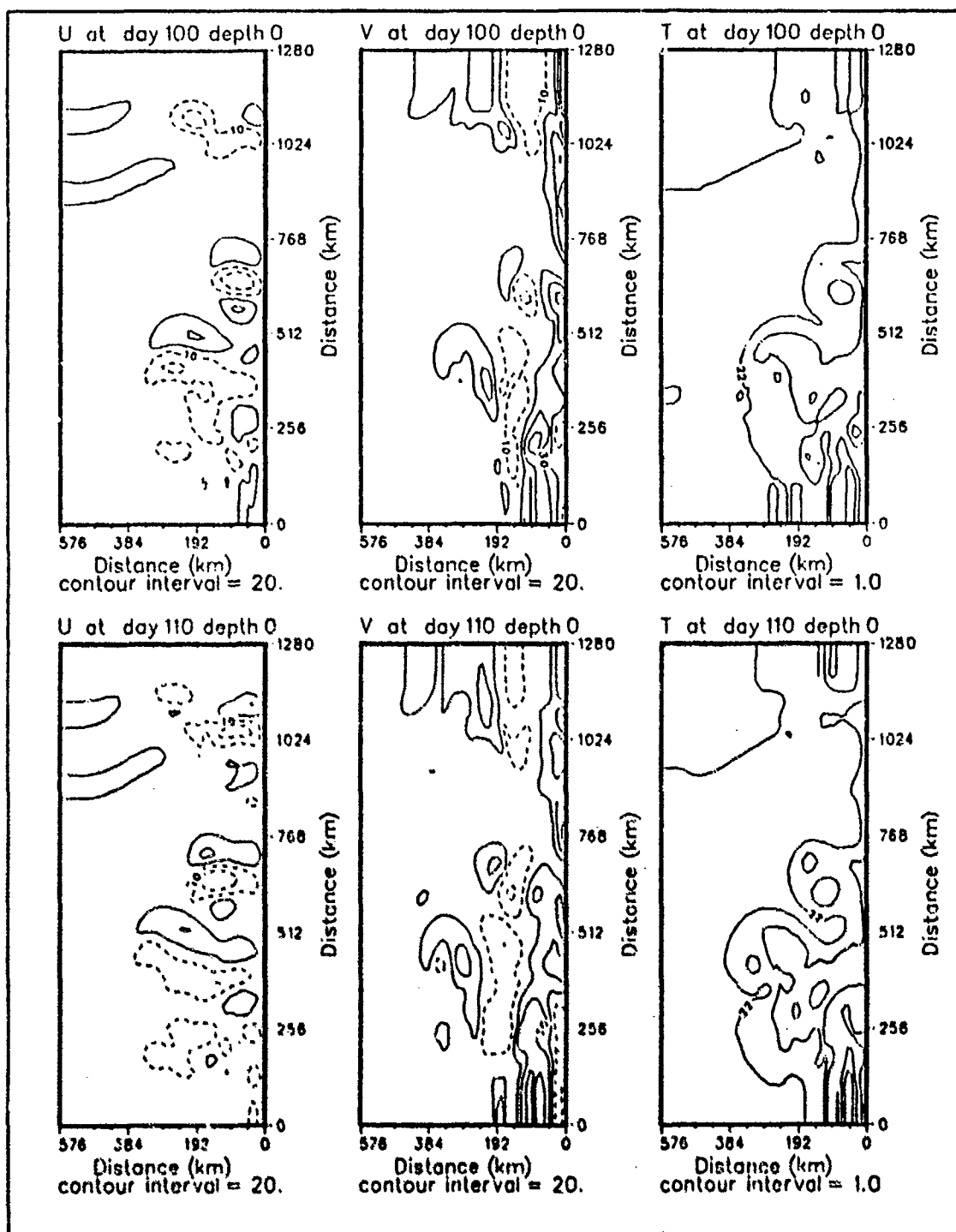


Figure 112. Case 5. Surface velocity and temperature fields, days 100 - 110: As for Figure 107.

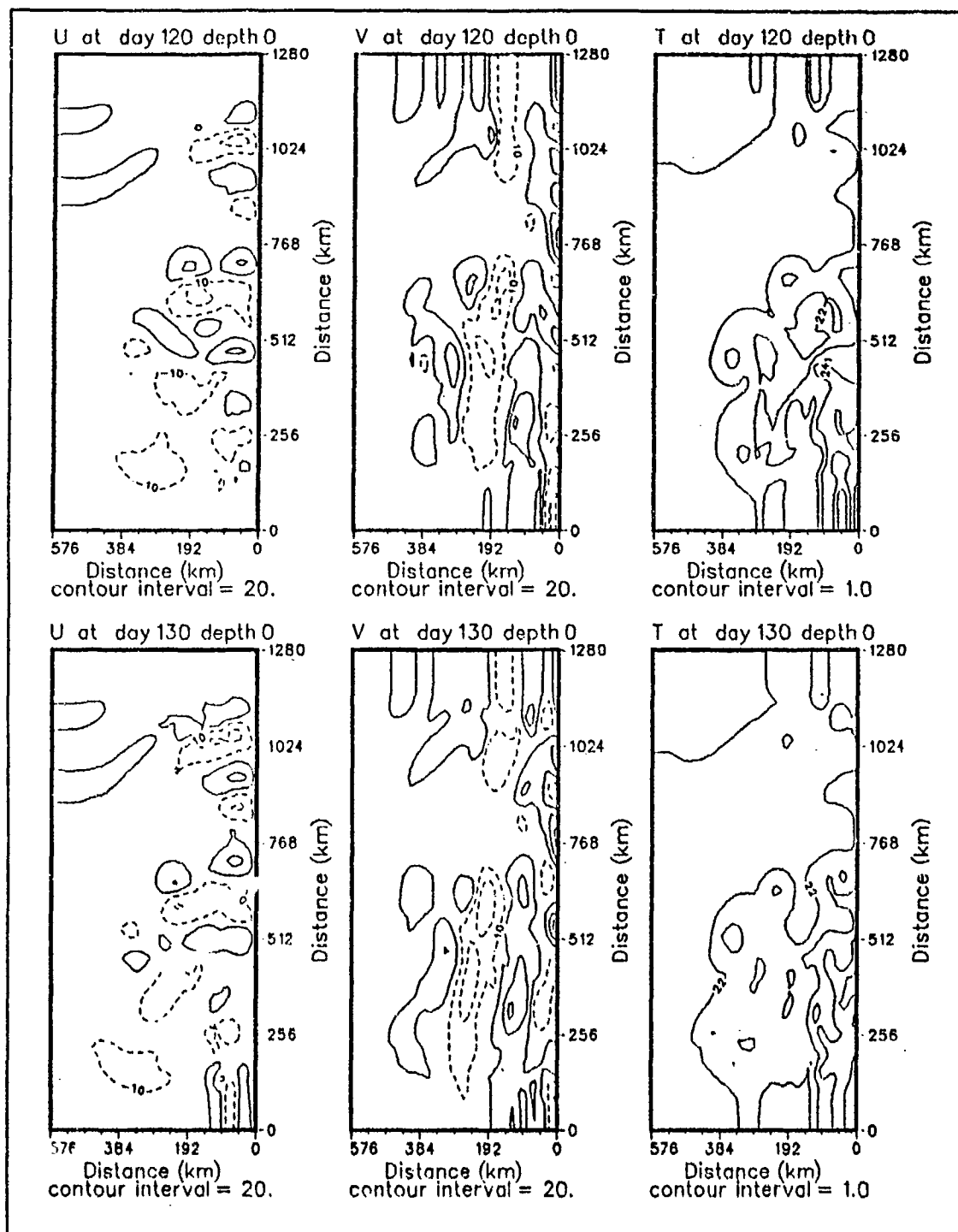


Figure 113. Case 5. Surface velocity and temperature fields, days 120 - 130: As for Figure 107.

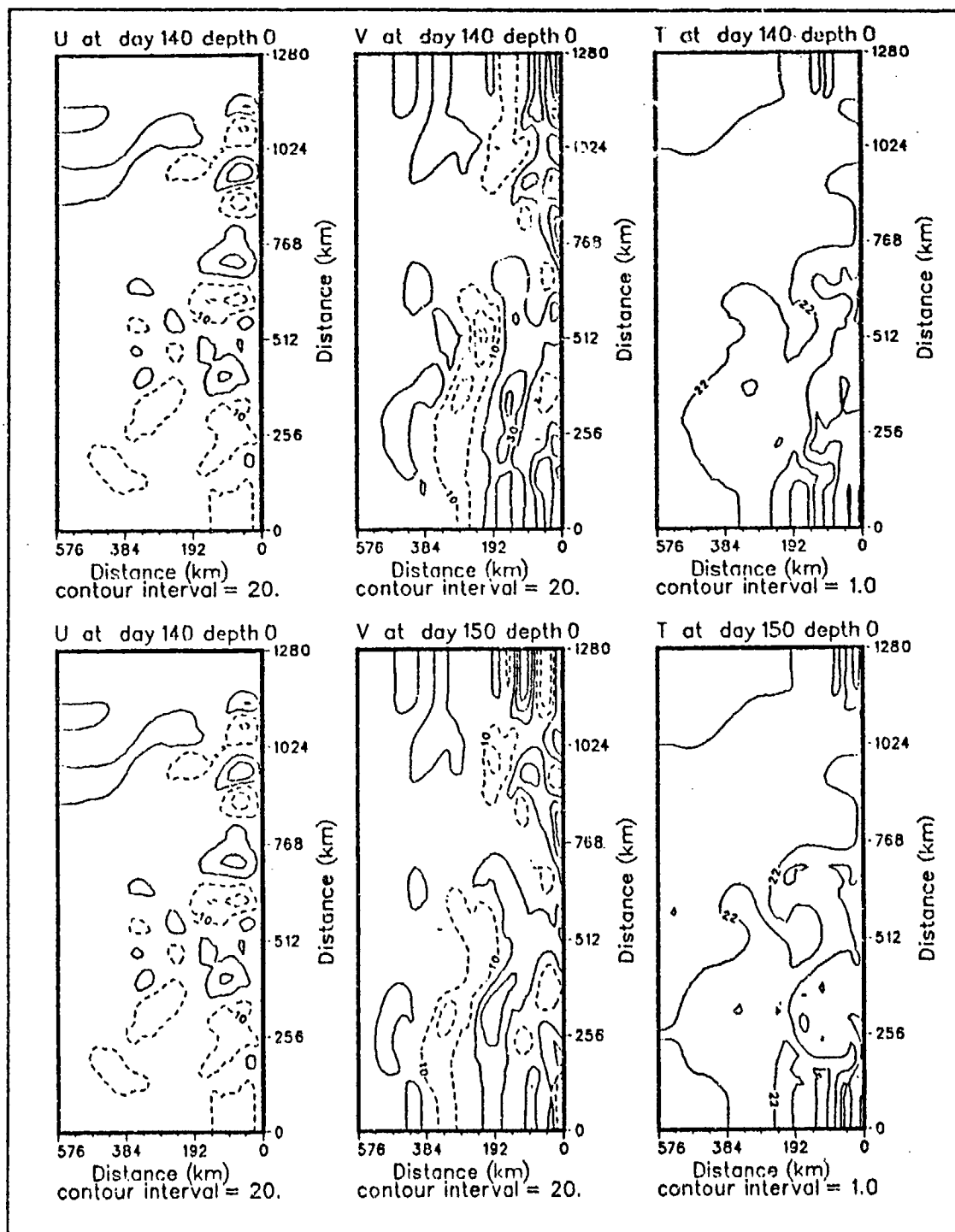


Figure 114. Case 5. Surface velocity and temperature fields, days 130 - 150: As for Figure 107.

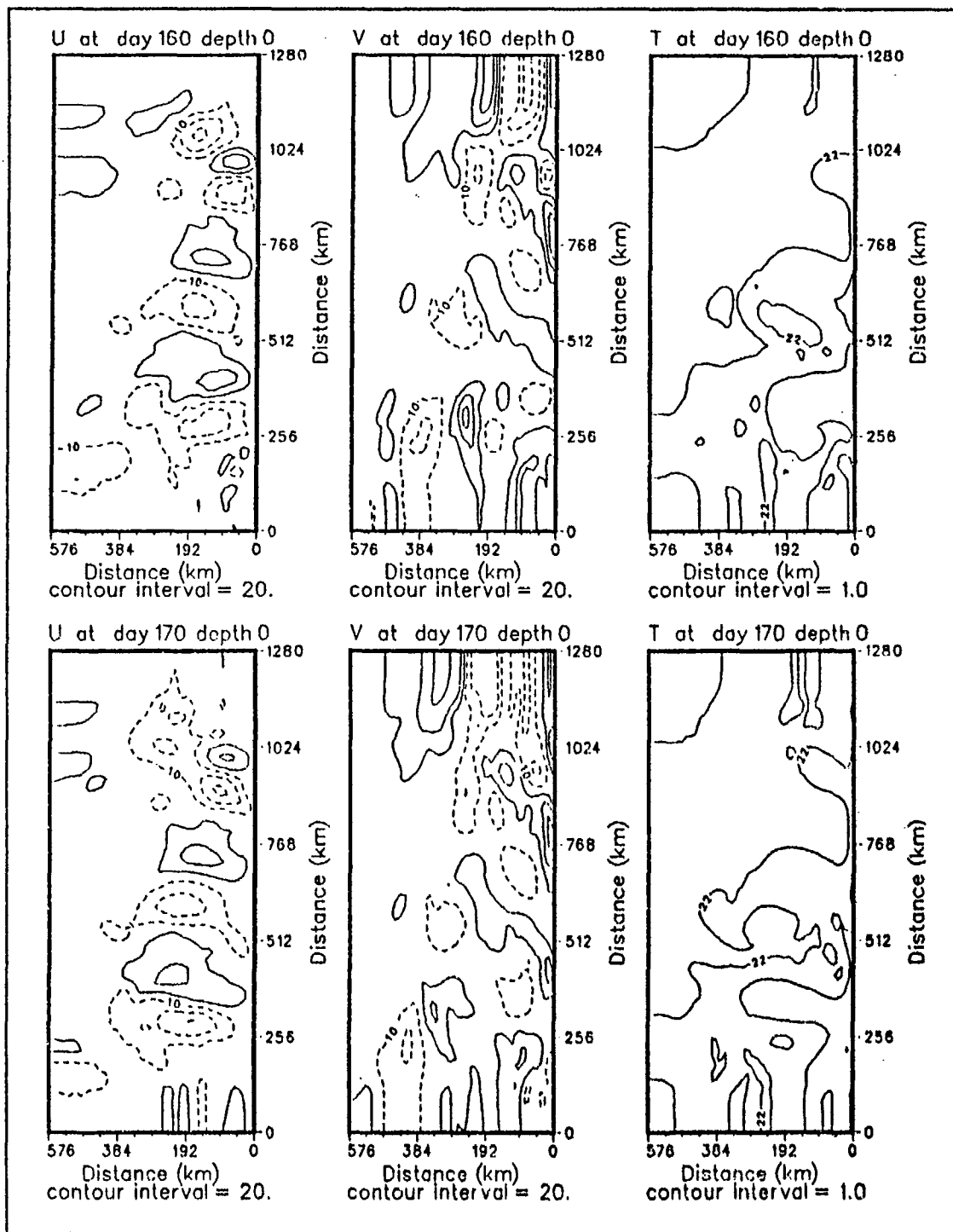


Figure 115. Case 5. Surface velocity and temperature fields, days 160 - 170: As for Figure 107.

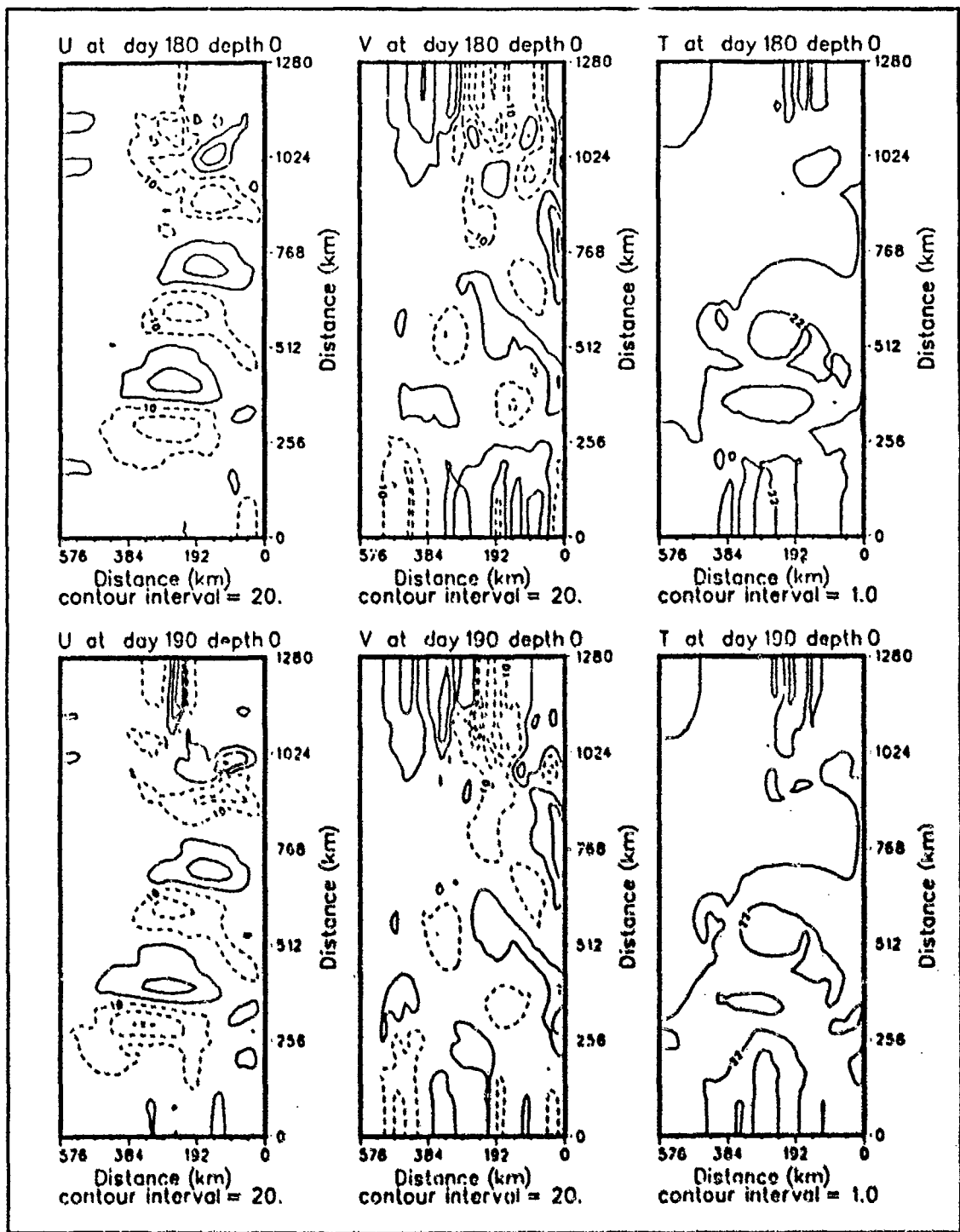


Figure 116. Case 5. Surface velocity and temperature fields, days 180 - 190: As for Figure 107.

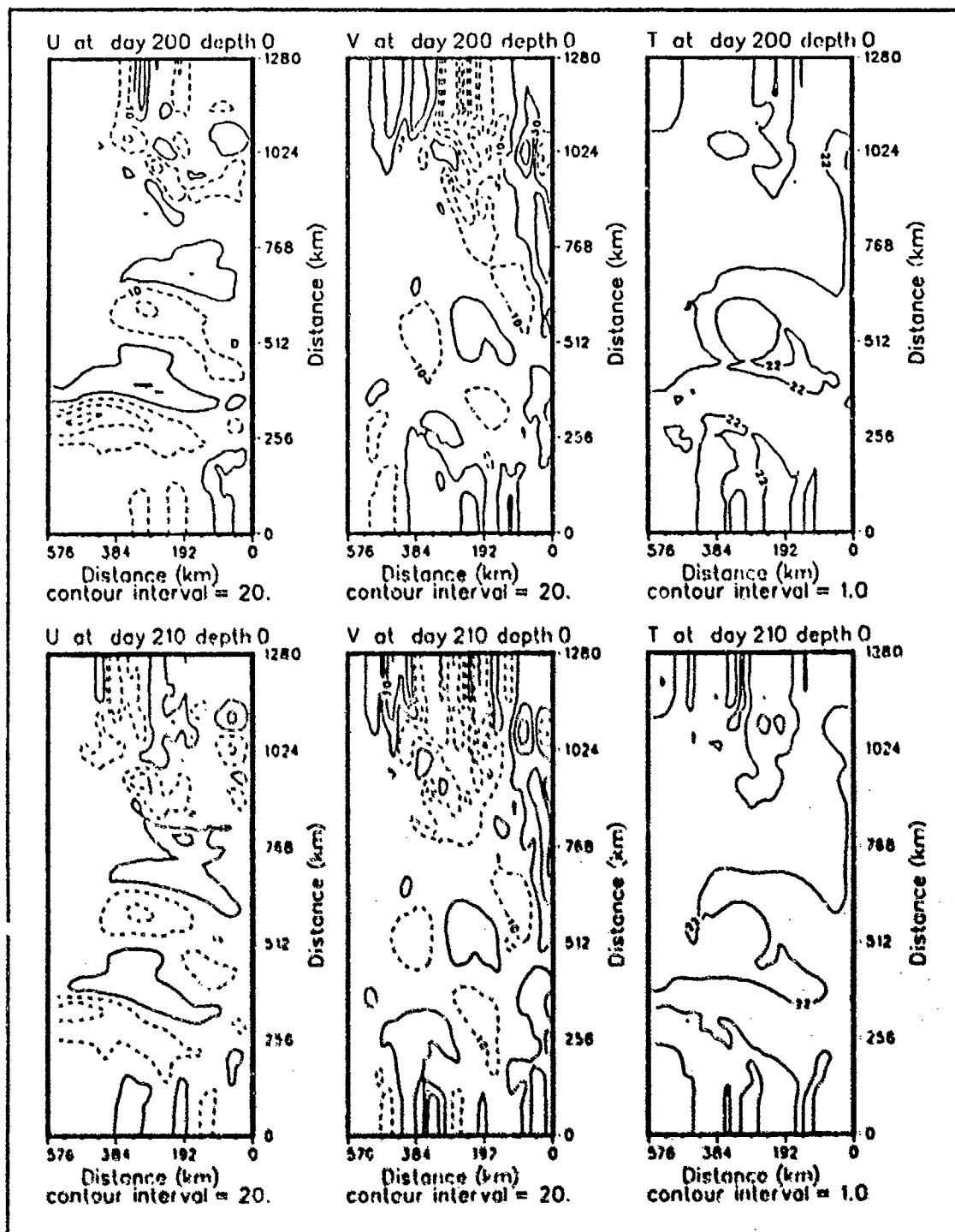


Figure 117. Case 5. Surface velocity and temperature fields, days 200 - 210: As for Figure 107.

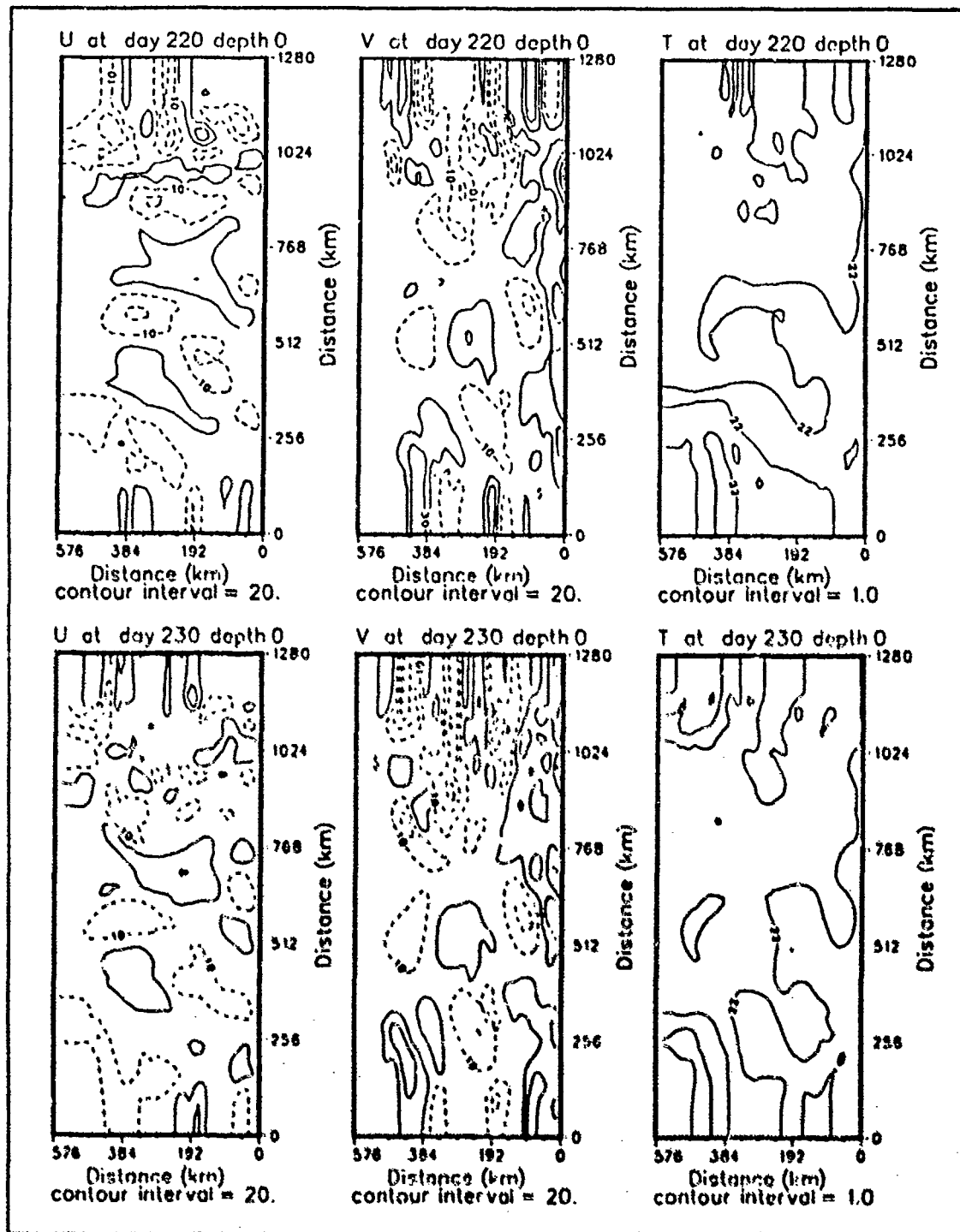


Figure 118. Case 5. Surface velocity and temperature fields, days 220 - 230: As for Figure 107.

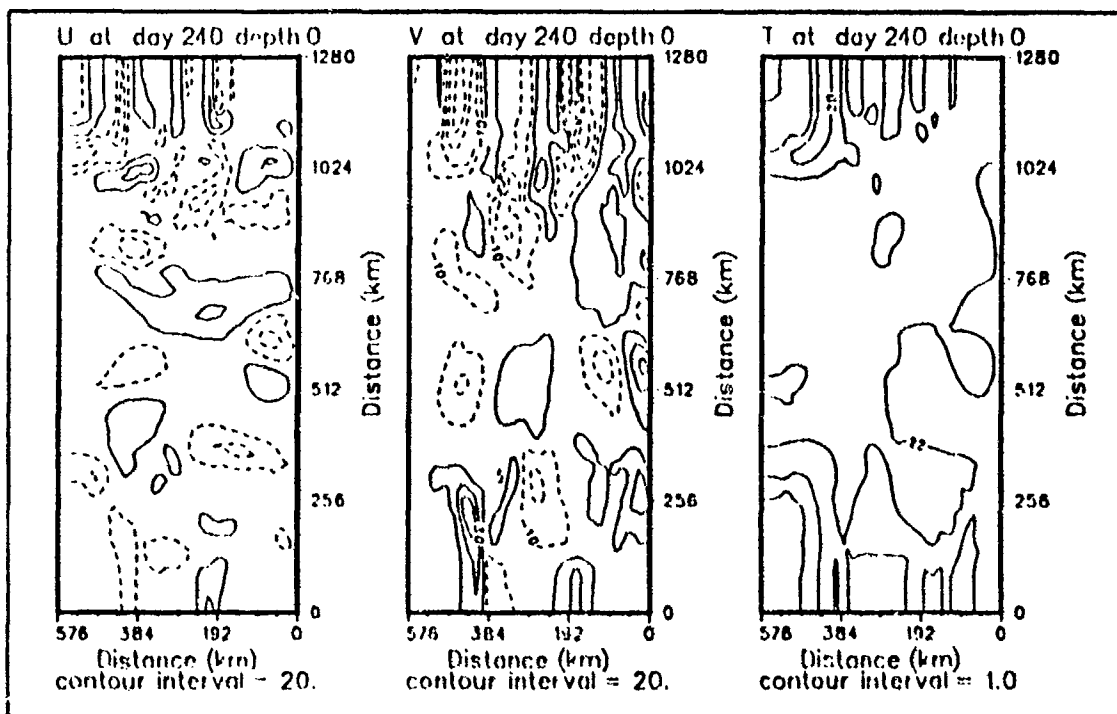


Figure 119. Case 5. Surface velocity and temperature fields, day 240: As for Figure 107.

at a wavelength of 160 km (alongshore wavenumber of $\sim 0.0062 \text{ km}^{-1}$), and from day 60 (Figure 128) to day 70 (Figure 129) has broadened and is now centered near 200 km (alongshore wavenumber of $\sim 0.005 \text{ km}^{-1}$). Also presented is the spectral density at day 160 (Figure 130) which shows two distinct wavelengths at 330 km (alongshore wavenumber of $\sim 0.003 \text{ km}^{-1}$), and 160 km (alongshore wavenumber of $\sim 0.006 \text{ km}^{-1}$). This is presented because it corresponds to the final day of Cases 2, 3 and 4.

Figure 131 shows the time series of spectral density for the 240 days of Case 5, calculated over the upper five layers and the entire domain. Two dominant scales exist at wavelengths of near 200 km (alongshore wavenumber of $\sim 0.005 \text{ km}^{-1}$), and 120 km (alongshore wavenumber of $\sim 0.008 \text{ km}^{-1}$), at the end of the period.

The domain is then broken into two regions, the first extending 90 km from the coastal boundary and the second encompassing the remaining area. The spectra for these two regions are then investigated to determine whether either energy scale is associated with a specific regime. Figure 132 applies to the coastal region and Figure 133 the remaining area. The two scales are seen in both domains with the smaller wave-

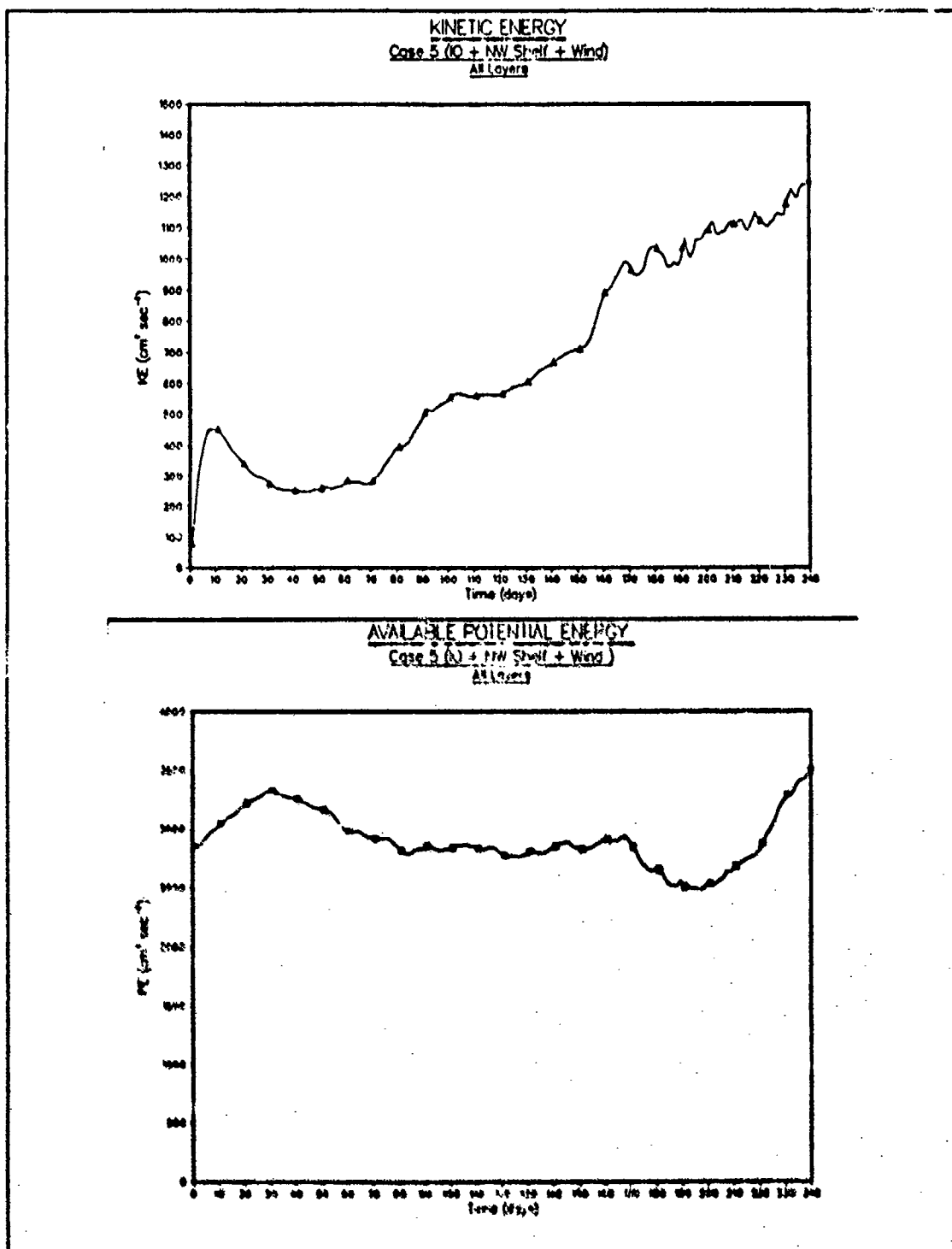


Figure 120. Case 5. Energy time series: Total kinetic and available potential energy ($\text{cm}^2 \text{s}^{-2}$) summed over all layers and the entire domain.

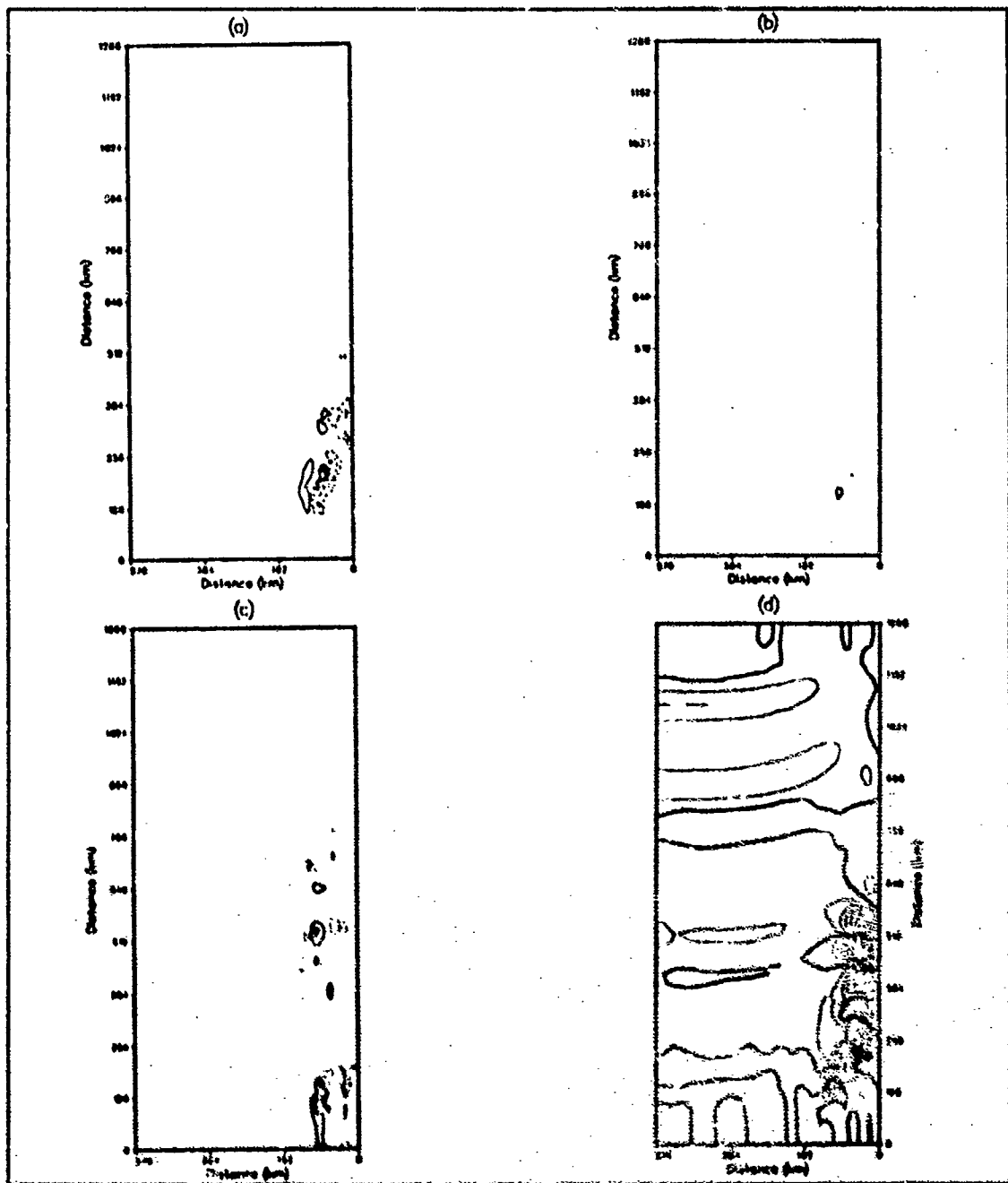


Figure 121. Case 5. Energy transfers - days 30 to 40: Energy transfers from (a) \bar{P} to P' , (b) P' to K' and (c) \bar{K} to K' in units of $\text{ergs cm}^{-1} \text{s}^{-1}$. Transfers are averaged over days 30-40 and summed over the upper five layers. Contour interval is $4.0 \times 10^{-3} \text{ ergs cm}^{-1} \text{s}^{-1}$. Subplot (d) is the cross-shore velocity component at day 40. Contour interval is 5.0 cm s^{-1} .

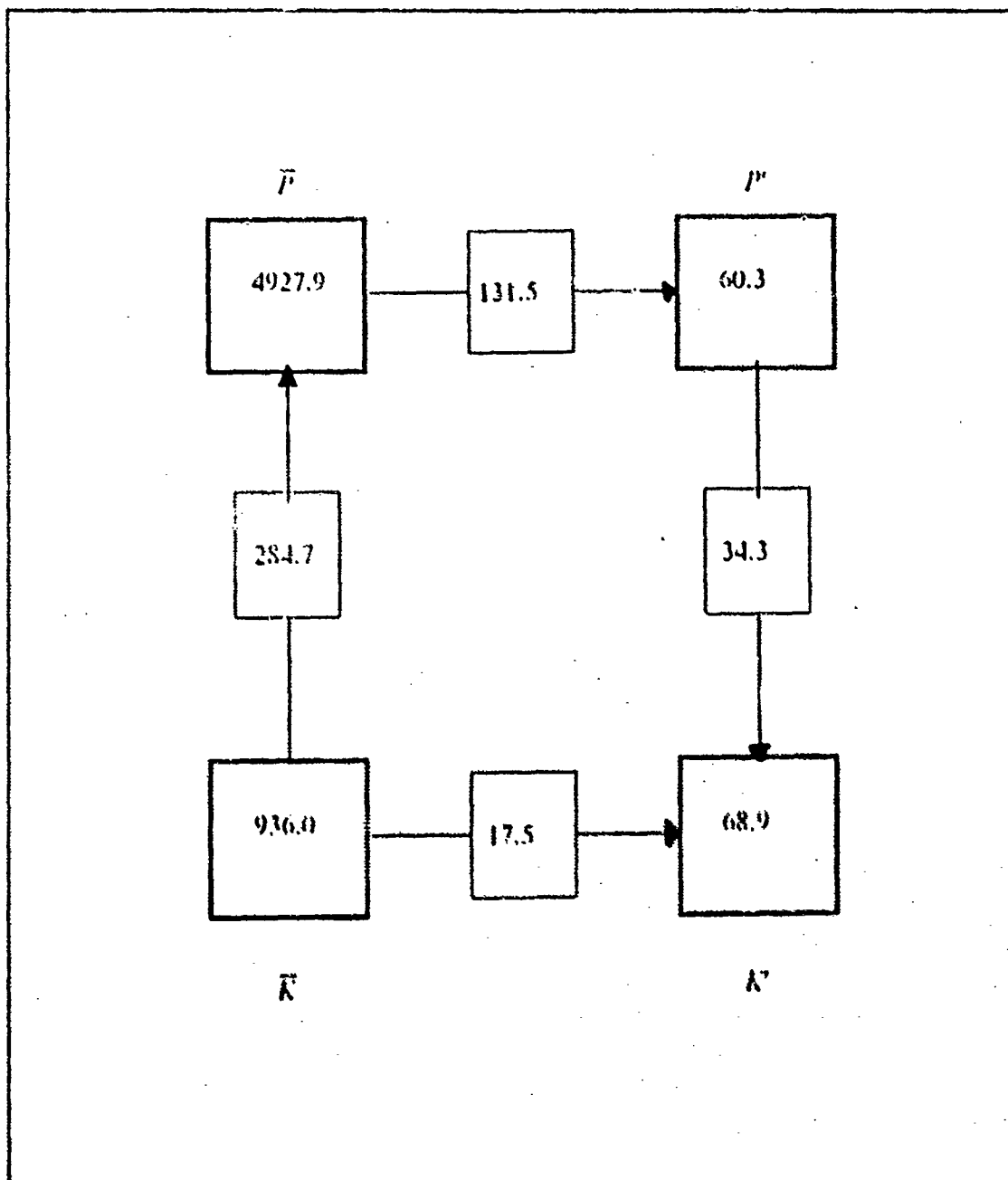


Figure 122. Case 5. Energy transfer diagram - days 30 to 40: The energy transfer diagram for upper five layers for the region between alongshore distances 400 km and 640 km, extending 90 km offshore. Units for \bar{P} , \bar{K} , P' and K' are ergs cm^{-2} , and transfers are in units of $\text{ergs cm}^{-2} \text{s}^{-1} \times 10^{-4}$.

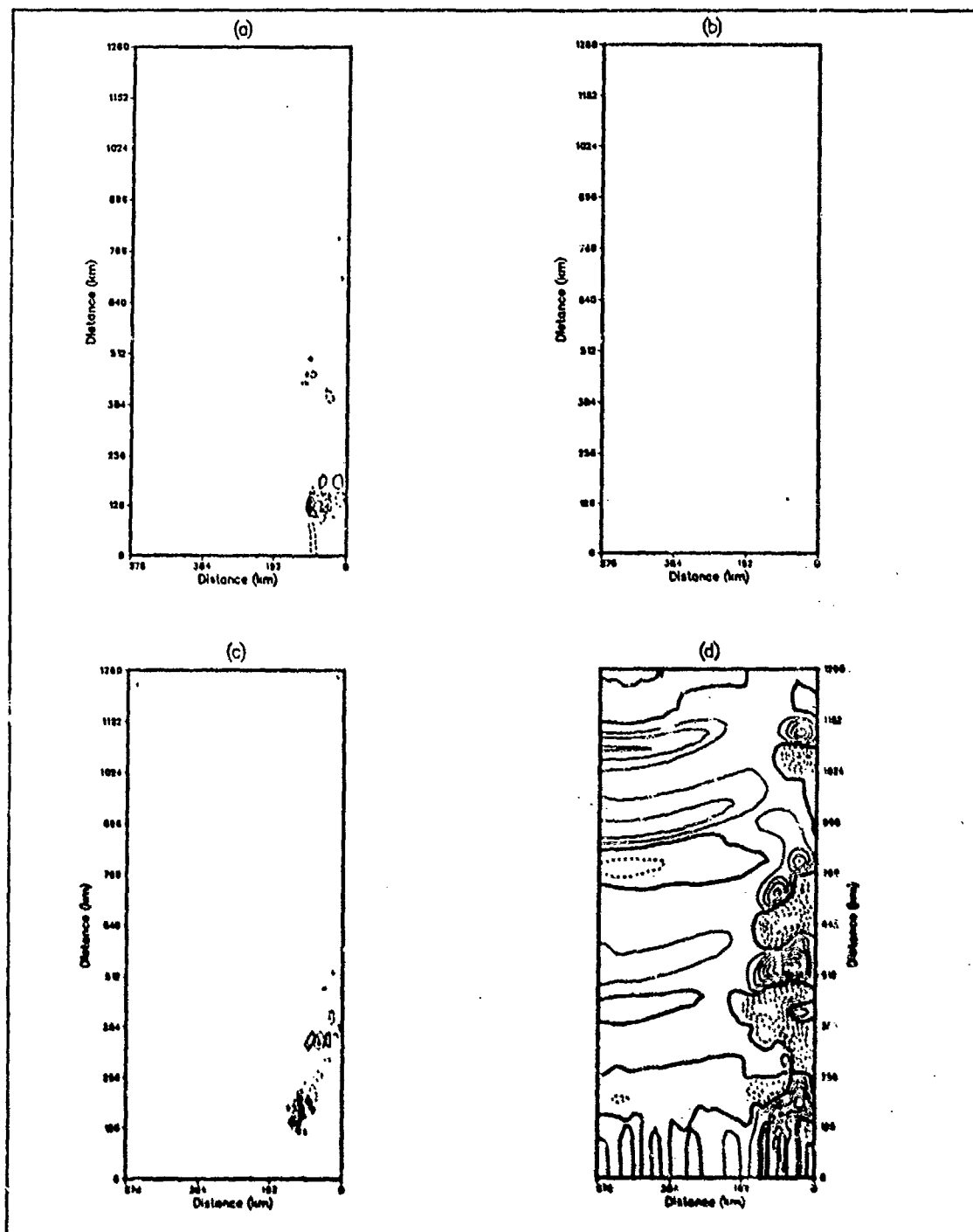


Figure 123. Case 5. Energy transfers - days 60 to 70: As for Figure 121. Subplot (d) is now at day 70.

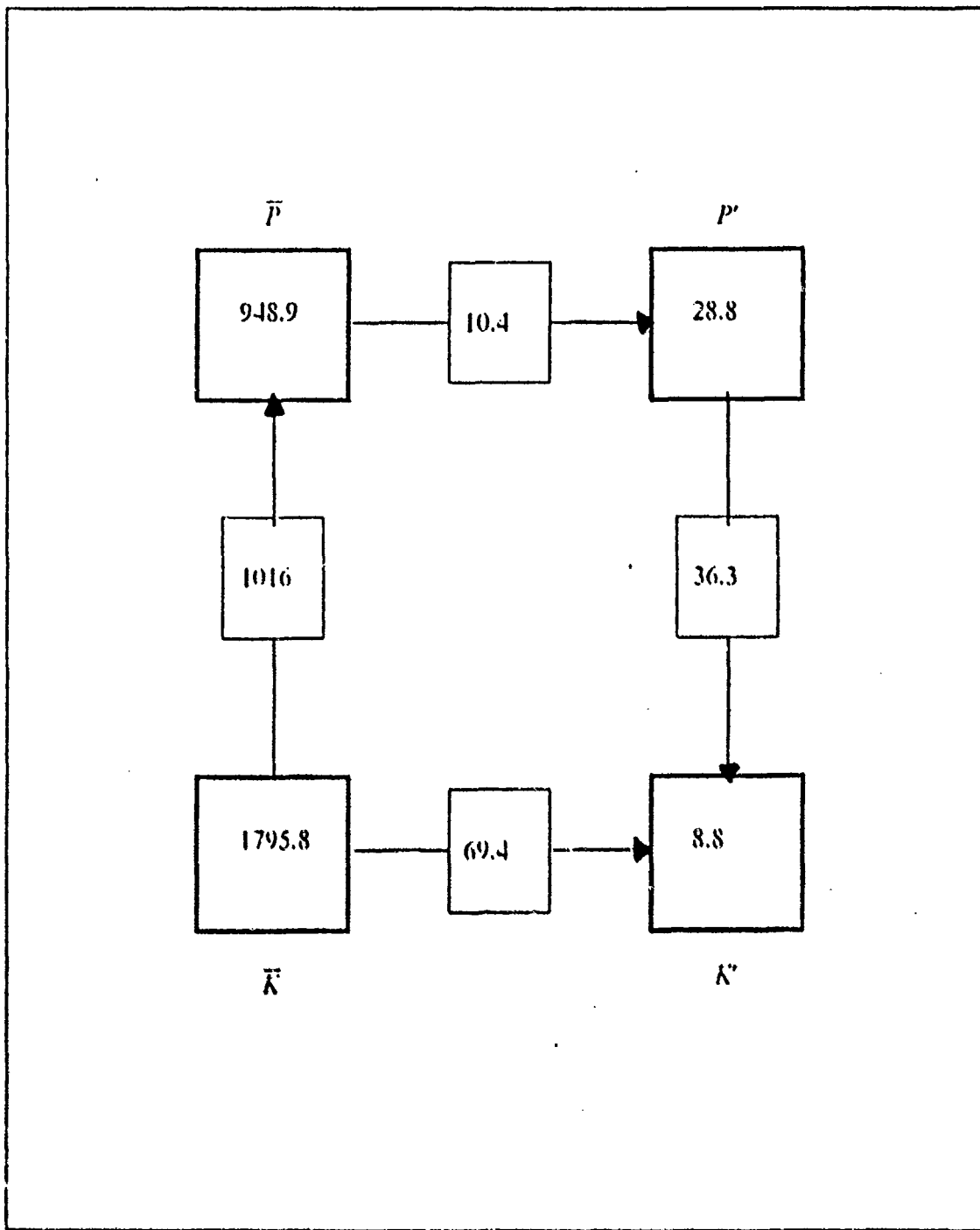


Figure 124. Case 5. Energy transfer diagram - days 60 to 70: As for Figure 122 for the upper five layers for the region between alongshore distances 980 km and 1160 km, extending 90 km offshore.

length scale more common in the inshore region associated with the current. Examination of Figure 132 shows growth at scales of 155 km (alongshore wavenumber of $\sim 0.0065 \text{ km}^{-1}$), from day 60 then shifting to the 120 km scale by day 240. The second peak in Figure 132 develops at a wavelength around 330 km (alongshore wavenumber of $\sim 0.003 \text{ km}^{-1}$), then shifts towards a 200 km wavelength scale. This shift to smaller wavelengths may be associated with an increased barotropic contribution to instability as the forcing due to the temperature initializations decreases whilst the wind forcing is maintained at each time step. The scale of unstable development offshore is seen in Figure 133. Comparing this figure with Figure 132, the spectral energy is much lower as the features apparently form later offshore. The initial growth is near a scale of 180 km (alongshore wavenumber of $\sim 0.0055 \text{ km}^{-1}$), which was the same scale associated with offshore development in Case 4, when no NW Shelf water was present. The offshore eddy scales at the end of the experiment are the same (120 km and 200 km as found inshore).

c. Instability Analysis

Figures 134 and 135 contain the plots of the cross-shore derivative of potential vorticity (a) and the mean alongshore velocity (b) for days 30-40 and 60-70 respectively. The necessary conditions are clearly satisfied for both regions for their respective periods. dq/dx changes sign and has a positive product with the alongshore component of velocity in each case, and strong horizontal and vertical gradients provide a large source of energy for the unstable growth. The Rossby radius, calculated from the thermal structure in the current at day 40 is 25.6 km. Based on these radii, the expected wavelength of maximum growth is around 160 km, which compares well with the spectral density maximum at 155 km, seen for the same period and location in Figure 132.

d. Conclusions

The forcing of the Leeuwin Current by the Indian Ocean and NW Shelf density fields along with the mean wind stress creates an unstable current with mixed instability. Baroclinic instability is dominant inshore in the middle of the domain and weakens as the effects of the NW Shelf water lessen poleward. The barotropic instability is strongest in the immediate vicinity of the NW Shelf waters at the equatorward end of the domain. The barotropic contribution is also strong where the combined effects of the Indian Ocean and wind forcing are stronger than the NW Shelf waters, such as at the poleward end of the region. Two distinct wavelength scales are present. Initial growth inshore is at wavelengths of 155 km and 330 km and by day 160, both wave-

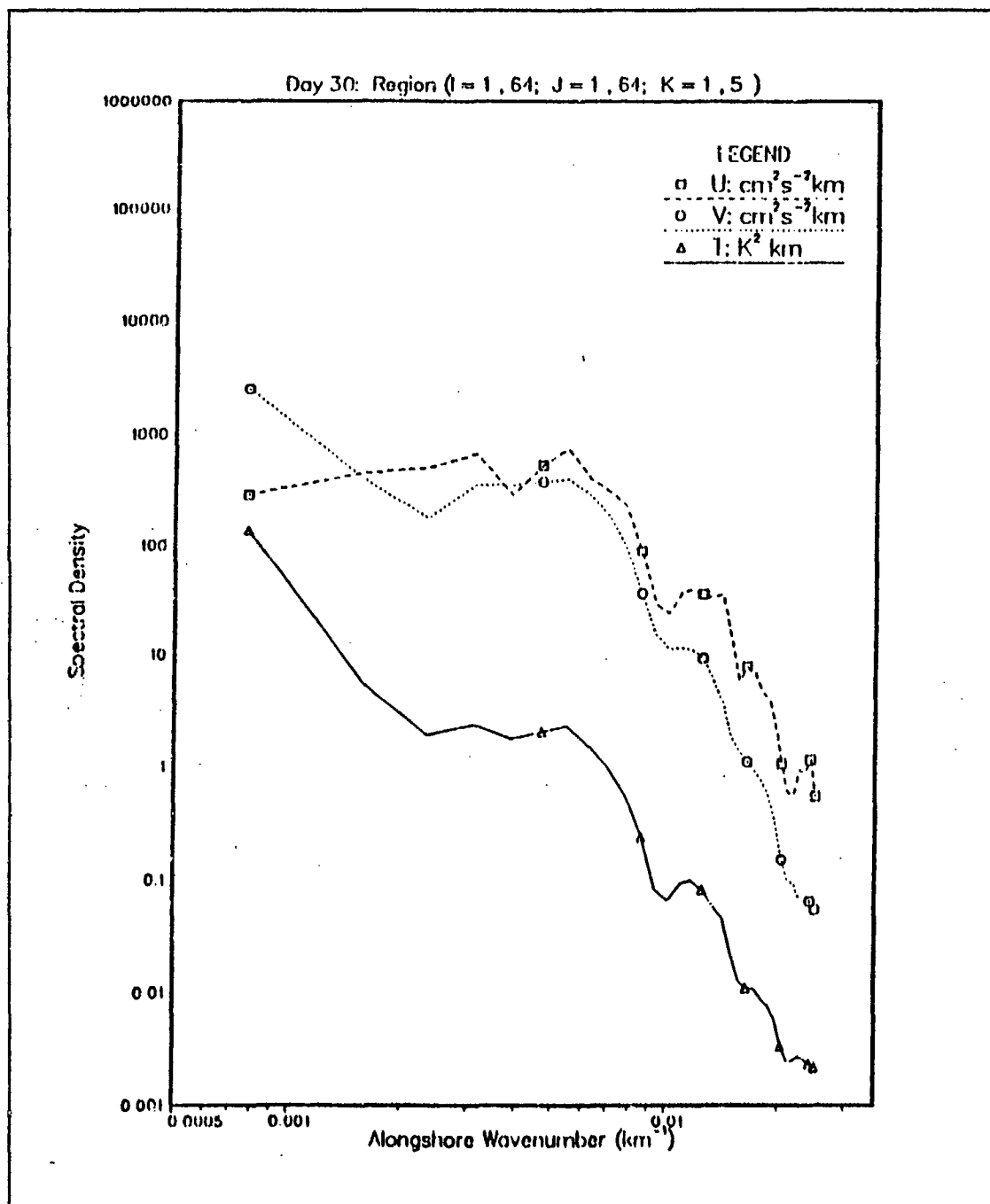


Figure 125. Case 5. Spectral density at day 30: Spectral density versus alongshore wavenumber at day 30. The wavenumber has been scaled by $\frac{1}{2\pi}$ and so is an inverse wavelength. A logarithmic scale is used for the spectral energy.

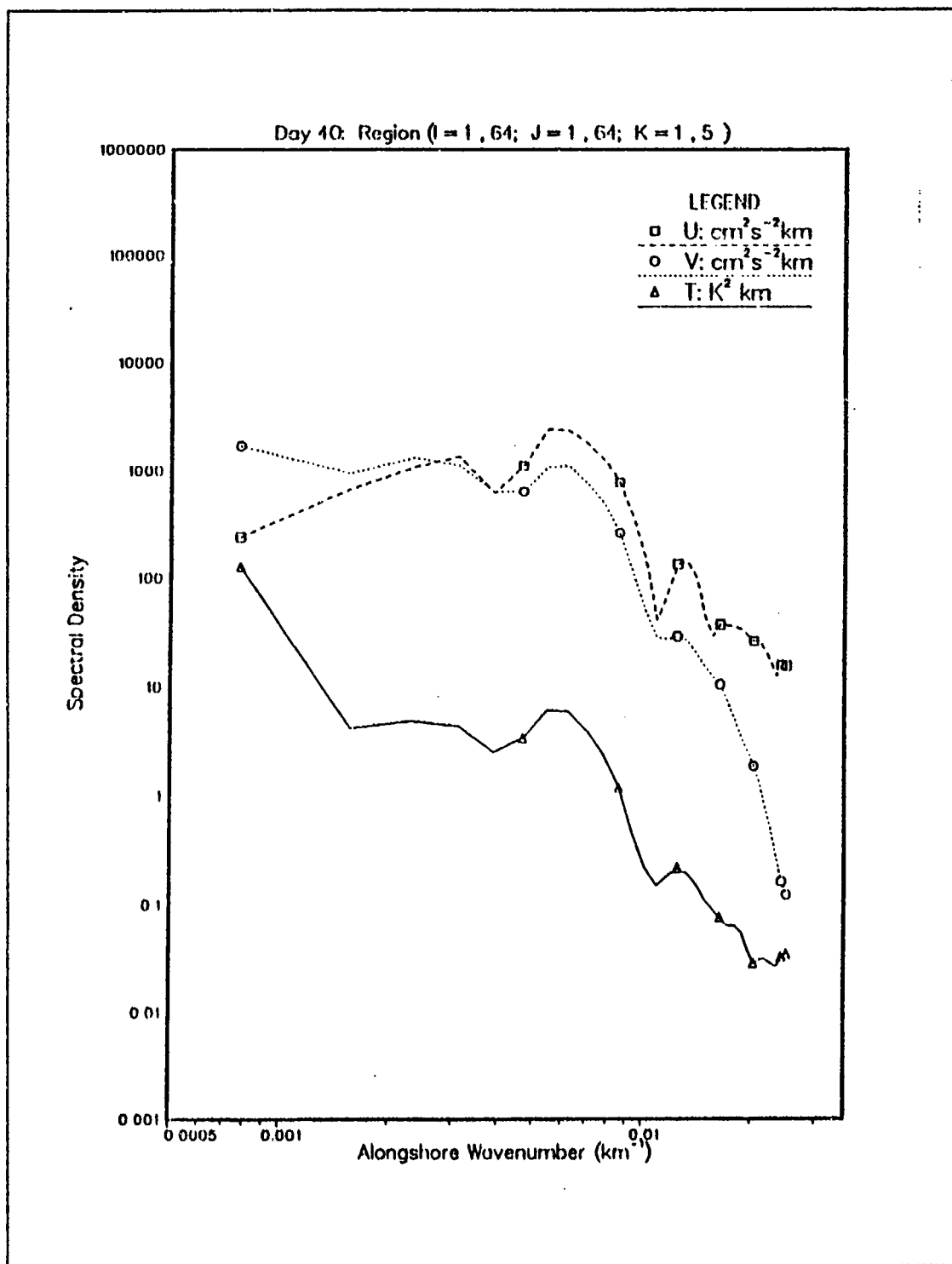


Figure 126. Case 5. Spectral density at day 40: As for Figure 125 but at day 40.

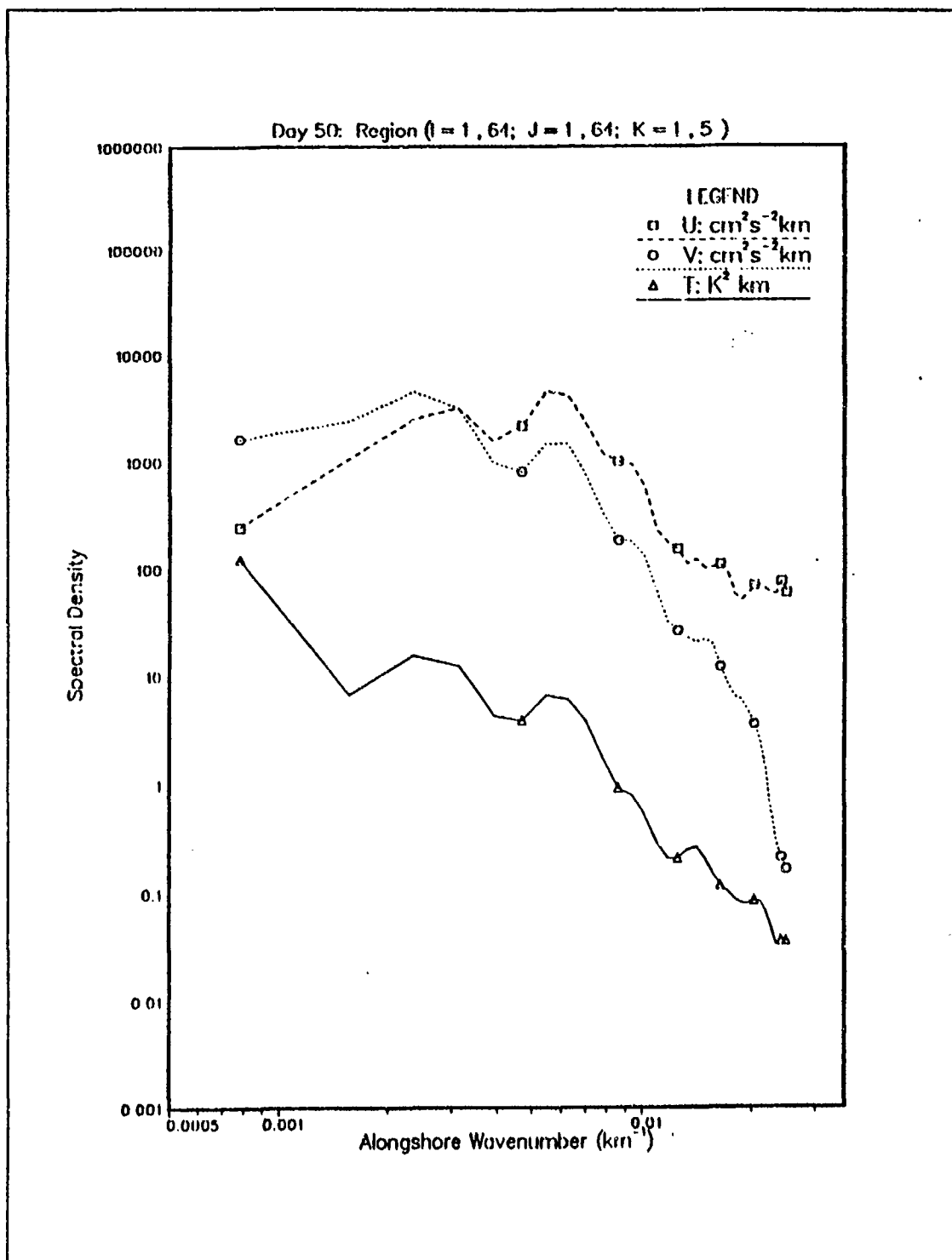


Figure 127. Case 5. Spectral density at day 50: As for Figure 125 but at day 50.

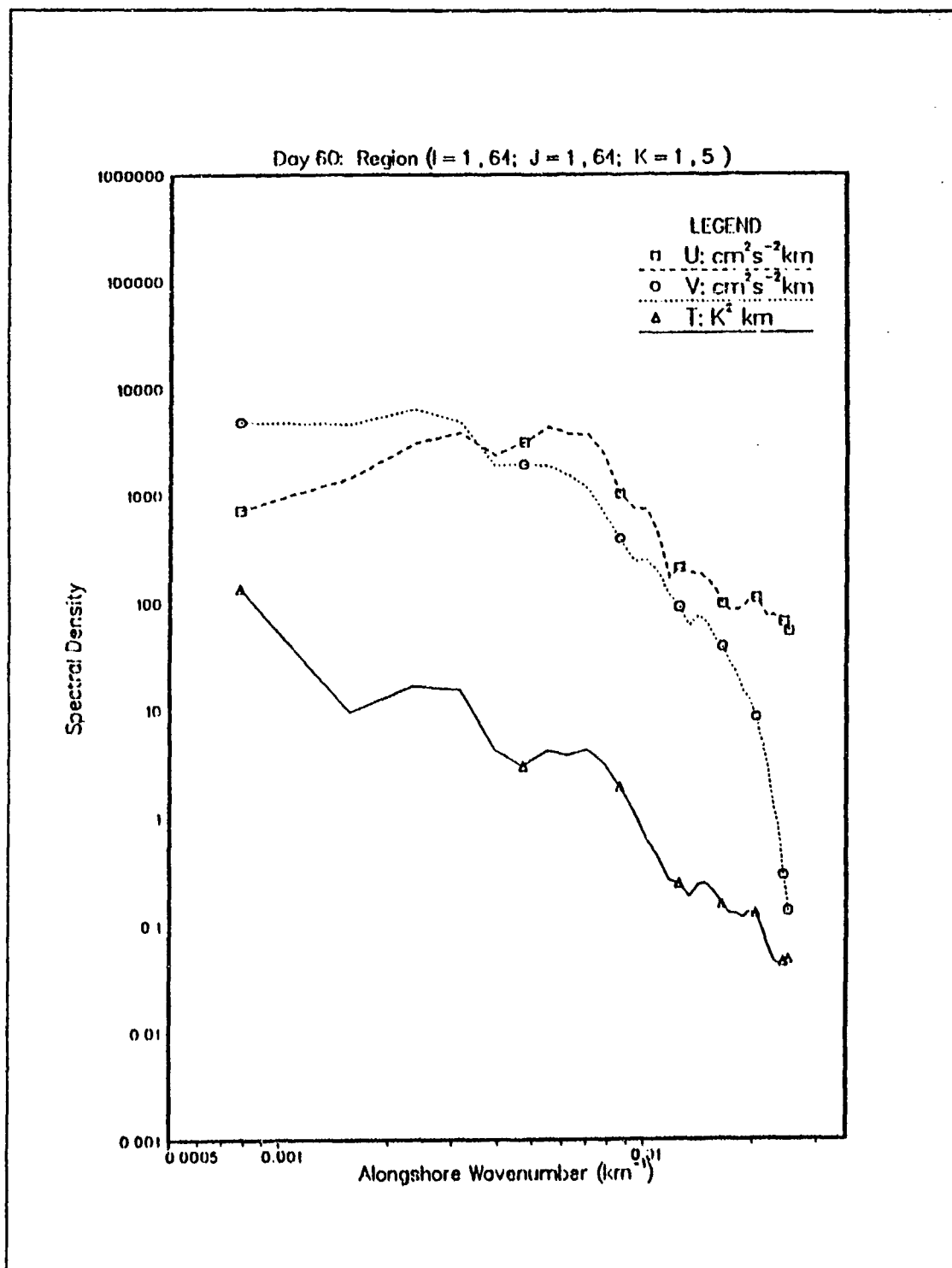


Figure 128. Case 5. Spectral density at day 60: As for Figure 125 but at day 60.

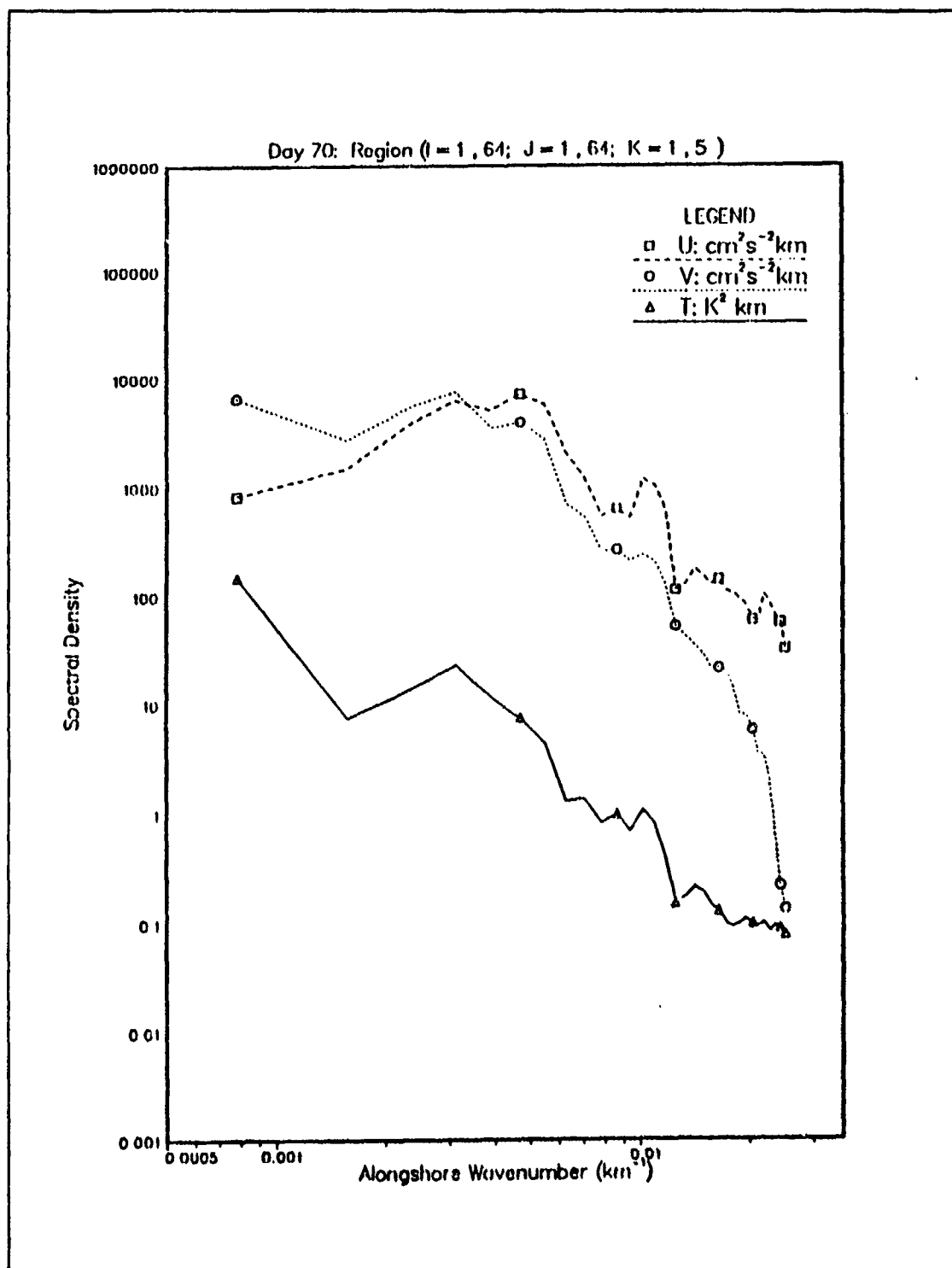


Figure 129. Case 5. Spectral density at day 70: As for Figure 125 but at day 70.

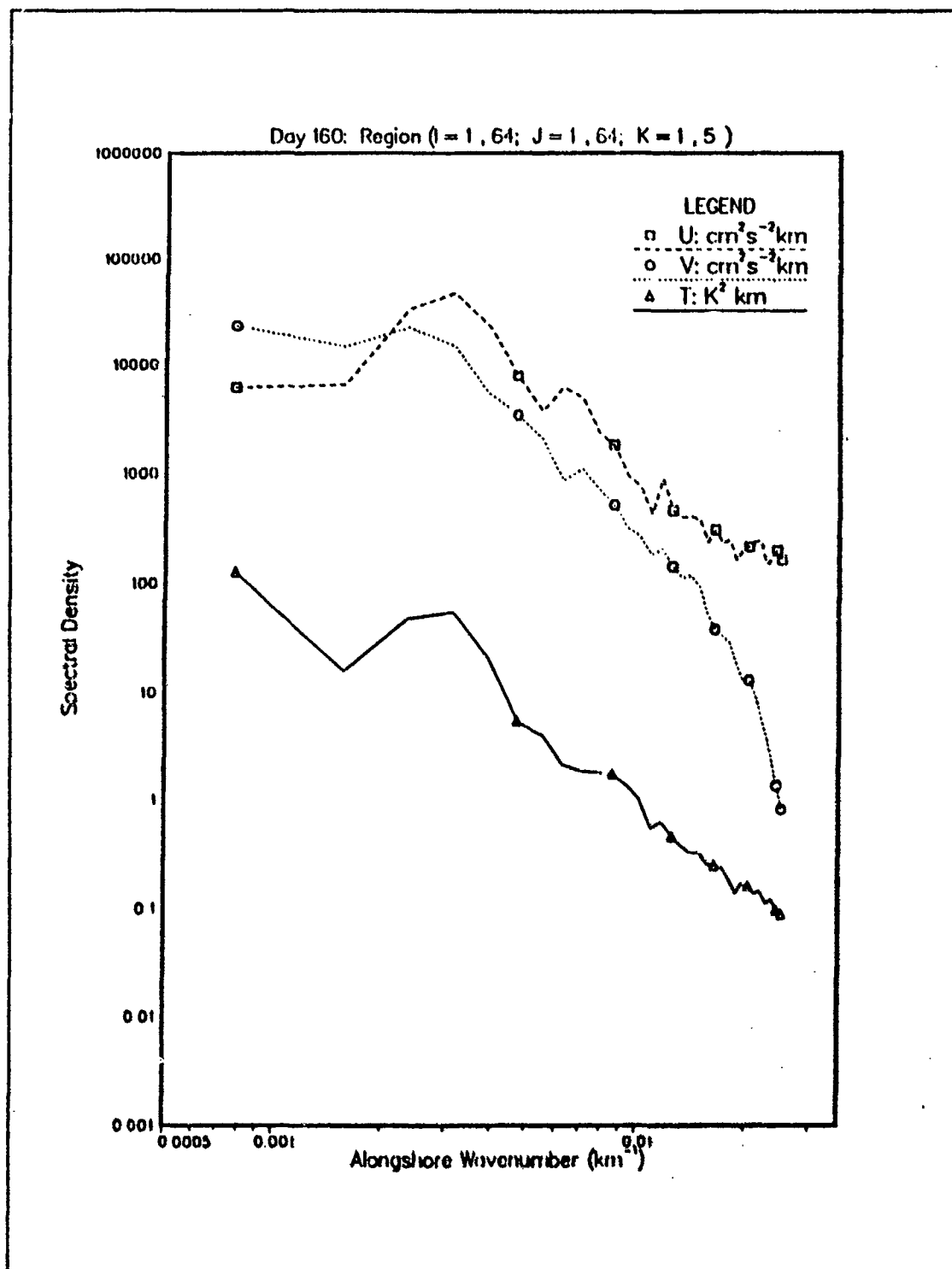


Figure 130. Case 5. Spectral density at day 160: As for Figure 125 but at day 160.

Region (I = 1, 64; J = 1, 64; K = 1, 5)

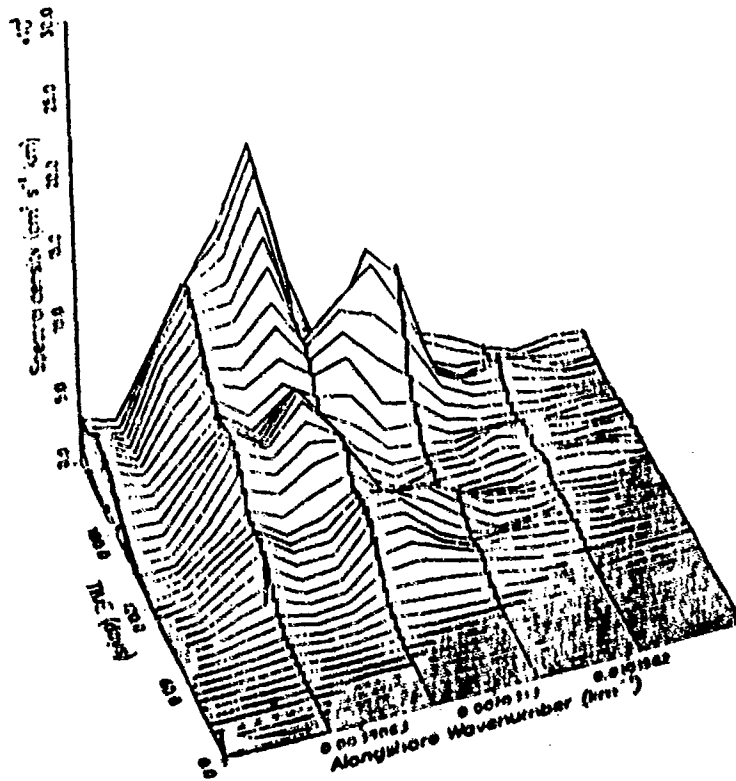


Figure 131. Case 5. Spectral density time series: The time series of spectral density from days 0 to 160 over the entire domain. Note: the amplitude of the spectral energy is on a linear scale.

Region ($I = 55, 64$; $J = 1, 64$; $K = 1, 5$)

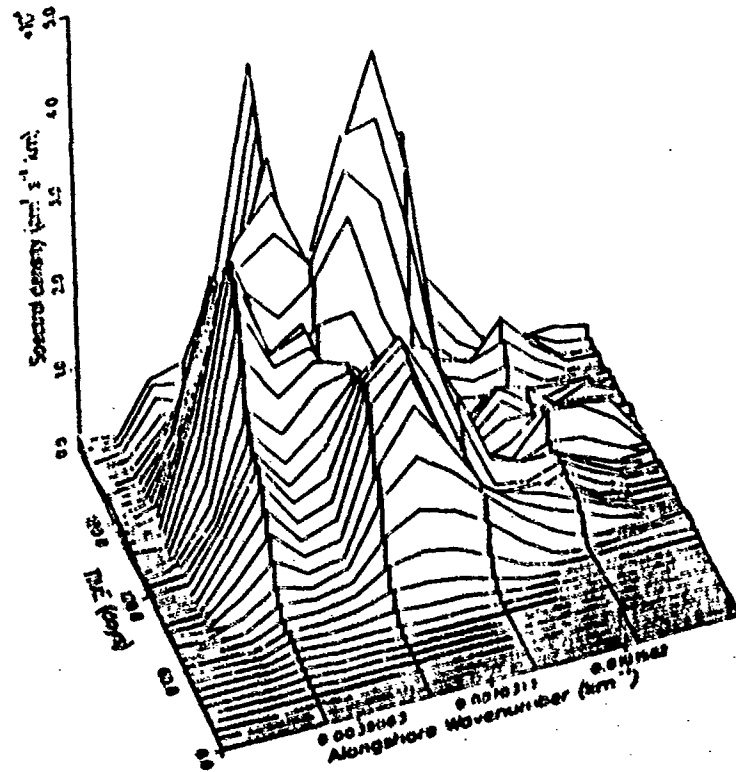


Figure 132. Case 5. Spectral density time series: As for Figure 131 but in a region extending 90 km offshore.

Region (I = 1.54; J = 1.64; K = 1.5)

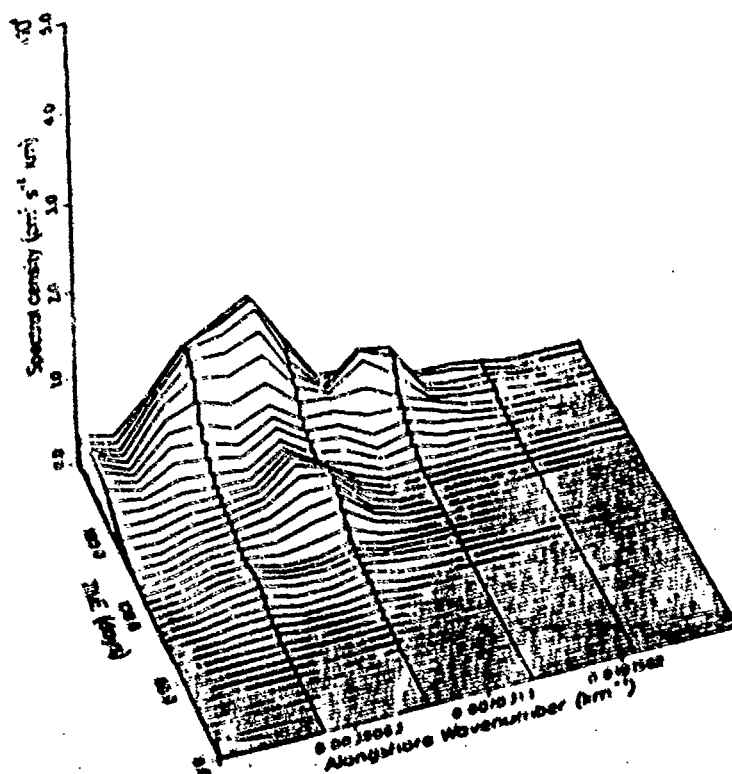


Figure 133. Case 5. Spectral density time series: As for Figure 131. The domain is the offshore region not covered by Figure 132.

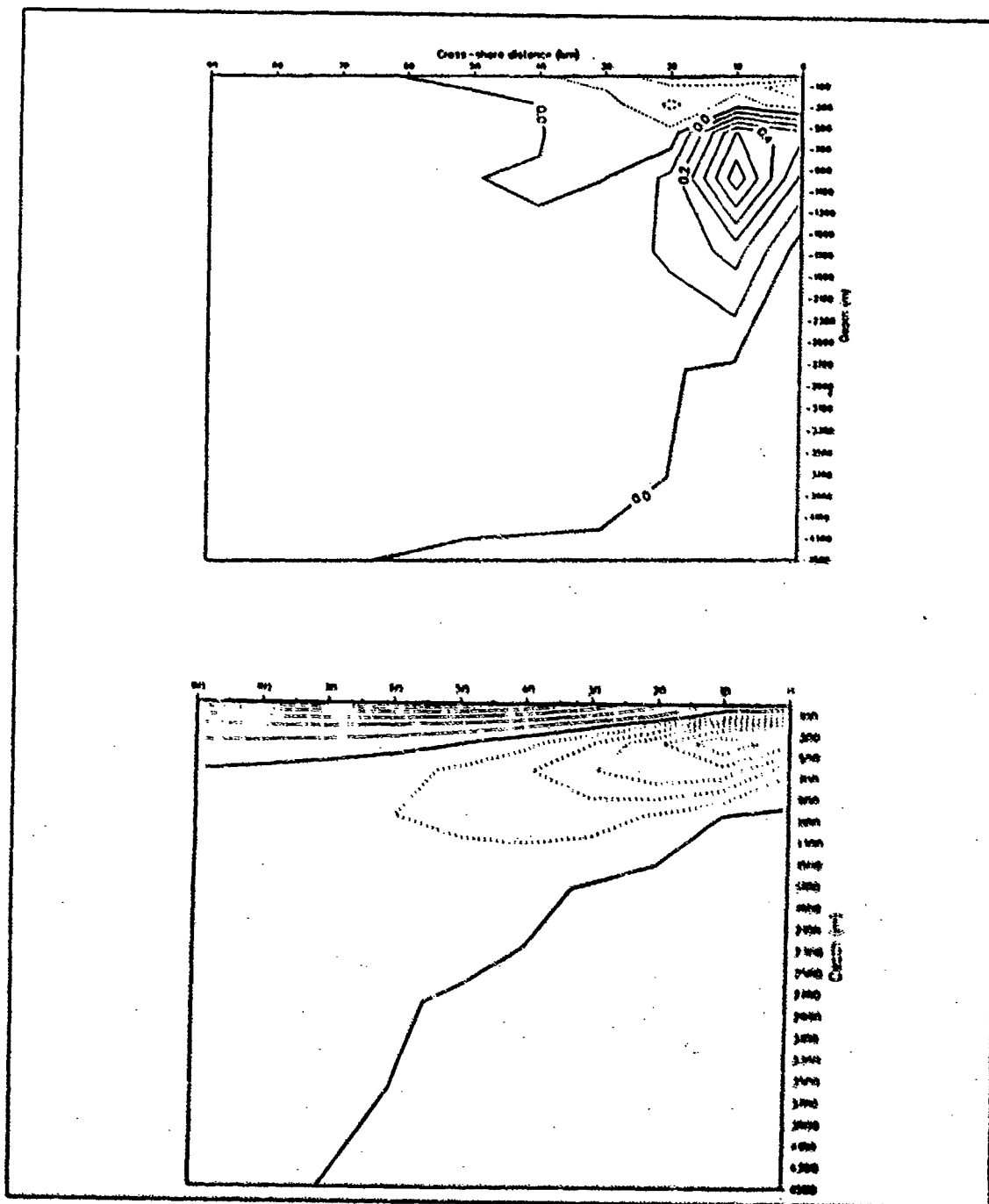


Figure 134. Case 5. Cross sections of dq/dx and alongshore velocity: As for Figure 53. Time averaging is over days 30-40 and the cross-section at alongshore distance 5-10 km. Contour intervals are (a) $0.1 \text{ } ^\circ\text{C m}^{-1} \text{ s}^{-1}$ and (b) 5.0 cm s^{-1} .

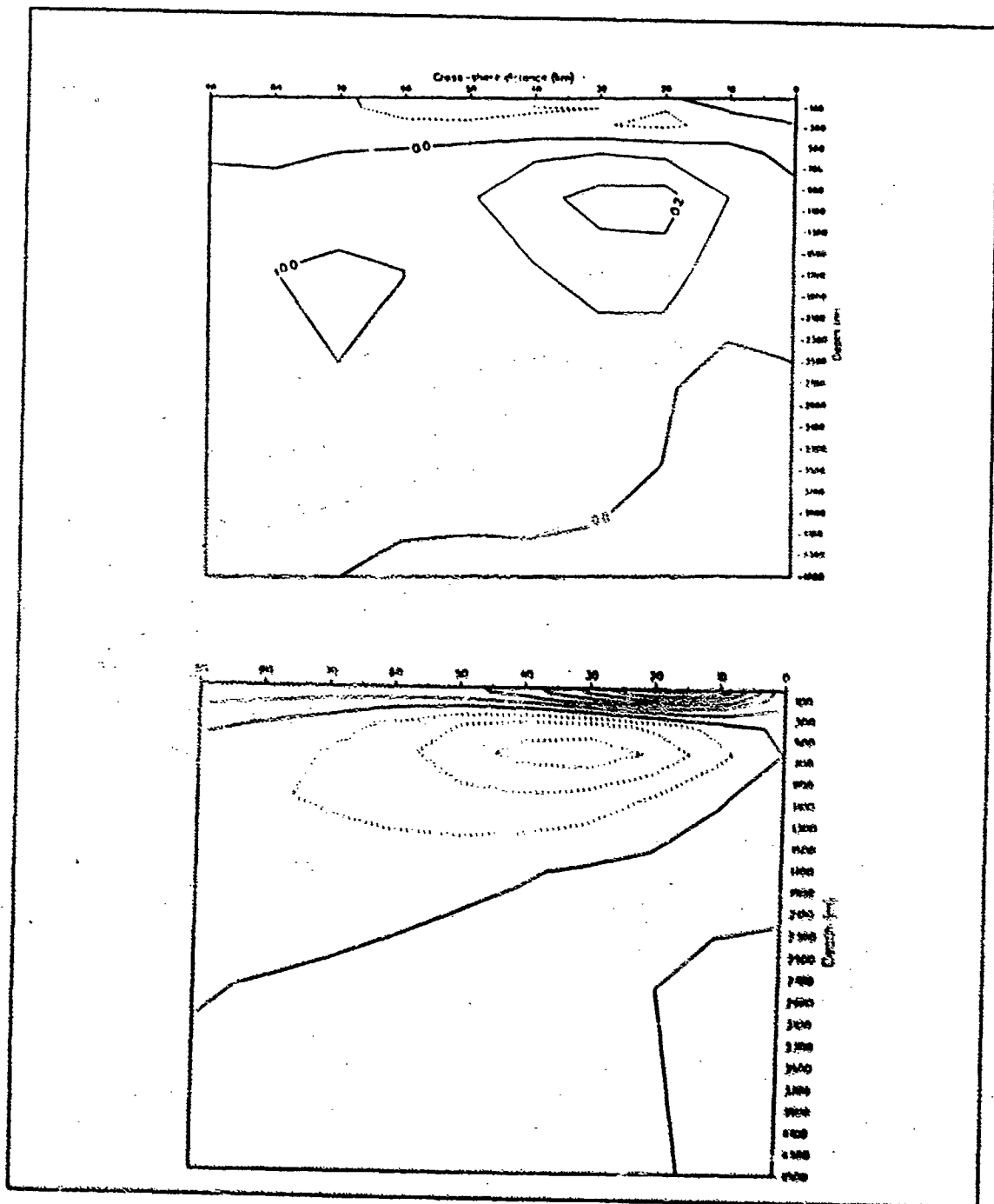


Figure 135. Case 5. Cross sections of dq/dx and alongshore velocity: As for Figure 53. Time averaging is over days 60-70 and the cross-section at alongshore distance 1060 km. Contour intervals are (a) $0.1 \text{ } ^\circ\text{C m}^{-1} \text{ s}^{-1}$ and (b) 5.0 cm s^{-1} .

lengths are still dominant. The offshore advection and growth of the shorter scale instability is seen in Figure 133 from day 120. At day 240 the dominant scales, both inshore and offshore are at around 120 km and 200 km. The observed shift towards shorter scales with time is considered to be due to the wind forcing overwhelming the density initializations. This creates instability which is predominantly barotropic and hence grows at a smaller scale than instability due to baroclinicity which was dominant during the early stages of eddy growth.

VI. SUMMARY AND RECOMMENDATIONS

A. SUMMARY

A full primitive equation (PE) model was initialized with climatological data to investigate the generation and stability of the Leeuwin Current. Initialization was done using climatological mean densities for the Indian Ocean and NW Shelf for the austral autumn and winter, which corresponds to the observed period of strongest flow, and a representative mean wind forcing applied to some experiments. The current generated by the model was assessed by making comparisons with observational data collected during LUCIE and determining the contribution to the current due to the Indian Ocean temperature field, NW Shelf density field and wind forcing. The current generated by the model was unstable in each of the four experiments in which climatological initialization and forcing was used and mesoscale features were observed. A series of analysis techniques used to determine the instability mechanisms was evaluated with a test experiment in which the model was initialized with the mean velocity and temperature structure of the current observed at its maximum strength. The analysis techniques were then applied to each of the climatologically forced experiments and the instability mechanisms and dominant length scales determined. A summary of the results from each the two phases of this study, generation and instability, is presented below.

1. Leeuwin Current Generation

1. The Indian Ocean temperature structure is sufficient to drive an unstable poleward surface flow and an equatorward undercurrent. The surface current is augmented by onshore geostrophic inflow and accelerates downstream, into the prevailing wind.

2. The climatological mean wind forcing is stronger at the equatorward end of the domain than the geostrophic pressure gradient forcing of the Indian Ocean thermal field. The effect of the wind is to strengthen the poleward alongshore flow and to reverse the geostrophic onshore flow, creating a weak upwelling regime, more typical of other eastern boundary currents.

3. The mean wind stress decreases in the latitude range 25 to 30°S. Coupled with an increase in the strength of the geostrophic flow driven by the Indian Ocean steric height gradient, the wind driven current becomes weaker than the density driven current at some point near the centre of the domain.

4. South of 30°S , the density driven current, augmented by inflow from the Indian Ocean, is much stronger than the Ekman transport, despite stronger winds.

5. The inclusion of NW Shelf waters strengthens the inshore, alongshore density gradient and increases the magnitude of both the poleward surface current and the equatorward undercurrent. The effects of the NW Shelf waters completely dominate the flows driven by the Indian Ocean and the wind stress at the equatorward end of the domain. Further poleward, the NW shelf contribution decreases as the warm waters advected poleward are countered by upwelling due to the wind forcing.

6. The current generated by the model generally compares well with LUCIE observations, particularly in relation to the strength and vertical structure of the alongshore surface current and undercurrent.

2. Instability and Eddies

7. The current driven by the Indian Ocean temperature gradient is unstable with a mixed source of eddy instability. At the poleward end of the domain, barotropic instability is dominant and eddy generation occurs on the offshore side of the core of the current with a wavelength of 150 km.

8. The addition of the NW Shelf waters creates a far more energetic and unstable current. The NW Shelf waters increase the vertical shear by strengthening the surface flow and the undercurrent, and hence add to the baroclinicity of the current. The NW Shelf waters also locally increase the barotropic instability near their source region. The dominant wavelength associated with eddies developing in the current forced by the Indian Ocean and NW Shelf water density fields is 180 km.

9. The combination of the Indian Ocean thermal forcing and the wind stress, which corresponds to the forcing regime observed during the austral spring and summer leads to eddy formation on the offshore edge of the poleward jet with a dominant wavelength of 385 km. The wind forcing acting away from the coastal boundary also generates eddies, but at a scale of 180 km. Barotropic instability is dominant in both regions with a weak baroclinic contribution in the core of the current.

10. The combined effect of the three forcing mechanisms, corresponding to the austral fall and autumn when the Leeuwin Current is strongest, is to generate a vigorous current with instability at two dominant wavelengths: 155 km and 330 km. These wavelengths agree well with available observations. The instability is again mixed. The current is baroclinically unstable over its entire range, with the baroclinicity weakening away from the NW Shelf water source region. The barotropic contribution is strongest at the poleward end of the domain where geostrophic flow and wind forcing are strong.

est. The NW Shelf water also increases the barotropic instability in the vicinity of its source region.

11. A summary of the experiments along with the Rossby radius of deformation, the dominant instability mechanism and the scale of the dominant wavelength is given in Table 12. The Rossby radius is calculated in the location of the eddy growth for the growth period as listed. Hence, for example, Case 4 (inshore) is at alongshore distance 800 km whereas Case 5 (inshore) is at alongshore distance 550 km. The spectral analysis requires that the entire alongshore extent of the domain be used to determine the scale of dominant growth. In Case 5 (inshore) therefore, the two scales may be due to eddy growth at two scales at different alongshore locations. The 155 km scale appears to coincide with the strongly baroclinic instability at alongshore distance 550 km, at which point the Rossby radius is 26.3 km. The 330 km scale is most likely to be found at the poleward end of the domain where the effects of the NW Shelf water are weak and, as seen in Case 4 (inshore), the wind mixing creates an entirely different stratification with Rossby radius around twice that found where the effects of wind forcing are weak.

Table 12. SUMMARY OF EDDY INSTABILITY AND GROWTH

Case	Duration (days)	Eddy Growth (day)	R_d (km)	Scale(km)	Instability
1	40	1-10	21.9	135	Mixed (BC dominant)
2	160	70-90	27.6	150	Mixed (BT dominant)
3	160	30-40	27.9	180	Baroclinic
4(inshore)	160	40-60	58.4	385	Mixed (BT dominant)
4(offshore)	160	40-60	33.0	180	Barotropic
5(inshore)	240	30-40	26.3	155 & 330	Mixed (BC dominant)
5(offshore)	240	100-110	33.0	180	Mixed (BT dominant)

B. RECOMMENDATIONS

This study has shown that the Leeuwin Current can be successfully modeled using a PE model forced by the mean climatology. Contrary to the findings of Weaver and Middleton (1989), a shelf is not required in the model to produce and maintain the current. The mesoscale features which have been missing from previous modeling studies are produced by the model and at scales comparable with observations. Thus, the objectives of the study have been successfully attained.

This study should now form the basis for a series of ongoing studies. It is recommended that a southern hemisphere version of the model be developed and dedicated to the Leeuwin Current. Time dependent forcing would allow the model to spin up to steady state and also allow more realistic forcing than the climatological mean used in this study. The use of a smooth function to define spatial variations in the wind forcing is also recommended.

Additional research topics which are suggested for investigation are:

- a. annual variability in the Leeuwin Current due to El Nino events (with the Pacific to Indian Ocean throughflow providing the link);
- b. the triggering mechanism for the release of NW Shelf waters and the onset of the strong fall/winter Leeuwin Current; and
- c. the Leeuwin Current extension to the south of Australia.

APPENDIX A. VALUES OF CONSTANTS USED IN THE MODEL

	VALUE	DEFINITION
C	$0.958 \text{ cal gm}^{-1}(\text{K})^{-1}$	specific heat of sea water
C_D	1.2×10^{-3}	drag coefficient
T_0	278.2 K	constant reference temperature
ρ_a	$1.23 \times 10^{-3} \text{ gm cm}^{-3}$	density of air
ρ_0	$1.0276 \text{ gm cm}^{-3}$	density of sea water at T_0
α	$2.01 \times 10^{-4} (\text{K})^{-1}$	thermal expansion coefficient
K	10	number of levels in vertical
Δx	$9 \times 10^4 \text{ cm}$	cross-shore grid spacing
Δy	$2 \times 10^4 \text{ cm}$	alongshore grid spacing
D	$4.5 \times 10^4 \text{ cm}$	ocean depth
Δt	800 s	time step
g	980 cm s^{-2}	gravitational acceleration
A_M	$2 \times 10^{11} \text{ cm}^4 \text{ s}^{-1}$	biharmonic momentum diffusion coefficient
A_H	$2 \times 10^{11} \text{ cm}^4 \text{ s}^{-1}$	biharmonic heat diffusion coefficient
K_M	$0.5 \text{ cm}^2 \text{ s}^{-1}$	vertical eddy viscosity
K_H	$0.5 \text{ cm}^2 \text{ s}^{-1}$	vertical eddy conductivity

LIST OF REFERENCES

- Adamec, D., R.L. Elsberry, R.W. Garwood, Jr., and R.L. Haney, 1981: An embedded mixed layer-ocean circulation model. *Dyn. Atmos. Oceans*, 5, 69-96.
- Andrews, J.C., 1977: Eddy structure and the West Australian Current. *Deep-Sea Res.*, 24, 1133-1148.
- Andrews, J.C., 1983: Ring structure in the poleward boundary current off Western Australia in summer. *Aust. J. Mar. Freshwat. Res.*, 34, 547-561.
- Arakawa, A., and V.R. Lamb, 1977: Computational design of the basic dynamical processes of the UCLA general circulation model. *Methods in Computational Physics*, (J. Chang, Ed.), Academic Press, 17, 173-265.
- Batteen, M.L., R.L. Haney, T.A. Tielking and P.G. Renaud, 1989: A numerical study of wind forcing of eddies and jets in the California Current System. *J. Mar. Res.*, 47, 493-523.
- Boland, F.M., J.A. Church, A.M.G. Forbes, J.S. Godfrey, A. Huyer, R.L. Smith and N.J. White, 1988: Current-meter data from the Leeuwin Current Interdisciplinary Experiment. CSIRO Australia Marine Laboratories Report No. 198.
- Colborn, J.G., 1975: The thermal structure of the Indian Ocean. International Indian Ocean Expedition Monograph No. 2.
- Camerlengo, A.L., and J.J. O'Brien, 1980: Open boundary conditions in rotating fluids. *J. Comput. Physics*, 35, 12-35.
- Cresswell, G.R. and T.J. Golding, 1979: Satellite-tracked buoy data report III. Indian Ocean 1977. Tasman Sea July-December 1977. CSIRO Australia Division of Fisheries and Oceanography Report 101.
- Cresswell, G.R. and T.J. Golding, 1980: Observations of a south-flowing current in the southeastern Indian Ocean. *Deep-Sea Res.*, 27A, 449-466.
- Dakin, W.J., 1919: The Percy Sladen Trust Expeditions to the Abrolhos Islands (Indian Ocean). Report 1. *Journal of the Linnean Society*, 34, 127-180.
- Gentili, J., 1972: Thermal anomalies in the Eastern Indian Ocean. *Nature (London) Physical Sciences*, 238, 93-95.
- Godfrey, J.S., 1988: Steric height gradients, the Indonesian throughflow and the Leeuwin Current. Unpublished manuscript.
- Godfrey, J.S. and T.J. Golding, 1981: The Sverdrup relation in the Indian Ocean, and the effect of Pacific-Indian Ocean throughflow on Indian Ocean circulation and on the East Australia Current. *J. Phys. Oceanogr.*, 11, 771-779.

- Godfrey, J.S. and K.R. Ridgeway, 1985: The large-scale environment of the poleward-flowing Leeuwin Current, Western Australia: Longshore steric height gradients, wind stresses and geostrophic flow. *J. Phys. Oceanogr.*, 15, 481-495.
- Godfrey, J.S., D.J. Vaudrey, and S.D. Hahn, 1986: Observations of the shelf-edge current south of Australia, winter 1982. *J. Phys. Oceanogr.*, 16, 668-679.
- Golding, T.J., and G. Symonds, 1978: Some surface circulation features off Western Australia during 1973-1976. *Aust. J. Mar. Freshwat. Res.*, 29, 187-191.
- Hamon, B.V., 1965: Geostrophic Currents in the south-eastern Indian Ocean. *Aust. J. Mar. Freshwat. Res.*, 16, 255-271.
- Hamon, B.V., 1972: Geopotential topographies and currents off Western Australia, 1965-69. CSIRO Australia Division of Fisheries and Oceanography Technical Paper No. 32.
- Hamon, B.V. and G.R. Cresswell, 1972: Structure functions and intensities of ocean circulation off east and west Australia. *Aust. J. Mar. Freshwat. Res.*, 23, 99-103.
- Han, Y.-J., 1975: Numerical simulation of mesoscale eddies. Ph.D. thesis, UCLA, 154pp.
- Haney, R.L., W.S. Shriver and K.H. Hunt, 1978: A dynamical-numerical study of the formation and evolution of large-scale ocean anomalies. *J. Phys. Oceanogr.*, 8, 952-969.
- Holland, W.R., 1978: The role of mesoscale eddies in the general circulation of the ocean-numerical experiments using a wind-driven quasi-geostrophic model. *J. Phys. Oceanogr.*, 8, 363-392.
- Holland, W.R., and M.L. Batteen, 1986: The parameterization of subgrid scale heat diffusion in eddy-resolved ocean circulation models. *J. Phys. Oceanogr.*, 16, 200-206.
- Holloway, P.E. and H.C. Nye, 1985: Leeuwin Current and wind distributions on the southern part of the Australian North West Shelf between January 1982 and July 1983. *Aust. J. Mar. Freshwat. Res.*, 36, 123-137.
- Hsiung, J., 1985: Estimates of the global oceanic meridional heat transport. *J. Phys. Oceanogr.*, 15, 1405-1413.
- Kamenkovich, V.M., M.N. Koshlyakov, and A.S. Monin, 1986: *Synoptic Eddies in the Ocean*. D. Riedel, 433 pp.
- Kitani, K., 1977: The movement and physical characteristics of the water off Western Australia in November 1975. *Bull. Far Seas Fish. Res. Lab. (Shimizu)*, 15, 13-19.
- Kundu, P.J. and J.P. McCreary, 1986: On the dynamics of the throughflow from the Pacific into the Indian Ocean. *J. Phys. Oceanogr.*, 16, 2191-2198.

- Levitus, S., 1982: Climatological Atlas of the World Ocean. NOAA Professional Paper 13. US Department of Commerce: National Oceanic and Atmospheric Administration.
- List, R.J. 1963: *Smithsonian Meteorological Tables*. Smithsonian Institution, Washington, DC., 527pp.
- Lopes da Costa, C.N., 1989: A numerical study of wind forcing in the eastern boundary current system off Portugal. M.S. thesis, Naval Postgraduate School, 114 pp.
- Markina, N.P., 1976: Biogeographic regionalization of Australian waters of the Indian Ocean. *Oceanology*, 15, 602-604.
- McCreary, J.P., S.R. Shetye and P.K. Kundu, 1986: Thermohaline forcing of eastern boundary currents: With application to the circulation off the west coast of Australia. *J. Mar. Res.*, 44, 71-92.
- McCreary, J.P., P.K. Kundu, and S.-Y. Chao, 1987: On the dynamics of the California Current System. *J. Mar. Res.*, 45, 1-32.
- Nelson, C.S., 1977: Wind stress and wind stress curl over the California Current. *NOAA Tech. Rep. NMFS SSRF-714*, U.S. Dept. Commerce, 87 pp.
- Olivier, D.A., 1987: Numerical simulations of the California Current: filament formation as related to baroclinic instability. M.S. thesis, Naval Postgraduate School, 69pp.
- Parrish, R.H., A. Bakun, D.M. Husby and C.S. Nelson, 1983: Comparative climatology of selected environmental processes in relation to eastern boundary current pelagic fish reproduction. In Sharp, G. D. and J. Csirke (eds.), *Proceedings of the Expert Consultation to Examine Changes in Abundance and Species of Neritic Fish Resources*. San Jose, Costa Rica, 18-19 April 1983. *FAO Fish Rep.* (291, Vol. 3: 731-778).
- Paulson, C.A. and J.J. Simpson, 1977: Irradiance measurements in the upper ocean. *J. Phys. Oceanogr.*, 7, 952-956.
- Pearce, A.F. and G.R. Cresswell, 1985: Ocean circulation off Western Australian and the Leeuwin Current. CSIRO Australia Division of Oceanography Information Service Sheet No. 16-3, July 1985.
- Rochford, D.J., 1969: Seasonal variations in the Indian Ocean along 110°E. I. Hydrological structure of the upper 500m. *Aust. J. Mar. Freshwat. Res.*, 20, 1-50.
- Rochford, D.J., 1986: Seasonal changes in the distribution of Leeuwin Current waters off southern Australia. *Aust. J. Mar. Freshwat. Res.*, 37, 1-10.
- Saville-Kent, W., 1897: *The Naturalists in Australia*. Chapman and Hall, London.
- Semtner, A.J. and Y. Mintz, 1977: Numerical simulation of the Gulf Stream and mid-ocean eddies. *J. Phys. Oceanogr.*, 7, 208-230.

- Thompson, R.O.R.Y., 1984: Observations of the Leeuwin Current off Western Australia. *J. Phys. Oceanogr.*, 14, 623-628.
- Thompson, R.O.R.Y., 1987: Continental-shelf-scale model of the Leeuwin Current. *J. Mar. Res.*, 45, 813-827.
- Thompson, R.O.R.Y., and G. Veronis, 1983: Poleward boundary current off Western Australia. *Aust. J. Mar. Freshwat. Res.*, 34, 173-185.
- USSR Ministry of Defense, 1979: World Ocean Atlas, Vol. 2: Atlantic and Indian Oceans. (S.G. Gorshkov, Ed.), Pergamon Press. 351 pp.
- Walpole, R.E., and R.H. Myers, 1985: *Probability and Statistics for Engineers and Scientists*. 3rd Edition. New York. Macmillan Publishing Company. 639 pp.
- Weaver, A.J., and J.H. Middleton, 1989: On the dynamics of the Leeuwin Current. *J. Phys. Oceanogr.*.
- Wyrtki, K., 1962: Geopotential topographies and associated circulation in the southeastern Indian Ocean. *Aust. J. Mar. Freshwat. Res.*, 13, 1-17.

INITIAL DISTRIBUTION LIST

	No. Copies
1. Defense Technical Information Center Cameron Station Alexandria, VA 22304-6145	2
2. Library, Code 0142 Naval Postgraduate School Monterey, CA 93943-5002	2
3. Chairman (Code 68Co) Department of Oceanography Naval Postgraduate School Monterey, CA 93943	1
4. Chairman (Code 63Rd) Department of Meteorology Naval Postgraduate School Monterey, CA 93943	1
5. LCDR Martin J. Rutherford RAN Australian Joint Maritime Warfare Centre RAN Air Station NOWRA NSW 2540 AUSTRALIA	3
6. Dr. M.L. Batteen (Code 68Bv) Department of Oceanography Naval Postgraduate School Monterey, CA 93943	3
7. Dr. D.C. Smith IV (Code 68Si) Department of Oceanography Naval Postgraduate School Monterey, CA 93943	1
8. Director, Oceanography and Meteorology Department of Defence (Navy Office) Russell Offices (1-15) CANBERRA ACT 2600 AUSTRALIA	1
9. Commander, Naval Weather Centre RAN Air Station NOWRA NSW 2540 AUSTRALIA	1

10. Officer in Charge 1
Australian Oceanographic Data Centre
161 Walker Street
NORTH SYDNEY NSW 2060
AUSTRALIA
11. Dr. G.S. Cresswell 1
CSIRO Marine Laboratories
GPO Box 1538
HOBART TAS 7001
AUSTRALIA
12. Dr. J.S. Godfrey 1
CSIRO Marine Laboratories
GPO Box 1538
HOBART TAS 7001
AUSTRALIA
13. Dr. A.J. Semtner (Code 68Se) 1
Department of Oceanography
Naval Postgraduate School
Monterey, CA 93943
14. Director of Research Administration (Code 012) 1
Naval Postgraduate School
Monterey, CA 93943
15. Director, Naval Oceanography Division 1
Naval Observatory
34th and Massachusetts Avenue NW
Washington, DC 20390
16. Dr. Tom Spence, Director 1
Physical Oceanography
National Science Foundation
Washington, DC
17. Commander 1
Naval Oceanography Command
NSTL Station, MS 39529
18. Commanding Officer 1
Naval Oceanographic Office
NSTL Station
Bay St. Louis, MS 39522